DESIGN OF A NOVEL ROBOTIC SURGICAL INSTRUMENT

DESIGN OF A NOVEL ROBOTIC SURGICAL INSTRUMENT

By

HEATHER KER, B.ENG.

A Thesis

Submitted to the School of Graduate Studies

in Partial Fulfillment of the Requirements

for the Degree

Master of Applied Science

McMaster University

MASTER OF APPLIED SCIENCE (2009)   McMaster University

(Department of Mechanical Engineering)   Hamilton, Ontario

TITLE: Design of a Novel Robotic Surgical Instrument

AUTHOR: Heather Ker, B.Eng. (McMaster University)

SUPERVISOR: Dr. Gary Bone

NUMBER OF PAGES: xix, 214

ABSTRACT

Compared with traditional laparoscopic surgery, robot-assisted surgery can return all six degrees of freedom (DOF) to the surgeon, provide stereovision, filter tremors and increase precision for positioning and manoeuvring the surgical instruments. The instruments used with commercially available surgical robots use external actuation in the form of relatively large motors located outside the patient with a cable transmission system to bring rotation to the instrument's wrist. The goal of this research is to shift away from the external actuation and design a surgical instrument that is internally actuated. This is expected to miniaturize the overall device, enable instruments to be created with a greater number of DOF than possible using the cable-driven approach, enable the creation of modular designs with a "plug and play" capability and increase the precision of position and force control.

A novel internally-actuated instrument has been designed and prototyped using 6 mm DC motors and miniature transmissions. It features four DOF: an elbow joint, a roll joint, and a wrist joint that employs two independently-actuated gripper jaws to allow for both rotation and grasping ability. The elbow joint is a unique feature that helps to avoid collisions with internal organs.

The design of the instrument has been explored in detail. After outlining the target specifications of the device, justification is provided for the selection of the DC motors. Additionally, the thermal properties of the motors have been examined to determine safe current limits. The design of the transmission mechanism (lead screw plus slider-crank) has been analysed and an optimization algorithm for the slider-crank parameters has been

developed. Design calculations have been conducted to analyse the kinematics and static loading of the device and finite element analysis (FEA) has been executed to determine the stress concentrations due to the loading. Justification is also given for the component and material selection.

A prototype intended as a kinematic model has been manufactured and assembled. The speed performance of the prototype has been tested using two methods: the first used video motion analysis to determine the average speeds of the elbow, roll and wrist joints; the second utilized a potentiometer to measure the instantaneous speed profile across the range of elbow joint motion. Overall, the elbow joint operated at an average speed of 2.0 rpm, the roll joint operated at 40 rpm, and the gripper jaws in the wrist operated at around 3.8 rpm. The potentiometer tests revealed that the joint performed in accordance with the theoretical speed profile, particularly when a correction factor was applied to account for the actual current that was drawn by the motor.

A force experiment was also conducted to confirm the torque capabilities of the miniature brushed DC motor used in the prototype. Results showed that the motor, attached to the lead screw and slider components of the elbow joint mechanism, performed at about 15% efficiency. The motor was able to supply a torque of up to 4.2 mNm while maintaining an acceptable current level to avoid over-heating.

ACKNOWLEDGMENTS

TABLE OF CONTENTS

LIST OF FIGURES

LIST OF TABLES

CHAPTER 1

INTRODUCTION

1.1 Background

Prior to 1985, abdominal surgery was performed exclusively via open surgery. For this procedure, a large incision is made in the abdominal cavity to reach the major organs. Advantages of this method are visibility and manoeuvrability; opening the abdomen and exposing the organs allows the surgeon to see exactly what they are doing and use the dexterity in their wrists to perform the surgery. This dexterity allows not only for the use of all six degrees of freedom[1] (DOF), but also for a relatively large range of motion of each DOF. One major disadvantage of this method is the trauma to the body caused by the large incision. This results in longer recovery times and more use of hospital resources. In order to reduce the trauma to the patient, increase rate of recovery and decrease hospital costs, there has been a shift to minimally invasive surgery (MIS).

One form of MIS is traditional laparoscopic surgery. The first laparoscopic surgery was performed by Mühe in 1985. Within the next ten years, laparoscopic surgery became the preferred method over open surgery for relatively simple procedures, such as the removal of the gall bladder (a cholecystectomy). In 1993, the laparoscopic method

---

[1] The six DOF include translation along three axes and rotation about those axes, often referred to as roll, pitch and yaw.

was used for 67% of all cholecystectomies performed in the United States (Graves, 1993).

Traditional laparoscopic surgery involves creating small incisions roughly 1 cm in length, into which trocars (or ports) are placed to allow insertion of the instruments. The abdominal cavity is sealed off and filled with CO_2 gas to create room for the instruments to manoeuvre. Since the abdomen is sealed off and therefore not directly visible to the surgeon, an endoscope with a camera is inserted through a port and the image is projected onto a screen. Laparoscopic instruments are typically long and thin, less than 10 mm in diameter, with a small gripper at the tool tip. These manually operated instruments are inserted into the ports to cut, sew and manipulate tissue. Due to the nature of the instrument inserted through a fixed port, the movement is limited to four DOF, as shown in Figure 1.1. Not only have two forms of translation been eliminated, but the pitch and yaw are also constrained to a smaller range of motion than is available for a surgeon's wrist in open surgery. In addition to reducing the dexterity available to the surgeon, traditional laparoscopic surgeries are not very ergonomic and can cause strain on the surgeon during long procedures.
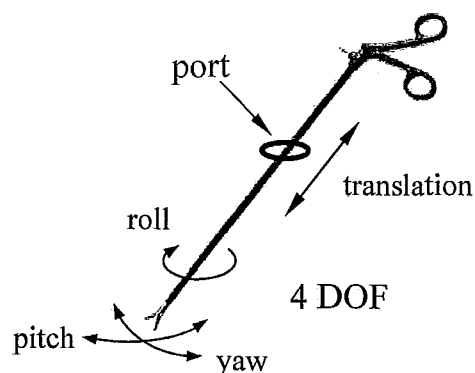
Figure 1.1 Traditional laparoscopic instrument with limited degrees of freedom.

The development of robot-assisted surgery can fix many of the problems associated with traditional laparoscopic surgery. The goal is not to replace the surgeon with a robot, but rather to assist the surgeon in achieving better performance during surgery. Namely, the robotic system can return all six DOF to the surgeon and improve the surgeon's dexterity, provide stereovision, restore hand-eye coordination, filter tremors and increase precision for positioning and manoeuvring surgical instruments, as well as provide an ergonomic working position for the surgeon at the surgeon's console, thus reducing surgeon fatigue (Rassweiler, Binder & Frede, 2001). These benefits allow the surgeon to produce better clinical results, reduce the need for repeated surgery, and results in lower net costs due to shorter hospital stays and quicker recovery times (Taylor et al., 1996).

One problem that remains, and is in fact intensified, is the lack of tactile feedback. There is a learning curve for the use of visual feedback in lieu of tactile indicators, but it has been shown that experienced surgeons can quickly become accustomed to this method (Rassweiler et al., 2001). Another issue associated with the shift to robot-assisted surgery is the high cost of the robotic system, with a capital cost of about US$800,000 and an additional cost of US$100,000 per year (Rassweiler et al., 2001).

To further reduce the invasiveness of surgeries, two new surgical methods are being explored: Natural Orifice Transluminal Endoscopic Surgery (NOTES) and single port access (SPA) surgery. NOTES involves inserting the surgical tools via a natural orifice, either transorally or transgastrically (Rattner & Kalloo, 2006). SPA, on the other hand, involves inserting the instruments through a single incision in the anterior

3

abdominal wall (Rentschler & Oleynikov, 2007). Both procedures aim to reduce visible scarring and trauma to the patient.

1.2 Motivation

Current commercially-available surgical robotic systems, such as the da Vinci surgical system by Intuitive Surgical (2005), are used exclusively for laparoscopic procedures and cannot be used for NOTES or SPA. These robots use cable-driven joints that are driven by motors located outside the patient. The external actuation uses relatively large motors, with cable transmission to bring the rotation axis down to the wrist joints inside the instrument. The friction and mechanical flexibility associated with these cables limit the instrument's positioning precision and its ability to control the interaction forces. Also, this form of external actuation causes the robot to be bulky outside the patient, and provides less access to the patient in case of complications.

The purpose of this thesis is to design an instrument that can be internally actuated. This new internal actuation approach has the following expected benefits:

- Remove the bulky external motors from the surgical field,

- Improve the positioning precision and force control capability due to collocation of the actuators and joints,

- Enable instruments to be created with a greater number of degrees of freedom than possible using the cable-based approach,

- Enable the creation of modular designs with a "plug and play" capability.

The latter two benefits deserve further explanation. With the cable-based approach, to provide each degree of freedom at the distal end of the instrument requires

running two tensioned cables over one or more pulleys. With the internal approach, only small electrical wires need to be supplied to each actuator. Unlike the cables, these wires can be directed without using pulleys and can be bundled together, so more degrees of freedom can be powered. Since the actuators are collocated with the joints (and sensors as necessary) they could be combined into modules that could be reconfigured depending on the surgical requirements. For example, one procedure may require a rotary motion module with a high torque output for tightly closing the grasper coupled to a high precision linear motion module for positioning the tool-tip, whereas another procedure such as suturing may require a series of rotary motion modules for achieving high dexterity.

The internal actuation approach will require the creation of miniature scale actuators, transmission mechanisms and structural components that exhibit sufficient power, strength and speed. These components must also be both sterilizable and biocompatible.

1.3 Organization of Thesis

The thesis is organized as follows. Chapter 2 reviews previous technologies that have been developed for minimally invasive surgeries, including traditional laparoscopic surgery, robot-assisted surgery, NOTES and SPA. Chapter 2 also provides a detailed review of medical devices that use miniature actuators, including electromagnetic motors, piezoelectric motors, hydraulic and pneumatic cylinders and shape memory alloy (SMA) actuators. Chapter 3 outlines the basic concept design, describes how the design specifications were chosen, provides justification for the DC motor selection and

examines the design options for the transmission mechanism. This chapter also explores in detail the design of the lead screw plus slider-crank mechanism that was chosen for this device. Furthermore, the chapter contains design calculations and justification for component and material selection. Chapter 4 describes the manufacture and assembly of the first prototype. This chapter also includes the experimental setup and results for speed tests performed on the elbow, roll and wrist joints, as well as the setup and results of the force experiment that was conducted. Chapter 5 provides a summary of achievements and limitations of this design as well as recommendations for future work.

CHAPTER 2

LITERATURE REVIEW

2.1 Introduction

This chapter covers the relevant research literature that pertains to Minimally Invasive Surgery (MIS), specifically in the realm of surgical robotics. Traditional laparoscopic surgery is briefly discussed, along with a review of the hand-held robotic instruments that have been developed for this field. A review of surgical robotic manipulators is discussed, with an in-depth review of the miniature actuators and the transmission systems that have been used to drive the manipulators. Two new surgical methods, Natural Orifice Transluminal Endoscopic Surgery (NOTES) and single port access (SPA) surgery, are discussed with a review of the technology that has been developed for these applications. Finally, there is a review of micro-actuators used in miniature design and their use in medical robotics to date, including electromagnetic motors, piezoelectric (or ultrasonic) motors, hydraulic and pneumatic cylinders, and shape-memory alloy actuators.

2.2 Minimally Invasive Surgery

Minimally Invasive Surgery (MIS) is a term that covers any surgery that utilizes small incisions to access the organs of the patient, rather than the large incisions that

expose the entire abdomen for open surgery. Types of minimally invasive surgeries include traditional laparoscopic surgery, robot-assisted surgery, NOTES and SPA.

2.2.1 Traditional Laparoscopic Surgery

As described in the previous chapter, laparoscopic instruments pass through a small, fixed port (termed a trocar) to gain access to the abdominal organs. Due to this configuration, there is a reduced range of motion for the tool compared to open surgery and the instrument is limited to only 4 DOF (roll, pitch, yaw and insertion). Another limitation is that the projected view is restricted by the use of a 2-dimensional camera which then displays the image on a 2D monitor. This results in a loss of 3-dimensional depth perception for the surgeon and can severely hamper their ability to perform certain tasks (Rassweiler, Binder & Frede, 2001).

Another disadvantage of laparoscopic surgery is a reduced haptic sense, or tactile feedback, for the surgeon due to the frictional effects of the trocar (Rassweiler et al., 2001). Furthermore, eye-hand coordination becomes impaired due to the fulcrum effect of the instrument rotating about the trocar. When the hand moves in one direction outside the body, the tool moves in the opposite direction inside the body (Bailey & Flowers, 1995). A similar impact of the fulcrum effect is that the long instruments can amplify tremors. If the instrument is inserted deeply through the trocar, small movements outside the body will result in large movements inside. Similarly, if the instrument is not inserted as deeply, but rather is operating closer to the port, then large movements outside the body will be required to achieve small movements inside the body.

A number of researchers have attempted to return the dexterity to the surgeon by adding articulated joints to the end-effector of the laparoscopic instrument, thus increasing the number of degrees of freedom available. Frede et al. (2007) have developed a commercially available hand-guided mechanical manipulator called the Radius Surgical System, shown in Figure 2.1, which is a hand-held laparoscopic instrument with a deflectable and rotating tool-tip. According to Focacci et al. (2007), these hand controls are not very intuitive and require extensive training to achieve good dexterity. Another commercially available hand-held robotic laparoscopic instrument is the Endopath ETS Compact-Flex45 Linear Cutter, by Ethicon Endo-Surgery Inc. (Focacci et al., 2007). To manipulate the wrist joints of this device, the surgeon requires the use of both hands. As such, this device is not conducive for surgical practice, in which the surgeon is typically operating with more than one instrument at any given time.

Deflectable tip   Ergonomic handle

Rotation of the tip   Rotation of the nob
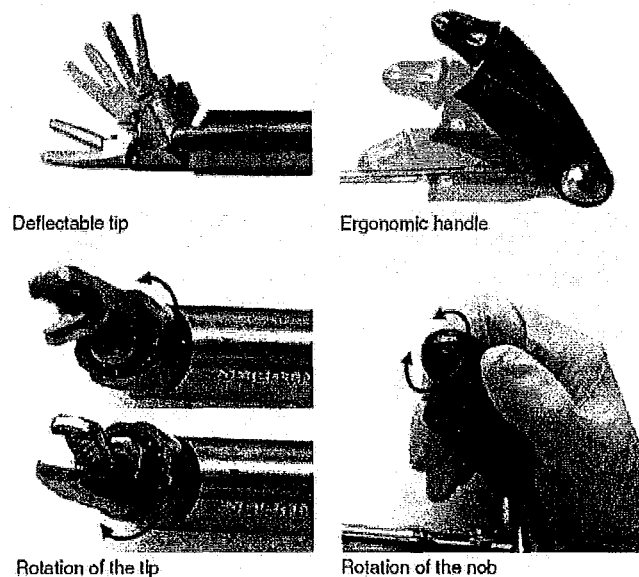
Figure 2.1 The Radius Surgical System (Frede, 2007).

A number of other researchers have developed mechatronic hand-held instruments that contain motors in the handle to drive the wrist joints (Dario et al., 2000; Matsuhira et al., 2003; Yamashita et al., 2004). Matsuhira et al. (2003) have developed what they call a hand-held "Master-Slave Combined Manipulator" (MCM). This device is cable-driven by DC servomotors mounted in the handle, otherwise referred to as the "master grip." The slave has a roll-yaw-roll axis structure, with a $\pm 90^{\circ}$ motion range for both roll and yaw. The instrument has an outer diameter of 12 mm and total length of 700 mm, with an overall weight of 0.6 kg.

One of the major drawbacks of these designs that locate the motors in the handle of the instrument is that the device becomes heavy and cumbersome for the surgeon (Focacci et al., 2007). In addition to the extra weight, the instrument tip is generally integral to the entire design and is therefore not easily interchangeable with the various tools, such as grippers, dissectors and forceps. To compensate for these design challenges, Focacci et al. (2007) have developed a mechatronic system that integrates the EndoWrist® from Intuitive Surgical with a hand-held laparoscopic instrument. They have situated the motors external to the system to avoid unnecessary weight for the surgeon, and connected the motors to the instrument via flexible cable transmission.

Despite the emergence of these mechatronic designs for laparoscopic instruments, Dr. Mehran Anvari (personal communication, June 26, 2007), an internationally-recognized surgeon specializing in robot-assisted surgeries, has indicated that they remain unintuitive for surgeons. The surgeon would need to focus on how to manipulate

individual joints of the instrument throughout the surgery, which takes their concentration away from the procedure itself.

2.2.2 Robot-Assisted Surgery

As mentioned in the previous chapter, robot-assisted surgery solves many of the problems encountered with traditional laparoscopic surgery. The dexterity is returned to the surgeon with additional joints located near the tool-tip; depth perception is restored with stereovision endoscopes; tremors can be filtered out through software; and motions can be scaled to allow more precise movements. These benefits result in better clinical results and quicker recovery times. The downside is the high capital cost and maintenance fees of the robotic system.

Surgical robots can be classified based on a number of criteria: manipulator design, such as kinematics or actuation types; level of autonomy, such as pre-programmed, teleoperated, or controlled with constrained cooperation; or the targeted anatomy or technique, such as cardiac, intravascular, percutaneous, laparoscopic, or microsurgical (Taylor & Stoianovici, 2003). The type of surgical robot of interest to this research falls into the categories of laparoscopic and teleoperated robotic systems.

There are a number of surgical robots that are commercially available for laparoscopy. The da Vinci Surgical System was developed by Intuitive Surgical in 1999. The surgical robot is mounted on a floor trolley and consists of two manipulators with 6 DOF each, and one endoscope with 4 DOF. The manipulator tool (EndoWrist®) has yaw and pitch joints that are cable-driven, and is available in a variety of 8mm or 5mm diameter instruments such as needle holders, scalpels, scissors or cautery instruments

(Intuitive Surgical, 2007). The surgical system is based on master-slave teleoperation, with a surgical console at which the surgeon can sit comfortably to operate the master manipulators, which send a signal to the robot (with the slave manipulators) to mimic the motions of the surgeon. Another surgical system, AESOP, was developed by Computer Motion in 1992. This system is controlled with pad, foot, voice and remote controls. It can be mounted to either a cart or a table. Each manipulator consisted of 3 DOF. Computer Motion also developed another surgical system, Zeus, in 1998. This system has since been bought by Intuitive Surgical and is no longer commercially available. Similar to the da Vinci system, Zeus is based on a master-slave setup. The robot is mounted on a table, and each manipulator has 3 DOF.

Aside from the commercially available surgical robotic systems, a number of other systems have also been developed by researchers. Çavuşoğlu, Williams, Tendick and Sastry (2001) have developed master-slave robotic manipulators with 6 DOF. The slave manipulators consist of 2 DOF wrists (called the "Millirobot") and 4 DOF positioning arms, depicted in Figure 2.2. This system also has force feedback in 4 axes. They designed their system specifically toward the target tasks of suturing and knot tying, which are difficult to perform with traditional laparoscopic tools. They note that for laparoscopic surgery, it is acceptable to design the instrument to be between 10 and 15 mm in diameter since there are other instruments, such as staplers, that require a 15 mm trocar. Their target design specifications for their Millirobot were to achieve a 1.5 N minimum force at the point of the needle (assuming a curved needle and 15 mm from the grasper to the needle tip), and a target gripping force of 40 N. The target joint speeds

were 540°/s (90 rpm) for wrist roll and 360°/s (60 rpm) for wrist flexion. The yaw and

roll axes are actuated by three DC servo motors located on the end of the tool arm outside

the body.
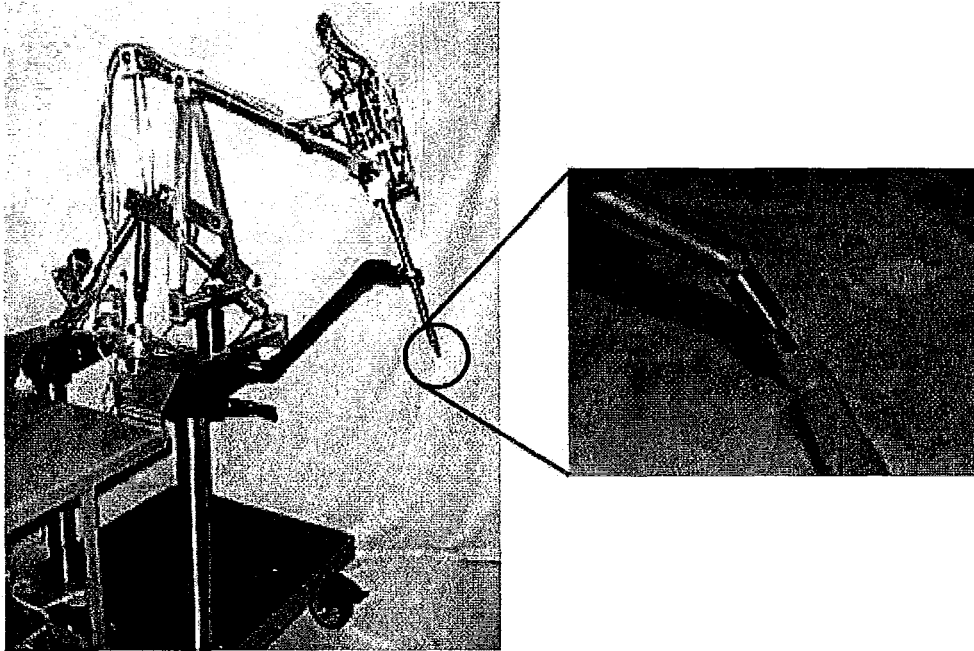
Figure 2.2 Slave manipulator of the UCB/UCSF laparoscopic telesurgical workstation
(left) and close-up view of the millirobotic wrist (right) (Çavuşoğlu et al., 2001).

Madhani, Niemeyer and Salisbury (1998) also developed a teleoperated slave for

minimally invasive surgery, called The Black Falcon. Their system was cable-driven,

with a 4 DOF wrist, a 1 DOF gripper, and a 3 DOF base for positioning. The kinematics

of the base used a double-parallelogram mechanism as a remote centre device, which

allowed there to be no redundant degrees of freedom while always placing the

manipulator through the incision point. The master manipulator was a modified Phantom

haptic interface (SensAble Technologies, 2009) with 7 DOF. The end-effector and

instrument shaft were less than 13 mm in diameter. The design specifications required the stroke within the patient to be from 23-25 cm, with a body penetration of up to 33 cm. The necessary forces were determined by asking surgeons to tug on some tissue through a force sensor "as hard as one might pull during surgery." These forces ranged from ½ to 2 lbs (2.2 - 8.8 N). The grip forces were found to be around 11 lbs (49 N). Maxon RE025 brushed DC servomotors were used to drive the cables for a roll-pitch-pitch-yaw wrist configuration.

It has been noted that current robotic surgical systems require a large workspace within the operating room (OR), up to nearly 100 cubic feet for the robot alone, with additional space required for the operator console and control instrumentation (Stevens & Buckner, 2005). This space required for the robot is due in large part to the actuators used to control each axis of the robot. The bulkiness of the robot prohibits the surgeon from easily accessing the patient, which can be particularly disadvantageous in the case of complications.

One area of research to solve this problem involves miniaturizing the surgical robot to reduce the amount of workspace required. Kobayashi et al. (2002) have designed a small-occupancy robot by using a passive positioning system that is affixed to the operating table and holds the surgical instrument directly above the trocar port. This research group has designed two major components for the surgical robot: an Active Trocar and multi-DOF Active Forceps. The Active Trocar has 3 DOF and determines the positioning of the end-effector inside the abdominal cavity. The Active Forceps are high-

stiffness linkage mechanisms driven by 2.5 watt DC servomotors, ball screws and linear guides. The motors are located outside the patient at the Active Trocar.

The lack of haptic feedback to the surgeon has been cited as another of the major disadvantages of telerobotic surgery. New technology is being developed to reintroduce force-feedback capabilities. Some of this research integrates sensors into existing laparoscopic tools using strain gages or force/torque sensors on the grippers or shaft of the tool to measure the tool-tissue interaction forces during surgery. Tholey and Desai (2007) note that due to the fact that current robotic surgical systems are designed to be non-modular and disposable, the retrofitting of these existing laparoscopic instruments with force sensors would be difficult and costly. As a result, they have developed a new modular, automated laparoscopic grasper that can measure force in three dimensions, using 4 strain gages along the shaft and a small resistive force sensor inside the grasping jaws (Tholey & Desai, 2007).

Other design considerations for surgical robots include sterilizing ability, back-drivability, stiffness, drive philosophy, and redundancy. If the end-effectors contain motors or sensors, gas or soak sterilization methods are commonly used (Taylor & Stoianovici, 2003). Alternatives would be to develop new sensor and actuator technology that would permit easier sterilization, such as autoclaving, or that is cheap enough to be disposable (Taylor & Stoianovici, 2003).

Designing for back-drivability also needs to be taken into consideration. Back-drivable systems allow the tool-to-tissue forces to be reflected to the actuators, which can be advantageous safety-wise to avoid exerting excessive forces on the tissue. However,

non back-drivable systems can also provide safety advantages. If there is a power loss, the robot would freeze in a non back-drivable system, and a heavy tool would not be dropped onto the patient. Also, high-ratio[2], non back-drivable transmissions allow for high precision and good load-carrying capabilities, while using relatively low-power actuators (Taylor & Stoianovici, 2003).

As for the drive philosophy, the most common rotary transmission that is used in surgical robots is the cable or belt drive. This form of transmission allows the motors to be located toward the base of the robot, reduces the size of the end-effector and simplifies the sterilization procedures, and is relatively backlash-free. However, this transmission method does compromise the stiffness of the device (Taylor & Stoianovici, 2003). Another type of transmission system uses small worm gears for the joint rotation. These have been found to be impossible to tune reliably for minimal backlash, although the advantages are the high transmission ratios and orthogonal axes. Since worm gears operate with sliding friction, there is significant wear, causing the backlash to worsen, they are energy inefficient and require sustained lubrication. Taylor & Stoianovici (2003) developed a ball-worm gear as a possible alternative. Other forms of transmission are explored in later sections.

2.2.3 NOTES and SPA

An emerging technique for minimally invasive surgery is called Natural Orifice Transluminal Endoscopic Surgery (NOTES), and involves sending the endoscope and tissue manipulating tools (i.e. grippers) to the abdominal cavity through a natural orifice

---

[2] Those transmissions with a large ratio of output torque to input torque.

in the body, through either a transoral or transgastric route. The basic concept is to minimize visible scarring, since the surgery can be performed without any external incisions, although incisions are still required either through the stomach or the colon wall to access the abdominal cavity. Research continues to be conducted on the viability of this procedure. A committee was formed by The Society of American Gastrointestinal and Endoscopic Surgeons (SAGES) and The American Society of Gastrointestinal Endoscopy (ASGE) to establish goals and tasks to be accomplished in order for this new technique to be implemented (Rattner & Kalloo, 2006).

The emergence of this technique signals a paradigm shift towards further minimizing visible scarring and making surgeries even less invasive than current minimally invasive techniques. Towards this goal, another approach is to develop Single Port Access (SPA) surgeries. Access to the abdomen would be achieved in a similar fashion to laparoscopy, by inserting a trocar into a small incision through the abdominal wall, although the damage would be minimized by requiring only a single incision. This technique would require similar devices to those used for NOTES.

Instruments have been developed that can be inserted through a single port to either acquire images (endoscopes) or manipulate tissue. Rentschler & Oleynikov (2007) have conducted an overview of *ex vivo* commercially-available robotic systems, as well as *in vivo* mechanisms. These *in vivo* mechanisms are medical robots in which all or most of the device enters the body. Different types of these mechanisms exist or are in development. There are manoeuvrable endoscopes that have actuators to manipulate the tip of the endoscope after it enters the body in order to change the surgical view. There

are also locomotion systems based on "inch-worm" motion, or rolling tracks that provide

traction on the slippery, deformable terrain of the abdominal cavity. These require

external power such as electricity or vacuum sources (Rentschler & Oleynikov, 2007).

One example of a mobile miniature robot for the NOTES application is made up

of two mobile wheels for turning, forward and reverse motion, with an adjustable-focus

camera mechanism for taking images during surgery (Rentschler & Oleynikov, 2007).

This robot, depicted in Figure 2.3, is 20 mm in diameter and 90 mm in length, and can be

modified to include an additional arm for biopsy capabilities. Rentschler & Oleynikov

(2007) have also developed a fixed-base robot, illustrated in Figure 2.4, which contains

an adjustable-focus camera that can be tilted up to 45° angles to adjust the line of sight.

The tilting motion is actuated by a DC motor and linkage system. This robot is inserted

and then positioned using traditional laparoscopic tools, and has spring-loaded tripod legs

that open after insertion. The drawback is that the tripod legs can be unstable when

standing on abdominal organs.
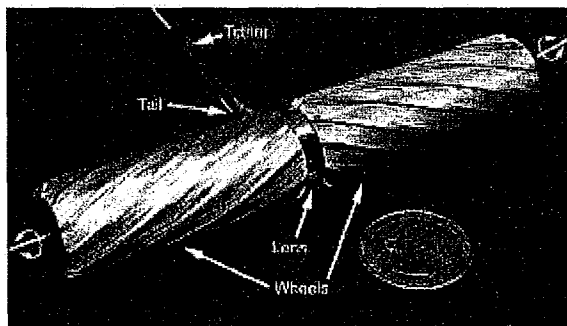
Figure 2.3 20-mm-diameter mobile adjustable-focus robotic camera with helical wheel profile (Rentschler & Oleynikov, 2007).
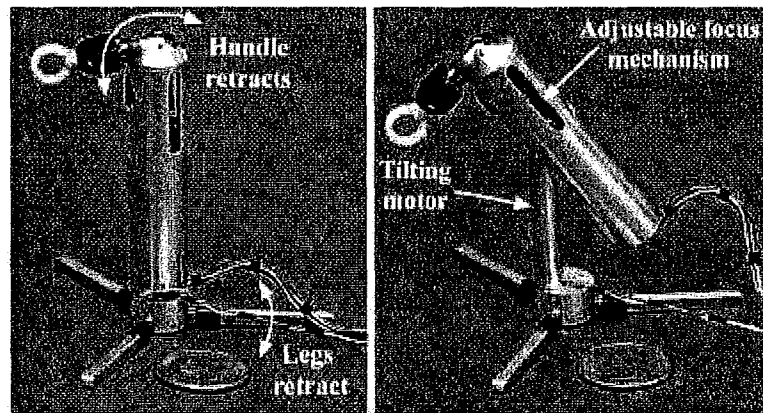
Figure 2.4 Tilting camera robot with spring-loaded tripod legs (Rentschler & Oleynikov, 2007).

Another insertable surgical imaging device has been developed by Hu, Allan, Hogle and Fowler (2008). As shown in Figure 2.5, this endoscopic device has pan and tilt capabilities, with a motorized CCD camera and LED light source for illumination. The tilting joint is actuated using a Smoovy brushless DC motor (0513G) with a 625:1 gearhead (series 06A). The pan motor is similar to that used for the tilt, and is coupled to a worm gear with a reduction ratio of 16:1. The prototype can achieve a panning range of 120° and a tilt range of over 90°. The device has a total length of 110 mm and is 11 mm in diameter to fit into a standard 12 mm trocar. Future designs of this device will incorporate a zooming mechanism, actuated using a 4.5 mm miniature stepper motor attached to a rack and pinion. This zooming mechanism will add an additional 56 mm in length to the device. This device has been tested using *in vivo* animal experiments for a number of surgical procedures, and has been found to be more intuitive and provides a better field of view than a standard laparoscope (Hu et al., 2008).
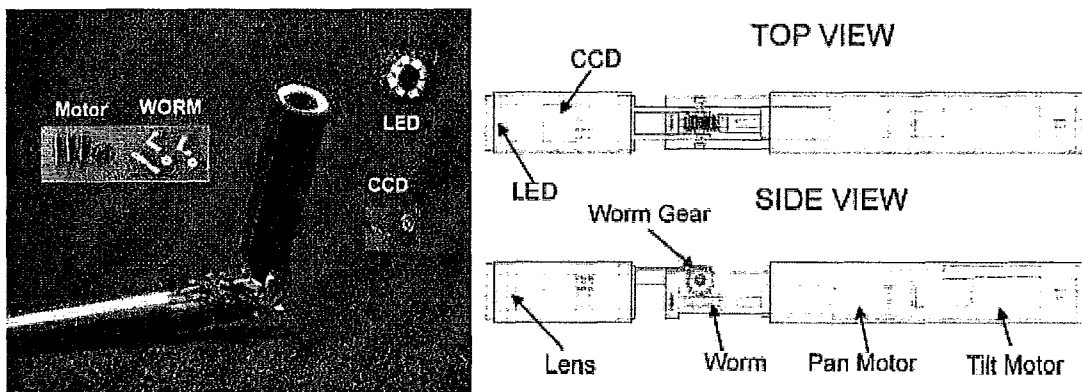
Figure 2.5 Prototype of endoscopic device with LED lighting and pan/tilt axes (right) and CAD model of device (left) (Hu et al., 2008).

Another miniature *in vivo* robot with stereoscopic vision has been developed by Lehman et al. (2008) that incorporates the functions of an endoscope, gripper, and cauterizing tool, as shown in Figure 2.6. The robot consists of two prismatic arms that are each connected to the central body by a rotational joint. The rotational joints utilize an offset slider-crank mechanism driven by a motor and leadscrew. The end-effectors on the left and right arms are a set of forceps and a cauterizing tool, respectively. The robot is attached to the interior abdominal wall by magnets embedded in the body of the robot that interact with an external magnetic handle. By moving this external magnetic handle it is possible to reposition the robot along the abdominal wall. This allows the surgeon to visualize and manipulate from various orientations throughout the procedure (Lehman et al., 2008).
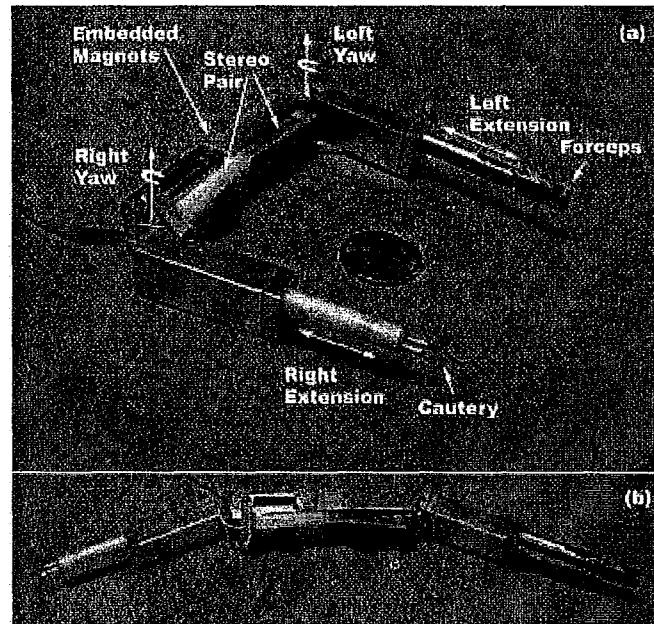
Figure 2.6 NOTES robot in (a) articulation and (b) insertion configurations (Lehman et al., 2008).

Future applications of these types of robots involve using multiple mobile or fixed-base robots with an array of sensors and manipulators that could all be inserted through a single incision to the abdominal cavity, either via natural orifice or otherwise, making up a robotic 'team' to perform the surgeries (Rentschler & Oleynikov, 2007).

2.3 Miniature Design

Micro-engineering design is a relatively new field that explores how best to increase the performance of miniature devices by incorporating miniaturized actuators and sensors and applying theoretical knowledge of micro-scale mechanics (Dario, Menciassi, Stefanini & Accoto, 2002). One of the difficulties of shifting from the macro-scale to the micro-scale is that the relative weight of the forces acting on the device is not

21

linearly related to the decrease in size. The scaling law of forces states that when the linear dimensions are scaled down, the acting forces (often frictional) can be drastically changed, resulting in unexpectedly inefficient behaviours (Dario et al., 2002). The relationship for the scaling law of forces is given in equation 2.1:

$$F \propto L^n \tag{2.1}$$

Where F is the force, L is the typical linear dimension of the machine and n is the scaling exponent. If a force has a positive scaling exponent, n, then it will diminish to insignificance in small scales.

The physics of friction are typically expressed by the Guillaume Amonton's law, in which the force of friction is proportional to the normal contact force times the coefficient of friction. However, this is only applicable in the macro-scale, where dimensions are larger than 1 mm. In the micro-scale, the dominating frictional forces become adhesive contact forces, such as electrostatic, Van der Waals and capillary (Dario et al., 2002). Most of the mechanisms in surgical robotics operate within the macro-scale, but with the miniaturization of devices this research is approaching the borderline of micro-scale systems and these effects may need to be considered.

Ultimately, however, the ability to miniaturize mechatronic devices is driven by the technology available for miniature actuators. The following sections discuss four prevalent miniature actuators used in surgical robotics, namely electromagnetic motors, piezoelectric motors, hydraulic and pneumatic cylinders, and shape memory alloy actuators.

2.3.1 Electromagnetic Motors

There are three types of miniature electromagnetic motors: brush, brushless and stepper. The brush type of electric motors are available from as small as 6 mm in diameter, whereas the brushless DC motors can be as small as 1.9 mm in diameter and 10 mm in length (Yesin, 2000). The limiting factor for the brush type is due primarily to the frictional losses from the brushed commutator, since the effect of these losses increases as the size and torque output decrease. In addition to this, miniature brush motors have a relatively short life expectancy due to the mechanical limitations of the small brushes combined with high motor speeds (Nicoud, Matthey & Caprari, 1998).

Brushless motors, meanwhile, avoid these friction-loss and wear issues since the coils are stationary (located on the stator) and the permanent magnets rotate (located on the rotor). The windings are excited in a coordinated manner to create a rotating magnetic field that drives the rotation of the permanent magnets. Brushless DC motors can also include Hall sensors to detect the position of the rotor and provide closed-loop control, although this feedback has only been implemented for motors larger than 5 mm in diameter (Nicoud et al., 1998).

Advantages of electromagnetic motors over other miniature actuators such as hydraulic cylinders or shape memory alloy (SMA) actuators is that motors are easier to control and are powered by thin, flexible electrical wires that provide less stiffness and space requirements than hydraulic tubing, for example (Peirs, Reynaerts & Van Brussel, 2001a).

There are a number of design considerations to take into account for miniature DC

motors. The first is that there is a general relationship between the size of the motor and

its torque capabilities. As the diameter increases, the circumference of the motor

increases to allow room for more coils, thus increasing the potential output torque. This

relationship is expressed in equation 2.2 (Yesin, 2000):

$$T = k \cdot D^2 \cdot L \qquad (2.2)$$

Where T is the torque, D is the armature diameter and L is the armature length. The

constant, k, depends on parameters such as magnetic field source (i.e. electro-magnet or

permanent magnet), bearings and brushes (Yesin, 2000).

Typical motor characteristics are depicted in Figure 2.7 for a nominal, fixed

voltage. The power output (P = torque x speed), current input (I) and efficiency are also

indicated on the speed-torque plot. For a fixed voltage, the torque increases linearly with

increased current. Similarly, the speed decreases linearly with an increased load. The

maximum efficiency occurs at about 10% of the stall (zero speed) torque.
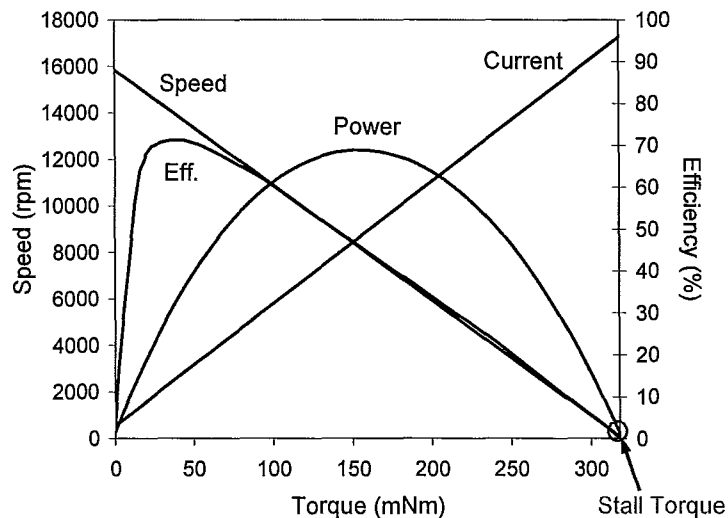
Figure 2.7 Motor characteristics for a fixed voltage (adapted from Yesin, 2000).

Another design consideration is the thermodynamics of the miniature electromagnetic motors. In such tight enclosures, it is imperative to dissipate the heat that is generated to avoid overheating. Dario, Carrozza, Stefanini and D'Attanasio (1998) developed a relationship for the heat transfer rate based on the assumption of heat dissipation by free convection, expressed in equations 2.3 and 2.4:

$$Q = A \cdot h \cdot (T - T_A) \tag{2.3}$$

$$Q = R \cdot I_m^{\,2} \tag{2.4}$$

Q is the heat transfer rate, A is the external surface area, h is the heat exchange coefficient, T is the safe temperature, T_a is the external temperature, R is the total resistance of the coils and I_m is the maximum current. Rearranging these equations, we can solve for the maximum allowable continuous current, I_m, shown in equation 2.5:

$$I_m = \sqrt{\frac{A \cdot h \cdot (T - T_A)}{R}} \tag{2.5}$$

There are a number of manufacturers currently selling miniature brushless DC motors. Specifications vary with size of the motor, with speeds ranging as high as 100,000 rpm and torques ranging from 25 to 600 μNm for motors between 3 to 10 mm in diameter. Power-to-weight ratios are as high as 0.7 W/g. Gearheads with ratios as high as 4000:1 can be attached to the motors to increase the output torque at the cost of increasing the overall length of the actuators (Faulhaber, 2008; Maxon Motor, 2008). These motors are also available in autoclavable, sterilizable versions for use in medical devices. These versions of the motors are made completely of stainless steel, the

lubrication is changed and the motor coils are coated in epoxy in order to achieve sterilizing ability (Faulhaber, 2008).

A number of researchers have used miniature motors as a means of actuation for medical robotic applications. Peirs et al. (2001a) developed a miniature robotic manipulator which extends from a self-propelling endoscope that moves with an inchworm motion. This manipulator is based on a 3 DOF Stewart parallel platform driven by three extending legs, as depicted in Figure 2.8. The extension of each leg is driven by an electromagnetic motor connected to a spindle. Each leg has a diameter of 4.4 mm and a length of 48 mm in its contracted state, with the ability to extend an extra 17 mm. Each leg could achieve a maximum force of 1.2 N and a speed of 5 mm/s. This translates to a joint torque of 9 mNm. The total size of the manipulator, including the three legs and the platform, is 15 mm in outer diameter and a total length of 50 mm in its shortest state.
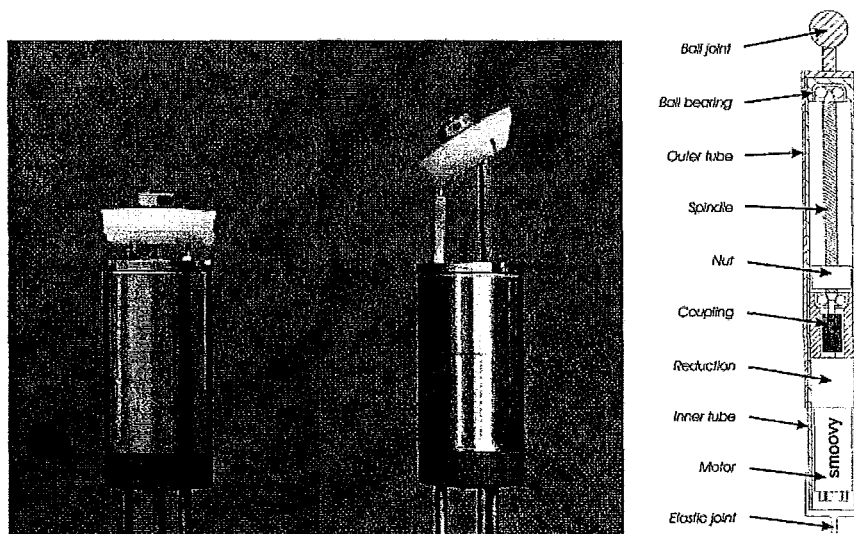
Figure 2.8 Parallel manipulator prototype (left) and design of a single telescopic leg (right) of the Stewart platform (Piers et al., 2001a).

Since this parallel design is larger than desired, Peirs et al. (2001a) also developed

a serial design for their manipulator. This new design has two bending modules arranged

in a serial combination, as shown in Figure 2.9. Each module uses a 3 mm RMB Smoovy

brushless DC motor with a 1:25 gearbox and a worm gear reduction. The range of motion

for each joint is 40° in either direction. Each module is 12.4 mm in diameter and 20 mm

long. According to the data sheets, the motor provides 25 μNm continuous torque and a

maximum speed of 100 000 rpm. With the reduction and input speed limit, the maximum

speed is 1200 rpm. Theoretically, the output torque of the motor with reduction should

be 0.5 mNm, but in practice the motor torque was found to be 0.2 mNm. When combined

with a 28:1 worm gear reduction at 20% efficiency, each module was found to produce

1.2 mNm of torque. They have further miniaturized the manipulator to 8.5 mm in outer

diameter for the next generation of their design. They also noted that the manipulator

should be hermetically sealed in order to protect the mechanical components from dirt

and electrical short circuiting.
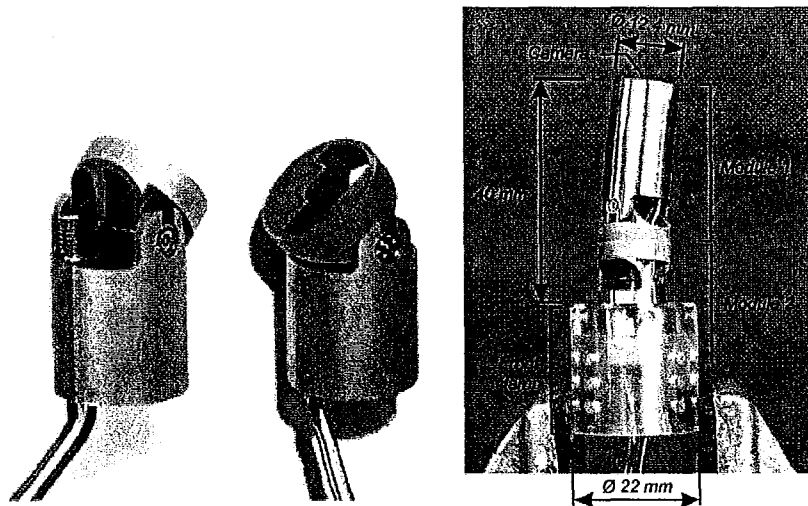
Figure 2.9 Serial module prototype with a 12.4 mm diameter (Piers et al., 2001a).

Yamashita et al. (2003) have also developed a robotic manipulator for laparoscopic surgery using small brushless DC servomotors. These motors, however, are relatively large and are located at the hand-held interface, with 3 units arranged in an equilateral triangle for a total outer diameter of 36 mm. The motors are connected to a lead screw with M3x0.5 threading to provide linear actuation of the linkages. Parallel slider linkages drive the 2 DOF bending mechanism, with a rotational range of 90° in each plane. The overall diameter of the end-effector is 9 mm. The linear motion of the slider linkages has been tested to have a repeatability of less than 1 mm.

Taylor et al. (1996) also designed a surgical manipulator using DC motors acting through a combined harmonic drive and worm gear transmission to drive the revolute joints. They note that one of the major advantages of using high-ratio drive trains is that only small, low-power motors are required, and the mechanism will not move when the power is cut to the motors.

2.3.2 Piezoelectric Motors

An important property of piezoelectric ceramics is the ability to expand when an electric charge is applied parallel to the direction of polarization of the crystals. This response is the driving principle behind piezoelectric motors (also known as ultrasonic motors), which usually consist of a stator made of piezoelectric ceramic layers and a rotor or slider component. There are several designs of ceramic stator geometries, which can allow for either rotary or linear motion. A high frequency voltage supply of around 30 to 50 kHz is supplied to the piezoelectric ceramic and causes high frequency mechanical vibrations in the stator. The rotor (or slider in the case of linear motors) is then driven

along the surface of the stator due to the frictional force caused by these vibrations (Morita, 2003).

A number of piezoelectric motors have been developed for use in miniature drive applications. Bexell and Johansson (1999) created a piezoelectric motor that consisted of 6 multi-layered piezoelectric ceramic beam elements. Each element consisted of two layers of PZT ceramic that could be alternately activated to cause bending and shrinking in each beam. This periodic activation generated an elliptical motion on the tip of the element which drove the rotor by frictional force. Figure 2.10 demonstrates the operating principle in their ultrasonic motor. The motor was 4 mm in diameter and generated a maximum torque of 3.75 mNm and a maximum speed of 65 rpm.
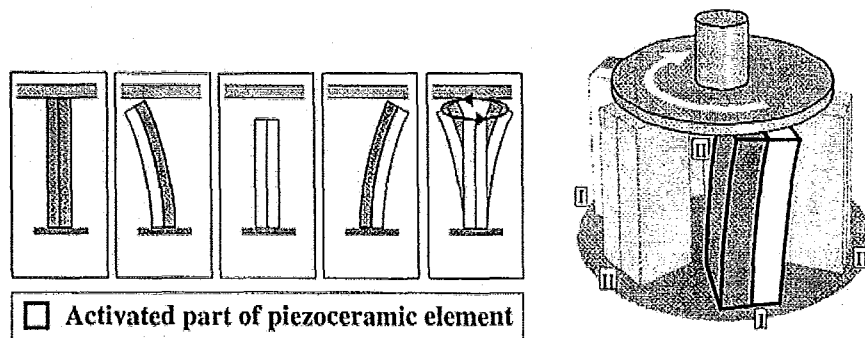
Figure 2.10 Working principle of an ultrasonic motor (Bexell & Johansson, 1999).

Flynn (1997) developed a miniature piezoelectric motor that was 3 mm in diameter and 8 mm in length. The motor was able to reach a maximum speed of 1710 rpm and a stall torque of 10 mNm. In 2003, another research group developed a stator transducer that was 1.4 mm in diameter and 5.0 mm in length (Morita, 2003). The starting torque was measured to 0.67 μNm. This is the smallest piezoelectric motor that has been developed to date.

Rather than using bulk PZT ceramic as in previous designs, Dong et al. (2003) developed a piezoelectric motor using a PZT ceramic/metal composite tube as the stator. The motor shaft was inserted through the center of the tube and attached to two rotors at the ends of the tube. The rotors were then driven by the wobbling motion of the excited stator. This ultrasonic micromotor was 1.5 mm in diameter and 7 mm in length. It was able to attain speeds of 2000 rpm and a maximum output torque of 45 μNm, which was far superior to previous micromotors of that size.

In the commercial sphere, Physkinstrument manufactures a miniature rotary piezoelectric motor that measures only 3 mm in diameter and 6 mm in length, operates at speeds of up to 1000 rpm, and can provide a torque of 0.4 mNm (Physkinstrument, 2008). This piezoelectric motor is the smallest that is available commercially.

A number of researchers have used miniature piezoelectric motors as a means of actuation for medical robotic applications. Polla et al. (2000) developed a piezoelectric linear stepper motor to be used for the precision delivery of a replacement lens into the human eye following cataract removal. The motor was designed to fit into a 1.2 cm x 15 cm hand-held cylinder. The operating principle was based a three-step inertial drive system, in which the fast and slow expansions and contractions of the piezoelectric material would generate movement of an attached mass. The prototypes developed for this design were found to achieve a speed of 1.2 mm/s for a 3 N attached load, a speed of 10 mm/s for no load, and a maximum output force of 4.6 N.

Designing active catheters, as opposed to those manipulated by a guide wire with limited range, is another field of research that has made use of micro ultrasonic motors.

Mashimo and Toyama (2008) developed a piezoelectric motor capable of both rotary and linear motion suitable for endovascular diagnosis and surgery. The stator prototype was a cube of 3.5 mm in length, with a hole in the center through which the motor shaft was actuated by the activation of four piezoelectric elements that were bonded to the sides of the stator. For an applied AC voltage of 42 V_{rms} and at a resonant frequency of 270 kHz, the motor was found to achieve a maximum rotational speed of 260 rpm and a maximum torque of 0.1 mNm. At a resonant frequency of 306 kHz, the motor could achieve a maximum linear speed of 50 mm/s and an axial force of 0.01 mN.

2.3.3 Hydraulic and Pneumatic Cylinders

Hydraulic and pneumatic actuators are attractive for miniature robotic applications due to their relatively high power-to-weight ratios. Hydraulic actuators are typically used in applications that require higher forces and slower speeds than pneumatic actuators can provide, and are thus more appropriate for surgical robot applications.

There are a number of disadvantages of using hydraulics for surgical robotics. One of these is the fact that a hydraulic circuit is required and the device cannot be directly driven electrically. The hydraulic tubes increase both the diameter and the stiffness of the joint (Peirs et al., 2001a). Leakage can also become a safety issue, and for this reason, water is used as the hydraulic fluid.

A number of researchers have integrated hydraulic actuation into designs for surgical robotics. In addition to designing a manipulator using electromagnetic motors, Peirs, Reynaerts and Van Brussel (2000) also designed a similar parallel manipulator using miniature hydraulic cylinders. The design was based on the 3 DOF Stewart

platform, which consisted of three legs that could be extended in parallel. The hydraulic manipulator is 12 mm in outer diameter and 30 mm in length. Each of the cylinders has an internal diameter of 3 mm and can generate forces up to 7 N at pressures up to 10 bar. The pressure was limited by the poor sealing potential of the small cylinders as well as for safety reasons. The real output force of each leg is actually 50% of the anticipated 7 N due to the elastic membrane that generates the return force of the pistons. With each leg then generating 3.5 N, the total force of the platform translates to 10 N. The platform has a stroke of 10 mm and tilts between 30-35°.

Suzumori, Iikura and Tanaka (1991) developed a flexible microactuator for miniature medical robotics. This system is actuated either pneumatically or hydraulically. The cylinders are made up of fiber-reinforced rubber and are divided equally into three chambers that run along the length of the tube. As the pressure in each of the chambers is controlled, bending and stretching is enabled in 3 degrees of freedom based on the elastic deformation of the rubber. A series of these microactuators was developed with outer diameters ranging from 1 to 20 mm. Experiments on a flexible microactuator with a 4 mm outer diameter and 20 mm length resulted in 6.5 mm of stretching, a bending angle of 95°, 0.15 N of bending force and 1.3 N of stretching force.

Sindrey (2006) developed a miniature rotary joint that is actuated by two single-acting hydraulic cylinders with a bore diameter of 4 mm. Since this device is intended for medical applications, the hydraulic fluid is water. The cylinders are attached to a rack and pinion mechanism that transmits the opposing linear actuation of the cylinders into a

rotary motion. Overall, the size of the joint is 11 mm in width, 8.8 mm in height, and 150

mm in length. The range of rotation for the joint was 180°.

2.3.4 Shape Memory Alloy Actuators

Shape memory alloy (SMA) actuators are small wires that extend or contract,

similar to human muscles, when a change in temperature is applied to the material

(Stevens & Buckner, 2005). The most common method for heating the actuator is by

passing an electric current through the material, usually with currents in the range of

milliamperes and voltages of less than 10 V. The material is a nickel titanium alloy that is

non-corrosive, biologically compatible and FDA-approved for medical applications. The

material typically demonstrates strains of 5% to 8% with unit forces as high as 150

N/mm^2 (Stevens & Buckner, 2005; Peirs et al., 2001b). Other advantages of SMA include

a high power/mass ratio, relatively large pulling forces, and simplicity of design

(Bergamasco, Salsedo & Dario, 1991). For these reasons, this form of miniature actuation

has been considered for surgical robotic applications.

Disadvantages of SMA include slow response time and difficulty in controlling

the actuation. Also, since heat is required for the micro-actuation, temperatures in the

system could potentially rise above the safety limit (Peirs et al., 2001b).

A number of researchers have integrated SMA actuation into surgical robotic

designs. Stevens and Buckner (2005) have developed a 10x scaled model of a surgical

manipulator using SMA wires for actuation. The manipulator consists of a frame, four

serial two-link mechanisms, a positioning rod, and a suturing device. A conceptual

diagram is depicted in Figure 2.11. The two links in the serial mechanisms are actuated

by SMA and are 5 mm in length. The robot frame is 8 mm x 12 mm. An artificial neural network along with real-time visual feedback was used to control the device. This allowed the system to "learn" the inverse dynamics and control the trajectory of the manipulator. They tested their 10x scaled model and results demonstrated that the manipulator could accurately track a planned trajectory to within 0.5 mm. This would translate to an accuracy of 0.05 mm for a true scale model.
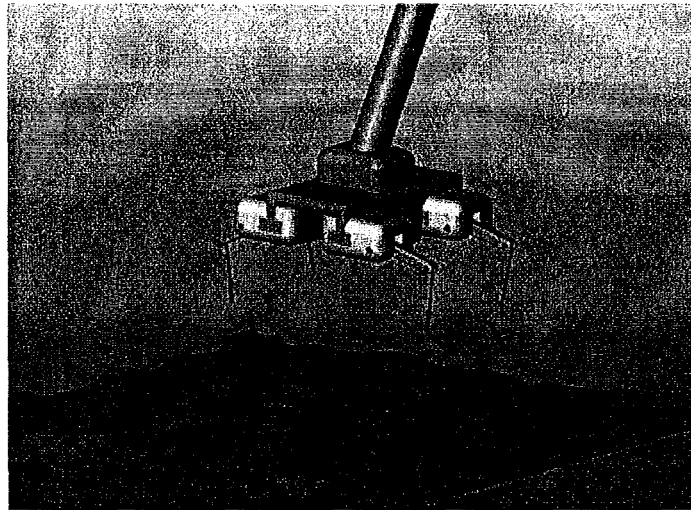
Figure 2.11 Solid model of a conceptual, semiautonomous surgical manipulator using SMA wires for actuation (Stevens & Buckner, 2005).

Nakamura, Matsui, Saito and Yoshimoto (1995) developed an active forceps device for laparoscopy using a structure of SMA pipes. The actuation was controlled by supplying heat via water circulation. The size of the device was 310 mm in length and 7.3 mm in outer diameter. Stiffness of the prototype was found to be 0.26 N/mm at 25 °C and 0.48 N/mm at 55 °C. They designed a controller by combining a theoretical model,

hysteresis compensation and a PID control. Even with this control, the response times of the device were in the range of 9 seconds.

Peirs et al. (2001b) developed three different miniature manipulators to be integrated into a self-propelling endoscope using three types of actuation: SMA, hydraulic and electromagnetic. They compared the performance of these three devices. Originally, they assumed that SMA actuation would be the most favourable due to the high work density and supposed simplicity of the fabrication of the SMA device. However, after testing the various prototypes it was found that the SMA devices actually displayed the lowest work density (1 $\mu J/mm^3$) compared to both the electromagnetic motor (5 $\mu J/mm^3$) and the hydraulic actuator (50 $\mu J/mm^3$). There were also a number of practical complications that arose in constructing the SMA device, particularly in clamping the element and making miniature electrical connections. There was also a need for very high currents to heat the actuator due to the small electrical resistance of the wires. They also found that the SMA actuators were difficult to control due to their non-linearity and large hysteresis. Finally, the SMA actuators proved to have very low efficiency, in the range of about 1% in practice.

2.4 Summary

A review of the technologies used for minimally invasive surgeries, including traditional laparoscopy, robot-assisted surgery, NOTES and SPA has been examined. Towards the goal of miniaturizing surgical robotic devices and using internal actuation, devices that use miniature electromagnetic motors, piezoelectric motors, hydraulic and pneumatic cylinders and shape-memory alloy actuators have been explored. Miniature

electromagnetic motors were found to be the most promising for use in medical devices due to their ease of control, fast response, power density and ease of connection to the external power supply. For these reasons, this type of actuator was chosen for the design of the robotic instrument that follows.

CHAPTER 3

DESIGN

3.1 Introduction

This chapter covers the overall design process of the instrument. The basic concept is introduced along with a description of the joint configuration of the designed instrument. Justification is given for the target specifications, including the joint speeds, joint ranges of motion, the target tool-tip force and the overall size of the instrument. The selection of the DC motors for driving the joints is explained. Design options for the transmission mechanism are explored along with an in-depth analysis of the chosen mechanism: the lead screw plus slider-crank. This analysis includes an examination of the kinematics of the mechanism, the development of a method for defining and optimizing the design parameters, and a process to determine the crank angle range based on the motor torque limits. Component selection, design calculations and stress analysis results are also provided. Finally, an explanation is given for the selection of the materials used in the design.

3.2 Concept Design

An instrument has been designed with four internally-actuated joints: an elbow joint, a roll joint, and a wrist joint that employs two independently-actuated gripper jaws to allow for both rotation and grasping ability. This provides a total of 3 + 1 DOF, with

articulated motion about three axes of rotation plus gripping. See Figure 3.1 for a graphic representation of the basic concept design.
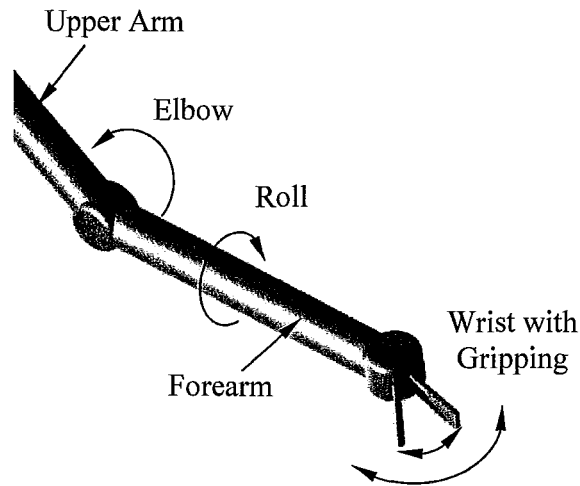
Figure 3.1 Concept design showing motion of elbow, roll and wrist joints.

The elbow joint is a novel design feature that enables better collision avoidance by helping to manoeuvre around internal organs, as demonstrated in Figure 3.2. This design feature was recommended by Dr. Mehran Anvari (personal communication, June 26, 2007).
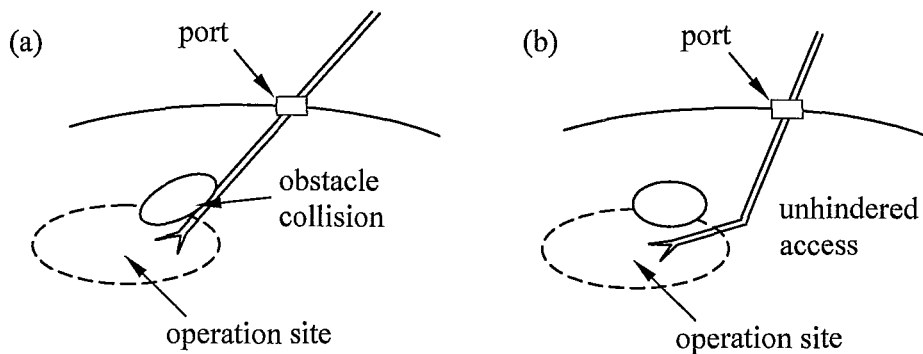
Figure 3.2 (a) Traditional instrument collides with internal organ. (b) Elbow feature of proposed design provides unhindered access.

Although it would be ideal to keep three DOF in the wrist in addition to including an elbow joint, the challenge of incorporating miniature internal actuation for such a design is insurmountable with today's technology. The current design concept therefore provides better collision avoidance but less dexterity than the da Vinci system.

The motion of the elbow joint will bend from the centre in only one direction; by rolling the upper arm it is possible to provide elbow movement in the opposite direction. This should maximize the workspace that can be reached by the instrument.

As mentioned in Chapter 2, miniature DC motors have been chosen for the actuation due to their ease of control, fast response, power density and ease of connection to the external power supply. In miniature sizes, the length of these DC motors is significantly larger than their diameter so the motor rotation axis must be parallel to the housing of the instrument. For three of the four joints (i.e. the elbow joint and two gripper jaws in the wrist), the joint rotation occurs at a right-angle to the direction of rotation provided by the motor, so this necessitates some form of right-angle transmission mechanism to convert the axis of rotation. A diagram illustrating this actuation concept for these joints is shown in Figure 3.3. The primary components include the DC motor, a right-angle transmission mechanism, and the output shaft (or driven link). In addition to converting the rotary motion of the motor by 90°, the transmission mechanism can also provide some mechanical advantage.
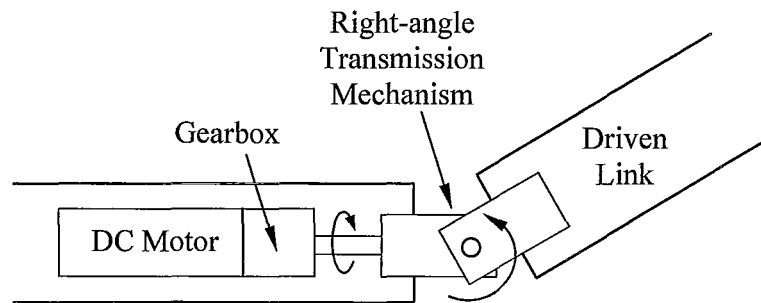
Figure 3.3 Actuation concept for the elbow and wrist joints.

3.3 Specifications

Specifications of the average joint speeds and range of motion, the target tool-tip force and the overall size of the instrument were determined based on a number of factors.

A target for the average joint speeds was determined by performing video motion analysis on existing videos of surgical procedures. Video motion analysis software from the Institute for Rehabilitation Research and Development (2009) was used to determine the angular speeds of joints in pitch, roll, and gripping. This software, which is used primarily in biomechanical field for gait analysis, allows the user to upload videos and measure angles and time on the still-frame images. The videos that were analyzed for this research consist of suturing procedures performed with the EndoWrist® as part of the da Vinci Surgical System. Suturing was chosen because this procedure requires speed and dexterity to perform the relatively complex sewing motions, and it was deemed to be a good gauge for the speeds and angle ranges that would be required. The videos were

downloaded from a number of online sources (OR-Live, 2009; University of Southern California, 2007).

The EndoWrist has different joint configurations than the proposed design for this work; both the pitch and gripping occur at the wrist, so an examination of the pitch and gripping speeds of the EndoWrist can provide a benchmark for target joint speeds for the wrist of this design. The raw data for these results is listed in Table A.1 in Appendix A, and an example of images of the video motion analysis results are shown in Figures A.1 to A.6, also in Appendix A. The speed results of the pitch ranged from 4 rpm to 24 rpm over eleven samples, with a mean of 11 rpm. The speed results of the gripper ranged from 11 rpm to 39 rpm over six samples, with a mean of 21 rpm. From these results, the target wrist speed for this design was set to 20 rpm.

The roll speeds of the EndoWrist were calculated by recording the time it took for the instrument to roll roughly 90° or 45°. These angles were based on visual estimates, an example of which is shown in Figures A.3 and A.4 in Appendix A. The speed results of the roll ranged from 11 rpm to 30 rpm over six samples, with a mean of 19 rpm. From these results, the target roll speed has also been set to 20 rpm.

Since the elbow joint is a novel addition to the design, and is intended mostly for gross positioning of the instrument around organs rather than fine movements, the target speed has been chosen to be 10 rpm, slightly lower than that measured for the pitch of the EndoWrist®. These target speeds are initial estimates that would need to be tested clinically to confirm that they are suitable targets for the joint configuration of this design.

The target ranges of motion for each joint have been chosen to approximately mimic the motion of a human wrist and forearm. Thus the target range for the elbow joint is 90° from centre, the target range for the roll joint is a 180° rotation, and the target range for the wrist is 45° to either side, with a total range of 90°.

Based on the performance goals set by a few research groups developing similar devices, most notably Çavuşoğlu et al. (1999) and Madhani, Niemeyer and Salisbury (1998), the target force at the tool-tip has been chosen to be 2 N. Based on the moment arm from the tool-tip to each of the joints, this force dictates the torque limit that each joint will have to withstand.

Size constraints have been determined based on a number of factors. For the overall diameter of the instrument, it is necessary that the tool can be inserted into a standard trocar, which is typically 15 mm in diameter. The standard size tube that would provide adequate clearance into this sized trocar is 12.7 mm in outer diameter (1/2 inch tube). The length of the forearm, or the distance from the tool-tip to the elbow joint, has been designated to be roughly half the distance between the abdominal wall and the organs when the abdomen is pressurized. Standard laparoscopic instruments are typically about 330 mm in length, with the exception of pediatric or bariatric (obese) cases, in which the lengths are around 200 mm or 450 mm, respectively (Stryker, 2009). As such, the maximum length of the forearm should be no more than 100 mm.

The target specifications for the speed and range of motion for each joint, the tool-tip force requirement, and the overall dimensions are listed in Table 3.1.

Table 3.1 Target design specifications.

Specification	Value
Speed: Elbow Joint	10 rpm
Speed: Roll Joint	20 rpm
Speed: Wrist Joint	20 rpm
Range of Motion: Elbow	90°
Range of Motion: Roll	180°
Range of Motion: Wrist	90°
Tool-tip Force	2 N
Length of Forearm	100 mm
Instrument Diameter	12.7 mm

3.4 DC Motor Selection

Due to the overall size constraint and knowing that the wrist would require two motors located side-by-side[3] to deliver independent actuation of each gripper jaw, it was determined that the motors could be no more than 6 mm in diameter.

Two types of DC motor are available in this size, brushed and brushless. A DC brush motor includes a stationary stator consisting of permanent magnets, a rotating armature or rotor consisting of several coils, and a commutator that uses brushes to switch the direction of current flow through the armature coils. This creates a magnetic attraction that drives the rotation.

For a brushless DC motor, on the other hand, the coils are situated as the stator and the permanent magnets are used as the rotor. The coils are switched in a coordinated fashion to create a rotating magnetic field that drives the rotor. To ensure reliable switching, the position of the rotor is sensed using several hall effect sensors. Due to this

---

[3] The option of staggering the motors was rejected because it would result in only a small reduction in diameter while greatly increasing the overall length of the wrist joint.

need for external control, the brushless DC motor requires much more complex electronics than a brushed DC motor, which requires simply a DC voltage supply to operate.

Another impact of this is the number of wires required for each motor. For a brushed DC motor, only two wires are required: one to supply the power and one for the ground. For a brushless DC motor with three phases, eight wires are required: three to supply power to each coil, three to receive the signal from the hall effect sensors, one to supply power to the sensors and one for the ground. With three motors located in the forearm, to use brushless DC motors would require at least twenty wires to travel through the elbow joint, which could cause issues for available space.

One downside to the brushed motors is that, due to the contact between the brushes and the coils, there are increased losses due to friction. The brushes are also susceptible to wear. The outcome of these friction losses is a lower power density for the brushed DC motors compared to the brushless type. A brushless DC motor of the same size can produce anywhere from five to ten times the amount of power as a brushed motor.

Another significant discrepancy between the brushed and brushless DC motors is their cost. Miniature brushed motors can be obtained for as low as $20 (Gizmoszone, 2009). The brushless DC motors, on the other hand, cost over seventeen times that, at about $350 each (Faulhaber, 2009).

The manufacturer's motor specifications for the Faulhaber and Gizmoszone motors are given in Table 3.2, along with specifications for two different gearboxes for

each motor. The specification sheets from which these values have been drawn can be found in Appendix E. The gearbox efficiencies of the Gizmoszone motors have not been provided by the company; however, comparing similar gearboxes from various manufacturers indicates that efficiencies of about 60% and 50% can be expected for gear ratios of 136:1 and 700:1 (Faulhaber, 2009; Maxon Motor, 2009).

For the Faulhaber motor operating at its maximum power of 1.58 W, the motor torque is given as 0.37 mNm at a speed of 40,000 rpm. For a 64:1 gearbox with a 70% efficiency, the output torque at maximum power (M_{out}) can be calculated to be 16.6 mNm, based on equation 3.1, where M_{max} is the motor torque at maximum power, *Ratio* is the gearbox ratio, and η_{gear} is the gearbox efficiency.

$$M_{out} = M_{max} \times Ratio \times \eta_{gear} = (0.37 \text{ mNm})(64)(0.70) = 16.6 \text{ mNm} \qquad (3.1)$$

Similarly, one could expect an output torque of 4.74 mNm at maximum power for the 16:1 gearbox with 80% efficiency, and 56.8 mNm at maximum power for the 256:1 gearbox with a 60% efficiency. However, due to the friction caused by the gear trains as well as the mechanical strength of the small gears, a limit of 25 mNm is specified for the 256:1 gearbox, as indicated in Table 3.2. The Gizmoszone motor with a 700:1 gearbox experiences a similar phenomenon. Based on a motor torque of 0.12 mNm and a gearbox efficiency of 50%, one could expect an output torque of 43.0 mNm at maximum power. However, a limit of 19.6 mNm is specified for this motor and gearbox.

The maximum output power has been calculated using equation 3.2, where N is the output speed in rpm and T is the output torque in Nm. For the Faulhaber motor with a 64:1 gearbox operating at 625 rpm at a torque of 16.6 mNm, the power is 1.09 W. The

maximum output power values for the other motor and gearbox configurations have been

calculated in a similar manner and are listed in Table 3.2.

$$P = N \times T \times \frac{2\pi}{60 \text{ s/min}}$$ (3.2)

Table 3.2 Manufacturer's motor specifications (Faulhaber, 2009; Gizmoszone, 2007).

Specification	Faulhaber 0620 012 B			Gizmoszone GH6123S GH6124S	
Motor Type	Brushless			Brushed	
Operating Voltage	12 V			3 V	
Motor Speed at Max Power	40,000 rpm			14,000 rpm	
Motor Torque at Max Power	0.37 mNm			0.12 mNm	
Torque Constant	2.91 mNm/A			N/A	
Motor Resistance	59 Ω			8 Ω	
Gear Ratio	16:1	64:1	256:1	136:1	700:1
Gearbox Efficiency	80%	70%	60%	60%	50%
No Load Speed	6250 rpm	1560 rpm	390 rpm	200 rpm	40 rpm
Output Speed at Max Power	2500 rpm	625 rpm	156 rpm	100 rpm	20 rpm
Output Torque at Max Power	4.7 mNm	16.6 mNm	25 mNm	10.0 mNm	19.6 mNm
Max. Output Power	1.23 W	1.09 W	0.41 W	0.10 W	0.04 W

These given specifications are misleading, however, because there are a number

of limitations to the speed, torque and current that significantly impact the motor's

performance. For example, the manufacturers have recommended a limit to the input

speed for the gearboxes. If the input speed is too high, it causes larger impact forces on

the gears and could cause them to fail. This limit on the input speed greatly decreases the

speed potential of the motors. The Faulhaber motor, for example, can theoretically attain

speeds of up to 100,000 rpm according to the manufacturer's spec sheet given in

Appendix E, but the gearbox can only take speeds up to 8,000 rpm. From the Faulhaber

torque curve given in Appendix E, one can linearly interpolate between a maximum torque of 0.58 mNm at no speed and a torque of 0.37 mNm at a speed of 40,000 rpm. This gives a maximum torque of 0.576 mNm for a speed of 8,000 rpm.

Because the instrument may be in near continuous use during a medical procedure lasting more than an hour, it is important to determine the continuous motor current which corresponds to a maximum allowable steady-state motor winding temperature. The time constant of the Faulhaber motor is 149 seconds, so it will reach 99% of its steady-state value after 12 minutes of continuous use. The steady-state winding temperature of the motor can be calculated using equations 3.3 and 3.4, from the motor calculation sheet by MicroMo Electronics (2009), where the steady-state winding temperature is T_w, the ambient temperature is T_{amb} and the steady-state temperature increase is T_{inc}. In equation 3.4, the current is I, the motor resistance is R, the thermal resistance from the winding to the motor housing is given by R_{th1} (in °C/W) and the thermal resistance from the housing to the ambient is R_{th2}.

$$T_w = T_{amb} + T_{inc} \tag{3.3}$$

$$T_{inc} = I^2 R \times (R_{th1} + R_{th2}) \tag{3.4}$$

If the maximum allowable winding temperature is known, it is possible to limit the continuous current by rearranging these equations to give equation 3.5.

$$I_{max} = \sqrt{\frac{(T_w)_{max} - T_{amb}}{R \times (R_{th1} + R_{th2})}} \tag{3.5}$$

For the Faulhaber brushless DC motor, the motor resistance is 59 Ω and the thermal resistances are 14 °C/W and 88 °C/W, respectively. For a maximum allowable winding

temperature of 100 °C (from the Faulhaber specifications shown in Appendix E) and an

ambient temperature of 37 °C, which is approximately the temperature within the human

body (Elert, 2005), this gives a maximum continuous current of 0.1 A. This analysis

assumes that the body can safely dissipate the heat produced by all four motors which is

$4I^2R = 4(0.1 \text{ A})^2(59 \text{ }\Omega) = 2.36$ W. This is reasonable given that a human dissipates

approximately 80 W when dry (Bronzino, 2005) and up to 600 W when perspiring

(Kosaka et al., 2004).

With the continuous current limit, the maximum continuous motor torque can be

calculated to be 0.291 mNm, considering a torque constant of 2.91 mNm/A given by the

manufacturer. This can then be used to calculate the actual output torque of the motor.

From equation 3.6, the maximum continuous output torque for the 64:1 gearbox would be

13 mNm.

$$M_{out} = (0.291 \text{ mNm})(64)(0.70) = 13 \text{ mNm} \qquad (3.6)$$

The Gizmoszone DC motor, on the other hand, has a motor resistance of 8 Ω. The

manufacture's specifications do not specify thermal resistances, although comparing

similar motors (series RE 6 and 0615 from Maxon Motor and Faulhaber, respectively)

indicates that thermal resistances of around 20 °C/W and 75 °C/W for R_{th1} and R_{th2} is a

reasonable assumption (Faulhaber, 2009; Maxon Motor, 2009). Once again, for a

maximum continuous winding temperature of 100 °C and an ambient temperature of 37

°C, the maximum continuous current for this motor is 0.29 A. However, the Gizmoszone

specifications indicate a rated load for these motors at which the current is lower than this

maximum continuous current. At the rated load, the motor torque is 0.4 gcm (0.0392

mNm), the speed is 23,620 rpm, and the current is 0.0678 A. For a 136:1 gear reduction

and assuming a 60% gearbox efficiency, the maximum continuous output torque

becomes:

$$M_{out} = (0.0392 \text{ mNm})(136)(0.60) = 3.2 \text{ mNm} \qquad (3.7)$$

Similarly, the maximum torque at the rated load for the 700:1 gearbox is 13.7 mNm.

With these additional limits in place, the actual operating specifications have been listed

in Table 3.3.

Table 3.3 Realistic motor specifications under operational loads.

Specification	Faulhaber 0620 012 B			Gizmoszone GH6123S GH6124S	
Motor Speed at Rated Load	8,000 rpm			23,620 rpm	
Max. Continuous Current	0.1 A			0.0678 A	
Gear Ratio	16:1	64:1	256:1	136:1	700:1
Output Speed at Rated Load	500 rpm	125 rpm	31.25 rpm	173 rpm	34 rpm
Max. Cont. Output Torque	3.7 mNm	13 mNm	25 mNm	3.2 mNm	13.7 mNm
Max. Cont. Output Power	0.19 W	0.17 W	0.08 W	0.06 W	0.05 W

The Faulhaber motors, with 16:1, 64:1 and 256:1 gearboxes, are ideal for attaining

the necessary torques required for the wrist, elbow and roll joints, respectively. The

torque requirements are analyzed in further detail in section 3.6. However, due to the

lower cost, ease of control and fewer wires of the brushed DC motors, the Gizmoszone

motors with 136:1 gearboxes (GH6123S) have been used for the wrist and elbow joints

and the motor with a 700:1 gearbox (GH6124S) has been used for the roll joint in the

prototype.

3.5 Design Options for Transmission Mechanism

The two requirements for the transmission mechanism are that it provides mechanical advantage and a right-angle drive to convert the rotary motion from the motor by 90°, as depicted in Figure 3.3 in section 3.2. If we assume a 2 N tool tip force is applied 100 mm from the joint (as it is for the elbow joint), enough mechanical advantage must be supplied by this transmission system to allow the motor, which can only provide torque in the range of 10 mNm, to support a 200 mNm load. Four different transmission mechanisms are examined in the following sections, including bevel gears, worm gears, a lead screw plus rack and pinion, and a lead screw plus slider-crank mechanism.

3.5.1 Bevel Gear

A diagram of the actuation concept for the bevel gear transmission mechanism is shown in Figure 3.4. In order to supply mechanical advantage, the output gear must be larger in diameter than the input gear. For an applied torque of 200 mNm and assuming the motor can supply up to about 10 mNm, for example, the gear ratio would need to be 20:1. Given the sizes of commercially available bevel gears, a gear ratio of this magnitude would be impossible to fit within the size constraints. For the purpose of analysis, however, a set of miter gears (of equal diameter) has been examined to determine the stress capabilities of this type of system.

Driven Link

DC Motor
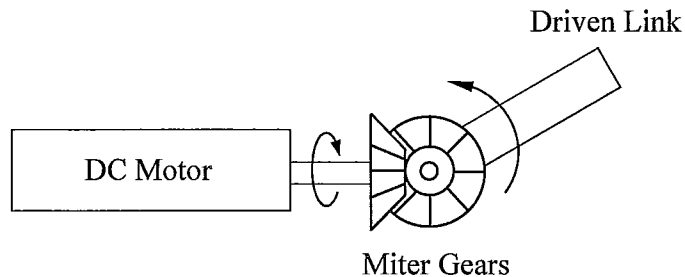
Miter Gears

Figure 3.4 Actuation concept for the miter gear transmission mechanism.

The smallest size of miter gear that is available commercially, from the SDP/SI catalogue (SDP/SI, 2009), has an outer diameter of 7.95 mm (0.313 in). Combining the two gears at right angles would require at least 14 mm clearance.

The allowable torque for these gears can be calculated based on the following equations (Boston Gear, 2006). The safe tooth load, W, is given by equation 3.8, where S is the safe material stress in psi, F is the face width in inches, Y is the Lewis tooth form factor, P is the diametral pitch and V is the pitch line velocity in feet per minute.

$$W = \frac{SFY}{P}\left(\frac{600}{600+V}\right) \times 0.75$$
(3.8)

The allowable torque can then be calculated using equation 3.9, where D is the pitch diameter.

$$T = \frac{W \cdot D}{2}$$
(3.9)

The parameters used for these equations and the resulting load values (converted to SI units) are given in Table 3.4. It can be seen that these gears can withstand a torque of up to 100 mNm, which is less than the 200 mNm that would be required for the elbow joint.

Table 3.4 Miter gear parameters.

Parameter	Value
Safe material stress, S	82.7 MPa (12,000 psi)
Face width, F	2.38 mm (0.09375 in)
Tooth form factor, Y	0.333
Diametral pitch, P	1.9 teeth/mm (48 teeth/in)
Pitch line velocity, V	7.4 mm/s (1.45 ft/min)
Pitch diameter, D	7.95 mm (0.313 in)
Safe tooth load, W	26 N (5.8 lbf)
Allowable torque, mNm	103 mNm

3.5.2 Worm Gear

Another right-angled transmission system that would be able to provide mechanical advantage is a worm drive. A diagram of the actuation concept for this system is shown in Figure 3.5. The smallest sizes of worm and worm gear that are easily available commercially, from the SDP/SI catalogue (SDP/SI, 2009), have pitch diameters of 0.333 in (8.5 mm) and 0.417 in (10.6 mm), respectively. This would require a housing tube of at least 20 mm in diameter, which is significantly larger than the maximum size designated in the specifications.
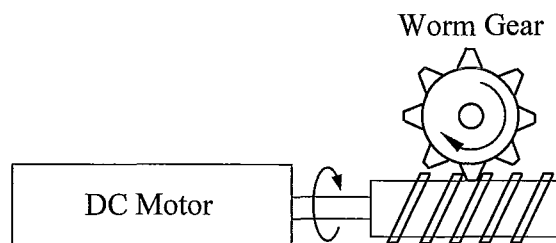
Figure 3.5 Actuation concept for the worm drive transmission mechanism.

Despite the undesirable size for this design, the allowable torque for this worm drive can be calculated based on the following equations (Shigley, Mischke & Budynas,

2003). The allowable tangential force is given in equation 3.10, where C_s is the materials factor, D_m is the gear diameter, F_g is the face width of the gear, C_m is the ratio correction factor, and C_v is the velocity factor.

$$(W_t)_{all} = C_s D_m^{\ 0.8} F_g C_m C_v$$

(3.10)

The parameters used in this equation are listed in Table 3.5. The materials factor, ratio correction factor and velocity factor are defined by equations 3.11-3.13, respectively, where C is the centre-to-centre distance between the worm and worm gear, m_g is the gear ratio, and V_s is the sliding velocity.

$$C_s = 270 + 10.37C^3 \text{ (for C} \leq 3 \text{ in)}$$

(3.11)

$$C_m = 0.2\sqrt{-m_g^{\ 2} + 40m_g - 76} + 0.46$$

(3.12)

$$C_v = 0.659 \exp(-0.0011 V_s)$$

(3.13)

The sliding velocity is defined by equation 3.14, where n_w is the rotative speed of the worm, d_m is the mean worm diameter, and λ is the lead angle.

$$V_s = \frac{\pi \cdot n_w \cdot d_m}{12 \cos \lambda}$$

(3.14)

The allowable torque of the worm gear can then be determined based on equation 3.15.

$$(T_g)_{all} = \frac{(W_t)_{all} \cdot D_m}{2}$$

(3.15)

The values of the parameters defined by these equations are also listed in Table 3.5. It can be seen that the allowable torque was calculated to be 1.68 Nm, which is more than adequate for the 0.2 Nm required.

Table 3.5 Worm gear parameters.

Parameter	Value
Materials factor, C_s	270.6
Gear diameter, D_m	10.6 mm (0.417 in)
Face width of gear, F_g	3.18 mm (0.125 in)
Ratio correction factor, C_m	6.707
Velocity factor, C_v	0.634
Centre-to-centre distance, C	9.53 mm (0.375 in)
Gear ratio, m_g	20
Sliding velocity, V_s	177 mm/s (34.9 ft/min)
Rotative speed of worm, n_w	400 rpm
Mean worm diameter, d_m	8.46 mm (0.333 in)
Lead angle, λ	3.58 deg
Allowable tangential force, $(W_t)_{all}$	318 N (71.4 lbf)
Allowable torque, $(T_g)_{all}$	1.68 Nm

3.5.3 Lead Screw plus Rack and Pinion

By attaching the motor to a lead screw, it is possible to extract mechanical advantage and transform the rotational motion into a linear motion. This can then be used in conjunction with another mechanism such as a rack and pinion to extract rotation that is a right-angle to the original rotation supplied by the motor. A diagram that depicts the actuation concept for this type of transmission system is given in Figure 3.6.
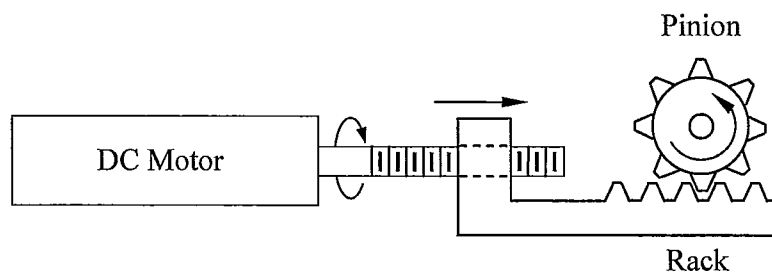
Figure 3.6 Actuation concept for the lead screw plus rack and pinion transmission mechanism.

In order to determine the capability of such a transmission mechanism, the material limits have been determined for the pinion, which is the component that bears the brunt of the 200 mNm applied torque. Equations 3.16 and 3.17 (Boston Gear, 2006) are used to determine the torque rating for the spur gear, where W is the tooth load in lbs, S is the safe material stress in psi, F is the tooth width in inches, Y is the Lewis Form Factor, P is the diametral pitch and V is the pitch line velocity in feet/minute. In equation 3.17, T is the maximum torque that can be supplied to the spur gear, and D is the pitch diameter.

$$W = \frac{SFY}{P} \left(\frac{600}{600 + V} \right) \tag{3.16}$$

$$T = \frac{W \times D}{2} \tag{3.17}$$

The largest size pinion that could fit into a standard half-inch diameter tube would have an outer diameter of 9 mm. From the SDP/SI online catalogue (SDP/SI, 2009), the parameters of the spur gear that meets this criteria are listed in Table 3.6. The material of the gear is 303 stainless steel, which dictates the safe material stress parameter. The pitch line velocity was calculated assuming a 0.1 m/s speed at the tool-tip located 100 mm away from the elbow joint. With these parameters, the torque rating was calculated to be 170 mNm. This is less than the 200 mNm that is required for the elbow joint. In order to meet this specification, the pinion gear would need to be at least 10.5 mm in outer diameter, forcing the overall size of the instrument beyond the desired 12.7 mm diameter.

Table 3.6 Spur gear parameters (SDP/SI, 2009).

Parameter	Value
Outer diameter, O.D.	8.9 mm (0.35 in)
Pitch diameter, D	8.5 mm (0.3333 in)
Diametral pitch, P	4.72 teeth/mm (120 teeth/in)
Face width, F	2.36 mm (0.093 in)
Number of teeth	40
Safe material stress, S	207 MPa (30,000 psi)
Lewis form factor, Y	0.389

Assuming the 8.9 mm spur gear could withstand the 200 mNm applied torque, the maximum linear force acting on the lead screw would be 22.5 N. Additionally, there would be a bending moment applied to the lead screw based on the offset of the rack from the lead screw axis, but for the purposes of this preliminary analysis it is assumed that the effect of this is negligible. Based on equation 3.18, the torque that would be reflected to the motor would be 1.43 mNm.

$$T = \frac{F \cdot l}{\left(2\pi / rev\right)}$$

(3.18)

In addition to determining limits of the pinion gear and the torque reflected to the motor, it is also necessary to determine the stresses that would act on the lead screw based on the following equations (Shigley, Mischke & Budynas, 2003). The maximum nominal shear stress is given in equation 3.19, where T is the torque and d_r is the minor diameter.

$$\tau = \frac{16T}{\pi \cdot d_r^{\,3}}$$

(3.19)

The axial stress due to the load is given in equation 3.20.

$$\sigma = \frac{4F}{\pi \cdot d_r^{\,2}} \tag{3.20}$$

The bearing stress is given in equation 3.21, where F is the axial load acting on the screw, d_m is the pitch diameter, n_t is the number of engaged threads, and p is the pitch.

$$\sigma_B = \frac{-2F}{\pi \cdot d_m \cdot n_t \cdot p} \tag{3.21}$$

Finally, the bending stress at the root of the thread is given in equation 3.22.

$$\sigma_b = \frac{6F}{\pi \cdot d_r \cdot n_t \cdot p} \tag{3.22}$$

The parameters used in these equations are given in Table 3.7, and the resulting stresses are listed in Table 3.8, assuming a M2x0.4 thread. It can be seen that these values all fall well below the 250 MPa maximum allowed stress for stainless steel.

Table 3.7 Lead screw parameters used in stress calculations.

Parameter	Value
Applied torque, T	1.43 mNm
Axial force, F	22.5 N
Minor diameter, d_r	1.5 mm
Pitch diameter, d_m	1.74 mm
Threads engaged, n_t	6.25
Pitch, p	0.4 mm

Table 3.8 Calculated values of M2x0.4 lead screw stresses for rack and pinion transmission mechanism.

Type	Max. Stresses (MPa)
Nominal shear stress, τ	2.1
Axial stress due to load, σ	12.6
Bearing stress, σ_B	3.3
Bending stress at thread root, σ_b	11.4

Although the applied torque translates to acceptable stresses in the lead screw, the size of the pinion that would be needed to withstand the 200 mNm torque is too large considering the space constraints. An additional drawback to this design is that the rack would need to extend beyond the joint.

3.5.4 Lead Screw plus Slider-Crank

Another linear-to-revolute mechanism that could be attached to a lead screw consists of a slider and crank. A diagram that depicts the actuation concept for this type of transmission system is given in Figure 3.7. An advantage of this mechanism is the simplicity and flexibility of the design. There is no limit based on the size of commercially available components, since the small parts can be manufactured with relative ease compared to the gears for the previous mechanisms.

This combination was chosen for the transmission system because it was found from preliminary calculations that this mechanism would be able to support the required loads while remaining within the space requirements. A detailed examination of the torque and stress capabilities of this mechanism are examined in the following sections. Please note that the dimensions assumed for the components, such as pins, are verified in section 3.7.
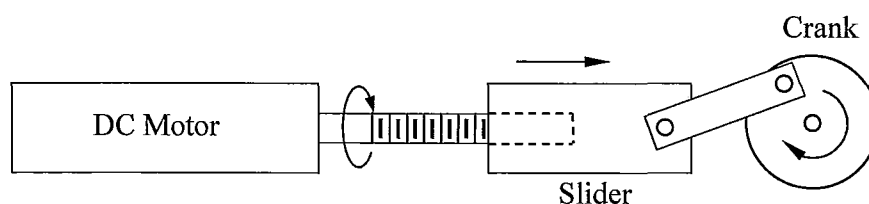
Figure 3.7 Actuation concept for the lead screw plus slider-crank transmission mechanism.

3.6 Detailed Design of Lead Screw plus Slider-Crank Mechanism

3.6.1 Kinematics and Governing Equations

A diagram of the parameters of a slider-crank mechanism is given in Figure 3.8. The angle between the x-axis and r_1 is zero in the proposed design, where the slider moves in a line parallel to the x-axis. The radius of the crank is r_2, the coupler length is r_3, and the offset between the crank pivot and the slider axis is represented by r_4. The linear speed of the slider is the change in r_1 over time, or $\dot{r}_1$. If these parameters are known, based on the geometric relationships it is possible to solve for the crank angle, θ_2. The formula used to solve this case is given in equation 3.23, where t is defined in equation 3.24 and A, B and C are defined in equation 3.25, as derived by Waldron & Kinzel (1999).

$$\theta_2 = 2\tan^{-1} t \tag{3.23}$$

$$t = \frac{-B + \sqrt{B^2 - C^2 + A^2}}{C - A} \tag{3.24}$$

$$\left.\begin{array}{l} A = -2r_1r_2\cos\theta_1 - 2r_2r_4\cos\theta_4 \\ B = -2r_1r_2\sin\theta_1 - 2r_2r_4\sin\theta_4 \\ C = r_1^{\,2} + r_2^{\,2} + r_4^{\,2} - r_3^{\,2} + 2r_1r_4(\cos\theta_1\cos\theta_4 + \sin\theta_1\sin\theta_4) \end{array}\right\} \tag{3.25}$$

Once the crank angle position is known, it is possible to solve for the coupler angle, θ_3, using equation 3.26.

$$\theta_3 = \tan^{-1}\left[\frac{r_1\sin\theta_1 + r_4\sin\theta_4 - r_2\sin\theta_2}{r_1\cos\theta_1 + r_4\cos\theta_4 - r_2\cos\theta_2}\right] \tag{3.26}$$

59

Once θ_2 and θ_3 are known, the associated angular speed of the crank, $\dot{\theta}_2$, and the coupler,

$\dot{\theta}_3$, can be solved using equation 3.27.

$$\begin{bmatrix} -r_2 \sin\theta_2 & -r_3 \sin\theta_3 \\ r_2 \cos\theta_2 & r_3 \cos\theta_3 \end{bmatrix} \begin{Bmatrix} \dot{\theta}_2 \\ \dot{\theta}_3 \end{Bmatrix} = \begin{Bmatrix} \dot{r}_1 \cos\theta_1 \\ \dot{r}_1 \sin\theta_1 \end{Bmatrix} \tag{3.27}$$
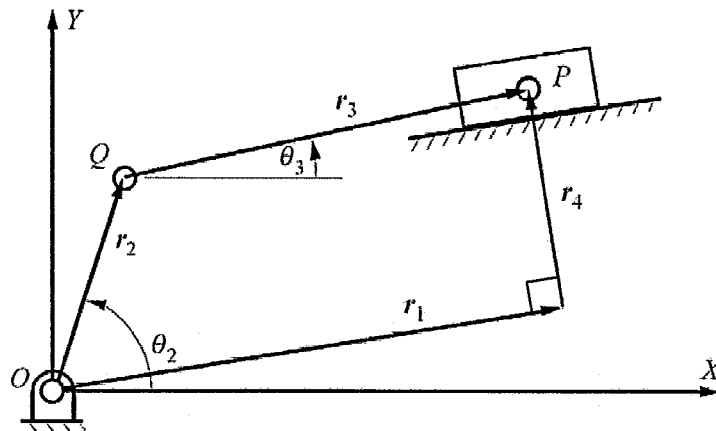
Figure 3.8 Slider-crank schematic (modified from Waldron & Kinzel, 1999).

For a slider-crank mechanism with a constant applied torque, the forces acting on the components change depending on the crank angle. Based on the geometry, at a single crank angle position it is possible to determine the linear force that is applied to the slider due to the moment arm of the crank acting in that direction. Alternatively, it is possible to develop a relationship between the torque that is applied to the crank and the linear force acting on the slider using the law of conservation of energy. If it is assumed that the coupler has no inertia (no mass), it can be said that the work performed by the slider equals the work done on the crank, as expressed in equation 3.28, where F_1 is the force

acting on the slider, $\dot{r}_1$ is the speed of the slider, M_2 is the torque acting on the crank, and

$\dot{\theta}_2$ is the angular speed of the crank.

$$F_1 \cdot \dot{r}_1 = M_2 \cdot \dot{\theta}_2 \qquad (3.28)$$

Two types of software have been used in determining the slider-crank design.

Working Model 2D (Knowledge Revolution, 1996) is a good tool for visualizing the

mechanism and determining the mechanical limits of the design, due to the coupler

colliding with the crank pivot, for example. Another function of Working Model 2D

allows the user to input an applied force to the slider and measure the resulting torque on

the crank at any crank position, or vice versa. See Figure 3.9 for an example. This

software was used for preliminary analysis of the design, but was ultimately deemed to

have insufficient versatility since a new model needed to be created with every parameter

change.
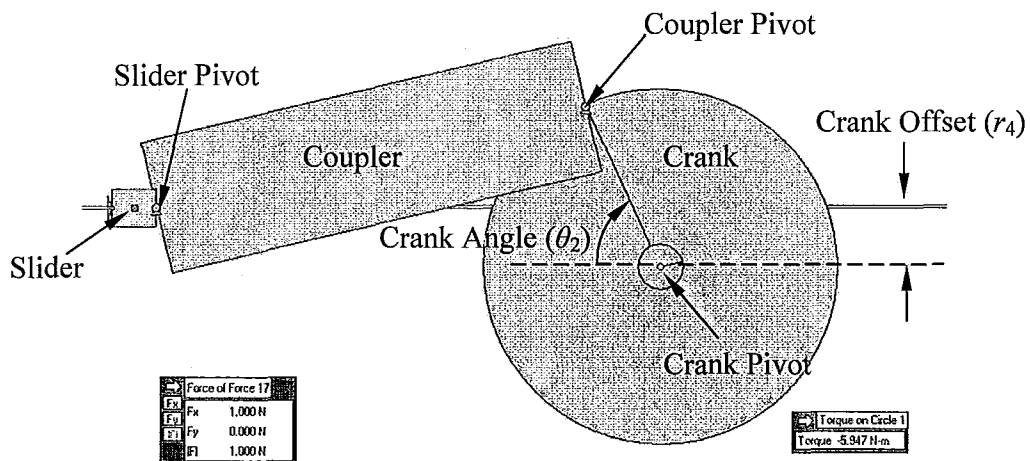
Figure 3.9 Slider-crank design using Working Model 2D.

Matlab code incorporating the kinematics of the slider-crank mechanism was developed to allow iterative changes in the parameters as needed. The original code by Waldron and Kinzel (Waldron & Kinzel, 1999) provides a function that reads the input parameters (r_2, r_3, r_4 and $\dot{r}_1$) and returns the associated crank speed, $\dot{\theta}_2$, at each crank angle, θ_2. The code was modified to also calculate the force that would be exerted by the slider for a given torque applied to the crank, based on equation 3.28 and rearranged to equation 3.29, where M_a is the applied torque given by equation 3.30. In this equation, M_t is the torque due to a 2 N force exerted at the tool-tip and M_w is the torque due to the weight of the instrument beyond the given joint.

$$F_a = \frac{M_a \cdot \dot{\theta}_2}{\dot{r}_1} \tag{3.29}$$

$$M_a = M_t + M_w \tag{3.30}$$

For the design of the elbow joint, which is located 120 mm away from the tool-tip, M_t is 240 mNm and M_w accounts for the weight of the forearm. This parameter is analyzed in detail in section 3.8, where it can be seen that the average applied torque due to gravity is 26 mNm. This gives the elbow joint a total applied torque of $M_a = 240 + 26 = 266$ mNm.

For the design of the wrist joint, which is assumed to be located 15 mm away from the tool-tip, M_t is 30 mNm and M_w is equal to zero since the relative weight of the gripper jaws is negligible. This gives the wrist joint a total applied torque of $M_a = 30$ mNm.

This applied torque was then converted, based on the mechanical advantage

provided by the lead screw (equation 3.18 in section 3.5.3), to the torque that would be

reflected to the motor. Taking the lead screw efficiency into account, the torque reflected

to the motor can be given by equation 3.31, where F_a is the force applied by the slider, as

defined above, F_n is the force acting normal to the direction of motion, μ is the coefficient

of friction between the slider and the support structure, P is the pitch of the lead screw (in

rev/mm), and e is the lead screw efficiency, assumed to be 40% (Mazurkiewicz, 2007).

$$M_{ref} = \frac{1}{2\pi} \frac{F_a + \mu F_n}{Pe} \qquad (3.31)$$

If it is assumed that there is no friction between the slider and the support

structure, especially if the slider is designed to use bearings as a rolling contact, as in the

elbow joint, then the torque reflected to the motor can be simplified to equation 3.32.

$$M_{ref} = \frac{F_a}{2\pi \cdot Pe} \qquad (3.32)$$

The maximum torque that can be reflected to the motor is determined based on

the motor torque limits given in section 3.4, such that the maximum allowable M_{ref} is

equal to M_{out}. The values used in the design for M_a and M_{out} for the elbow and wrist joints

are listed in Table 3.9.

Table 3.9 Applied torque and maximum reflected torque
for elbow and wrist joints.

Joint	M_a	M_{out}
Elbow	266 mNm	13 mNm
Wrist	30 mNm	3.7 mNm

3.6.2 Lead Screw Calculations

The lead screw chosen for both elbow and wrist joints is made from 302 stainless steel with an M2x0.4 thread. The maximum axial force applied to the lead screw can be calculated based on the maximum allowable M_{ref} (equivalent to M_{out} and the maximum torque applied to the lead screw). Rearranging equation 3.32 gives equation 3.33, which results in a maximum applied force of 81 N for the elbow joint and 20 N for the wrist joint.

$$F_a = 2\pi \cdot M_{ref} Pe \qquad (3.33)$$

The stresses in the lead screw are calculated using equations 3.19-3.22 given in section 3.5.3. The parameters used in these equations are given in Table 3.10 and 3.11, for the elbow joint and wrist joint, respectively. The resulting stresses are listed in Table 3.12 and 3.13. It can be seen that these values all fall well below the 260 MPa maximum allowed stress for stainless steel, which indicates that these applied forces are acceptable.

Table 3.10 Lead screw parameters used in stress calculations for elbow joint.

Parameter	Value
Applied torque, T	13 mNm
Axial force, F	81 N
Minor diameter, d_r	1.5 mm
Pitch diameter, d_m	1.74 mm
Threads engaged, n_t	6.25
Pitch, p	0.4 mm

Table 3.11 Lead screw parameters used in stress calculations for wrist joint.

Parameter	Value
Applied torque, T	3.2 mNm
Axial force, F	20 N
Minor diameter, d_r	1.5 mm
Pitch diameter, d_m	1.74 mm
Threads engaged, n_t	6.25
Pitch, p	0.4 mm

Table 3.12 Calculated values of M2x0.4 lead screw stresses for elbow joint.

Type	Max. Stresses (MPa)
Nominal shear stress, τ	19.3
Axial stress due to load, σ	45.7
Bearing stress, σ_B	12.0
Bending stress at thread root, σ_b	41.3

Table 3.13 Calculated values of M2x0.4 lead screw stresses for wrist joint.

Type	Max. Stresses (MPa)
Nominal shear stress, τ	4.7
Axial stress due to load, σ	11.2
Bearing stress, σ_B	2.9
Bending stress at thread root, σ_b	10.2

Additionally, buckling in the lead screw must be considered for the case of compression loading. The critical load necessary to place the lead screw in a condition of unstable equilibrium is defined by equation 3.34 (Shigley, Mischke & Budynas, 2003), where E is the modulus of elasticity of stainless steel (200 GPa), I is the second moment of area of the lead screw, L is the length of the lead screw between the supported ends, and C is the end-condition constant. If we assume a worst-case scenario where both ends are pin-connected (rather than rigidly fixed), then C would be equal to one. When the

65

slider is fully extended, the maximum unsupported length of the lead screw is 9.75 mm in

the elbow joint. With these conditions, the critical load (P_{cr}) is equal to 5,160 N.

Considering the elbow joint exhibits loads no higher than 81 N, this design is well within

the safe range to avoid buckling.

$$P_{cr} = \frac{C\pi^2 EI}{L^2}$$ (3.34)

3.6.3 Slider-Crank Parameters Limits

The first step in determining the slider-crank parameters is to establish physical

limits based on the geometry for both the elbow joint and the wrist joint. The input

parameters to be determined are the radius of the crank, r_2, the coupler length, r_3, and the

crank offset, r_4.

Radius of the crank (r_2):

The radius of the crank can be determined by examining the space available

within a 12.7 mm diameter tube[4], with an inner diameter of 11.7 mm (5.85 mm radius). It

is also necessary to examine the slider-crank mechanism from a front-view, as opposed to

the side-view, as depicted in Figure 3.10.

---

[4] The tube is stainless steel 304 annealed round tubing with a ½" outer diameter (part #GPTX-35/08) from Small Parts (2009).
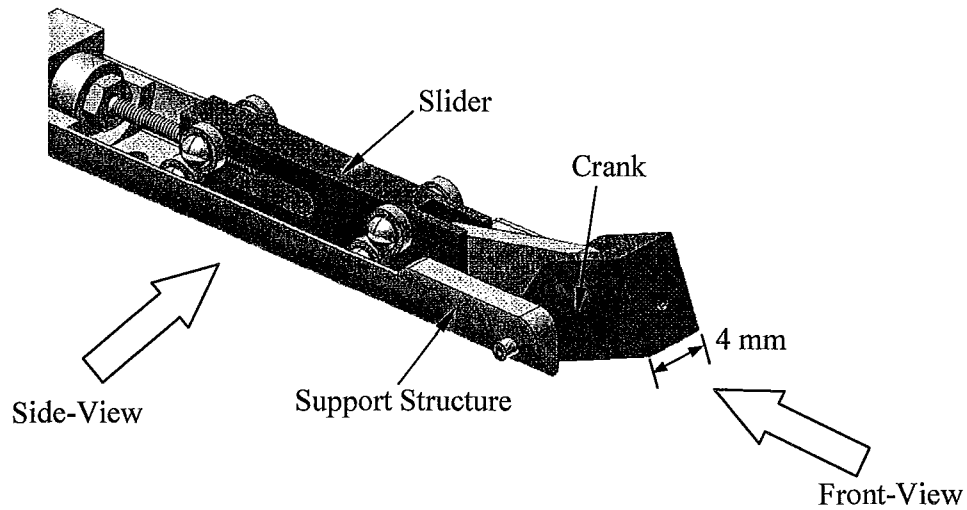
Figure 3.10 Front- and side-views of the slider-crank joint designs.

Initially, it is assumed that the slider axis and joint pivot are aligned (that the crank offset is zero), and thus that the radius of the crank extends upwards from the centre line of the tube. This assumption will be modified later.

For the elbow joint, it was assumed that the coupler-crank mechanism would be at least 4 mm wide and that 1.5 mm clearance for the pin radius and material above the pin would be required. This geometry is represented in Figure 3.11. Using the Pythagorean theorem in equation 3.35, it was found that the radius of the crank could be no more than 4 mm.
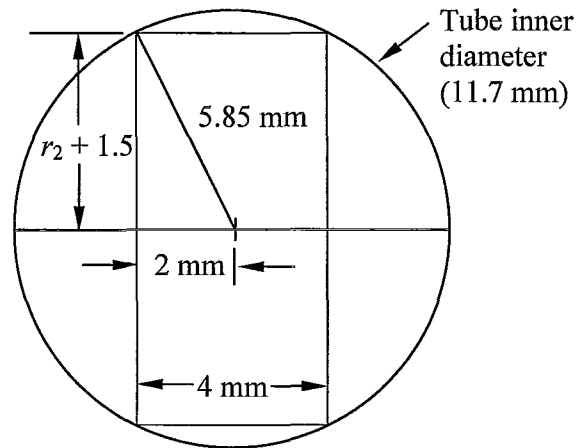
Figure 3.11 Geometric constraints for elbow crank size, r_2.

$$r_2 = \sqrt{5.85^2 - 2^2} - 1.5 = 4 \text{ mm} \qquad (3.35)$$

For the wrist, it was assumed that the coupler-crank mechanism would be at least

3.25 mm wide, including two couplers on either side of the crank, each component being

1 mm in width with additional room for clearance between parts. The motors are each 6

mm in diameter and the inside of the tube was assumed to be approximately 11.7 mm in

diameter (5.85 mm radius), although an elliptical design was ultimately chosen to

accommodate the two motors side-by-side. Additionally, 1.5 mm clearance for the pin

radius and material above the pin was required. This geometry is represented in Figure

3.12, with an expanded view including the dimensions of the pertinent geometry. From

equation 3.36, it was found that the radius of the crank could be no more than 2 mm.
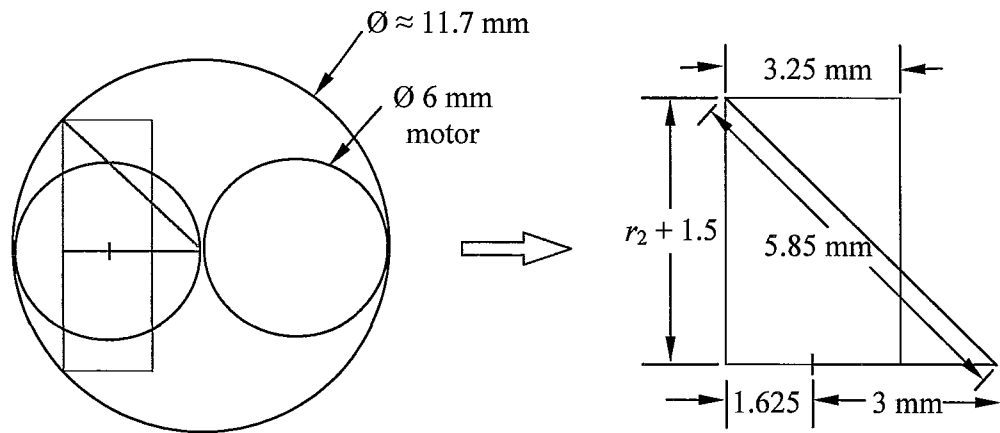
Figure 3.12 Geometric constraints for wrist crank size (left) and expanded schematic with dimensions (right).

$$r_2 = \sqrt{5.85^2 - (1.625 + 3)^2} - 1.5 = 2.08 \text{ mm} \qquad (3.36)$$

As mentioned, it was assumed that the radius of the crank would extend from the centre line of the tube. This is based on the assumption that the crank pivot is located in line with the slider axis. The prospect of lowering the crank pivot, and thus allowing the crank radius to increase, is discussed in the following section on determining the crank offset, r_4.

Coupler length (r_3):

The maximum coupler length was limited to prevent the overall length of the instrument from being too large. An arbitrary length of 20 mm was chosen as the maximum coupler length for the elbow joint, and 10 mm for the wrist joint, for which overall length was more critical.

The minimum coupler length was designated based on the mechanical limits. With the edge of the slider touching the crank pin (i.e. at the closest possible position),

the centre-to-centre distance between the slider and crank pivots would be 2.25 mm. A mechanism has been built in Working Model 2D with typical dimensions for the wrist joint as an example to determine limits due to collision, shown in Figure 3.13. A mechanical stop has been included to prevent the slider from moving closer, to represent this minimum distance between the slider and the crank pin. It can be seen that for the wrist a coupler shorter than 4.5 mm is technically feasible, but would begin to severely limit the crank range potential. With the aim of being able to obtain a crank angle range of at least 100°, a minimum coupler length of 4.5 mm has been chosen. Similarly, for the larger dimensions of the elbow joint, a minimum coupler length of 8 mm is required.
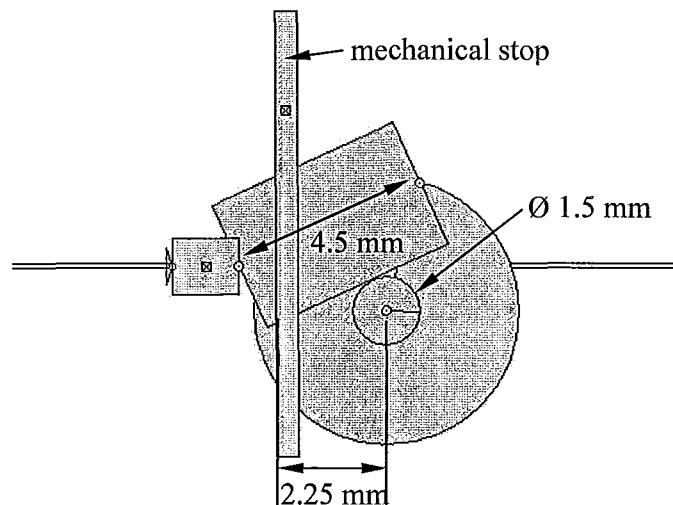
Figure 3.13 Geometric constraints for minimum coupler length, r_3.

Crank offset (r_4):

Another parameter is the vertical offset between the slider axis and the crank pivot, as expressed by r_4 in the diagram in Figure 3.8. There are two ways to increase the

crank offset: the crank pivot can be lowered, or the slider axis can be raised, either by raising the motor and lead screw or simply by raising the slider pivot location.

By again examining the slider-crank mechanism from a front-view, as opposed to the side-view, it was possible to determine the limits due to the support structure that was constrained to a diameter of 11.7 mm. For both the elbow and wrist joints, it was found that crank pivot could be lowered to a maximum of 2 mm, since any lower and the support material for the pivot would become too flimsy, as depicted in Figure 3.14.
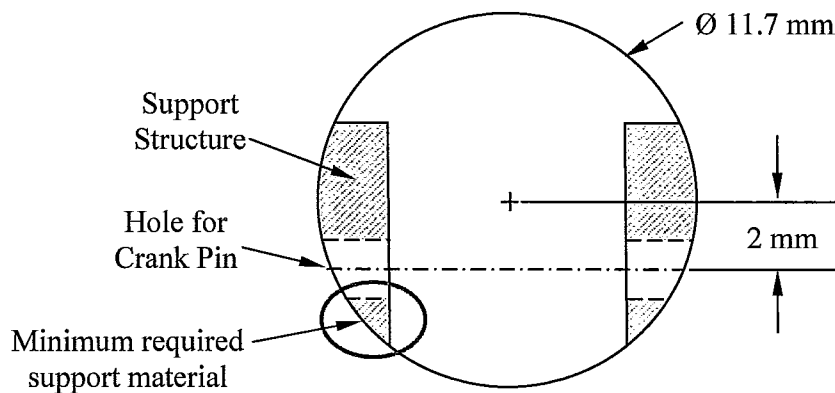
Figure 3.14 Front-view of the support structure to determine geometric constraints for lowering the crank pivot.

As for raising the slider axis, for the elbow joint it was determined that the slider pivot could be raised by a maximum of 1.85 mm. As depicted in Figure 3.15, this was based on the slider's overall height of 6.7 mm, and a 1.5 mm pin that was required to be no less than 1.5 mm from the edge of the material (see section 3.7.1 for the design of the slider). When combined with a 2 mm lowered crank pivot, the maximum crank offset, r_4, would be 3.85 mm for the elbow joint.
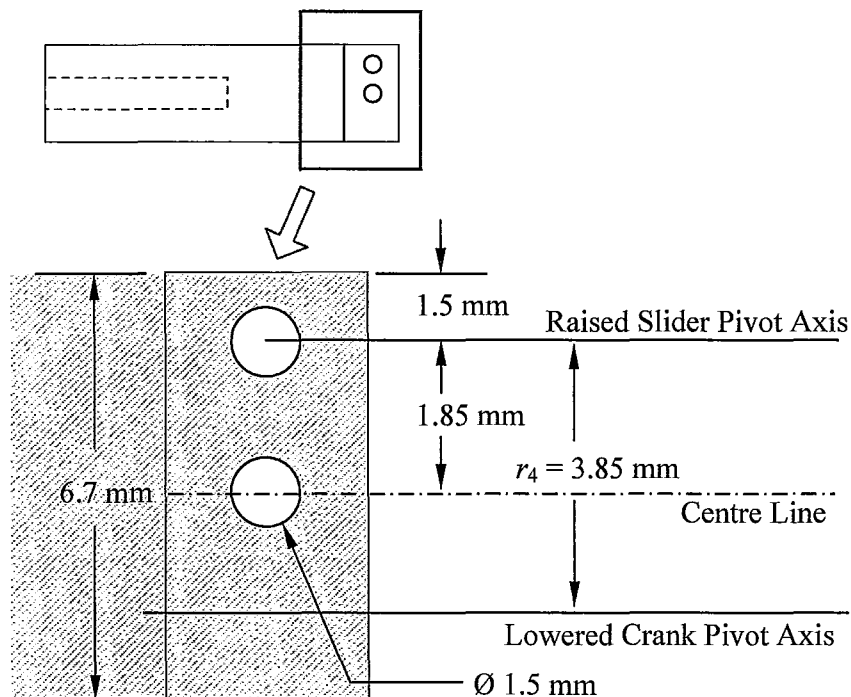
Figure 3.15 Side-view of the slider to determine geometric constraints for raising the slider pivot.

Since the sliders for the wrist joint will be much smaller due to spatial constraints, there is no potential for raising the slider pivot. Due to this, the maximum crank offset for the slider joint is 2 mm, achieved by lowering the crank pivot.

Another advantage to lowering the crank pivot and increasing the crank offset is that the length of the crank, r_2, can then increase. If the crank pivot is lowered by 2 mm for both the elbow and wrist joints, those crank radii can then increase to 6 mm and 4 mm, respectively.

3.6.4 Parameter Optimization

An algorithm was developed to optimize the coupler length (r_3), crank offset (r_4), and lower crank angle limit (θ_{lowlim}). The objective was to determine the design

parameters of the slider-crank mechanism that would minimize the torque reflected to the motor over a given crank angle range. The algorithm (see Table 3.14) uses the Nelder-Mead multidimensional unconstrained nonlinear minimization method, which starts at some pre-defined inputs for r_3, r_4 and θ_{lowlim}, and searches within the bounds of the minimum and maximum limits of these parameters to find the values at which the function is minimized. The function, in this case, is the sum of the torque reflected to the motor at the lower and upper crank angle limits, given by equation 3.37.

$$\sum M_{ref} = M_{ref}(\theta_{upper\lim}) + M_{ref}(\theta_{low\lim}) \qquad (3.37)$$

The upper angle range limit ($\theta_{upperlim}$) is defined to be 100° above the lower angle range limit (θ_{lowlim}), and is limited to be no higher than 180°. For values that exceed the specified limits, the algorithm returns a default function value, in which the default value is higher than any potential viable solution in order to avoid being found as the minimum. A default value of 50 mNm was chosen for this algorithm, since it is significantly higher than twice the maximum allowable motor torque (M_{out}).

The algorithm was executed in Matlab and utilized the modified slider-crank code mentioned in section 3.6.1 in order to determine the associated values of the torque reflected to the motor at each crank angle. The program was run multiple times for each joint with varying initial inputs until the best minimum value was found. This was performed by incrementing each of the input values in a sequential fashion, in increments of 1 mm for the coupler length, 0.5 mm for the crank offset, and 5 degrees for the lower angle limit. This served to mitigate finding local minima.

Table 3.14 Algorithm for optimizing design parameters.

1) Set minimum and maximum coupler lengths, r_{3min} & r_{3max}

2) Set maximum offset, r_{4max}

3) Set maximum lower crank angle limit, $\theta_{low\,lim}^{max}$ (in our case, we chose $\theta_{low\,lim}^{max} = 80°$, such that $\theta_{upper\,lim}^{max} = 180°$)

4) Set $i = 0, j = 0, k = 0$.

5) Enter initial variables and run optimization code:

    a) Initialize design variables:

        i) coupler length: $r_3 = r_{3min} + i \cdot 1\,mm$

        ii) offset: $r_4 = j \cdot 0.5\,mm$

        iii) lower angle limit: $\theta_{low\,lim} = k \cdot 5\ deg$

    b) If $r_{3min} \le r_3 \le r_{3max}$ and $r_4 \le r_{4max}$ and $\theta_{lowlim} \le \theta_{low\,lim}^{max}$, go to 5(c). Else, set $\sum M_{ref} = default$, where $default > 2M_{out}$ (in our case, default = 50 mNm) and go to 5(f).

    c) Determine torque reflected, M_{ref}, at both lower and upper angle limits, where: $\theta_{upper\,lim} = \theta_{low\,lim} + 100°$

    d) Calculate the sum of the torque reflected:

$$\sum M_{ref} = M_{ref}(\theta_{upper\,lim}) + M_{ref}(\theta_{low\,lim})$$

    e) If $\theta_{upper\,lim}$ or $\theta_{low\,lim}$ do not exist (as in, the mechanism cannot be assembled at those values) set $\sum M_{ref} = default$.

    f) Minimize the sum of the torque reflected using the Nelder-Mead method: $\min \sum M_{ref}$

    g) Return design variables at this minimum:

        i) coupler length, r_3

        ii) offset, r_4

        iii) lower angle limit, θ_{lowlim}

6) Set $i = i + 1$ and return to step 5 to vary initial value of the coupler length. When $r_3 = r_{3max}$, go to step 7.

7) Set initial r_3 to the initial value that returned the smallest minimum torque reflected value.

8) Set $j = j + 1$ and return to step 5a(ii) to vary initial value of the crank offset. When $r_4 = r_{4max}$, go to step 9.

9) Set initial r_4 to the initial value that returned the smallest minimum torque reflected.

10) Set $k = k + 1$ and return to step 5a(iii) to vary initial value of the lower crank angle limit. When $\theta_{lowlim} = \theta_{low\,lim}^{max}$, go to step 11.

11) Report the design variables that returned the smallest minimum torque reflected.

12) Stop.

For the elbow joint, the best solution occurred when the coupler length was 9 mm and the crank offset was 3.85 mm. The value of the lower crank angle limit was 52°, although this will be further improved by the algorithm presented in section 3.6.5.

Unfortunately, values for these design parameters had been initially determined using an earlier method and some components of the prototype were manufactured before this optimization algorithm was performed. As a result, the elbow joint of the current prototype has slightly different values. Specifically, the crank offset does not incorporate the potential to raise the slider pivot, and so only the 2 mm lowering of the crank pivot is represented. Also, the coupler length was chosen to be 15 mm.

For the wrist joint, this algorithm was iterated thirty times with varying inputs. Many of the results were very similar, with the minimized torque reflected values all within ±0.0005 mNm of one another. For these results, the coupler length ranged from 9 mm to 10 mm. Thus the optimum value was chosen to be 9 mm to conserve space. The optimum crank offset was found to be 2 mm and the lower crank angle limit was 43°. These results are summarized in Table 3.15. Note that the optimized wrist joint dimensions were used in the prototype.

Table 3.15 Design parameters for elbow and wrist joints.

Parameter	Optimized Elbow Joint	Elbow Joint of Prototype	Optimized Wrist Joint
Crank radius, r_2	6 mm	6 mm	4 mm
Coupler length, r_3	9 mm	15 mm	9 mm
Crank offset, r_4	3.85 mm	2 mm	2 mm
Lower angle limit, θ_{lowlim}	52°	N/A	43°

3.6.5 Crank Angle Range

The operating crank angle range, and subsequently the geometry design for the crank itself, will now be determined based on the motor torque limits and the torque reflected to the motor. The algorithm shown in Table 3.16 was developed to provide a step-by-step procedure for the design process. First, the optimized coupler length and crank offset from the algorithm in Table 3.14 are entered into the slider-crank Matlab code to plot the torque reflected to the motor curve as a function of the crank angle (M_{ref} vs. θ_2). These curves – for the optimized elbow joint, the current prototype elbow joint, and the optimized wrist joint – are given in Figures 3.16-3.18, respectively. Limits are then set on these curves based on the maximum allowable motor torque, which is 13 mNm and 3.7 mNm for the Faulhaber motors in the elbow and wrist joints, respectively, as outlined by the motor specifications in section 3.4. The points at which the motor limits cross the torque reflected to motor curve are designated as the upper and lower crank angle limits, $\theta_{upper\,lim}$ and $\theta_{low\,lim}$.
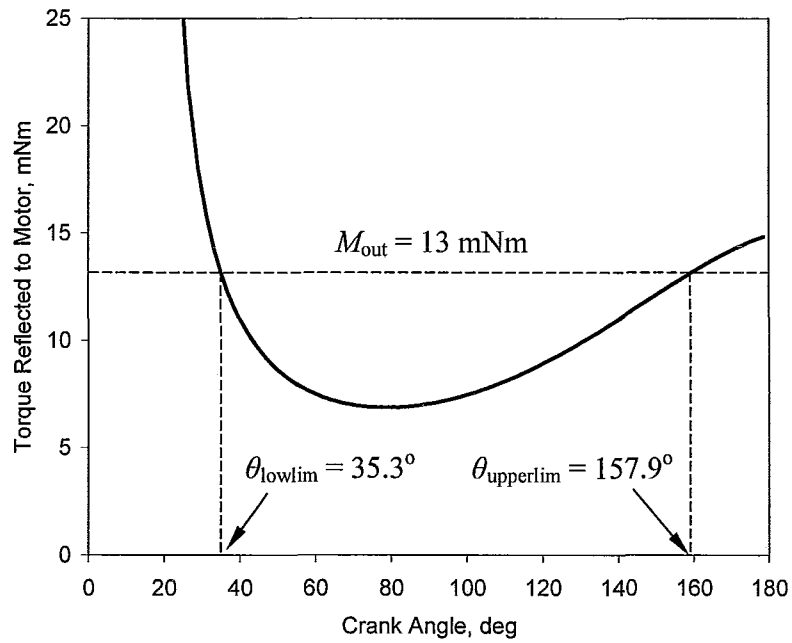
Figure 3.16 Torque reflected to motor curve for the optimized elbow joint.
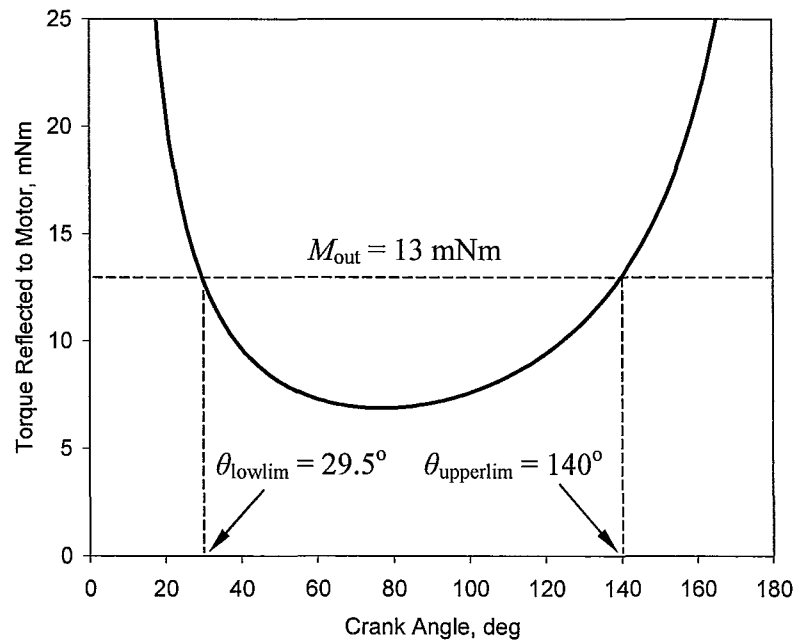
Figure 3.17 Torque reflected to motor curve for the current prototype of the elbow joint.
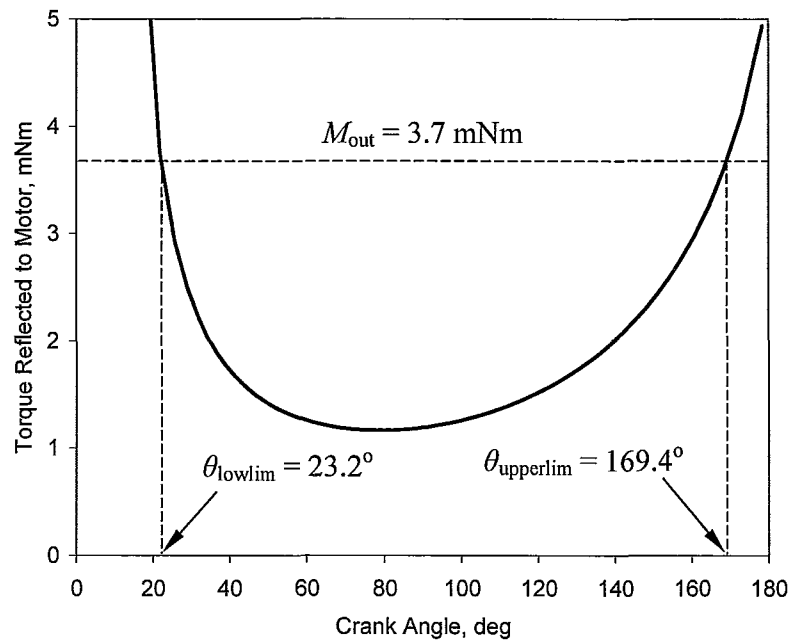
Figure 3.18 Torque reflected to motor curve for the optimized wrist joint.

Once this has been completed, the maximum crank angle is checked against the mechanical limits due to collision, using Working Model 2D. The mechanical limit for the optimized elbow joint, shown in Figure 3.19, occurs at $154.5°$ due to collision between the slider and the mechanical stop that represents the distance at which the edge of the slider material and the crank pin would collide. The mechanical limit for the current prototype of the elbow joint, shown in Figure 3.20, occurs at $143.3°$ due to collision between the coupler and the crank pin. Similarly, the mechanical limit for the optimized wrist joint, shown in Figure 3.21, occurs at $120.3°$. If any of the original upper limits are greater than the corresponding mechanical limits, the upper limits are redefined to be equivalent to the mechanical limits in step 5 of the algorithm.

| Value of Rotation of Circle 1 23 |
| Y Value | 25.532 |

$\theta_{mechlim} = 154.5°$
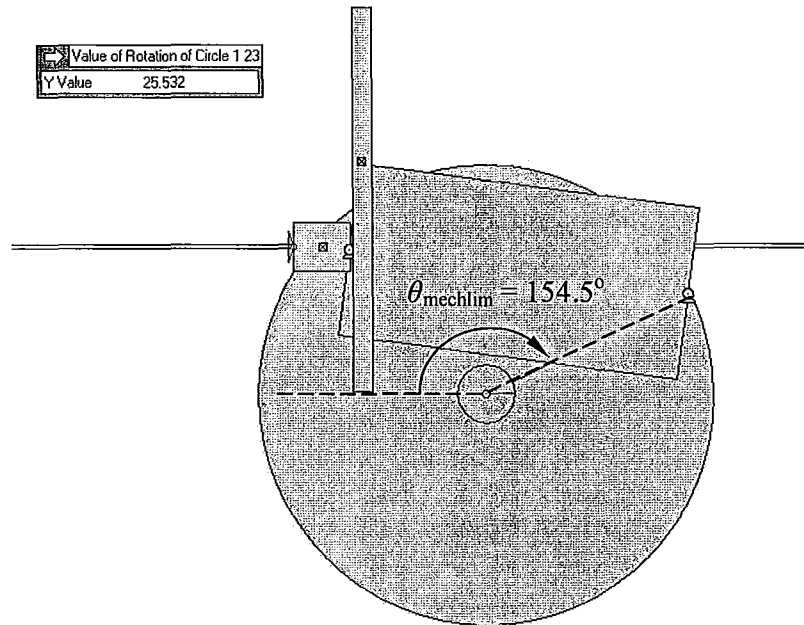
Figure 3.19 Mechanical limit for optimized elbow joint.

| Value of Rotation of Circle 1 23 |
| Y Value | 36.694 |

$\theta_{mechlim} = 143.3°$
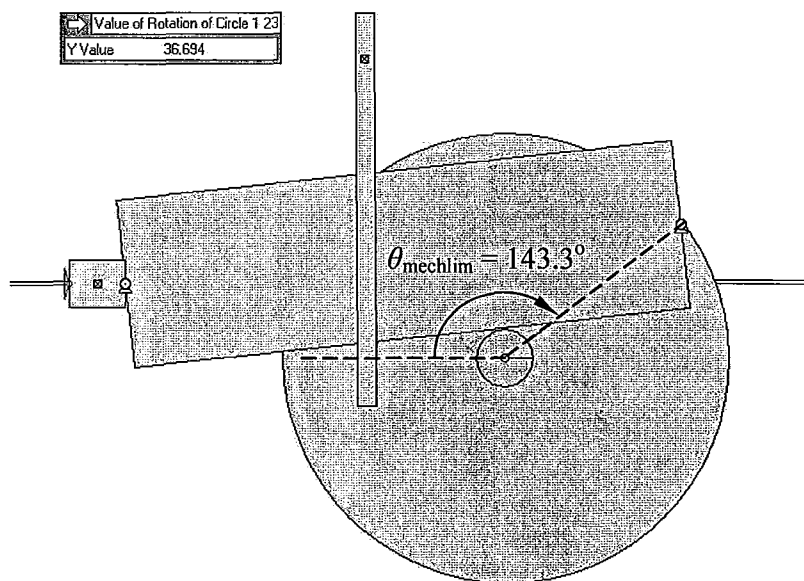
Figure 3.20 Mechanical limit for the current prototype of the elbow joint.
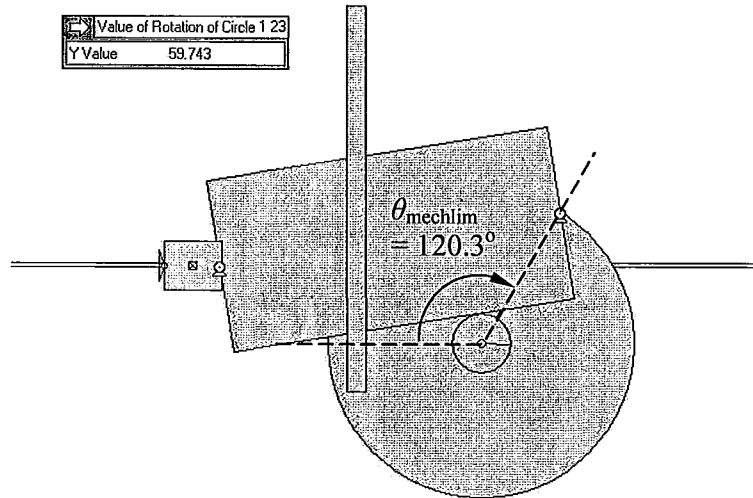
Figure 3.21 Mechanical limit for optimized wrist joint.

The geometry of the crank is then determined based on the upper and lower crank angle limits. There are two potential cases: the first is for a joint that has equal motion to either side of the centre axis, as in the wrist joint; the second case is for a joint that moves from centre only in one direction, similar to a human elbow. This second case applies to the elbow joint, as mentioned in section 3.2. The geometry variables are defined in Figure 3.22 and the equations for solving these variables are found in the algorithm in Table 3.16.

Table 3.16 Algorithm for defining the crank angle geometry.

1) Enter optimized parameters from the algorithm in Table 3.14 (r_3 and r_4) into the slider-crank code to plot the torque reflected to motor curve (M_{ref} vs. θ_2).

2) Limit the torque reflected to motor at the maximum allowable motor torque, such that $M_{ref} \leq M_{out}$

3) Find the crank angles where $M_{ref} = M_{out}$. Set these angles as the upper and lower crank angle limits, $\theta_{upper\,lim}$ and $\theta_{low\,lim}$.

4) Check for mechanical limits due to coupler-pin collision or slider-pin collision (in Working Model 2D). Let maximum crank angle due to mechanical limits be $\theta_{mech\,lim}$.

5) If $\theta_{upper\,lim} > \theta_{mech\,lim}$, then set $\theta_{upper\,lim} = \theta_{mech\,lim}$.

6) Thus the crank angle range is: $\theta_{low\,lim} < \theta_2 < \theta_{upper\,lim}$.

7) Find midpoint between $\theta_{low\,lim}$ and $\theta_{upper\,lim}$:

$$\theta_{mid} = \frac{\theta_{upper\,lim} - \theta_{low\,lim}}{2} + \theta_{low\,lim}$$

8) The joint angle range is:

$$\Delta\theta_{joint} = \theta_{upper\,lim} - \theta_{low\,lim}$$

9) Determine crank geometry based on the following:

    a) CASE I: Joint has equal motion to either side of the centre line.

        i) $-\frac{1}{2}\Delta\theta_{joint} < \theta_{joint} < \frac{1}{2}\Delta\theta_{joint}$

        ii) When $\theta_{joint} = 0$, then $\theta_2 = \theta_{mid}$ and $\alpha = 90^o - \theta_2$

        iii) Therefore $\alpha = 90^o - \theta_{mid}$

    b) CASE II: Joint moves from centre in only one direction (like a human elbow)

        i) $0^o < \theta_{joint} < \Delta\theta_{joint}$

        ii) When $\theta_{joint} = 0$, then $\theta_2 = \theta_{upper\,lim}$ and $\alpha = 90^o - \theta_2$

        iii) Therefore $\alpha = 90^o - \theta_{upper\,lim}$

10) Stop.
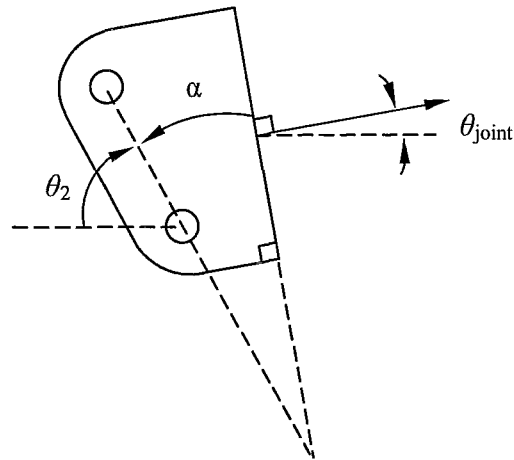
Figure 3.22 Basic geometry for crank design.

Working through the algorithm for the crank geometry of the optimized elbow joint, from the torque reflected to motor curve (Figure 3.16), we see that the lower angle limit is 35.3° and the upper angle limit is 157.9°. However, a mechanical limit occurs at 154.5°, as shown in the Working Model 2D diagram in Figure 3.19, so the upper limit becomes 154.5°. The elbow is designed for case II, where the joint moves from centre in only one direction. In this case, the crank geometry is defined based on equation 3.38, which results in an angle of -59.5°. This is represented in Figure 3.23.

$$\alpha = 90^{o} - \theta_{upper\,lim} \tag{3.38}$$
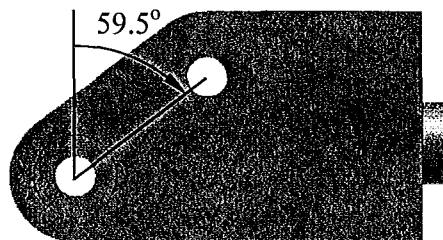
Figure 3.23 Geometry for the crank design of the optimized elbow joint.

Similarly, for the elbow joint of the current prototype, from the torque reflected to motor curve in Figure 3.17, we see that the lower angle limit is 29.5° and the upper angle limit is 140°. The mechanical limit occurs at 143.3°, according to the Working Model 2D diagram shown in Figure 3.20, so the upper angle limit remains at 140°. As in the previous example, equation 3.37 is used to determine the crank geometry. In this case, the angle is calculated to be -50°, as represented in Figure 3.24.
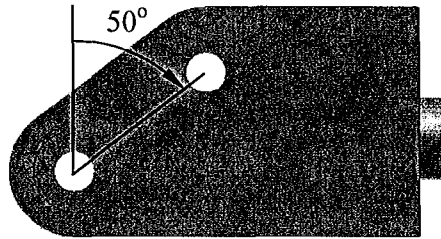
Figure 3.24 Geometry for the crank design of the current prototype's elbow joint.

For the optimized wrist design, from the torque reflected to motor curve shown in Figure 3.18, we see that the lower angle limit is 23.2° and the upper angle limit is 169.4°. However, a mechanical limit occurs at 120.3° based on the Working Model 2D diagram in Figure 3.21, so the upper limit becomes 120.3°. The elbow is designed for case I, where the joint moves equally to either side of centre. In this case, equations 3.39 and 3.40 are used to determine the crank geometry, which results in an angle of 18.3°. The cranks for the wrist joint have been fashioned into top and bottom gripper jaws using this geometry, as depicted in Figure 3.25.

$$\alpha = 90^{o} - \theta_{mid} \tag{3.39}$$

$$\theta_{mid} = \frac{\theta_{upper\,lim} - \theta_{low\,lim}}{2} + \theta_{low\,lim} \tag{3.40}$$
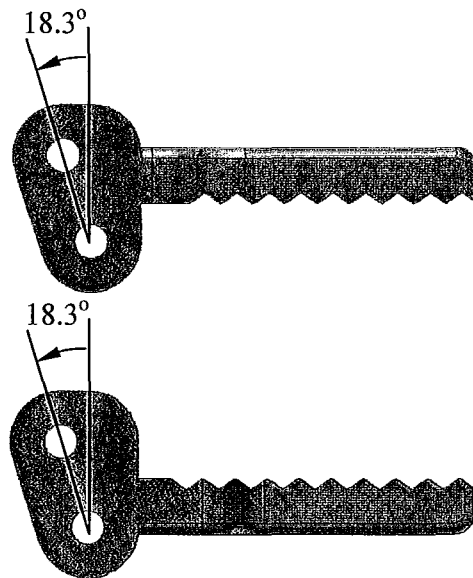
Figure 3.25 Geometry for the crank design of the upper and lower gripper jaws.

3.6.6 Joint Speeds

The joint speeds are calculated based on a number of factors, including the maximum allowable speeds of the motors, the lead provided by the screw, the slider-crank design parameters, and the crank angle limits.

The design of the elbow joint assumes the use of the Faulhaber brushless DC motor (0620 012B) and 64:1 gearbox (06/1), which can supply the necessary torque of 13 mNm. This motor, as specified in section 3.4, can provide a maximum input speed to the gearbox of 8000 rpm, which converts to a speed of 125 rpm with the 64:1 gear reduction. With a lead of 0.4 mm/rev provided from the M2x0.4 threaded lead screw, this rotation translates to a linear slider speed of 0.833 mm/s. From the slider-crank kinematics outlined in section 3.6.1, the crank angular velocity can be calculated based on this slider input and the design parameters for the optimized elbow joint. This crank speed has been plotted in Figure 3.26, and the average speed over the crank angle range has been

calculated to be 1.44 rpm. This is clearly significantly slower than the desired speed of 10

rpm as outlined in section 3.3. It is important to note, however, that the elbow joint is a

novel design and would be used more for gross positioning of the instrument within the

body. With this in mind, this lower speed may in fact be adequate considering the

function of the elbow joint. This would need to be confirmed in clinical testing.

Additionally, if a gearbox or equivalent mechanism could be created that could operate at

the full speed of the Faulhaber motor (40,000 rpm rather than 8,000 rpm), then an

average elbow speed of 7.2 rpm could be achieved.
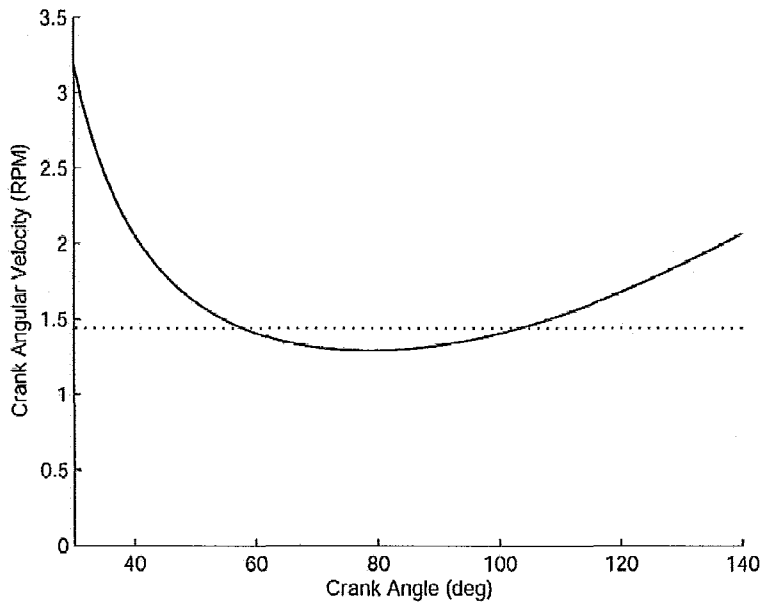
Figure 3.26 Theoretical optimized elbow joint speeds across full range of motion with an average speed of 1.44 rpm (slider = 0.833 mm/s).

For ease of control of the elbow joint prototype, a simple DC motor was chosen

despite the fact that the design calls for the Faulhaber brushless DC motor (mentioned

above) to achieve the necessary torque. The motor used in the prototype is a Gizmoszone

DC motor (GH6123S) with a 1:136 gear reduction. This motor, as specified in section

3.4, can provide a no load speed of 200 rpm. With a lead of 0.4 mm/rev provided from

the M2x0.4 threaded lead screw, this rotation translates to a linear slider speed of 1.333

mm/s. As before, the crank angular velocity can be calculated based on this slider input

and the design parameters for the elbow joint of the current prototype. This crank speed

has been plotted in Figure 3.27, and the average speed over the crank angle range has

been calculated to be 2.48 rpm.
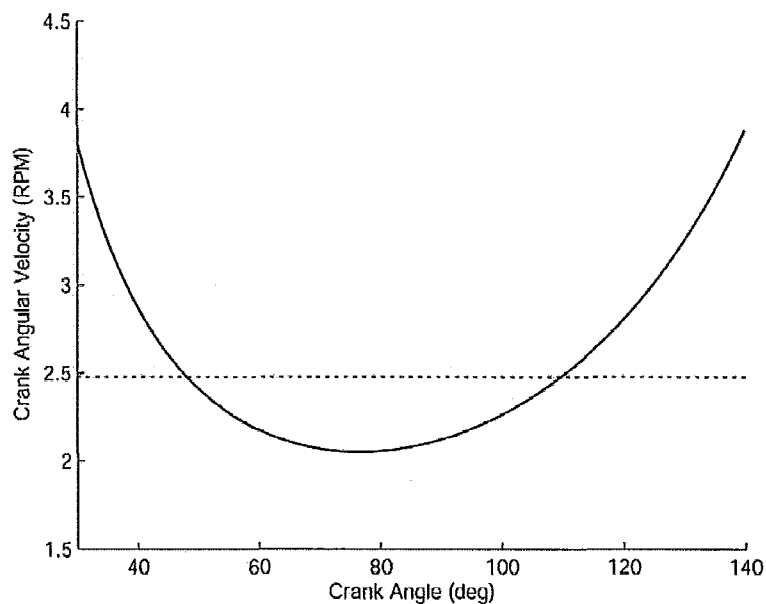
Figure 3.27 Theoretical elbow joint speeds for prototype across full range of motion with an average speed of 2.48 rpm (slider = 1.333 mm/s).

The design of the wrist joint calls for the use of the Faulhaber brushless DC motor

(0620 012B) and 16:1 gearbox (06/1), which can supply the necessary torque of 3.7

mNm. This motor, as specified in section 3.4, can provide a maximum input speed to the

gearbox of 8000 rpm, which converts to a speed of 500 rpm with the 16:1 gear reduction.

With a lead of 0.4 mm/rev provided from the M2x0.4 threaded lead screw, this rotation

translates to a linear slider speed of 3.333 mm/s. The associated crank speed has been

plotted in Figure 3.28, and the average speed over the crank angle range has been

calculated to be 9.53 rpm. This is slower than the desired speed of 20 rpm as outlined in

section 3.3. If a higher speed was desired, there would be a trade-off from the torque that

could be supplied. For example, if a Faulhaber brushless DC motor (0620 012B) and 4:1

gearbox (06/1) was used instead, the joint speed could be increased to an average of 38

rpm, but the maximum torque that could be reflected to the motor would be 1.05 mNm.
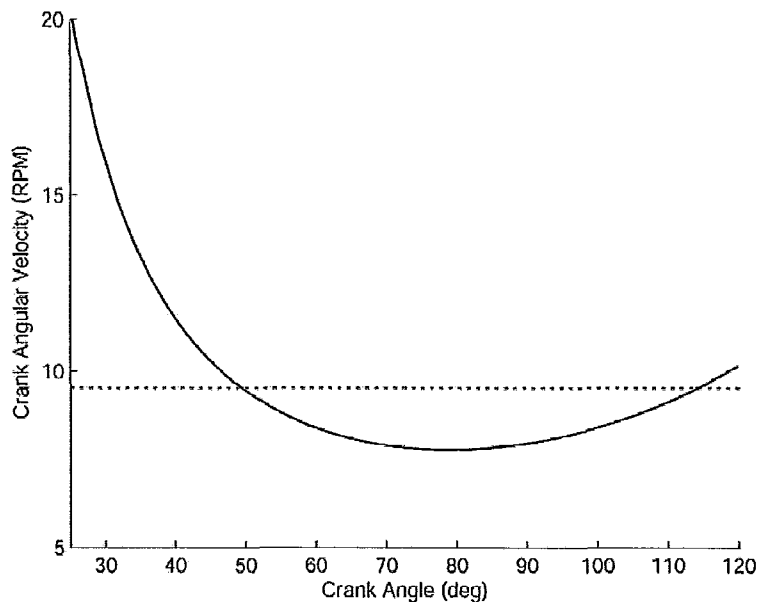
Figure 3.28 Theoretical ideal wrist joint speeds across range of motion with an average
speed of 9.53 rpm (slider = 3.333 mm/s).

As with the elbow prototype, however, for ease of control the wrist joint in the

prototype uses the Gizmoszone DC motors (GH6123S) with a 1:136 gear reduction,

which can supply a no load speed of 200 rpm. Note that this motor is still adequate as far

as providing enough torque for the wrist, although the speed is significantly reduced due to the lower power of the brushed motor. The crank angular velocity was calculated based on the slider input of 1.333 mm/s and the design parameters for the optimized wrist joint. This crank speed has been plotted in Figure 3.29, and the average speed over the crank angle range has been calculated to be 3.70 rpm. This value is significantly lower than the 20 rpm desired speed based on the specifications described in section 3.3.
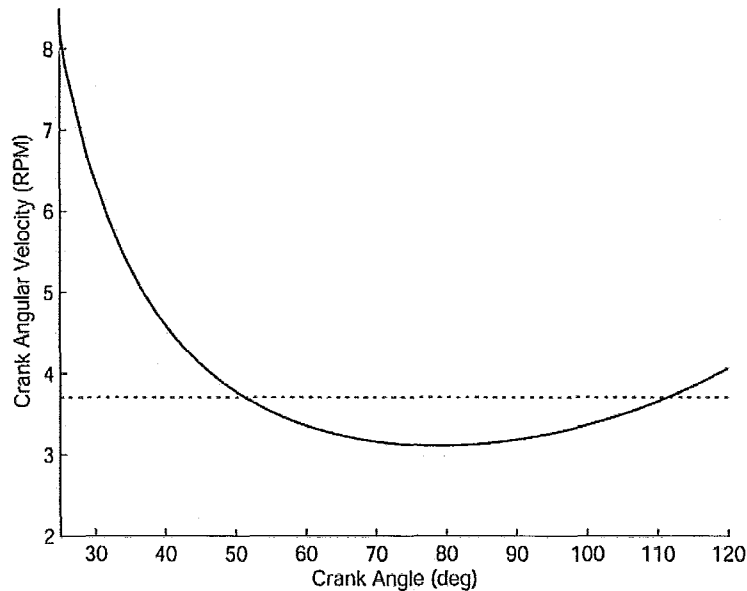
Figure 3.29 Theoretical wrist joint speeds for prototype across range of motion with an average speed of 3.70 rpm (slider = 1.333 mm/s).

3.7 Design Calculations & Component Selection

The CAD design of the surgical robotic instrument is shown in Figure 3.30, combining all elements of the elbow, roll and wrist joints. Explanations for the geometry of the parts and the selection of components, with accompanying design calculations and stress analysis for each of the components are included in the following sections.
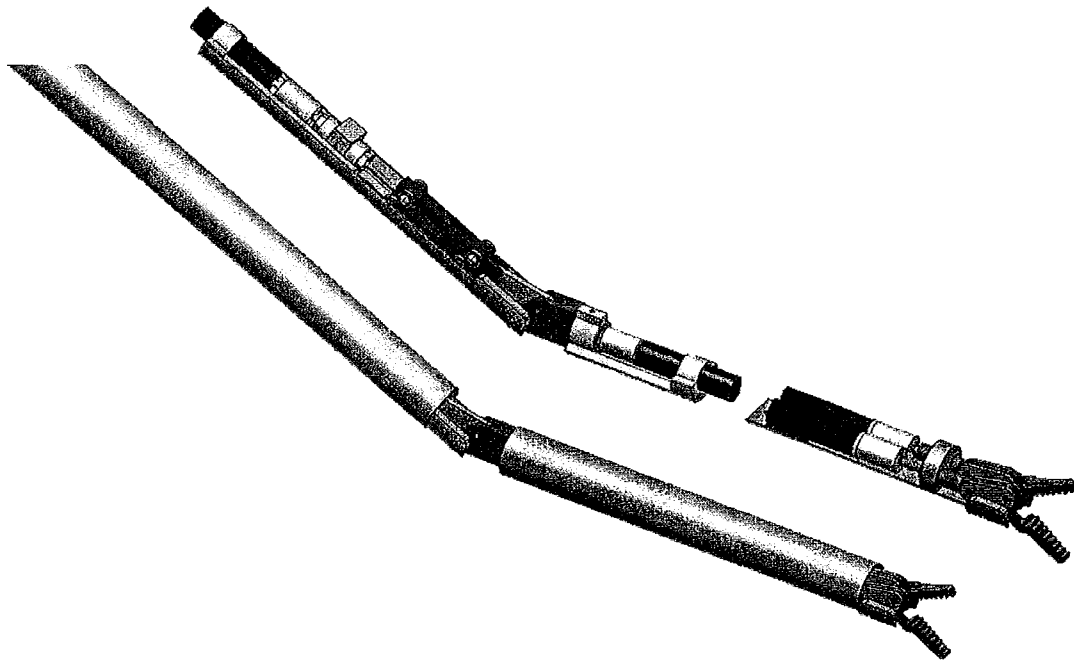
Figure 3.30 CAD design of the surgical robotic instrument with and without the outer shell.

3.7.1 Elbow Joint

The CAD design of the elbow joint is depicted in Figure 3.31. An analysis follows

on the design considerations and selection criteria for each component, which are listed in

Table 3.17.
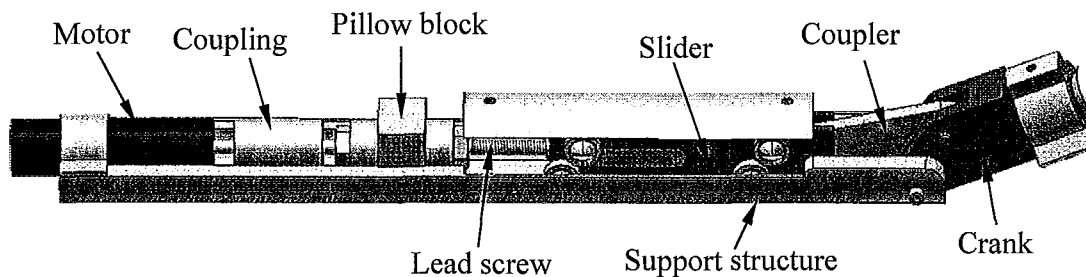
Figure 3.31 CAD design of the elbow joint.

Table 3.17 Component list for the elbow joint.

Component List	Description
Motor	Faulhaber brushless DC motor (0620 012B), 64:1 gearbox (06/1)
Coupling	Micro Reli-a-flex Coupling (RCS A 6 – 1.5-1.5)
Thrust Bearings (x2)	6 mm OD thrust bearings (F2-6)
Radial Bearing	5 mm OD radial bearing (MR52)
Lead Screw	M2x0.4 threaded rod
Slider "Wheels" (x8)	4 mm OD radial bearings (SMR681-X)
Slider	Manufactured – stainless steel
Coupler	Manufactured – stainless steel
Crank	Manufactured – stainless steel
Support Structure	Manufactured – stainless steel
Pins	1.5 mm diameter dowel pins (MD6325MQ0015x020)

The loading in the joint is derived from the governing equations outlined in section 3.6.1. The free-body diagrams for each of the components are shown in Figure 3.32. Note that the free-body diagrams of the slider and lead screw are general, simplified versions that do not take the specific bearing supports into account. These will be addressed in further detail later in this section.
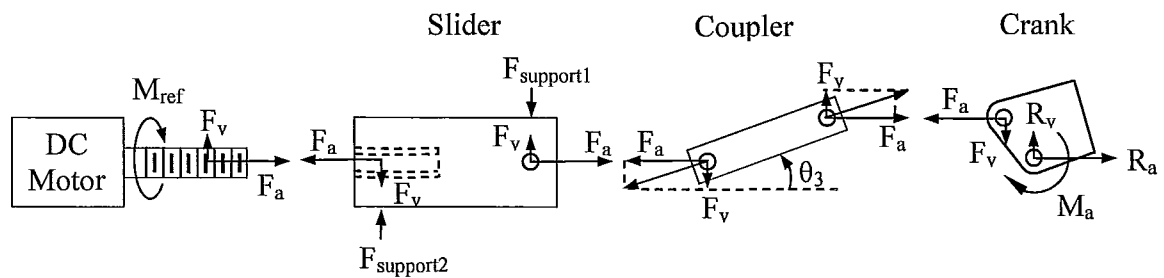
Figure 3.32 Free-body diagrams of the lead screw plus slider-crank mechanism.

The axial loading, or horizontal force acting on the slider (F_a), is given by equation 3.29 (section 3.6.1), and the radial loading, or vertical force acting on the slider (F_v), is given by equation 3.41, where θ_3 is the coupler angle.

$$F_v = F_a \tan \theta_3 \qquad (3.41)$$

Solving these equations for the kinematics of the current prototype parameters, the horizontal and vertical forces across the crank angle range are given in Figures 3.33 and 3.34, respectively. It can be seen that the maximum horizontal force exerted on the slider is 81 N at both extremes of the crank angle range. The maximum vertical force exerted on the slider is -13 N at a crank angle range of 111°. These forces are used in the design calculations and selection criteria that follow for each component.
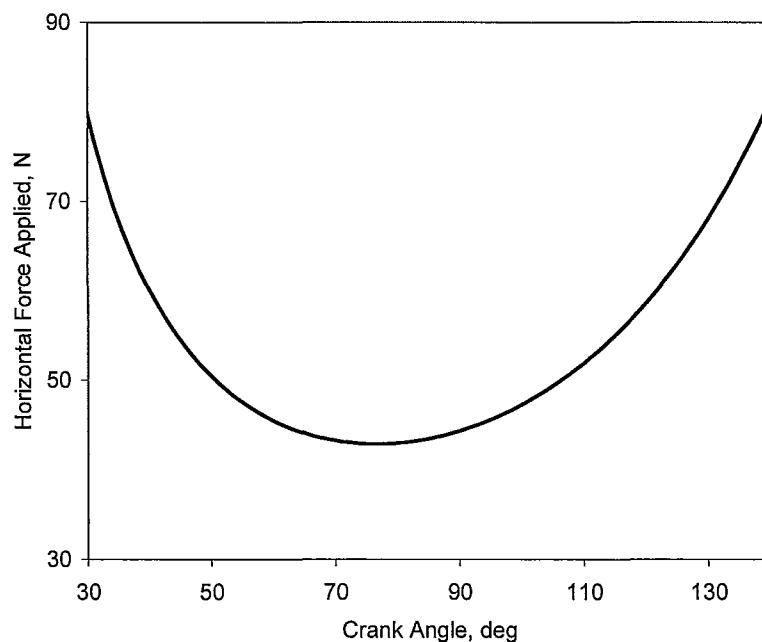
Figure 3.33 Horizontal force applied to slider for the elbow joint of the current prototype, with maximum force of 81 N.
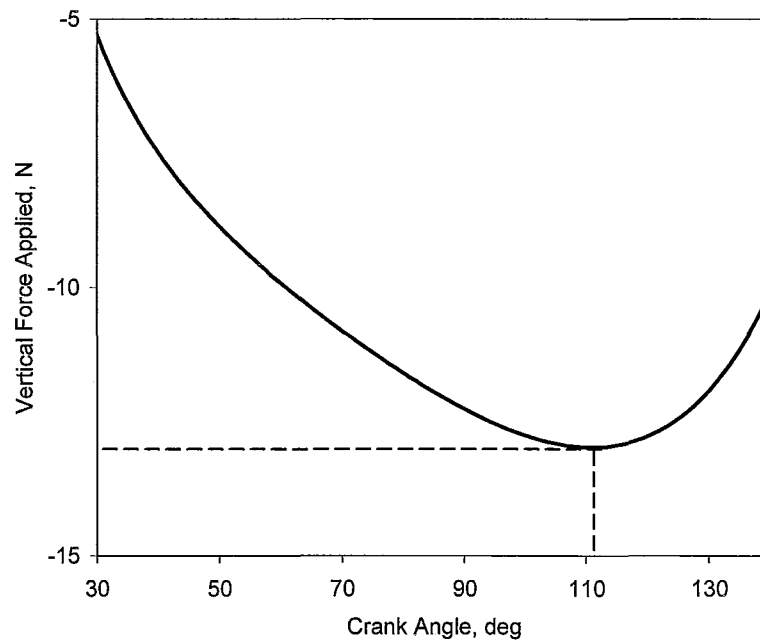
Figure 3.34 Vertical forces applied to the slider of the elbow joint of the current prototype, with maximum force of -13 N at a crank angle of 111°.

As outlined in section 3.4, the motor chosen for this design is a Faulhaber brushless DC motor (0620 012B) with a 64:1 gearbox (06/1), which can provide the necessary torque of 13 mNm. The motor is attached to a micro Reli-a-flex Coupling (RCS A 6 – 1.5-1.5) by Reliance Precision Mechatronics (2009). The coupling was chosen for its small size, being only 6 mm in outer diameter. It can withstand a torque of up to 0.25 Nm and a maximum speed of 70,000 rpm, which far exceeds the required specifications for the elbow joint. The coupling is attached to an M2x0.4 threaded rod, which extends through the pillow block and is threaded into the slider.

A diagram of the pillow block is shown in Figure 3.35. A feature that protrudes from the support structure houses the radial bearing and is sandwiched between two

thrust bearings. A washer is placed between the support structure and the thrust bearing to ensure that the thrust bearing does not come into contact with the moving component of the radial bearing. Each thrust bearing is held in place with a split lock washer and a hex nut. This design prevents any loading in either the radial or the axial direction from being transmitted to the motor.
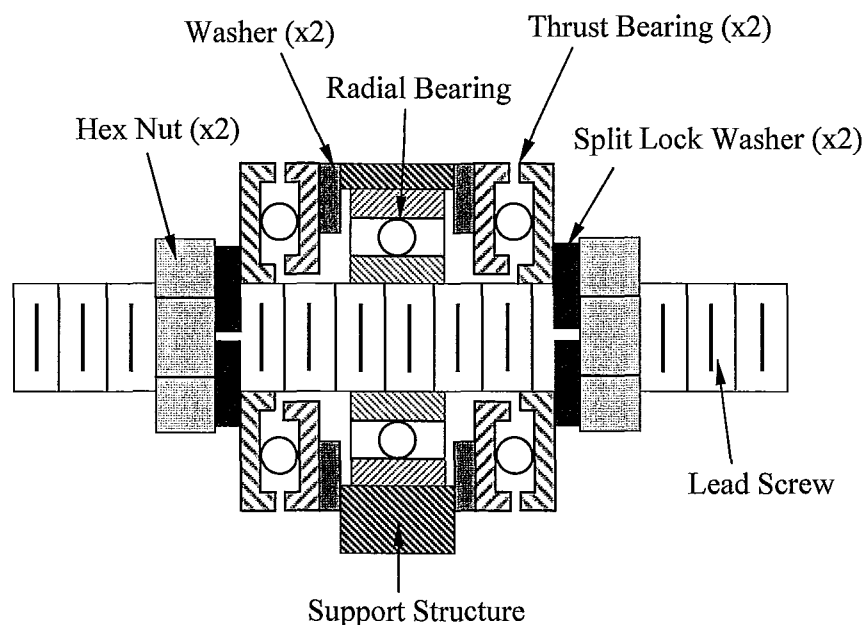
Figure 3.35 Diagram of pillow block in elbow joint.

As mentioned above, the maximum loading that can be expected in the axial direction is 81.0 N, transferred from the maximum horizontal force acting on the slider. The thrust bearings (F2-6) are able to support dynamic loads of up to 490 N (Boca Bearings, 2009). The maximum loading expected in the radial direction is assumed to be negligible because the slider has been designed to absorb all of the vertical forces in the system, which should not exceed 13 N. However, in the event that there is some

misalignment in the mechanism, the radial bearing (MR52) can support loads of up to 50

N (Boca Bearings, 2009).

In an attempt to minimize the sliding friction between the slider and the support

structure, the slider has been designed with eight "wheels" consisting of radial bearings.

This substitutes the sliding friction for a much smaller bearing friction with a rolling

contact. See Figure 3.36 for an isometric view of the elbow slider assembly. Some

combination of these eight wheels will be in contact with the support structure at any

particular time.
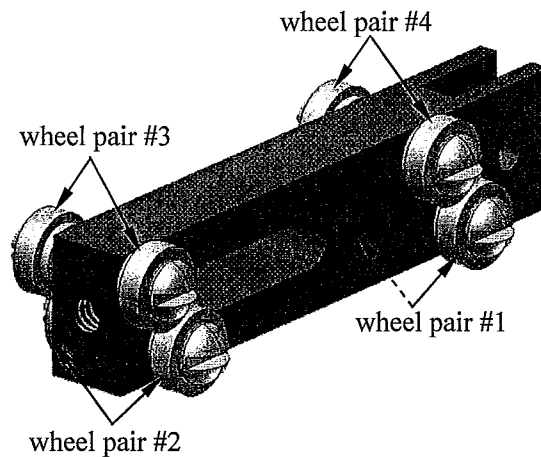
Figure 3.36 Assembly of the elbow slider with four wheel pairs.

The loading in an extreme case is represented by the diagram in Figure 3.37,

where the slider is only supported by the outermost wheel pairs (#1 and #3 in Figure

3.36). Note that this represents the worst-case scenario since the wheel pairs closest to the

slider pin (where the vertical force is applied) would support most of the load and d_1 is

shorter than d_4. Lengths d_1 and d_3 are 3.75 mm and 26 mm, respectively. Equations 3.42

and 3.43 are derived from the sum of forces and sum of moments. From these equations

and using the maximum vertical applied force of 13 N, it is possible to solve for the reaction forces, F_{R1} and F_{R3}. These forces are determined to be 15.2 N and 2.2 N, respectively, as seen in equations 3.44 and 3.45. Each of these loads will be distributed across two bearings, located to either side of the slider. The bearings (SMR681-X) can support loads of up to 35 N (Boca Bearings, 2009).
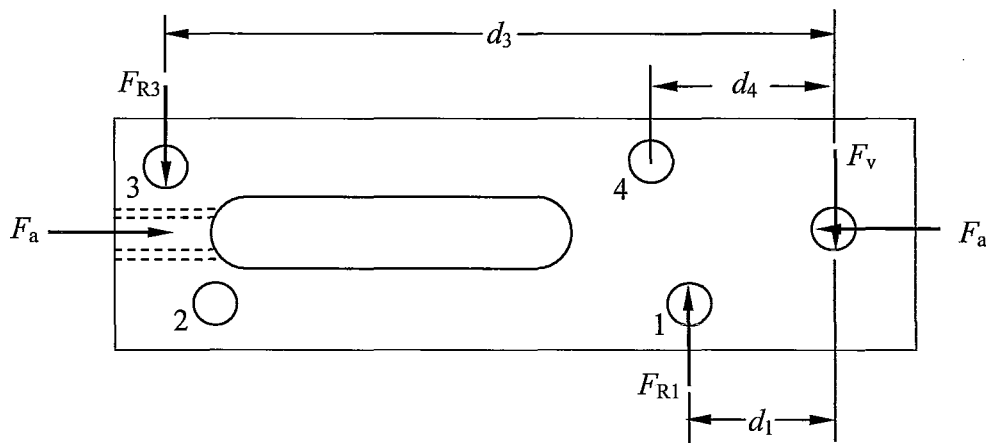
Figure 3.37 Worst case loading diagram of the elbow slider.

$$F_{R1} = F + F_{R3} \tag{3.42}$$

$$d_1 F_{R1} = d_3 F_{R3} \tag{3.43}$$

$$F_{R1} = \frac{F}{1 - \dfrac{d_1}{d_3}} = \frac{13\,\text{N}}{1 - \dfrac{3.75\,\text{mm}}{26\,\text{mm}}} = 15.2\,\text{N} \tag{3.44}$$

$$F_{R3} = F_{R1} - F = 15.2\,\text{N} - 13\,\text{N} = 2.2\,\text{N} \tag{3.45}$$

Stress analysis was performed on the slider using loading similar to that shown in Figure 3.37, with the maximum applied force in the horizontal direction being 81 N. This force occurs at a crank angle of 140°, where the vertical force is -10 N (Figure 3.34). In this case, the reaction forces F_{R1} and F_{R2} are 11.7 N and 1.7 N, respectively. Images from finite element analysis (FEA) using the ANSYS workbench software package depicting

these applied loads and meshing are shown in Figures B.1-B.4 in Appendix B, along with the resulting von Mises stress distribution and deformation. From these figures it can be seen that the maximum von Mises stress was found to be 26.9 MPa. The maximum deformation for a slider manufactured from stainless steel was found to be 0.89 μm.

The maximum tension in the coupler was determined by resolving the horizontal stress of 81 N through the coupler angle, θ_3, which is equal to 7.1° when the crank angle is 140°. Using equation 3.46, the force acting on the coupler was found to be 81.63 N. Due to symmetrical geometry and loading, only half of the coupler has been analyzed. The loading, meshing and resulting von Mises stress distribution and deformation are shown in Figures B.5-B.8 in Appendix B. From these figures it can be seen that the maximum von Mises stress was found to be 24.4 MPa. The maximum deformation for this component made from stainless steel was found to be 0.4 μm.

$$F_c = \frac{F_h}{\cos\theta_3} \tag{3.46}$$

All of the pins used in this design are stainless steel precision dowel pins with a diameter of 1.5 mm. Assuming the pin joints are under direct shear loading and using equation 3.47, the shear stress acting on the coupler pins is 46.2 MPa.

$$\tau = \frac{V}{A} = \frac{81.63\,\text{N}}{\frac{\pi}{4}(1.5\,\text{mm})^2} = 46.2\,\text{MPa} \tag{3.47}$$

The loading that was applied to the crank can be seen in Figure B.9 in Appendix B, using the maximum horizontal and vertical loads of 81 N and 5 N distributed across two pin holes and an applied torque of 266 mNm at the forearm attachment. The meshing is shown in Figure B.10. From Figure B.11, it can be seen that the maximum von Mises

stress was 113.8 MPa, located at the output shaft that leads to the forearm due to the applied torque. The maximum deformation was 1.4 μm for the crank made from stainless steel, as seen in Figure B.12.

Similarly, the loading applied to the support structure can be seen in Figure B.13, with the meshing shown in Figure B.14. From Figure B.15, it can be seen that the maximum von Mises stress was 126.7 MPa, concentrated at the holes for attaching the support structure to the outer shell. From Figure B.16, the maximum deformation was 24.5 μm. A summary of the maximum stresses and deformations for the components of the elbow joint are listed in Table 3.18.

Table 3.18 Maximum von Mises stress and maximum deformation
for elbow components.

Component List	Max. von Mises Stress (MPa)	Max. Deformation (μm)
Slider	26.9	0.9
Coupler	24.4	0.4
Crank	115.9	2.7
Support Structure	126.7	24.5

The pin joint for the main elbow pivot, attaching the crank to the support structure, can be analyzed using the free-body diagram and shear and moment curves shown in Figure 3.38. The maximum bending stress and shear stress can be calculated using equations 3.48 and 3.49, respectively, where c is the radius of the pin (0.75 mm), and I is the moment of inertia, given by equation 3.50. Solving for these values gives a maximum bending stress of 134.5 MPa and a maximum shear stress of 22.9 MPa.
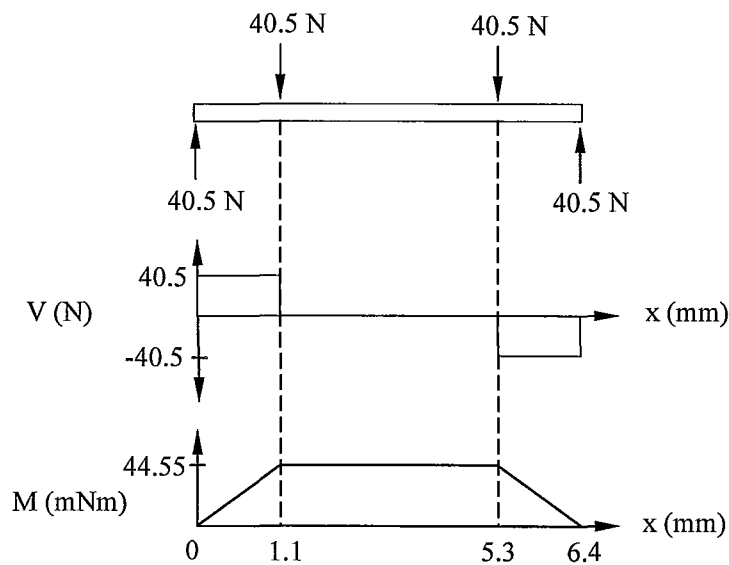
Figure 3.38 Free-body diagram, shear and moment graphs for elbow pivot pin.

$$\sigma_m = \frac{|M|_{max}\, c}{I} = \frac{(44.55\ \text{mNm})(0.75\ \text{mm})}{0.2485\ \text{mm}^4} = 134.5\ \text{MPa} \tag{3.48}$$

$$\tau_m = \frac{|V|_{max}}{A} = \frac{40.5\ \text{N}}{\dfrac{\pi}{4}(1.5\ \text{mm})^2} = 22.9\ \text{MPa} \tag{3.49}$$

$$I = \frac{\pi c^4}{4} = \frac{\pi(0.75\ \text{mm})^4}{4} = 0.2485\ \text{mm}^4 \tag{3.50}$$

3.7.2 Roll Joint

The CAD design of the roll joint is depicted in Figure 3.39. An analysis follows

on the design considerations and selection criteria for each component, which are listed in

Table 3.19.
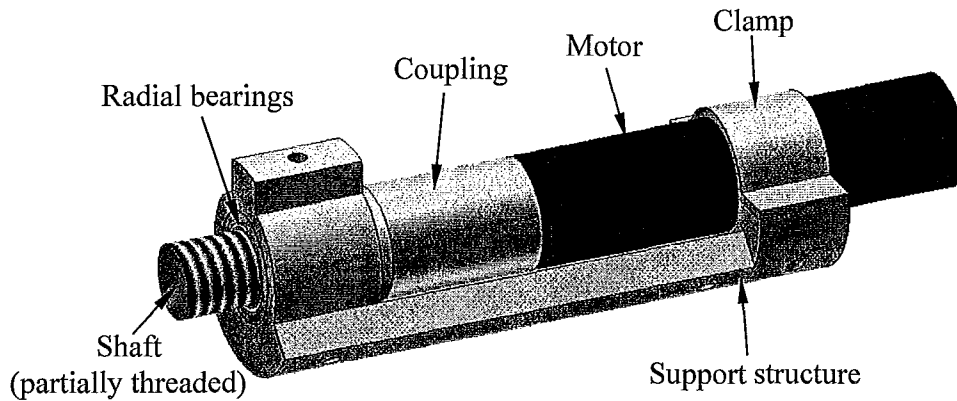
Figure 3.39 CAD design of the roll joint.

Table 3.19 Component list for the roll joint.

Component List	Description
Motor	Faulhaber brushless DC motor (0620 012B) with 256:1 gearbox
Coupling	Micro Reli-a-flex Coupling (RCS A 6 – 3-1.5)
Radial Bearings (x2)	6 mm OD radial bearings (SMR63)
Shaft	Machined M4x0.7 partially threaded rod
Support Structure	Manufactured – stainless steel

As outlined in section 3.4, the ideal motor for this design is a Faulhaber brushless DC motor (0620 012B) with a 256:1 gearbox (06/1), which can provide the necessary torque of 25 mNm needed to withstand the tool-tip force specification of 2 N about 12 mm from the roll axis. See Figure 3.40 for the relevant geometry.
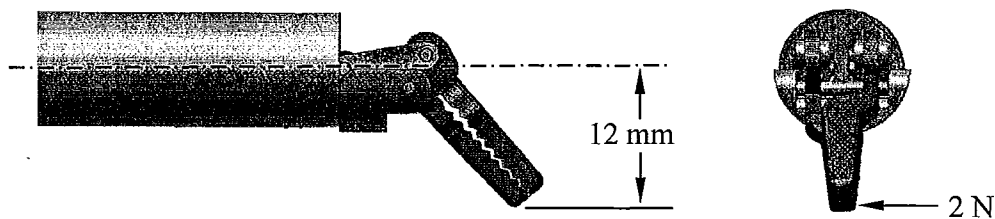
Figure 3.40 Geometry of applied tool-tip force causing roll torque.

The motor is attached to a micro Reli-a-flex Coupling (RCS A 6 – 3-1.5) by Reliance Precision Mechatronics (2009). As mentioned in the previous section, this coupling can withstand a torque of up to 0.25 Nm and a maximum speed of 70,000 rpm, both of which far exceed the required specifications for the roll joint.

The shaft consists of an M4x0.7 threaded rod that is machined down to a 3 mm diameter along most of its length to allow it to be inserted through the bearings and attached to the coupling. The threaded end is attached to the crank component of the elbow joint.

The radial bearings that were chosen to support the shaft have an inner diameter of 3 mm and can support radial loads of up to 73.5 N. The distance between the two radial bearings was determined based on the moment that these bearing would have to counter. A free-body diagram is shown in Figure 3.41, where M is the moment about the shaft and is equivalent to the maximum moment that the elbow joint experiences (266 mNm as described in section 3.8). F_1 and F_2 are the reaction forces acting on the bearings due to this moment, and are equivalent based on the sum of forces. These forces must be limited to no more than 73.5 N, in accordance with the bearing specifications. Based on the sum of moments, represented by equation 3.51, it is then possible to solve for the distance between bearings, d, by rearranging to give equation 3.52. From this equation, the minimum value of d was found to be 3.62 mm, so a design value of 4 mm was designated for this parameter.
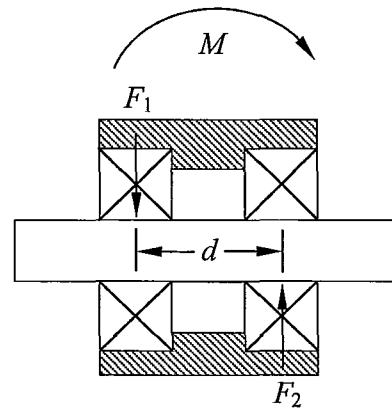
Figure 3.41 Loading diagram of forearm shaft supported by radial bearings.

$$M = (F_1 + F_2)\frac{d}{2} \tag{3.51}$$

$$d = \frac{2 \times 266 \text{ mNm}}{(73.5 \text{ N} + 73.5 \text{ N})} = 3.62 \text{ mm} \tag{3.52}$$

Using these reaction forces, FEA was performed on the support structure using ANSYS to determine its stress distribution. Images depicting the applied loads and meshing are shown in Figures B.17-B.20 in Appendix B, along with the resulting von Mises stress distribution and deformation. From these figures it can be seen that the maximum von Mises stress was found to be 14.6 MPa, concentrated at the holes for attaching the support structure to the outer shell. The maximum deformation was found to be 0.2 μm.

3.7.3 Wrist & Gripper

The CAD design of the elbow joint is depicted in Figure 3.42. An analysis follows on the design considerations and selection criteria for each component, which are listed in Table 3.20.
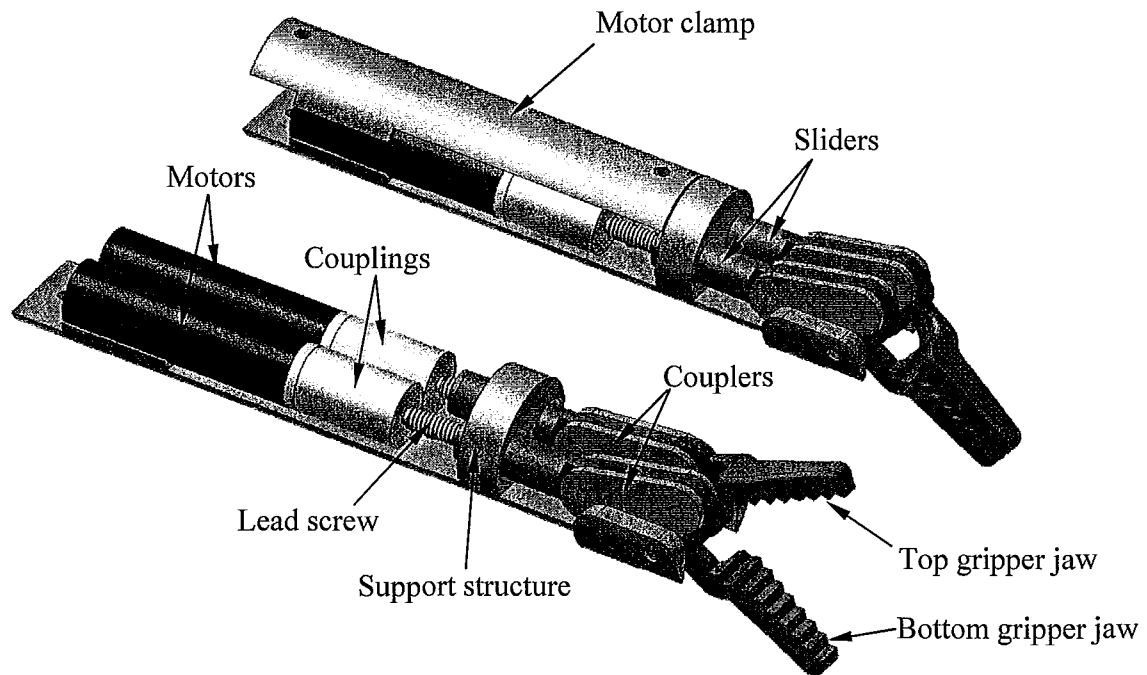
Figure 3.42 CAD design of the wrist joint with the gripper closed and including the top clamp (above) and with the gripper open (below).

Table 3.20 Component list for the wrist joint.

Component List	Description
Motors (x2)	Faulhaber brushless DC motor (0620 012B) with 16:1 gearbox
Couplings (x2)	Micro Reli-a-flex Coupling (RCS A 6 – 1.5-1.5)
Lead Screws (x2)	M2x0.4 threaded rod
Sliders (x2)	Manufactured – stainless steel
Couplers (x4)	Manufactured – stainless steel
Top Gripper Jaw	Manufactured – stainless steel
Bottom Gripper Jaw	Manufactured – stainless steel
Support Structure	Manufactured – stainless steel
Pins	1.5 mm diameter dowel pins (MD6325MQ0015x020)

The loading in the wrist joint is derived from the governing equations outlined in section 3.6.1 and is resolved into horizontal and vertical forces as shown in Figure 3.32 in section 3.7.1. The horizontal and vertical forces across the crank angle range are given in

Figures 3.43 and 3.44, respectively. It can be seen that the maximum horizontal force

exerted on the slider is 20.0 N at the lower crank angle limit of 24.4°. At this crank angle,

the force in the vertical direction is 0.8 N. The maximum vertical force exerted on the

slider is -1.75 N at a crank angle of 101°. These forces are used in the design calculations

and selection criteria that follow for each component.
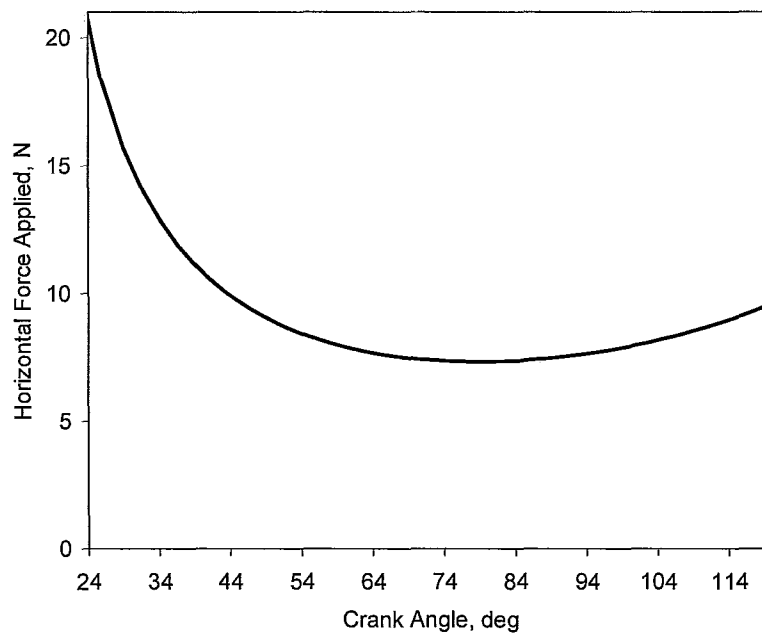
Figure 3.43 Horizontal force applied to slider for the optimized wrist joint, with maximum force of 20.0 N.
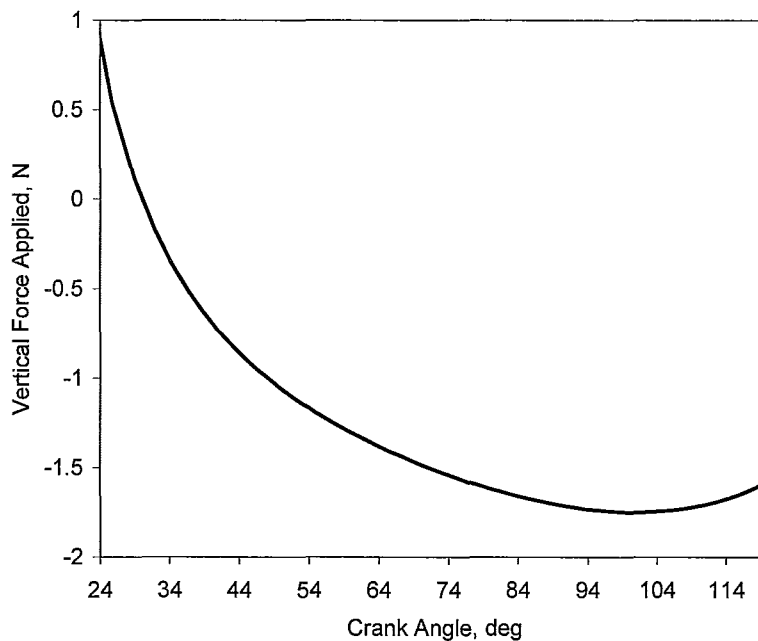
Figure 3.44 Vertical forces applied to the slider of the optimized wrist joint, with maximum force of -1.75 N at a crank angle of 101°.

As outlined in section 3.4, the motors chosen for this design is a Gizmoszone DC motor (GH6123S) with a 1:136 gear reduction. The motors are situated side-by-side, with their overall width of 12 mm acting as the driving constraint on the size of this device. In order to fit the two motors side-by-side inside an 11.7 mm inner diameter tube for the outer shell, the tube will be pressed into an elliptical form with an inner width of 12 mm and height of roughly 11.4 mm. With this in mind, the support structure was also designed with this elliptical shape.

Similar to the elbow joint, each of the motors are attached to a micro Reli-a-flex Coupling (RCS A 6 – 1.5-1.5) by Reliance Precision Mechatronics (2009). The couplings, being 6 mm in outer diameter, needed to be carefully ground down to a

diameter of 5.8 mm in order to have enough clearance to rotate side-by-side without interference.

Each coupling is attached to the machined end of an M2x0.4 threaded rod. The other end of the rod is threaded directly into the cylindrical slider. Unlike the elbow joint, there was no space to develop cart-like sliders with radial bearings. Instead, the sliders are supported by bores in the support structure which act as bushings. Assuming the slider support carries the full load (and none of the load is transferred to the lead screw), the free-body diagram on the slider can be represented by Figure 3.45, where F_v is the vertical force applied to the slider, and F_{R1} and F_{R2} are the reaction forces located at the edges of the support structure. The width of the support structure is given by d_1 and the distance between the slider pivot and the farthest edge of the support structure is given by d_2. The sum of forces and sum of moments are given in equations 3.53 and 3.54, respectively. At the point where d_2 is the greatest (when the crank angle is 120.3°), F_v is 1.6 N as shown in Figure 3.44. Solving for F_{R1} and F_{R2} with these equations gives values of 6.8 N and 5.2 N, respectively.
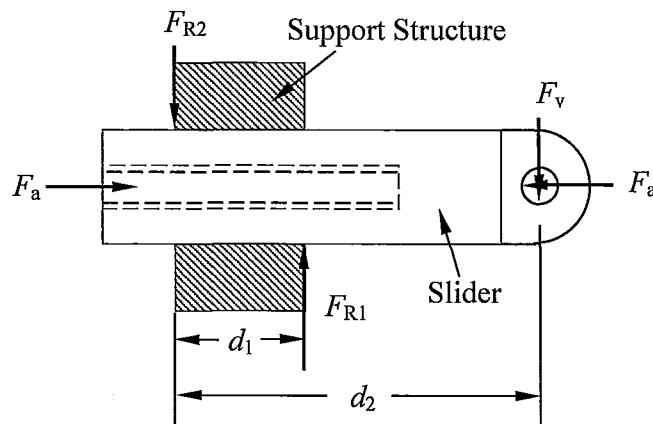
Figure 3.45 Diagram of the slider and support structure showing the forces acting on the slider.

$$\sum F = 0: \qquad F_{R1} - F_{R2} - F_v = 0 \qquad\qquad (3.53)$$

$$\sum M = 0: \qquad d_1 F_{R1} - d_2 F_v = 0 \qquad\qquad (3.54)$$

Using these values, stress analysis was performed on the slider support structure. The loading and meshing can be seen in Figures B.21 and B.22 in Appendix B. From Figures B.23 and B.24, the maximum von Mises stress is 9.6 MPa and the maximum deformation is 0.3 microns.

Stress analysis was also performed on the sliders themselves. A vertical force of 1.6 was applied on the pin joint, with a fixed support at the lead screw and a fixed displacement in the vertical direction where the slider support would be located at the sliders farthest stroke (at a crank angle of 120.3°). The loading and meshing is shown in Figures B.25 and B.26 in Appendix B, and the results (Figures B.27 and B.28) indicate that the maximum von Mises stress for this instance is 15.7 MPa, and the maximum deformation is 0.4 microns.

In an attempt to further conserve space, pillow blocks with thrust and radial bearings were not used to protect the motor. The effect of this is that any radial forces exerted on the slider may transfer to the motor. The sliding support acts as the only radial support for the slider, but it will essentially act as a pivot if the tolerancing is such that the slider is allowed to move vertically within the support. The diagram in Figure 3.46 shows an exaggeration of this possible scenario.
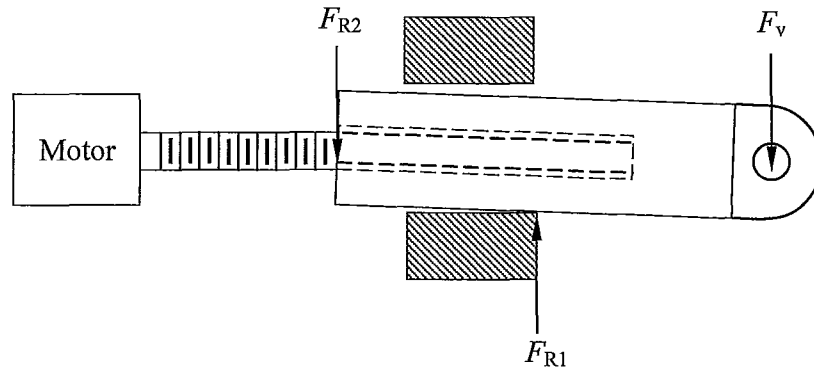
Figure 3.46 Extreme case where vertical force F_{R2} is due to the lead screw.

In this extreme case, the applied vertical force on the slider causes reaction forces from the sliding support, F_{R1}, and the leadscrew, F_{R2}. This force acting on the leadscrew will then cause an equal and opposite reaction force and a reaction moment at the motor. As the mechanism moves, the distance between the reaction and applied forces will change, affecting the values of the reaction forces. From the sum of forces and moments on the free-body diagram, we get equations 3.55 and 3.56, where C_1 is the length of the slider from the slider pivot to its edge, shown in Figure 3.47.

$$\sum F = 0: \qquad F_{R1} - F_{R2} - F_v = 0 \qquad\qquad (3.55)$$

$$\sum M = 0: \qquad d_1 F_{R1} - C_1 F_v = 0 \qquad\qquad (3.56)$$

The distance, d_1, between the reaction forces F_{R1} and F_{R2} is defined by equation 3.57, where r_1 is the variable horizontal distance between the crank pivot and slider pivot and C_2 is the constant distance between the crank pivot and the slider support structure, again as defined in Figure 3.47.

$$d_1 = r_1 + C_1 + C_2 \qquad\qquad (3.57)$$
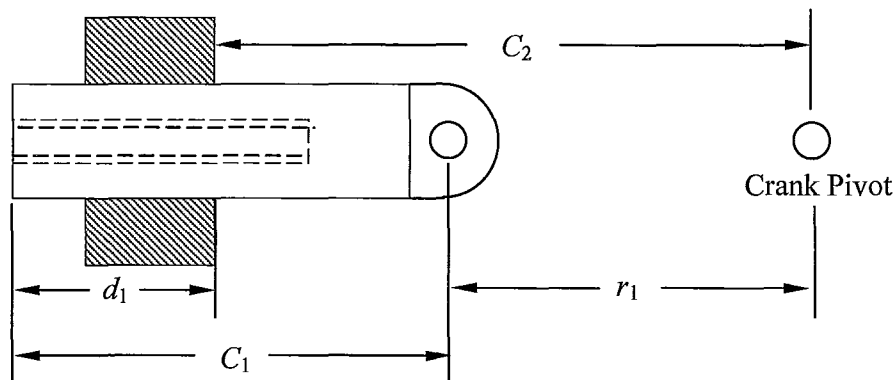
Figure 3.47 Diagram defining the slider and support geometry.

As the crank angle increases, moving the slider closer to the pivot, not only does the distance between reaction forces (d_1) decrease, but the magnitude of the vertical force acting on the slider also increases. Due to this relationship, the maximum force would occur when the slider is fully extended, when the crank is at its limit of $120.3°$. Solving for these equations for that case, the maximum magnitude of F_{R2} is 3.5 N. As stated, the magnitude of the radial force reflected to the motor is equal to F_{R2}, based on a free-body diagram of the motor shaft and lead screw unit shown in Figure 3.48. The reaction moment acting on the motor, M_m, is 59.5 mNm. This is more than the motor can support, so it is critical to ensure that the slider support does not allow these loads to be transferred to the motor. This can be accomplished by making the fit of the slider and bore tight enough that the loading occurs as in Figure 3.45.
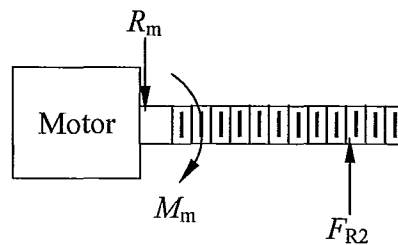
Figure 3.48 Loading diagram of the motor shaft and lead screw.

The end of the wrist support structure has also been analyzed by FEA, with forces of 20.0 N in the horizontal direction and 0.8 N in the vertical direction applied to the pin supports for the crank pivot. The loading and meshing is shown in Figures B.29 and B.30 in Appendix B. Figure B.31 shows the maximum von Mises stress is 88.5 MPa, located at the corner where the base and wall of the pivot support meet. From Figure B.32, the maximum deformation is 4.9 microns.

The maximum tension in the wrist couplers was determined by resolving the horizontal force of 20.0 N through the coupler angle, θ_3, which is equal to 2.2° when the crank angle is 24.4°. Using equation 3.46 and distributing across two couplers, the force acting on each coupler was found to be 10.0 N. Due to symmetrical geometry and loading, only half of the coupler has been analyzed. The loading, meshing and resulting von Mises stress distribution and deformation are shown in Figures B.33-B.36 in Appendix B. From these figures it can be seen that the maximum von Mises stress was found to be 10.2 MPa. The maximum deformation for this component made from stainless steel was found to be 0.14 μm.

Stress analysis has also been conducted on the top and bottom gripper jaws. The loading and meshing for the top gripper jaw can bee seen in Figures B.37 and B.38 in Appendix B. A force of 2 N has been applied to the tool-tip, and a fixed constraint applied to the pivot holes. The results are shown in Figures B.39 and B.40, where the maximum von Mises stress is 33.7 MPa and the maximum deformation is 7.6 microns. Similarly, the results for the bottom gripper jaw, shown in Figures B.43 and B.44, indicate a maximum von Mises stress of 33.9 MPa and a deformation of 8.4 microns.

All of the stress results for the wrist components have been compiled and are listed in Table 3.21.

Table 3.21 Maximum von Mises stress and maximum deformation for wrist components.

Component List	Max. von Mises Stress (MPa)	Max. Deformation (µm)
Slider	15.7	0.4
Slider Support	9.6	0.3
Pivot Support	88.5	4.9
Coupler	10.2	0.1
Top Gripper Jaw	33.7	7.6
Bottom Gripper Jaw	33.9	8.4

The pin joint for the main wrist pivot, attaching the grippers to the support structure, can be analyzed using the free-body diagram and shear and moment curves shown in Figure 3.49. The maximum bending stress and shear stress can be calculated using equations 3.58 and 3.59, respectively, where c is the radius of the pin (0.75 mm), and I is the moment of inertia. Solving for these values gives a maximum bending stress of 105.6 MPa and a maximum shear stress of 11.3 MPa.

$$\sigma_m = \frac{|M|_{max}\, c}{I} = \frac{(35\,\text{mNm})(0.75\,\text{mm})}{0.2485\,\text{mm}^4} = 105.6\,\text{MPa} \tag{3.58}$$

$$\tau_m = \frac{|V|_{max}}{A} = \frac{20\,\text{N}}{\frac{\pi}{4}(1.5\,\text{mm})^2} = 11.3\,\text{MPa} \tag{3.59}$$
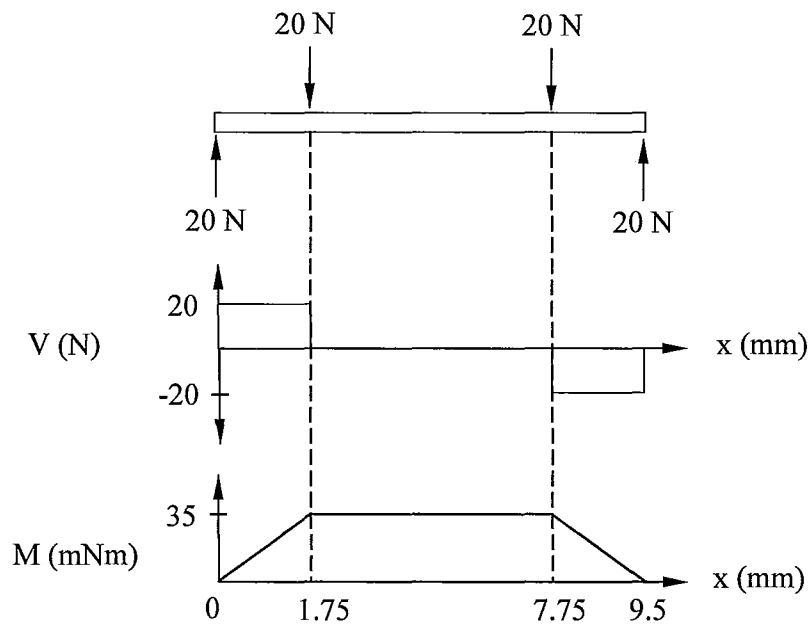
Figure 3.49 Free-body diagram, shear and moment graphs for wrist pivot pin.

3.8 Materials

The material chosen for this design is primarily stainless steel for both its biocompatibility and its strength (Davis, 2003). Annealed stainless steel (AISI 302) has a yield tensile strength of 260 MPa and a yield shear strength of 150 MPa. (Beer & Johnston, 1992). Another strong, biocompatible material that was considered is titanium, but due to its poor tribological properties it is not recommended for articulating joints (Davis, 2003). A summary of the component stresses determined in the previous section is listed in Table 3.22, along with the factor of safety for each component. The factor of safety was calculated by dividing the yield tensile strength of stainless steel by the maximum stress of each component. Examining this table, it can be seen that the highest stress occurs in the elbow pivot pin, which has a factor of safety of 1.9. Since many of the

111

factors of safety are quite high, some components could be miniaturized to conserve

weight. However, the smaller dimensions would be subject to manufacturing constraints.

Table 3.22 Maximum stresses and factor of safety for stainless steel
elbow, roll and wrist joint components.

Joint	Component List	Max. Stress (MPa)	Factor of Safety
Elbow	Slider	26.9	9.7
	Crank	115.9	2.2
	Coupler	24.4	10.7
	Support Structure	126.7	2.1
	Coupler Pins	46.2	5.6
	Elbow Pivot Pin	*134.5*	*1.9*
Roll	Support Structure	14.6	17.8
Wrist	Pivot Support	88.5	2.9
	Slider Support	9.6	27.1
	Slider	15.7	16.6
	Coupler	10.2	25.5
	Top Gripper Jaw	33.7	7.7
	Bottom Gripper Jaw	33.9	7.7
	Wrist Pivot Pin	105.6	2.5

With the selection of these materials, it is then possible to determine the weight of

the forearm. The weight of each of the forearm components has been listed in Table 3.22,

along with the distance between the component's centre of gravity and the elbow joint.

This enables the determination of the additional moment on the elbow joint due to the

effect of gravity. From Table 3.23, it can be seen that the total moment acting on the

elbow joint is 29.7 mNm. This moment applies to the case where the forearm is perfectly

horizontal. Depending on the inclination of the forearm relative to the horizontal plane,

this amount decreases since the centre of mass shifts inward due to the geometry. The

average torque (M_w) exerted on the forearm across a range of motion from θ_{min} to θ_{max} is

represented by equation 3.60 and simplified to equation 3.61, where M_h is 29.7 mNm and

θ is the angle of inclination. Since the elbow joint moves through a range of about 100°

and by centering the range of motion at the horizontal plane, θ_{min} to θ_{max} would be -50°

and 50°, respectively, as illustrated in Figure 3.50. Solving for M_w gives an average

torque due to gravity of 26 mNm. As mentioned in section 3.6.1, this is the value that has

been used in determining the overall applied torque for the elbow joint used throughout

the design.

$$M_w = \frac{M_h}{\theta_{max} - \theta_{min}} \int_{\theta_{min}}^{\theta_{max}} \cos(\theta)\,d\theta \qquad (3.60)$$

$$M_w = \frac{M_h \left(\sin(\theta_{max}) - \sin(\theta_{min})\right)}{\theta_{max} - \theta_{min}} \qquad (3.61)$$
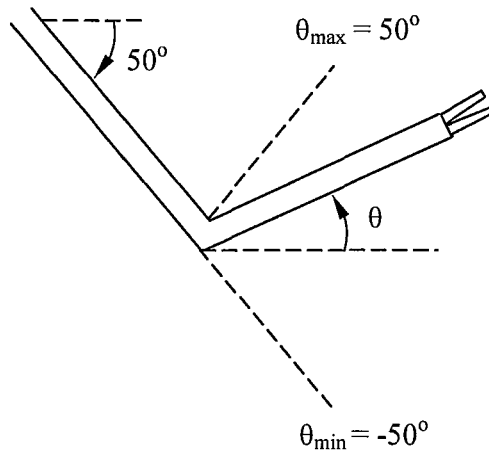
Figure 3.50 Inclination of forearm with centre of range of motion at horizontal.

Table 3.23 Weight distribution for forearm design components.

Component List	Material	Weight		Distance from Elbow Joint	Moment
		Unit (g)	Total (g)	(mm)	(mNm)
Bearings SMR63	Stainless Steel	0.22	0.22	12	0.026
Bearings SMR63	Stainless Steel	0.22	0.22	16	0.035
Motor 136:1 ratio (x2)	N/A	1.7	3.4	60	2.001
Motor 699:1 ratio	N/A	1.68	1.68	38	0.626
Coupling 3-1.5	Aluminum	0.5	0.5	22	0.108
Coupling 1.5-1.5 (x2)	Aluminum	0.65	1.3	76	0.969
Roll Shaft	Stainless Steel	0.828	0.828	14	0.114
Wrist Leadscrew (x2)	Stainless Steel	0.382	0.764	89	0.667
Structure - Roll	Stainless Steel	8.483	8.483	28	2.330
Structure - Wrist	Stainless Steel	11.06	11.06	78	8.463
Forearm Cover	Stainless Steel	15	15	60	8.829
Sliders (x2)	Stainless Steel	0.613	0.613	96	0.577
Couplers (x4)	Stainless Steel	0.08	0.32	109	0.342
Pins - 4mm (x4)	Stainless Steel	0.619	2.476	109	2.648
Pin - 10mm	Stainless Steel	0.18	0.18	114	0.201
Top Gripper Jaw	Stainless Steel	0.773	0.773	120	0.910
Bottom Gripper Jaw	Stainless Steel	0.764	0.764	120	0.899
				Total Moment (mNm) =	**29.7**

3.9 Summary

A novel internally-actuated instrument has been designed, featuring four DOF: an elbow joint, a roll joint, and a wrist joint that employs two independently-actuated gripper jaws to allow for both rotation and grasping ability. The target specifications for the speeds and ranges of motion were determined for each joint. The instrument has an outer diameter of 12.7 mm to fit into a standard 15 mm trocar. It has been designed to withstand a tool-tip force of 2 N.

114

The joints will be actuated by 6 mm DC motors. The Faulhaber brushless DC motors (0620 012 B) with a 16:1, 64:1 and 256:1 gearboxes have been selected as ideal for the designed wrist, elbow and roll joints, respectively, since they can provide the required torque. However, the prototype will employ the Gizmoszone brushed DC motors with 136:1 gearbox (GH6123S) for the elbow and wrist and 700:1 gearbox (GH6124S) for the roll joint due to their lower cost, ease of control and fewer wires.

The transmission system chosen for the elbow and wrist joints is the lead screw plus slider-crank mechanism. A method has been developed for defining and optimizing the slider-crank parameters. The optimized elbow joint has a 6 mm crank radius, a 9 mm coupler length, a 3.85 mm crank offset, and a crank angle range of 119°. The elbow joint of the prototype, however, has been manufactured with a 15 mm coupler length and a 2 mm offset, with a crank angle range of 110°. The optimized wrist joint has a 4 mm crank radius, a 9 mm coupler length, and a 2 mm crank offset, with a crank angle range of 96°. These configurations can theoretically provide joint speeds of 1.44 rpm for the optimized elbow joint and 9.53 rpm for the wrist joint, using the designated Faulhaber brushless DC motors. For the prototype with the Gizmoszone motors, the elbow joint and wrist joint can attain speeds of 2.48 rpm and 3.70 rpm, respectively. The roll joint can attain speeds of 31.3 rpm using the Faulhaber motor and 40.0 rpm in the prototype with the Gizmoszone motor. Design calculations and stress analysis results have also been discussed in detail, leading to the component and material selection based on the stress and force results.

The following chapter outlines the manufacture and assembly of the prototype, as well as the experiments that have been performed to test the speed and force capabilities of the prototype.

CHAPTER 4

EXPERIMENTAL TESTING

4.1 Introduction

This chapter covers the manufacture and assembly of the first prototype, describing the rapid prototyping method that was used and outlining the assembly of the elbow joint, roll joint, and wrist joint. The switchbox that was designed to control the prototype is also described. Next, the experimental setup for the elbow joint experiments is outlined, for both the video motion analysis and the potentiometer tests that were conducted to determine the joint speeds. Results for these tests are then discussed. Similarly, the experimental setup for the roll joint and wrist joint speed tests are outlined along with their respective results. Finally, the experimental setup for the force experiment is outlined, followed by results and discussion.

4.2 Manufacture and Assembly of First Prototype

4.2.1 Rapid Prototyping

The final design is intended to be manufactured out of stainless steel for its strength and biocompatibility. However, this material can be quite expensive to manufacture both in terms of its time and cost, so the first prototype has been manufactured primarily out of ABS plastic using a 3D rapid prototyping machine (Dimension BST 768). The rapid prototyping machine uses fused deposition modeling

(FDM) technology to construct the small, complex parts from CAD files with relative ease. Since this prototype is made primarily out of plastic, it provides a purely kinematic model and is not intended to support realistic loads.

4.2.2 Elbow Joint

An image of the assembled elbow joint is shown in Figure 4.1. As mentioned in section 3.6.6, although the design calls for the Faulhaber brushless DC motor, for ease of control a simple DC motor has been used for this prototype. The motor is a Gizmoszone DC motor (GH6123S) with a 136:1 gear reduction. The motor shaft is attached to a Reliaflex coupling (RCS A 6-1.5-1.5), which is in turn attached to the M2x0.4 lead screw. The lead screw has been inserted through the pillow block, which consists of a radial bearing (MR52) and two thrust bearings (F2-6). The lead screw is then threaded into the slider, which consists of eight radial bearings (SMR681-X) that act as wheels to reduce friction. Pin joints connect the slider to the coupler, the coupler to the crank, and the crank to the base. Each pin joint uses tight press-fits for the components on the outside ends of each pin, and a slip fit for the inside component to allow rotation of the joint.
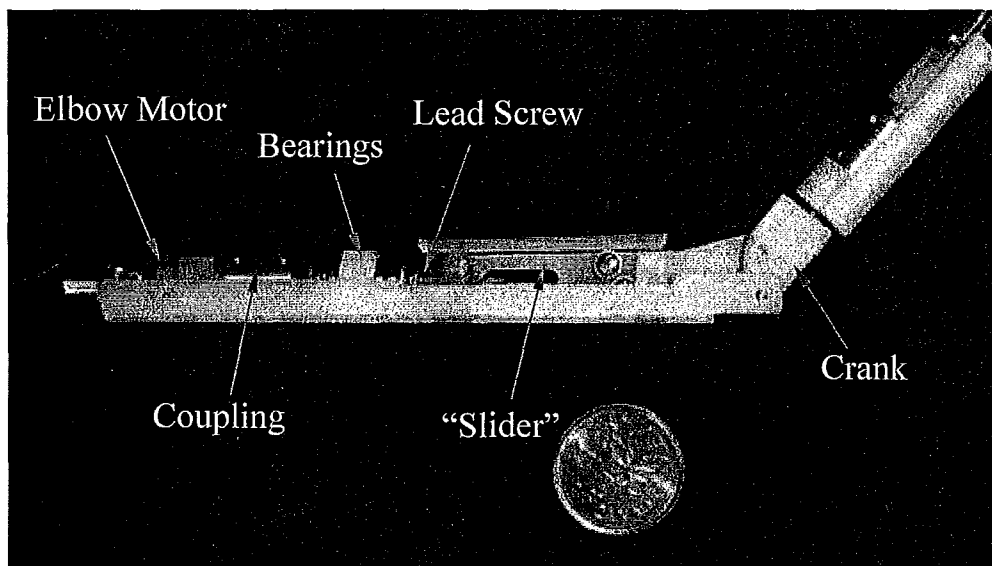
Figure 4.1 Photograph of the elbow joint prototype before final assembly.

4.2.3 Roll Joint

An image of the assembled roll joint is shown in Figure 4.2. Once again, although the design calls for the Faulhaber brushless DC motor, for ease of control a simple DC motor has been used for this prototype. The roll motor is a Gizmoszone motor (GH6124S) with a 700:1 gear reduction. The motor shaft is attached to a Reliaflex coupling (RCS A 6-3-1.5). A 3 mm-diameter shaft is attached to the other end of the coupling and is supported by two radial bearings located inside the support structure. The end of the shaft is threaded and glued into the elbow crank.
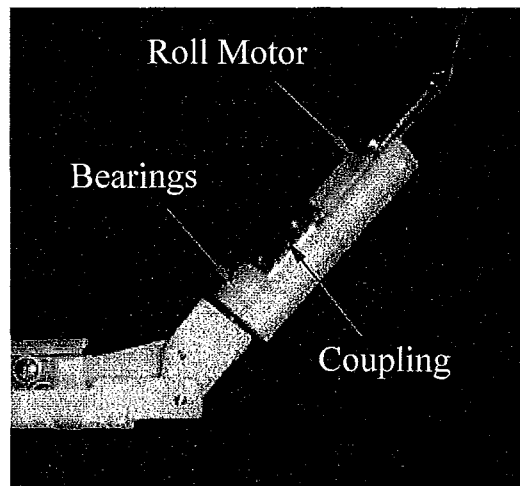
Figure 4.2 Photograph of the roll joint prototype before final assembly.

4.2.4 Wrist & Gripper

Top and side views of the assembled wrist joint are shown in Figure 4.3. Again, although the design calls for Faulhaber brushless DC motors, for ease of control simple DC motors have been used for this prototype. The two motors are Gizmoszone motors (GH6123S) with a 136:1 gear reduction. The motor shafts are each attached to a Reliaflex coupling (RCS A 6-1.5-1.5), which are in turn attached to the M2x0.4 lead screws. The lead screws have been threaded into the cylindrical sliders, which are attached to the couplers and the top and bottom gripper jaws (the cranks) by pin joints. The gripper jaws are then attached to the base with a 10 mm long dowel pin. All of the pin holes in the gripper jaws and sliders are slip fit to allow rotation, whereas the pin holes in the couplers and the base are designed for a tight press-fit. The motors are secured with a top clamp that has been attached to the base with two screws, one behind the motors and one

between the lead screws. The clamp has enough clearance beyond the motors to allow the

couplings to rotate freely.
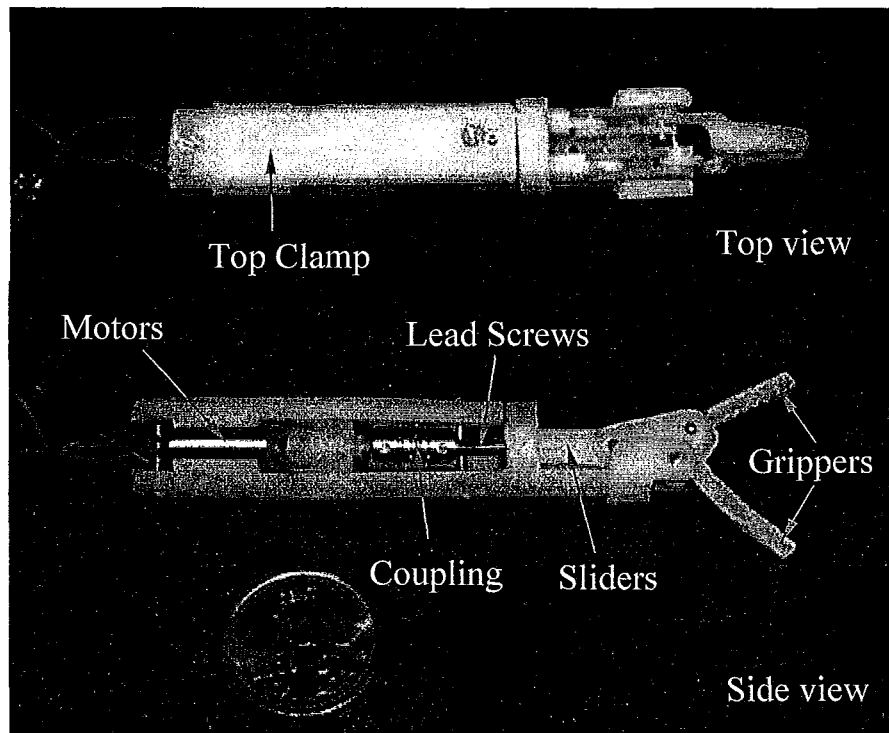
Figure 4.3 Photographs of the top and side view of the wrist joint prototype before final
assembly.

4.2.5 Preliminary Motor Testing

Prior to assembly, the motors were tested to confirm their specifications according

to the spec sheets supplied by the company and detailed in section 3.4. The tests were

conducted using a variation on the video motion analysis described in section 4.4.1, the

distinction being that the number of full rotations of the motor shaft was counted over

time. From these results, given in Appendix C, it can be seen that the Gizmoszone DC

motor (GH6123S) with a 136:1 gear reduction was confirmed to perform at 200 rpm for a

3 V input under ideal conditions. Similarly, the Gizmoszone motor (GH6124S) with a

700:1 gear reduction was confirmed to perform at 40 rpm.

4.2.6 Final Assembly

The elbow, roll and wrist joints were then assembled to the outer shell,

constructed from two pieces of standard half-inch (12.7 mm) outer diameter stainless

steel tube. For the forearm, the tube needed to be gently squeezed in a clamp to form an

ellipse with a width of 13 mm and a height of 12.4 mm. Next, the inside of the tube was

ground to an inner width of 12 mm using a Dremel tool to allow the insertion of the wrist

joint. The grinding was necessary to provide the clearance for the two 6 mm diameter

motors situated side by side. All of the parts were then attached to the shell using small

(#0-80) set screws. An image of the final assembly of the prototype and its dimensions is

shown in Figure 4.4.
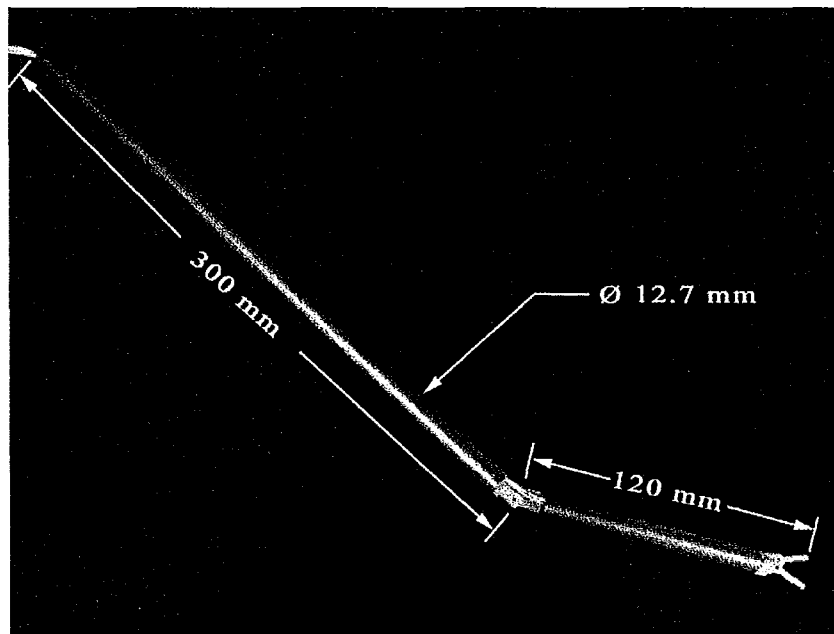
Figure 4.4 Photograph and dimensions of the prototype after final assembly.

4.2.7 Switchbox

A switchbox was designed and assembled to allow the DC motors in the prototype to be individually driven, by supplying them with a constant voltage when a switch is activated. The switches are all double-pole, double-throw (DPDT) to allow forward and reverse control of each motor. At their centre position, no voltage is supplied. A photograph of the switchbox is shown in Figure 4.5. There are four switches in total: one for bending and straightening the elbow joint; one for driving the roll joint in a clockwise or counterclockwise direction; and one each for opening and closing the top and bottom gripper jaws in the wrist. The red and black plugs extending from the front of the switchbox connect to the power source and ground, whereas the plugs extending from the back of the switchbox connect to each of the motors inside the prototype. The electrical schematic and wiring diagram for the switchbox are depicted in Figures 4.6 and 4.7, respectively.

Figure 4.5 Photograph of the switchbox.
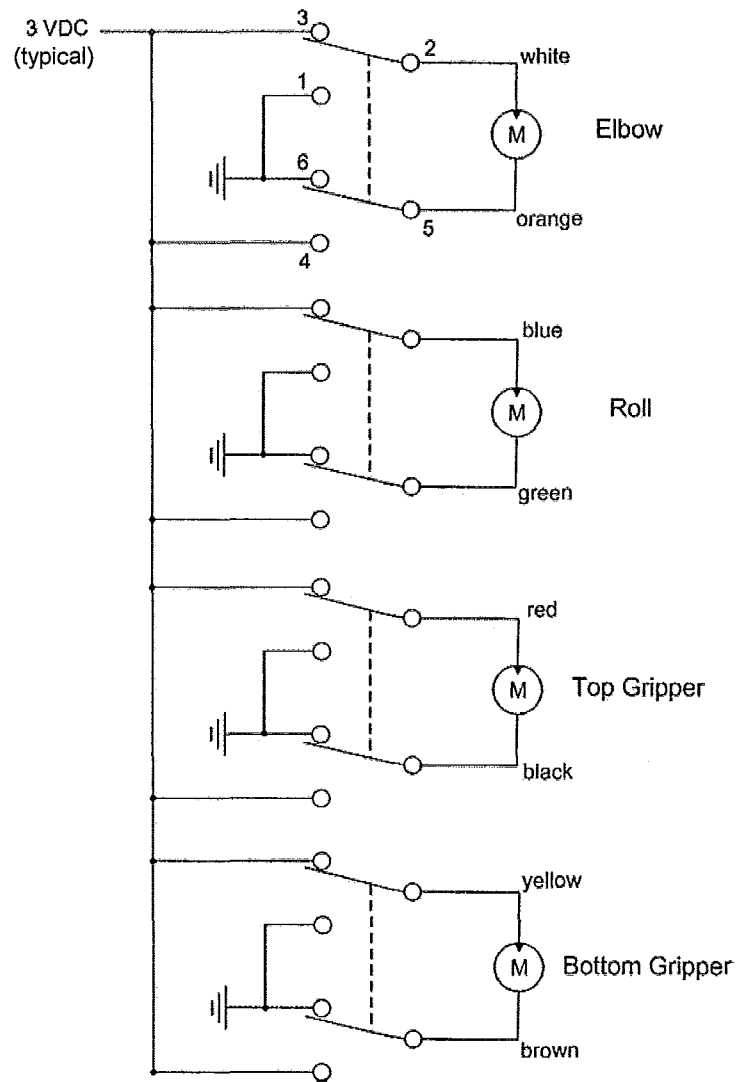
Figure 4.6 Electrical schematic for the switchbox.
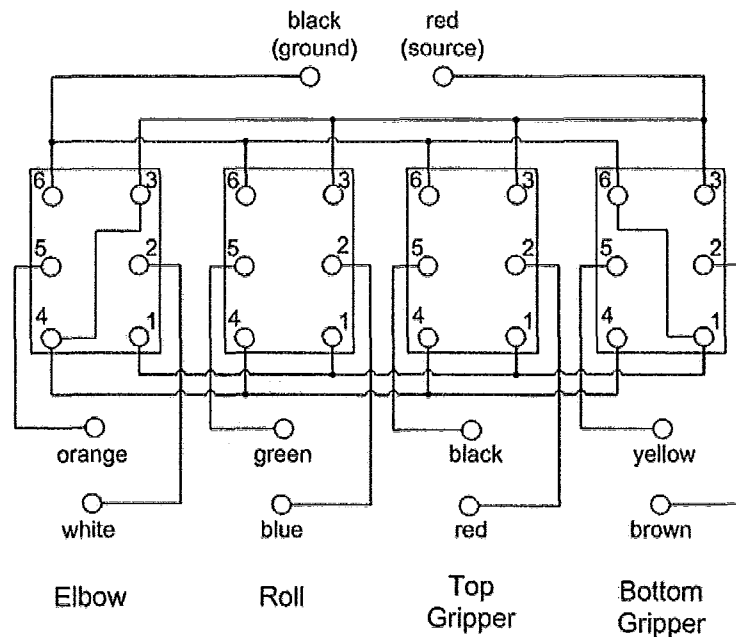
Figure 4.7 Wiring inside the switchbox.

4.3 Elbow Joint Experiments

4.3.1 Experimental Setup – Video Motion Analysis

Experiments to measure the average speeds of the elbow joint using the video motion analysis techniques discussed in section 3.3 were conducted for both horizontal and vertical testing. The videos were taken using a Sony Cyber-shot camera (model #DSC-P93A). For the horizontal tests, the prototype was mounted such that the forearm would sweep along a horizontal plane roughly 25 mm above the table. A camera was mounted directly above this setup and pointed downwards, such that it had a view orthogonal to the plane of joint motion. The joint was filmed bending and straightening across its full range of motion for constant voltage inputs, ranging from 1.25 V to 3.0 V. See Figure 4.8 for a photograph of the horizontal experimental setup. The footage was

125

then uploaded into the video motion analysis software program (Institute for Rehabilitation Research and Development, 2009) where the change in joint angles over time could be measured. Note that the associated crank angle equals 40° less than each joint angle measured due to the geometry of the design, as depicted in Figure 4.9.

To get an estimate of the prototype's performance under loading, specifically the gravitational pull due to its own weight, vertical tests were also conducted. For these tests, the prototype was mounted such that the forearm would sweep along a vertical plane. The elbow joint has a range from 0° (straight) to 100° (fully bent), so the prototype was mounted at a 50 degree inclination so that the forearm would be horizontal halfway along its motion, at which point the joint would experience the maximum torque due to the weight of the forearm. The weight distribution of the forearm will be discussed further in section 4.3.3. Similar to the horizontal tests, a camera was mounted pointing horizontally towards the setup, with a view orthogonal to the vertical plane. The joint was again filmed bending and straightening across its full range of motion for constant voltage inputs, this time ranging from 1.25 V to 4.0 V. See Figure 4.10 for a photograph of the vertical experimental setup.

This method had originally been intended to be used to measure the profile of the instantaneous angular velocities as well as the average speed across the entire range, but there was too much scatter in the results to obtain an accurate representation. As such, another test was designed to confirm instantaneous speeds, as outlined in the next section.
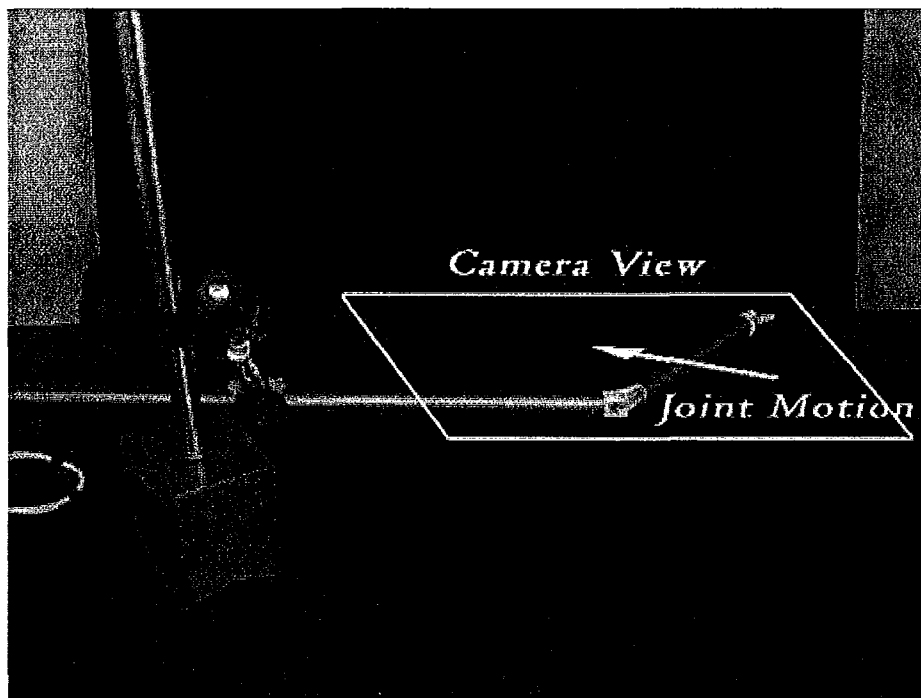
Figure 4.8 Experimental setup for horizontal tests.
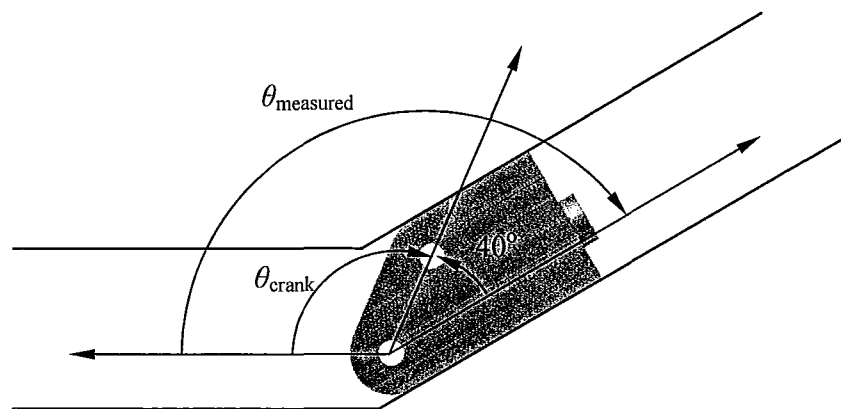
Figure 4.9 Geometric relationship between measured and crank angles.
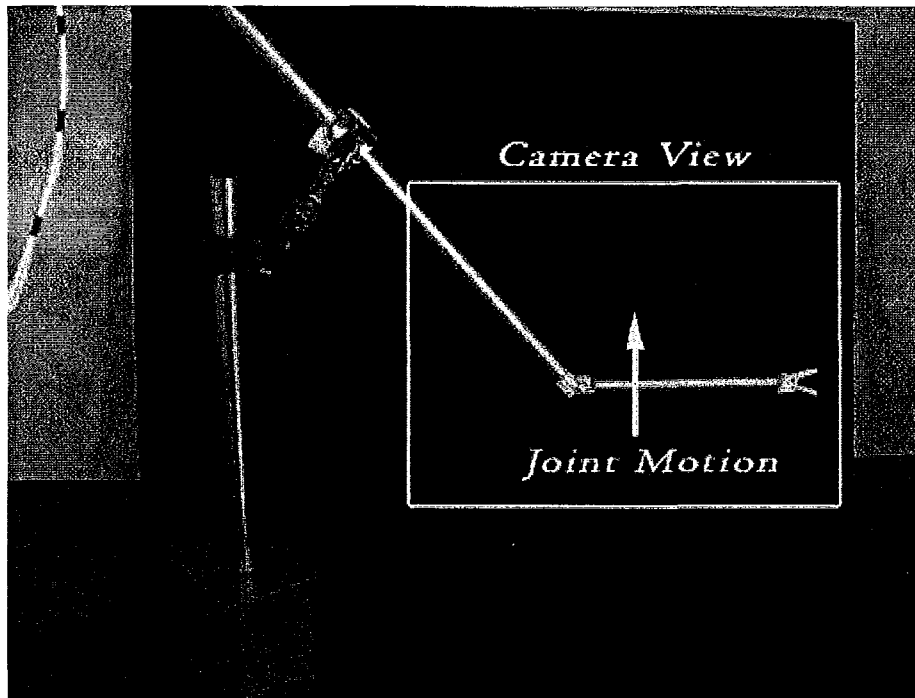
Figure 4.10 Experimental setup for vertical tests.

4.3.2 Experimental Setup – Potentiometer Test

To measure the instantaneous angular velocity profile of the elbow joint, another experiment was performed using a rotary potentiometer. A top view of the experimental setup is shown in Figure 4.11. The robotic instrument was mounted and fixed in place beyond the elbow joint such that the forearm would move horizontally several centimeters above the table. A pulley with a 6.5 mm radius was attached to a radial potentiometer and mounted so that the pulley was in plane with the horizontal sweep of the forearm. A low-friction fishing line (Spiderwire Stealth™) was used as the pulley cable and was attached to the pin at the wrist pivot. As the elbow joint rotated, the cable

would extend and cause the pulley to rotate. The distance of the cable extension could be

calculated based on the rotations recorded by the potentiometer.
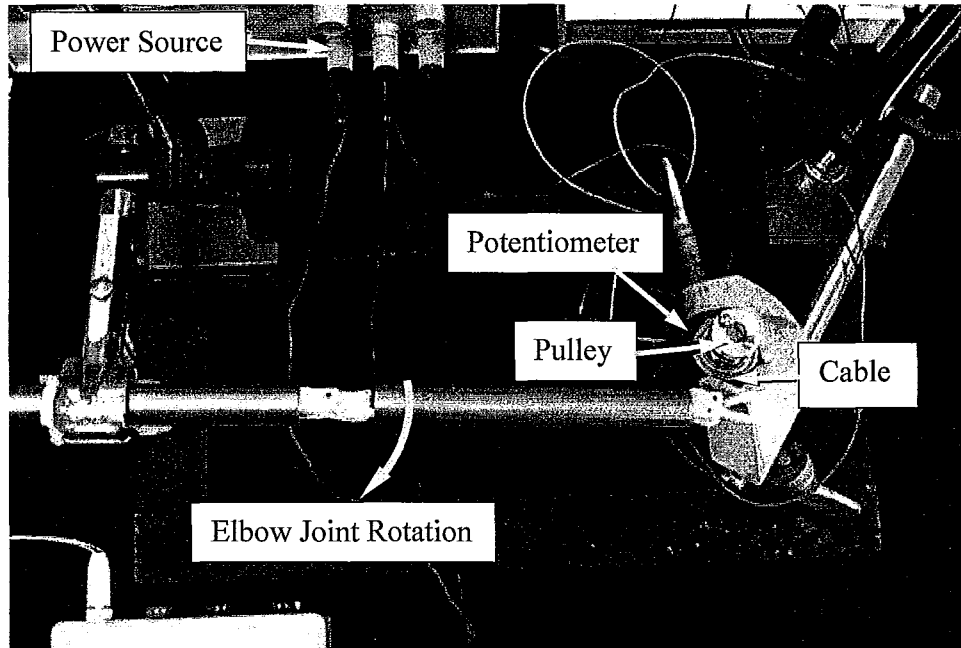
Figure 4.11 Experimental set-up for potentiometer tests.

A constant voltage of 3 VDC was supplied to the elbow motor, which was

connected in series to a 1 ohm resistor. The voltages across the motor and resistor were

measured in order to monitor the current being supplied to the elbow motor. Schematics

of the electrical circuits for both the potentiometer and the elbow motor in series with the

resistor are depicted in Figures 4.12 and 4.13.
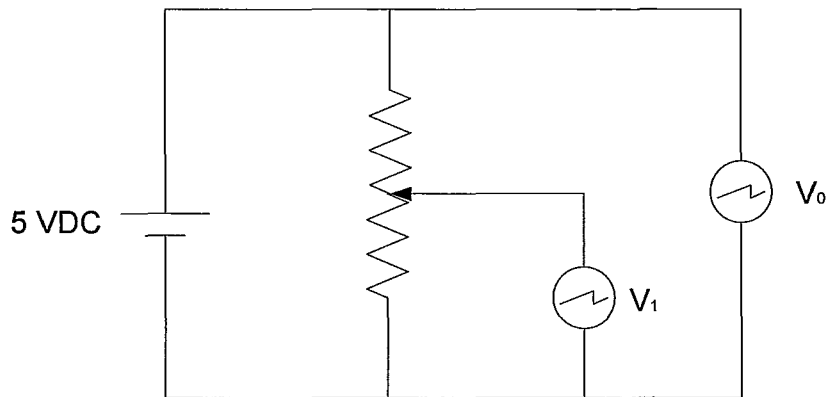
Figure 4.12 Electrical circuit for reading the voltages from the potentiometer.
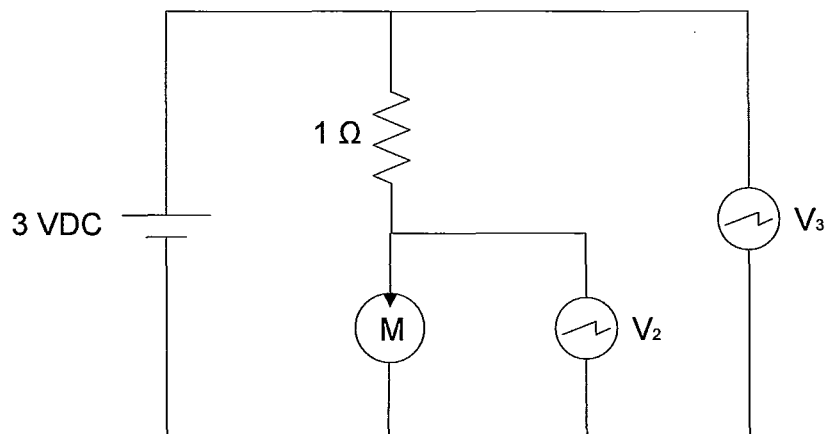
Figure 4.13 Electrical circuit for reading the voltages from the elbow motor and resistor.

A schematic of the geometry involved is depicted in Figure 4.14. The offset between the instrument in its straightened position and the centre of the pulley, d_1, was measured to be 20.0 mm. The distance between the elbow joint axis of rotation and the centre of the pulley, d_2, was measured to be 121.5 mm. The length of the forearm, a_2, was measured to be 119.25 mm. The rotation of the elbow, represented by θ, would determine the angle of the cable with respect to the pulley, represented by β.

To simplify the geometry, the extension of the cable was assumed to be a straight line from the wrist joint to the rightmost edge of the pulley. This geometry, shown in Figure 4.15, created two triangles. The first was a right-angled triangle of height d_1 and length $d_2 + r$, and was used to solve for angle γ. The second triangle had two sides of fixed length, a_2 and the hypotenuse of Triangle 1 (denoted as h_1), and a third side that could be approximated by $\beta r + d_3$, which represented the extension of the cable. Based on the total number of turns possible and the voltage input to the potentiometer, the voltage reading from the potentiometer was then converted to determine the extension of the cable. The angle of rotation of the elbow joint was then calculated using the law of cosines, as expressed in equation 4.1:

$$\theta = \cos^{-1}\left(\frac{a_2{}^2 + h_1{}^2 - (\beta r + d_3)^2}{2a_2 h_1}\right) - \gamma \qquad (4.1)$$
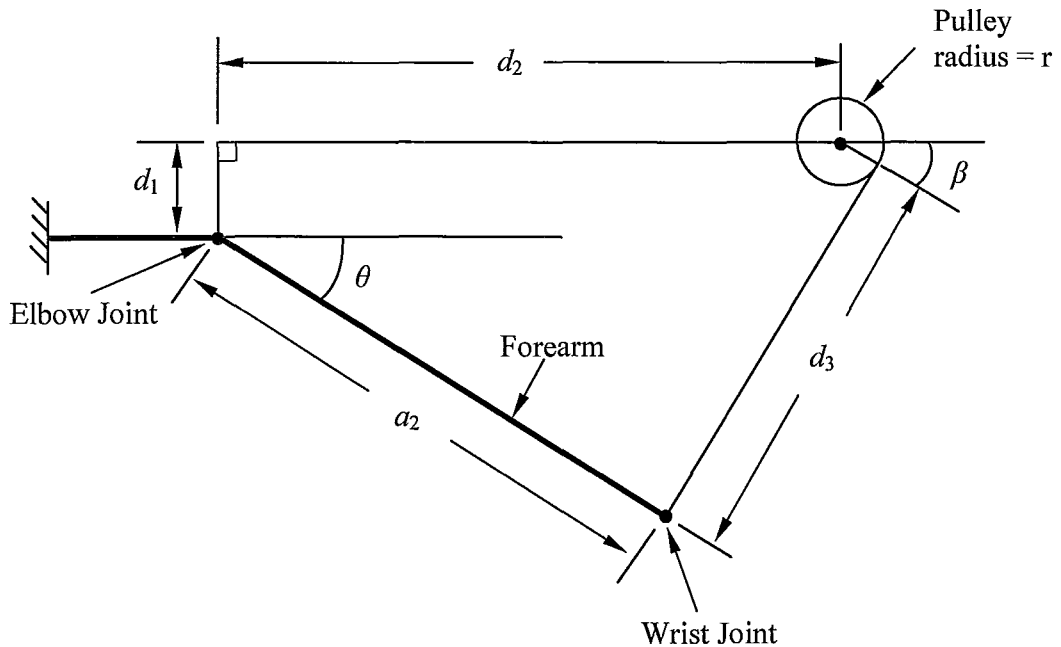
Figure 4.14 Schematic of potentiometer test set-up.
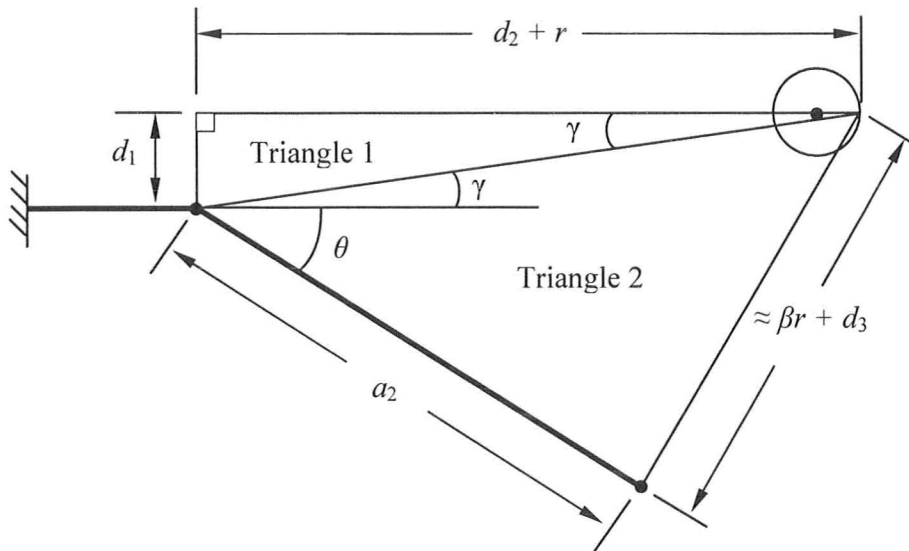
Figure 4.15 Simplified schematic of potentiometer test set-up.

4.3.3 Weight Distribution of Forearm

The weight of each component of the forearm was measured in order to estimate the amount of torque the elbow joint would experience due to the gravitational force acting on the forearm. The distance between the elbow pivot and the centre of mass of each part was determined based on the dimensions in the CAD design. These findings are listed in Table 4.1. The maximum total moment acting on the elbow joint due to the effect of gravity was found to be 16.8 mNm. As mentioned in section 3.8, depending on the inclination of the forearm, this amount decreases since the centre of mass shifts inward due to the geometry. Using the relationship given in equation 3.60, the average torque when moving through inclinations of -50° to 50° is 14.7 mNm.

Table 4.1 Weight distribution for components in the prototype.

Component List	Material	Weight		Distance from Elbow Joint	Moment
		Unit (g)	Total (g)	(mm)	(mNm)
Bearings SMR63	Stainless Steel	0.22	0.22	12	0.026
Bearings SMR63	Stainless Steel	0.22	0.22	16	0.035
Motor 136:1 ratio (x2)	N/A	1.70	3.40	60	2.010
Motor 699:1 ratio	N/A	1.68	1.68	38	0.625
Coupling 3-1.5	Aluminum	0.50	0.50	22	0.106
Coupling 1.5-1.5 (x2)	Aluminum	0.65	1.30	76	0.964
Roll Shaft	Stainless Steel	0.83	0.83	14	0.114
Wrist Leadscrew (x2)	Stainless Steel	0.38	0.76	89	0.665
Structure - Roll	ABS Plastic	0.99	0.99	28	0.269
Structure - Wrist	ABS Plastic	2.30	2.30	78	1.768
Forearm Shell	Stainless Steel	15.00	15.00	60	8.829
Sliders (x2)	ABS Plastic	0.13	0.26	96	0.246
Couplers (x4)	ABS Plastic	0.08	0.32	109	0.342
Pins - 4mm (x4)	Stainless Steel	0.05	0.20	109	0.213
Pin - 10mm	Stainless Steel	0.18	0.18	114	0.201
Top Gripper Jaw	ABS Plastic	0.15	0.15	120	0.177
Bottom Gripper Jaw	ABS Plastic	0.16	0.16	120	0.188
				Total Moment (mNm) =	**16.8**

4.3.4 Video Motion Analysis Results

An example of the footage used in the video motion analysis software for a horizontal test is shown in Figures 4.16 and 4.17. The first depicts the angle and time measurements taken for the elbow joint at the beginning of its bending motion, and the second depicts the angle and time measurements taken at the end of its bending motion. The average speed of the joint was calculated by dividing the angle change by the change in time across this range.

133
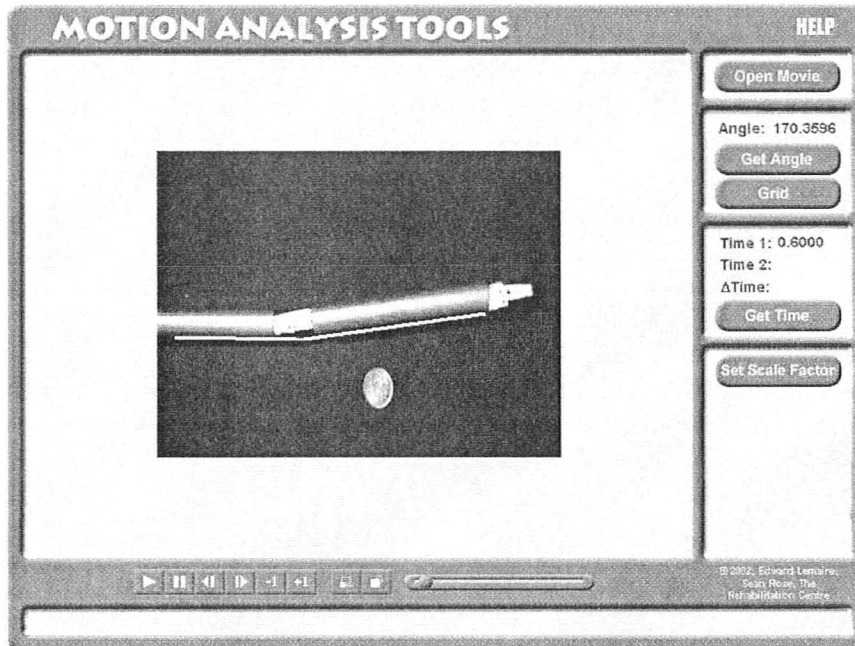
Figure 4.16 First measurement of bending angle and time for a horizontal elbow joint experiment.
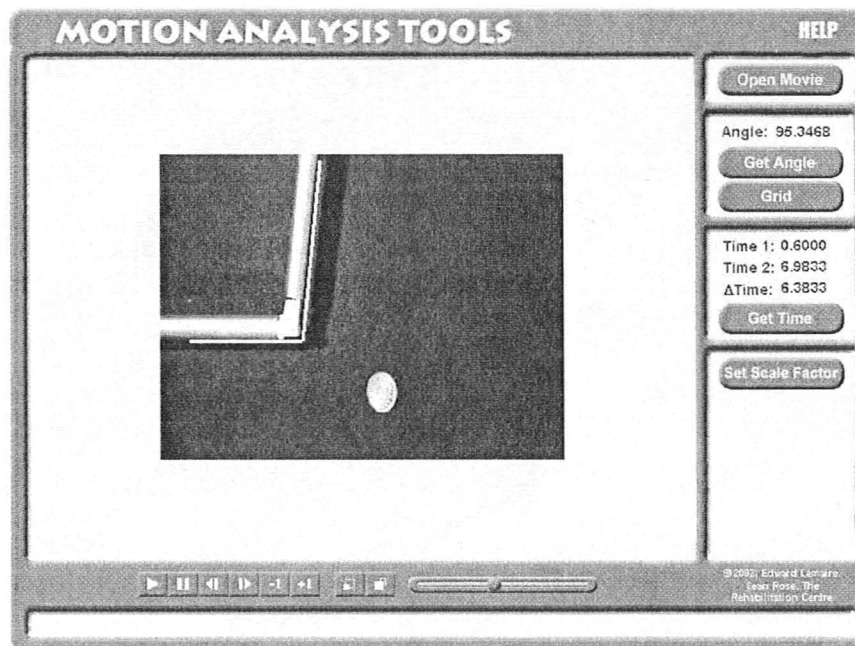
Figure 4.17 Second measurement of bending angle and time for a horizontal elbow joint experiment.

For the horizontal tests, the average experimental speeds were calculated for voltage inputs ranging from 1.25 V to 3 V. Four trials were conducted at each voltage for bending and straightening of the elbow joint. Both the bending and straightening results have been plotted independently in Figure 4.18, to show speed differences due to direction of motion. It can be seen that the straightening data exhibits a slightly steeper slope than the bending data.

Confidence intervals were calculated using equation 4.2 (Devore, 2004), where $\bar{x}$ is the sample mean, s is the sample standard deviation, n is the sample size (where n = 4 for these experiments), and α is 0.05 to form a 95% confidence interval based on equation 4.3. The t-value for these parameters is $t_{0.025,3} = 3.182$ (Table A.5 in Devore, 2004).

$$\bar{x} \pm t_{\alpha/2,n-1} \cdot \frac{s}{\sqrt{n}} \qquad (4.2)$$

$$C.I.\% = 100(1-\alpha)\% \qquad (4.3)$$

At 3 V, the mean[5] and 95% confidence interval of the average speeds was 1.96 ± 0.04 rpm for the straightening data and 1.79 ± 0.19 rpm for the bending data. This difference could be due to directional surface roughness, causing more friction in one direction than the other.

Extrapolating the linear trends for these results, the straightening and bending trend lines cross the x-axis at 0.57 V and 0.55 V, respectively, indicating that it takes this much voltage to overcome static friction at each starting position.

---

[5] In this thesis, "average speed" refers to the overall speed across the joint's range of motion, and "mean of the average speeds" refers to the mean value of the experimental data for the average speeds.
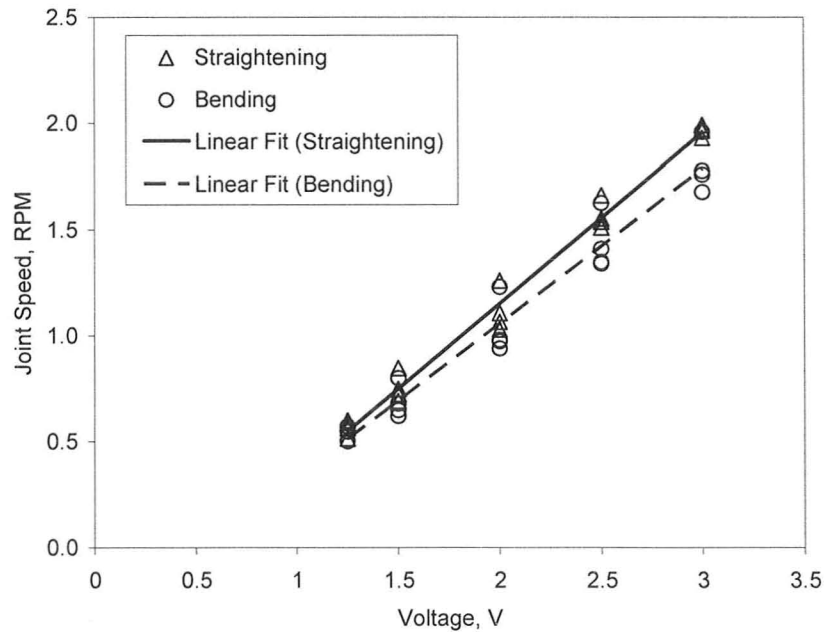
Figure 4.18 Average elbow joint speeds for straightening and bending in horizontal tests.

For the vertical tests, the average experimental speeds were calculated for voltage inputs ranging from 1.25 V to 4 V for straightening tests, which were moving in the direction of the gravitational pull. For the bending tests, which were opposing the gravitational forces, the speeds were calculated for voltage inputs of 2 V to 4 V since the elbow joint would not move at lower voltage inputs. Four trials were conducted at each voltage for bending and straightening of the elbow joint. Both the bending and straightening results have been plotted independently in Figure 4.19. In this case, the bending and straightening results exhibited similar slopes, with the bending tests performing on average 0.4 rpm slower than the straightening tests for all voltage inputs.

At 3 V, the mean and 95% confidence interval of the average speeds was 2.40 ± 0.09 rpm for the straightening data and 1.98 ± 0.17 rpm for the bending data.
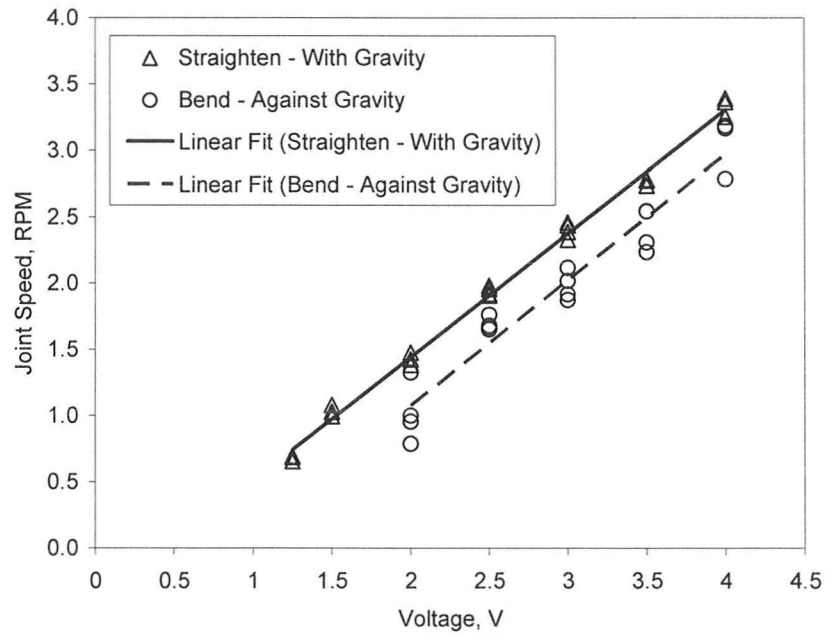
Figure 4.19 Average elbow joint speeds for straightening and bending in vertical tests.

The combined results, including all bending and straightening data, are plotted in Figure 4.20 to compare the overall horizontal and vertical results. It can be seen that the vertical tests performed better than the horizontal tests overall. This seems indicative of a higher frictional element when the joint is operating horizontally, since the weight of the forearm would cause the crank to press down on the support structure at the pin joints. In the vertical case, the crank would be allowed to move more freely since it would be suspended in the centre of the pin joint, maintaining the designed space tolerances on either side.
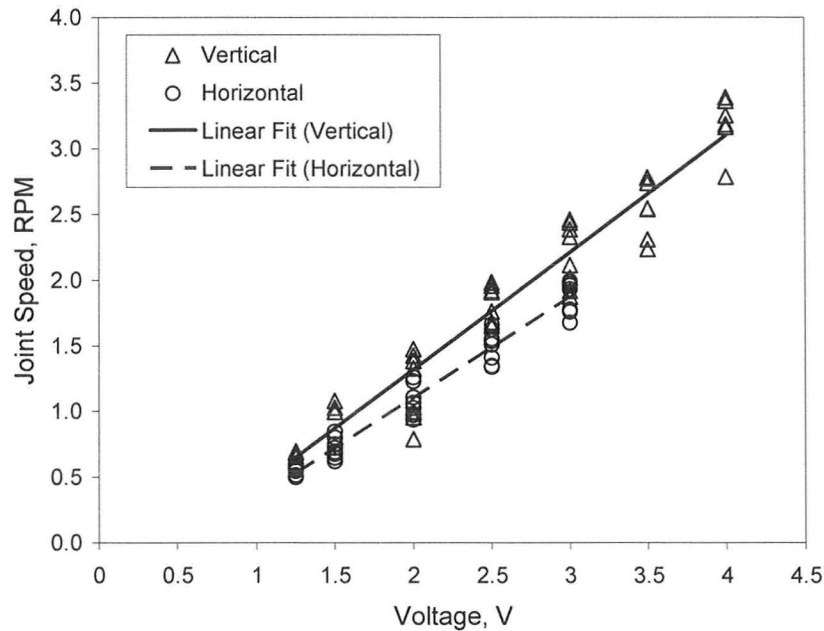
Figure 4.20 Average elbow joint speeds for horizontal and vertical tests.

From Figure 4.16 earlier in this section, note that the first measurement of the angle occurred at 170° rather than at the fully straight position of 180° (140° crank angle), at which the joint began moving. This was due to a measurement limitation in the motion analysis software that could not recognize joint angles higher than 170°. Also, due to the nature of the control of the joints via the switchbox and purely visual feedback, there was some risk of over-extending the joint past its mechanical limits if the switch was not released in time. This could result in mechanical collisions of the slider and thrust bearings. To avoid this risk, for these experiments the joint was stopped before reaching the final position of 70° (30° crank angle).

Under ideal conditions, the theoretical average speeds are highly dependent on the range of motion of the joint, as illustrated in Figure 4.21. The average speed for the full

crank angle range of motion from $30°$ to $140°$ is 2.48 rpm (as outlined in section 3.6.6), whereas decreasing the range of motion will result in a smaller average speed under ideal conditions since the joint has higher speed capabilities at the beginning and end of its motion. To account for this dependence, the theoretical average speeds were calculated for each test based on the actual range of motion measured. For example, for a 3 V input, the four horizontal bending tests were measured on average over a crank angle range of $54°$ to $129°$, which corresponds with an average theoretical joint speed of 2.30 rpm. The four vertical bending tests, on the other hand, were measured on average over a crank angle range of $38°$ to $131°$, which corresponds with an average theoretical joint speed of 2.35 rpm.
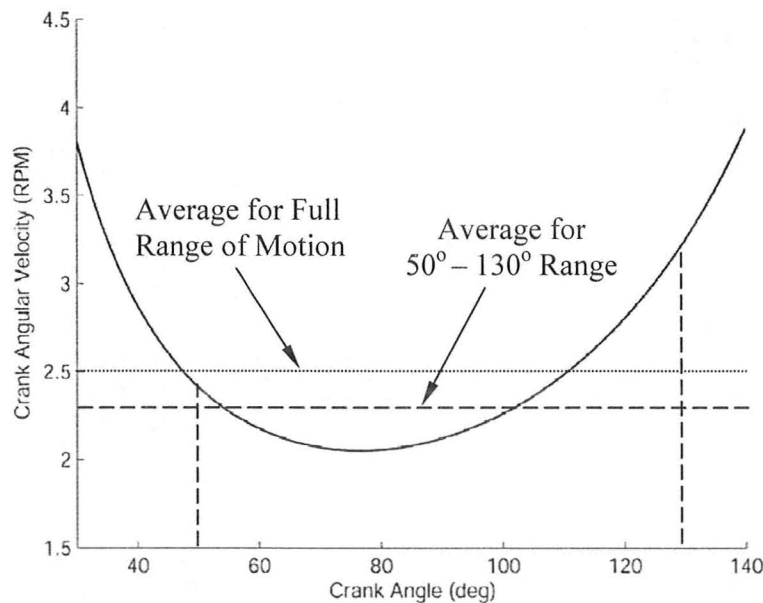
Figure 4.21 Theoretical elbow joint speed averages varying with range of motion.

The theoretical speeds for each test are listed in Table 4.2, along with the mean and 95% confidence intervals of the average speeds for the experimental results for each

test at 3.0 V. It can be seen that, overall, the bending motions performed worse than

expected compared to the straightening tests.

Table 4.2 Comparison of theoretical and experimental average speeds
for horizontal and vertical tests at 3.0 V.

Test	Avg. Theoretical Speed (rpm)	Avg. Experimental Speed (rpm)
Horizontal (Bend)	2.30	1.79 ± 0.19
Horizontal (Straighten)	2.30	1.96 ± 0.04
Vertical – against gravity (Bend)	2.35	1.98 ± 0.17
Vertical – with gravity (Straighten)	2.34	2.40 ± 0.09

As outlined in section 4.3.3, the average torque applied to the elbow joint due to

the effect of gravity was 14.7 mNm. This correlates to an average torque reflected to the

motor of 0.51 mNm. Linearly interpolating based on the linear relationship between the

torque and speed of the motor (as defined by the manufacturer's specifications, outlined

in section 3.4) with a constant voltage input of 3 V, this added torque would result in a

decrease in speed from the ideal 200 rpm down to 197.3 rpm. This motor speed would

result in a 1.315 mm/s linear slider speed, which in turn would result in an average crank

angle speed of 2.45 rpm, if measured across the full range of motion. This represents a

0.03 rpm decrease from the ideal average speed of 2.48 rpm.

From Table 4.2, the differences between bending and straightening under similar

circumstances (as in the horizontal tests at 3 V) are approximately 0.17 rpm. From the

previous analysis of the effect of gravity, the joint should exhibit a speed decrease of 0.03

rpm when working against gravity, and a speed increase of 0.03 rpm when the effect of

gravity is working in favour of the direction of motion. Combining these factors, it would

be expected for the vertical straightening and bending tests to exhibit differences of about 0.23 rpm. In fact, the averages of the vertical tests showed a difference of 0.42 rpm, although there is enough variation in the results (with confidence intervals up to ± 0.19 rpm) that the experiments can be said to match the expected results.

A significant source of error for this experiment is likely due to the limitations of the video motion analysis software. Sixteen measurements were checked for their accuracy and were determined to have an overall error of ± 1°, which would translate into an angular speed error of ± 0.33 rpm.

4.3.5 Potentiometer Test Results

To obtain more accurate results for the instantaneous angular velocity profile of the elbow joint, another experiment was performed by taking measurements of the voltages across a rotary potentiometer, as described in section 4.3.1. Five trials were conducted in total, and the results were shown to be repeatable, with a maximum error of ±0.23 rpm between trials. The following data is representative of a typical experimental result.

The readings from the potentiometer for one trial are illustrated in Figure 4.22. Based on a 5 VDC input to the potentiometer, which has a total of 10 turns, the output represents 0.0796 V per radian. This conversion factor was used to calculate the angular position of the elbow joint based on the geometry described in section 4.3.1, the results of which can be seen in Figure 4.23, plotted against time.
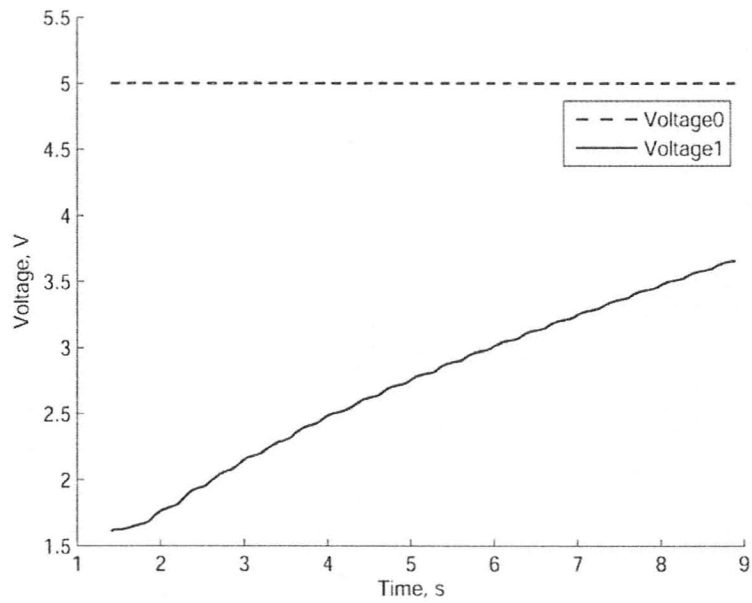
Figure 4.22 Raw experimental data of potentiometer voltages.
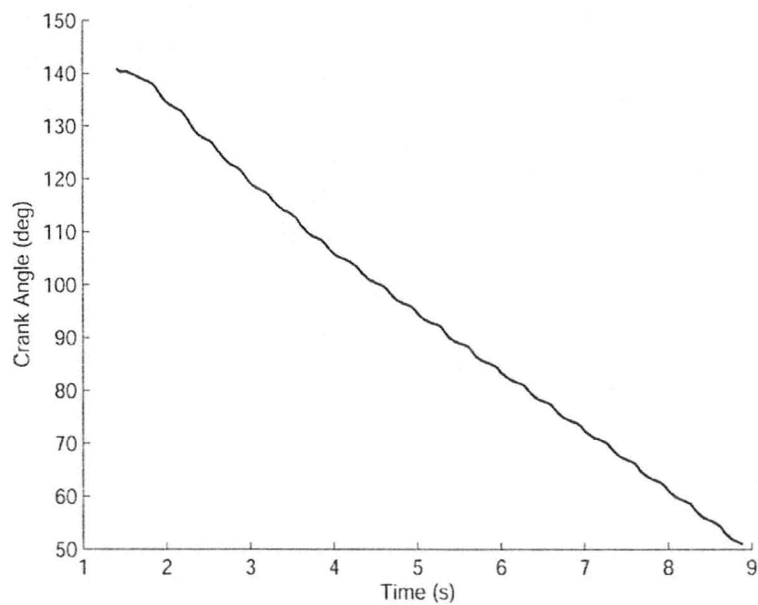
Figure 4.23 Crank angle position plotted with time.

Taking the first derivative of this data using the central difference formula, it was possible to determine the crank angular velocities at each point in time. A low-pass filter based on code from O'Haver (2008) with a 3 Hz cut-off was applied to the data that resulted from this derivation. The cut-off was determined by observing the power spectral density curve of this data, which showed a spike at 2.94 Hz (see Figure 4.24). The filtered crank angular velocity data was then plotted with respect to the crank angle position. Based on the kinematics of an ideal slider-crank mechanism with the prototype design parameters, assuming a motor speed of 200 rpm and no friction in the joint mechanism, a theoretical curve of the crank angular velocity with respect to its position was also generated. See Figure 4.25 for a comparison of the theoretical curve with the experimental data filtered with a 3 Hz cut-off.

It can be seen by this curve that there is significant vibration in the system, causing an oscillation in the speed of the elbow joint. This oscillation, represented by the 2.94 Hz spike on the power spectral density curve, is likely a form of runout caused by the motor rotation of slightly below the ideal 200 rpm (3.3 rotations per second). If there is any misalignment in the lead screw, for example, each rotation would cause the slider to push up or down against the slider support structure, thus causing mechanical vibrations in the joint mechanism at just under 3 Hz. Each time the spring energy of the joint is released, the speed of the joint is able to exceed the theoretical speed. By filtering the speed data with a cut-off of 2 Hz instead of 3 Hz, it is possible to examine the speed results without the effect of the runout, as shown in Figure 4.26.
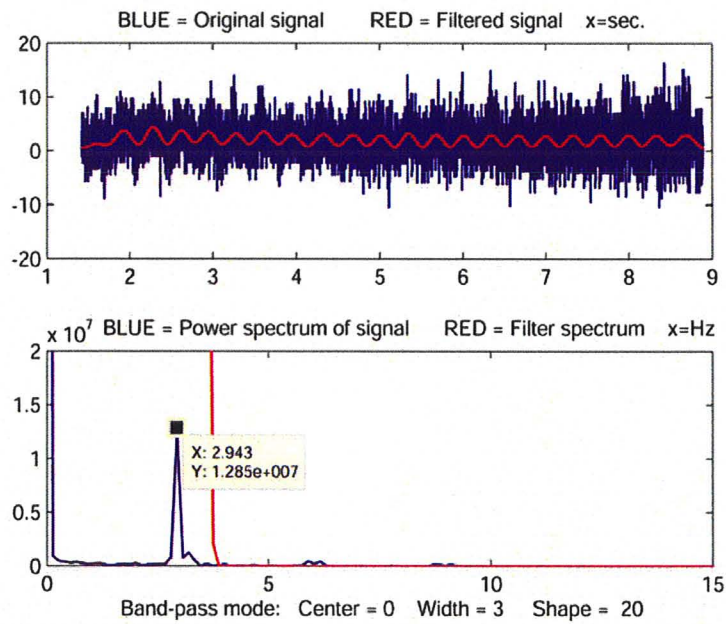
Figure 4.24 Original and filtered signal of the crank angular velocity (top) and power spectrum showing the low-pass filter with a 3 Hz cut-off (below).
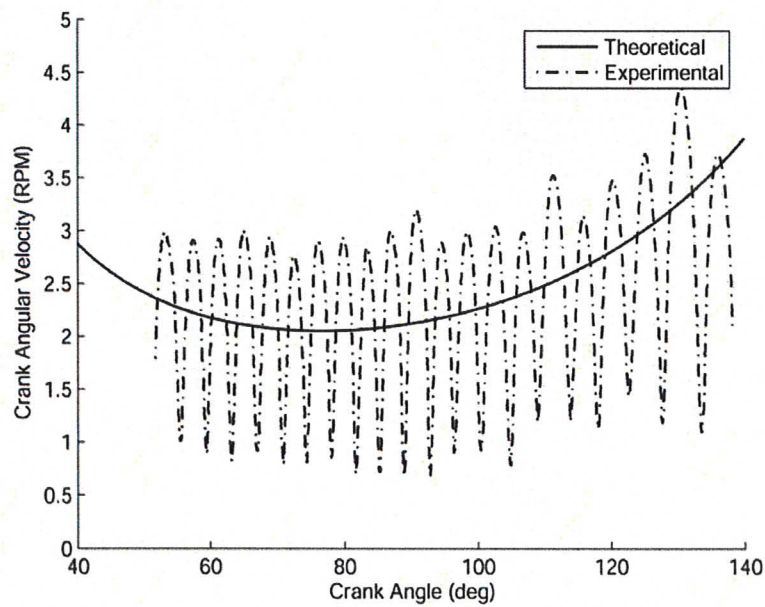
Figure 4.25 Experimental speed results for a 3 Hz cut-off.

From the voltage readings across the motor and the 1 ohm resistor, it was possible to get a measure of the current that was supplied to the motor. The power spectral density curves for the voltage readings also exhibited a peak at 2.94 Hz (see Figure D.2 in Appendix D), so a low-pass filter with a 2 Hz cut-off was applied to the voltage data. See Figures D.1 and D.3 in Appendix D for the raw voltage data as well as the calculated current with respect to time.

The current through a DC motor can give an estimate of the torque that is applied to the motor. The theoretical curve assumes the motor experienced zero torque since it was derived based on the assumption that there was no friction in the mechanism. It also does not account for the voltage drop due to the 1 Ω resistor that was placed in series with the elbow motor. Therefore, it is possible to apply a correction factor to the theoretical speed in order to account for the increase in torque as measured by the current, as well as for the addition of the 1 Ω resistor. The correction factor is denoted in equation 4.4, in which i_{ideal} represents the current that is supplied to the motor at zero torque (i_{ideal} = 0.0216 A, according to the motor specifications), i is the actual current measured across the motor and the 1 Ω resistor, and R_{motor} is the internal resistance of the motor, which was measured to be 8.0 Ω.

$$\text{Corrected Theoretical} = \left[\frac{3V - i \times (1\Omega + R_{motor})}{3V - i_{ideal} \times R_{motor}} \right] \times \text{Theoretical} \qquad (4.4)$$

This correction factor was applied to the theoretical speed, and has been plotted for comparison purposes in Figure 4.26. It can be seen that this corrected theoretical curve runs through the experimental results. Again, there is still some oscillation and

some instances in which the actual speed exceeds that of the corrected theoretical, but this can be accounted for by the mechanical vibrations of the joint (excited by the motor) that cause the arm to shake. When the spring energy of the joint is released, the actual speed is able to exceed that of the theoretical.
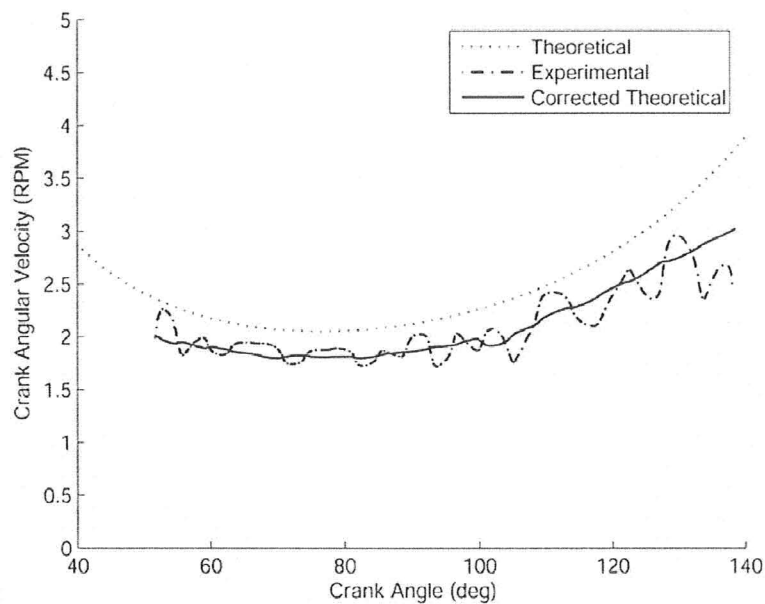
Figure 4.26 Experimental speed results filtered with a 2 Hz cut-off and plotted with corrected theoretical curve.

4.4 Roll Joint Experiments

4.4.1 Experimental Setup

The angular speeds of the roll joint were measured using the video motion analysis software. A scale was taped around the circumference of the joint so that relative angles could be measured. The scale consisted of 20 divisions over a linear distance of 33 mm, which equates to 1.65 mm per division. The angular displacement can then be measured using the radius and arc length. Since the geometry of the forearm is an ellipse

with a width of 13 mm and a height of 12.4 mm, as shown in Figure 4.27, the distance

from the axis of rotation to the edge of the tube varies with angular position. However,

the overall change in angle can be approximated by making the simplifying assumption

that the tube is a cylinder with radius 6.35 mm, which represents the average between 6.5

mm and 6.2 mm. The angular displacement between each division can then be calculated

to be 14.9°, as shown in equation 4.5.
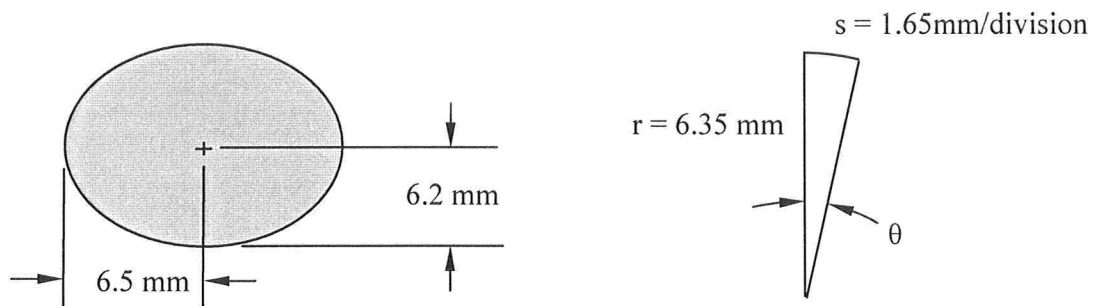
Figure 4.27 Geometry of forearm (left) and simplified angular displacement per division with average radius of 6.35 mm (right).

$$\theta = \frac{s}{r} = \frac{1.65mm\,/\,division}{6.35mm} = 0.2598rad\,/\,division = 14.9°\,/\,division \quad (4.5)$$

The joint was then filmed moving across ranges of around 180 degrees for

constant voltage inputs of 0.5 V to 3.0 V, with 0.5 V intervals. The footage was uploaded

into the video motion analysis software and two readings were taken of the time and

position. See Figure 4.28 for an example of one measurement. The angular speed was

then determined by dividing the angle range by the time it took to move from the first to

the second position. Four trials were conducted at each voltage, measuring both

clockwise and counterclockwise speeds.
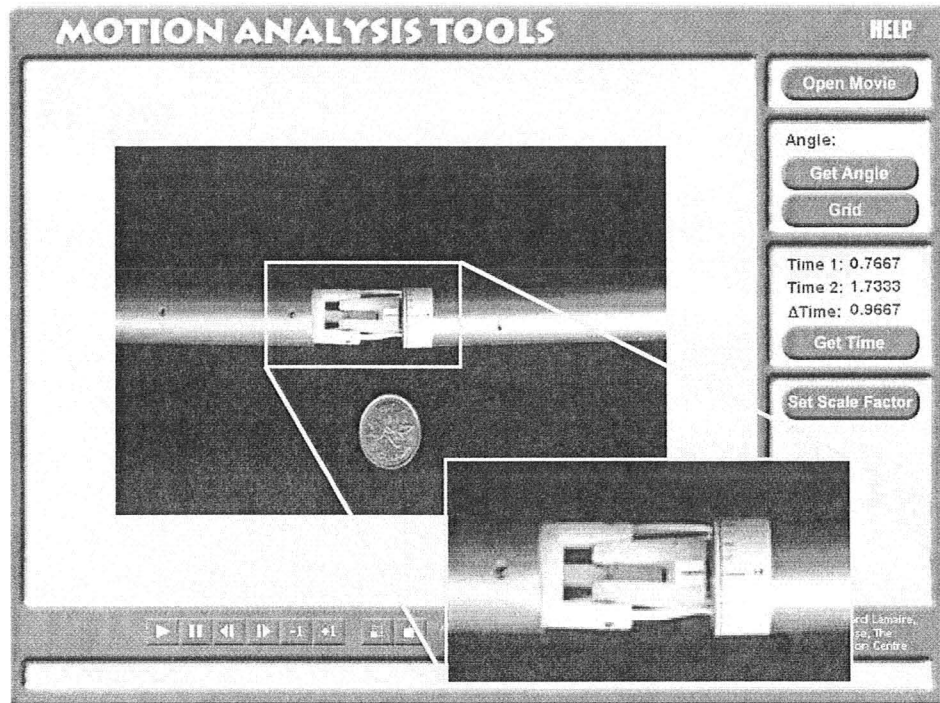
Figure 4.28 A measurement taken from roll joint footage in the motion analysis tool.

4.4.2 Video Motion Analysis Results

At 3 V, the expected motor speeds were 40 rpm for the Gizmoszone motor with a

700:1 gear reduction (as confirmed in Appendix C). From Figure 4.29 it can be seen that

the device performed within this expectation, attaining a mean of the average speeds with

a 95% confidence interval of 39.3 ± 0.9 rpm. For a sample size of 8, the t-value used to

calculate this interval was $t_{0.025,7} = 2.365$ (Table A.5 in Devore, 2004).

It can also be seen by the results shown in Figure 4.29 that there was very little

variation in the eight trials that were conducted at each voltage (four trials of both

clockwise and counterclockwise motion, as described in the section above). From 0.5 V

to 1.5 V, the trials had 95% confidence intervals as low as ± 0.2 rpm. At the higher

speeds, the confidence interval increased, likely due to the uncertainty caused by the blurring of the still-frame images, making accurate detection of the division markers more difficult.
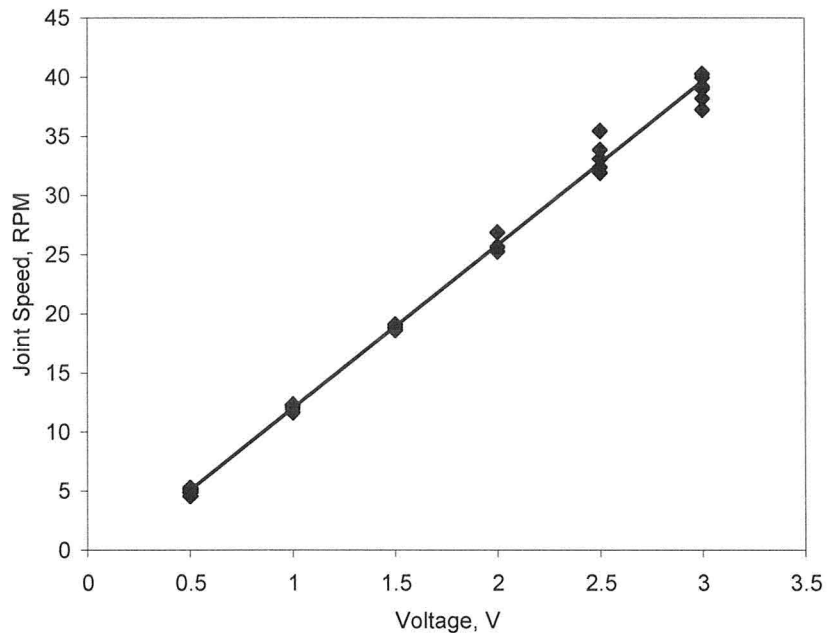
Figure 4.29 Average roll joint speeds for constant voltage inputs.

4.5 Wrist and Gripper Experiments

4.5.1 Experimental Setup

Similar to the elbow joint average speed tests, experiments were conducted to measure the average speeds of the wrist joint using the video motion analysis techniques. The prototype was mounted such that the gripper jaws would move along a horizontal plane a few centimeters above the table. A camera was mounted directly above this setup and pointed downwards to have a view orthogonal to the plane of joint motion. The

gripper jaws were filmed opening and closing across their full range of motion for constant voltage inputs, ranging from 0.75 V to 3.0 V.

An example of the video footage being analyzed in the motion analysis tool is shown in Figures 4.30 and 4.31. The angular speeds for the top gripper jaw were measured by keeping the bottom gripper jaw fixed and measuring the change in angle between the top and bottom gripper jaw. Similarly, the angular speeds for the bottom gripper jaw were measured by keeping the top gripper jaw fixed as a point of reference.
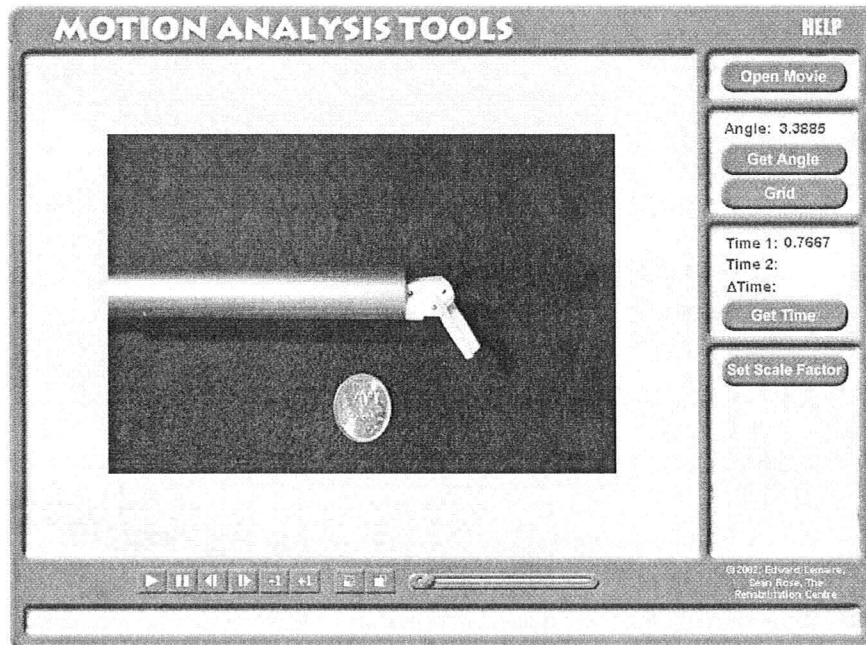
Figure 4.30 First measurement of angle and time for a top gripper jaw experiment.
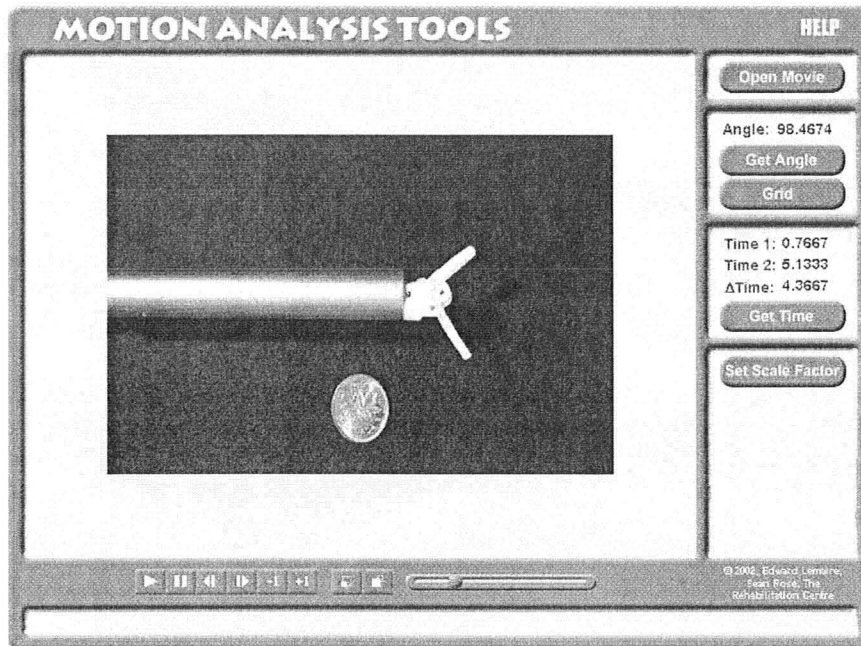
Figure 4.31 Second measurement of angle and time for a top gripper jaw experiment.

4.5.2 Video Motion Analysis Results

The results for the average wrist joint speeds for both the top and bottom gripper jaw are shown in Figure 4.32. The slope for the top gripper jaw is steeper than for the bottom gripper jaw, so at higher voltage inputs, the top jaw performed faster than the bottom jaw. Eight tests were conducted for each gripper jaw, so once again the t-value used to calculate the confidence interval was $t_{0.025,7} = 2.365$ (Table A.5 in Devore, 2004). The mean and 95% confidence interval of the average speeds was 3.98 ± 0.18 rpm for the top gripper jaw and 3.58 ± 0.06 rpm for the bottom gripper jaw results at 3.0 V.

The theoretical average speed for the wrist joint through the crank angle range of 24.4° to 120.3° is 3.70 rpm, as outlined in section 3.6.3. The bottom gripper jaw results are slightly under this speed, whereas the top gripper jaw results actually exceeded this

151

amount by 0.28 rpm. As mentioned in section 4.3.4, the limitations on the video motion analysis software could account for this disparity since the measurements are only accurate to within ± 0.33 rpm. Another factor that could partially account for the higher speed is the fact that the gripper jaws were driven through an angle range of up to 100°, which is larger than the 95° range accounted for in the design calculations. This would cause a similar phenomenon to that illustrated in Figure 4.21, where a larger angle range would result in a higher overall average speed. Specifically, for a crank angle range of 20° to 120°, the theoretical average speed for the wrist joint would increase to 3.81 rpm. Even with the angle range accounted for, the theoretical speed is less than the experimental results for the top gripper jaw, so the error is likely due primarily to the measurement limitations.
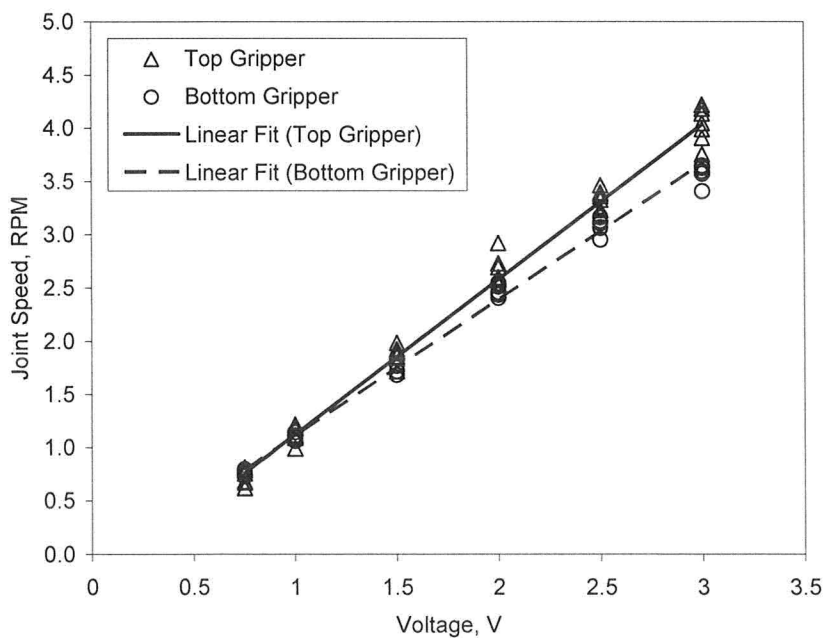
Figure 4.32 Average wrist joint speeds for both top and bottom gripper jaw tests.

4.6 Force Experiments

4.6.1 Experimental Setup

A test-bed was manufactured to measure the linear force that could be supplied by the mechanism, including the motor, bearings, leadscrew and slider and excluding the coupler and crank attachment. The slider was made from brass for its low friction properties and ease of manufacturing, although the design calls for stainless steel for its biocompatibility. The coefficient of friction for steel threaded into a brass nut is 0.23 (Shigley, Mischke & Budynas, 2003).

The Gizmoszone DC motor (GH6123S) with a 136:1 gear reduction was connected in series to a 56 ohm resistor, and the voltages across the motor, V_0, and across both the motor and resistor, V_1, were measured. See Figure 4.33 for the circuit diagram.

A digital force sensor (Imada DPS-110) was mounted onto the test-bed with a fraction of a millimeter of space between the slider and the force sensor probe. A constant DC signal was applied to the motor, causing it to drive the mechanism and push the slider into the force sensor. Once the motor reached zero velocity, the maximum force displayed by the force sensor was recorded. This test measures the quasi-static performance of the mechanism, since it requires some movement in order to push in the force sensor probe. The constant voltage inputs ranged from 4.0 V to 8.0 V in increments of 0.5 V. Five tests were performed at each voltage input. See Figure 4.34 for a photograph of the experimental setup.
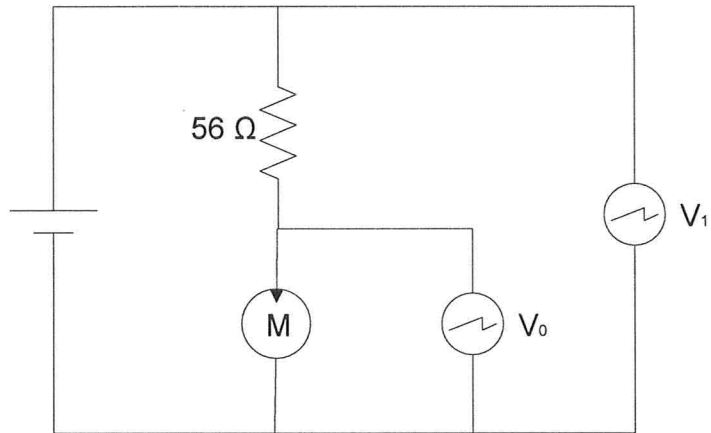
Figure 4.33 Electrical circuit for reading the voltages across the motor and resistor.
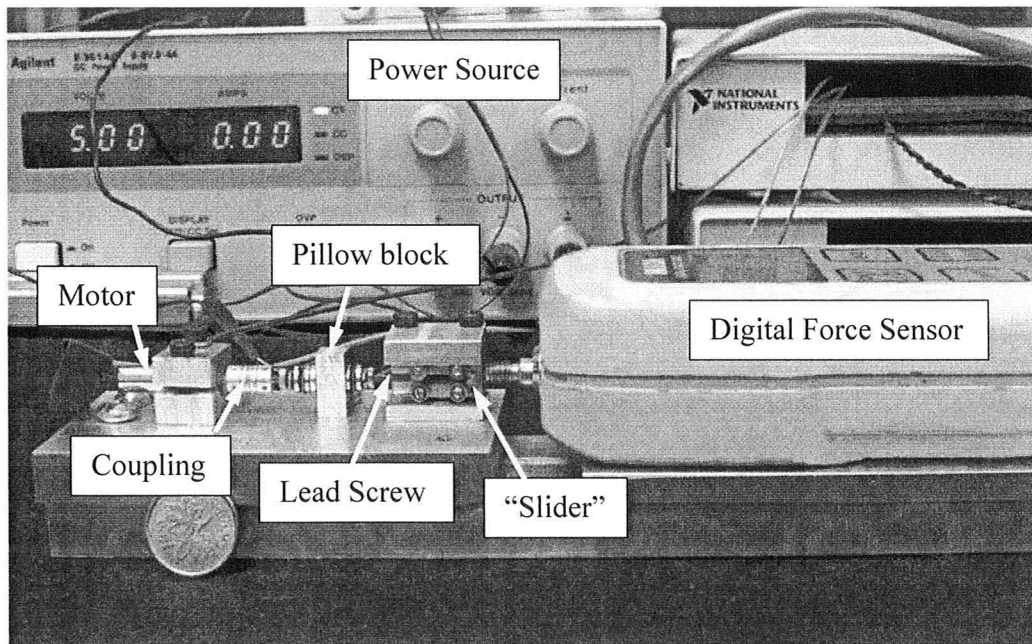
Figure 4.34 Experimental setup for force tests.

4.6.2 Force Results

The recorded forces were plotted with respect to the voltage measured across the motor (V_0), depicted in Figure 4.35. The results exhibit a mostly linear trend, with some variation that could be due to hysteresis in the force sensor.
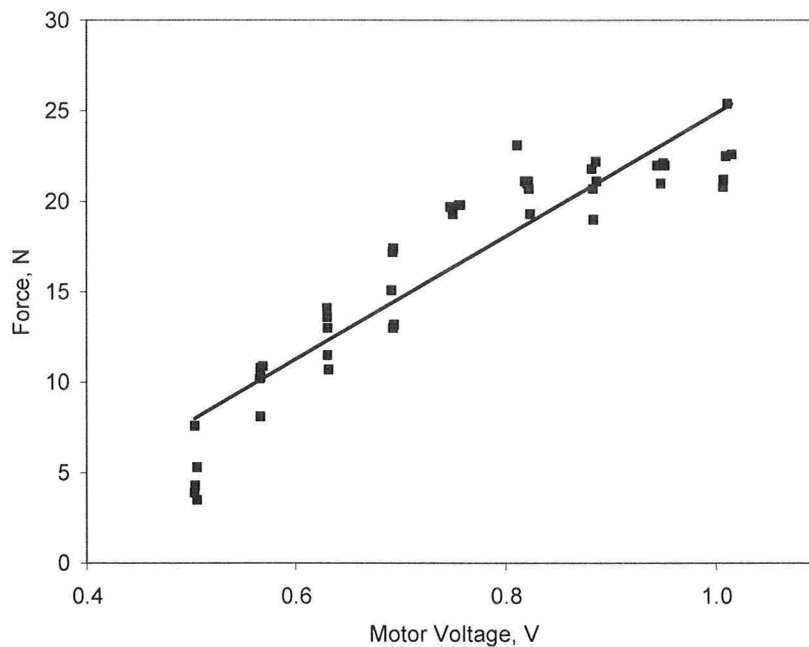
Figure 4.35 Forces recorded at each voltage supplied to the motor.

The linear force exerted by the mechanism is related to the torque produced by the motor through equation 4.6, where the lead, $l = 0.4$ mm/rev:

$$T = \frac{F \cdot l}{\left(2\pi / rev\right)} \tag{4.6}$$

Furthermore, since the voltages across the motor and resistor were measured, it is possible to determine the current that was supplied to the motor once it reached steady-state (zero velocity), using equation 4.7:

$$I = \frac{V_1 - V_0}{56\,\Omega} \tag{4.7}$$

It is therefore possible to determine a relationship between the motor stall torque and the current supplied to the motor, as shown in Figure 4.36. For comparison purposes, the theoretical torque-current curve (from the Gizmoszone motor spec sheet, multiplied by a 136.02 gearbox ratio) is also displayed in Figure 4.36. The linear trendlines of both the theoretical and experimental curves exhibited the following equations:

$$T_{theoretical} = 115.61 \cdot I - 2.50 \tag{4.8}$$

$$T_{experimental} = 17.613 \cdot I - 0.5843 \tag{4.9}$$

The efficiency of the mechanism was determined by dividing the experimental torque by the theoretical torque, and was found to be 15.2 %, as seen below:

$$\frac{T_{experimental}}{T_{theoretical}} \approx \frac{17.613 \cdot I}{115.61 \cdot I} = 15.2\% \tag{4.10}$$

This efficiency is due to various losses, including losses due to the leadscrew efficiency (about 40%, as discussed in section 3.6.1), gearbox efficiency (about 60%, as discussed in section 3.4), and bearing efficiency (about 62.5%). This is represented by equation 4.11:

$$\frac{T_{experimental}}{T_{theoretical}} \approx \eta_{leadscrew} \cdot \eta_{gearbox} \cdot \eta_{bearings} = 40\% \cdot 60\% \cdot 62.5\% = 15\% \tag{4.11}$$

To account for these inefficiencies, one can multiply the theoretical curve by a factor of 15.2 %. A comparison of the experimental and corrected theoretical curves are depicted in Figure 4.37. It can be seen that the experimental results closely match the corrected theoretical with a slight offset.
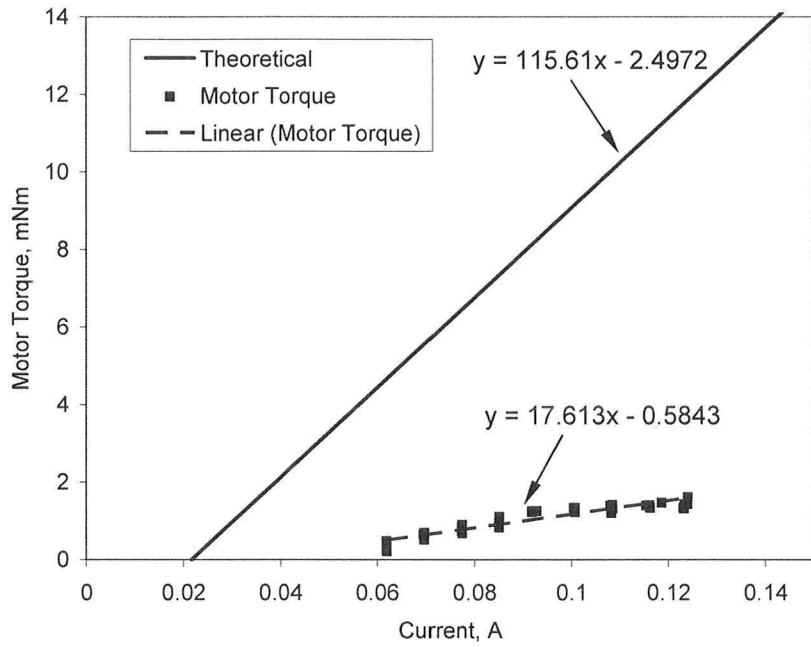
Figure 4.36 Experimental motor torque vs. current plotted with theoretical.
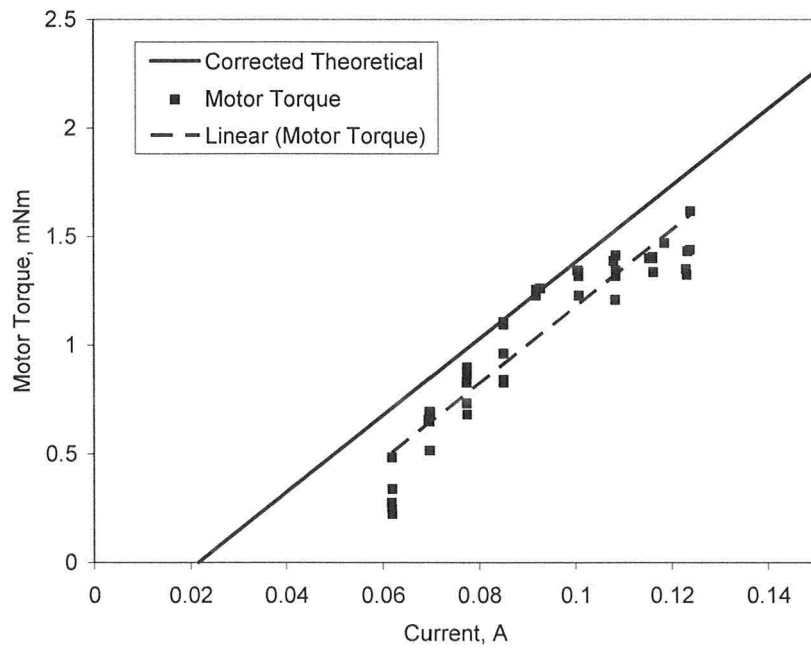
Figure 4.37 Experimental motor torque plotted with corrected theoretical.

Extrapolating from Figure 4.35, if we supplied a voltage of 3 V to the motor, the mechanism should be able to provide a force of 92.6 N. This equates to a 5.9 mNm torque supplied by the motor, based on equation 4.6. From the torque-current relationship exhibited in Figure 4.36, a torque of 5.9 mNm would pull a current of 0.37 A. Performing a motor temperature analysis similar to that shown in section 3.4, at a current of 0.37 A the temperature could rise to 152 °C, which is higher than the allowable motor winding temperature of 100 °C. To remain below the allowable winding temperature, the motor current must be limited to 0.29 A. Based on the experimental results, this would correspond to a torque of 4.3 mNm.

This torque is lower than that required for the elbow joint, and as such the brushless motors with higher torque capabilities would be required. However, the torque that can be supplied by the DC motor is higher than the 3.7 mNm torque limit used in section 3.6.5 for the design of the wrist joint. These motors would be suitable to meet the torque requirement for the wrist joint, although some losses would be expected due to the added friction from the bushing design of the sliders.

4.7 Summary

This chapter outlined the assembly of the prototype, which was manufactured primarily out of ABS plastic through rapid prototyping. The prototype was used as a model for kinematic behaviour since it cannot support realistic loads. Experimental tests were conducted to measure both the average and incremental speeds of the elbow joint using video motion analysis and a potentiometer test, respectively. Results showed that the elbow performed under the expected value for the average speed by about 0.4 rpm,

likely due to the effect of friction within the mechanism. When tested vertically to take into account the effect of gravity, the elbow joint performed as expected in straightening, where the load due to gravity countered the effects of friction in the joint. It performed slightly under the expected value in bending, again by about 0.4 rpm, when it was moving against the effect of gravity. The potentiometer tests revealed that the joint performed in accordance with the theoretical speed profile, particularly when a correction factor was applied to account for the actual current that was drawn to the motor. This current is directly related to the torque that the motor would experience due to the friction in the mechanism.

Experimental tests were also conducted for both the roll and the wrist joint using video motion analysis. The roll joint performed as expected, attaining a speed of 40 rpm with a 3.0 V input. The top gripper jaw of the wrist joint performed about 0.2 rpm faster than expected, whereas the bottom gripper jaw performed just over 0.2 rpm slower than expected. A summary of the video motion analysis results for the elbow, roll and wrist joints, along with the theoretical speed for each test, is listed in Table 4.3.

Table 4.3 Comparison of theoretical and experimental average speeds for elbow, roll and wrist joint tests at 3.0 V.

Joint	Test	Avg. Theoretical Speed (rpm)	Avg. Experimental Speed (rpm)
Elbow	Horizontal (Bend)	2.30	1.79 ± 0.19
Elbow	Horizontal (Straighten)	2.30	1.96 ± 0.04
Elbow	Vertical – against gravity (Bend)	2.35	1.98 ± 0.17
Elbow	Vertical – with gravity (Straighten)	2.34	2.40 ± 0.09
Roll	-	40.0	39.3 ± 0.9
Wrist	Top gripper jaw	3.81	3.98 ± 0.18
Wrist	Bottom gripper jaw	3.81	3.58 ± 0.06

A force experiment was also conducted to confirm the torque capabilities of the Gizmoszone DC motor (GH6123S) with a 136:1 gear reduction. Results showed that the motor, attached to the lead screw and slider components of the elbow joint mechanism, performed at about 15% efficiency. The motor was able to supply a torque of up to 4.2 mNm while maintaining an acceptable current level to avoid over-heating.

The next chapter details the achievements and limitations of the design and outlines recommendations for future work.

CHAPTER 5

CONCLUSIONS AND RECOMMENDATIONS

5.1 Summary

An introduction to minimally invasive surgeries has been presented, along with related literature on the technologies that have been developed for laparoscopic surgery, robot-assisted surgery, NOTES and SPA. A detailed review has been provided of miniature actuators and the selection of miniature electromagnetic motors has been justified for use in medical devices. The basic concept design and specifications for the surgical instrument and have been outlined, and the specific DC motors selected and the various design options for the transmission mechanism have been examined. The design of the lead screw plus slider-crank mechanism that was chosen for this device has also been explored in detail, including an optimization algorithm for the slider-crank parameters, design calculations (including analyses of motor performance, thermal limits, kinematics, statics and stresses) and justification for component and material selection. A prototype has been manufactured and assembled and experiments to test the speed of the prototype have been conducted. A force experiment to test the torque capabilities of the motor have also been conducted. The target specifications are summarized in Table 5.1 alongside the specifications achieved for the actual design and the prototype. Note that the prototype was built as a kinematic model and therefore cannot support realistic loads.

Table 5.1 Target, design and prototype specifications.

Specification	Target	Design	Prototype
Elbow Joint Speed	10 rpm	1.4 rpm	2.0 rpm
Roll Joint Speed	20 rpm	31.3 rpm	40.0 rpm
Wrist Joint Speed	20 rpm	9.5 rpm	3.8 rpm
Tool-tip Force	2 N	2 N	N/A
Length of Forearm	100 mm	120 mm	120 mm
Instrument Diameter	12.7 mm	12.7 mm	12.7 mm

5.2 Achievements

A robotic surgical instrument that incorporates miniature internal actuation has been designed, and a prototype intended as a kinematic model has been built using rapid prototyping. Space limitations were one of the primary challenges in this design, so ensuring that the instrument met the 12.7 mm diameter specification was a considerable success. The design also ensured that the instrument meets the 2 N tool-tip force requirement and the force experiment confirmed that the motors can provide the torque needed to overcome the friction in the mechanism and attain this goal. The roll joint was also able to meet and exceed speed requirements.

Furthermore, the design incorporated the novel addition of an elbow joint to the design. This enables the instrument to avoid collisions and manoeuvre around internal organs.

5.3 Limitations

One of the primary limitations of this design is the trade-off between the speed and torque. By adding more mechanical advantage to the motors in the form of larger reduction gearboxes and longer crank arms in the slider-crank mechanism, the speed is

compromised. By ensuring that the 2 N tool-tip force requirement was met, the result was that the speeds were slower than desired due to motor limitations. The elbow joint was able to attain speeds of 2.0 rpm. Since the elbow joint is a new addition and is intended for gross positioning rather than fine movements, it is possible that this lower speed may be adequate. Clinical testing would be required to confirm this. The gripper jaws in the wrist each attained speeds around 3.8 rpm. This is much lower than the 20 rpm target speed.

Another limitation in the design is the length of each joint. The wrist, including the motors, transmission mechanisms and grippers, was just over 70 mm in length. The roll joint measured around 50 mm, combining with the wrist to give a total forearm length of 120 mm. This exceeds the target forearm length of 100 mm. Beyond finding shorter couplings to protect the motors, which might save a few millimeters in length, there are very few options for shortening the overall length of these joints.

5.4 Recommendations for Future Work

There are a number of areas in which this research can be extended. The next generation prototype should be built with stainless steel in order to test the strength of the design and ascertain the ease of manufacturing and assembly of the components. Since steel-on-steel sliding joints can lead to galling, an examination of surface treatment (i.e. coatings) for various components in the joints could also be examined for reducing friction and wear.

Higher quality motors should be purchased and a control strategy should be developed. If the brushless motors are to be used in the design, more complex electrical

circuitry will need to be integrated into the system to control the motors. This would also enable position control due to the signals from the hall effect sensors in the brushless DC motors. One option that could be explored to reduce the number of wires that need to be supplied to each of the brushless motors would be to incorporate the control electronics inside the instrument itself. Then only three wires (power, ground and communication) would be required for each motor. To enable position control of the brushed DC motors, an electrical circuit could be designed to measure the speed from the commutation pulses in the motor.

The design could also be modularized to enable a "plug and play" capability. This would allow the surgeon to reconfigure the instrument as needed to suit the medical procedure. Joint modules could be created that met either higher speed, higher torque, position control or force control requirements and could then be interchanged according to the needs of the surgeon. A diverse range to tools could also be designed (i.e. graspers, needle-holders, scalpels, etc.) to be switched with ease during procedures.

This modularization would require designing both the mechanical and electrical connections for each module in order to ensure that each part can be quickly and securely affixed to the instrument while also transferring the electrical power safely and reliably across modules.

The next step for the implementation of this instrument would involve integrating it into the overall surgical robotic system and performing clinical testing.

REFERENCES

Bailey, R. W., & Flowers, J. L. (1995). *Complications of laparoscopic surgery.* Quality Medical Pub.

Beer, F.P. & Johnston, E.R. (1992). *Mechanics of materials.* (2nd ed.). McGraw Hill.

Bergamasco M., Salsedo F., Dario P. (1991). Shape memory alloy linear actuators for tendon-based biomorphic actuating systems. In Dario, P., Santini, G.and Aebischer, P. (Eds) *Robots and Biological Systems: Towards a New Bionics* (507-534). Springer-Verlag: Heiderberg.

Berkelman, P., Cinquin, P., Troccaz, J., Ayoubi, J., Letoublon, C., & Bouchard, F. (2002). A compact, compliant laparoscopic endoscope manipulator. *Proceedings of IEEE International Conference on Robotics and Automation, 2.*

Bexell, M. & Johansson, S. (1999). Fabrication and evaluation of a piezoelectric miniature motor. *Sensors and Actuators, A: Physical, 75,* 8-16.

Boca Bearings. (2009). Miniature bearings. Retrieved April 2008 from http://www.bocabearings.com

Boston Gear (2006). Gear catalogue: Engineering information. 133-156.

Bronzino, J.D. (2005). *The Biomedical Engineering Handbook: Medical Devices and Systems.* (3rd ed.). Taylor & Francis.

Çavuşoğlu, M. C., Tendick, F., Cohn, M. & Sastry, S. (1999, August). A laparoscopic telesurgical workstation, *IEEE Transactions on Robotics and Automation, 15*(4), 728–739.

Çavuşoğlu, M. C., Williams, W., Tendick, F. and Sastry, S. (2001, October). Robotics for telesurgery: Second generation Berkeley/UCSF laparoscopic telesurgical workstation and looking toward the future applications. *Proceedings of the 39th Allerton Conference on Communication, Control and Computing,* Monticello, IL.

Çavuşoğlu, M. C., Williams, W., Tendick, F., & Sastry, S. S. (2003). Robotics for telesurgery: Second generation Berkeley/UCSF laparoscopic telesurgical workstation and looking towards the future applications. *Industrial Robot, 30*(1), 22-29.

Cleary, K., & Nguyen, C. (2001). State of the art in surgical robotics: Clinical applications and technology challenges. *Computer Aided Surgery: Official Journal of the International Society for Computer Aided Surgery, 6*(6), 312-328.

Dario P., Carrozza, M.C., Stefanini, C. & D'Attanasio, S. (1998, March). A mobile microrobot actuated by a new electromagnetic wobble micromotor. *IEEE/ASME Transactions on Mechatronics, 3*(1), 9-16.

Dario, P., Carrozza, M. C., Marcacci, M., D'Attanasio, S., Magnami, B., Tonet, O., et al. (2000). A novel mechatronic tool for computer-assisted arthroscopy. *IEEE Transactions on Information Technology in Biomedicine : A Publication of the IEEE Engineering in Medicine and Biology Society, 4*(1), 15-29.

Dario, P., Menciassi, A., Stefanini, C., & Accoto, D. (2002). Miniaturization of biomedical micromachines. *Microtechnologies in Medicine & Biology 2nd Annual International IEEE-EMB Special Topic Conference on,* 291-296.

Davis, J.R. (2003). *Handbook of materials for medical devices.* ASM International.

Devore, J.L. (2004). *Probability and statistics for engineering and the sciences.* (6th ed.). Duxbury, Thomson Brooks/Cole.

Dong, S., Lim, S.P., Lee, K.H, Zhang, J., Lim, L.C. & Uchino, K. (2003). Piezoelectric ultrasonic micromotor with 1.5 mm diameter. *IEEE Transactions on Ultrasonics, Ferroelectrics, and Frequency Control, 50*(4), 361-367.

Elert, G (ed.) (2005). Temperature of a Healthy Human (Body Temperature). The Physics Factbook. Retrieved June 16, 2009 from http://hypertextbook.com/facts/LenaWong.shtml

Faulhaber Group (2009). Miniature drive systems. Retrieved April 2, 2008 from http://www.faulhaber-group.com/n164058/n.html

Flynn, A.M. (1998). Performance of ultrasonic mini-motors using design of experiments. *Smart Material Structures, 7,* 286-294.

Frede, T., Hammady, A., Klein, J., Teber, D., Inaki, N., Waseda, M. (2007). The radius surgical system - a new device for complex minimally invasive procedures in urology? *European Urology, 51*(4), 1015-22.

Focacci, F., Piccigallo, M., Tonet, O., Megali, G., Pietrabissa, A. & Dario, P. (2007, April). Lightweight Hand-held Robot for Laparoscopic Surgery. *IEEE International Conference on Robotics and Automation,* 599-604.

Gizmoszone (2007). Miniature planetary gear motors. Retrieved March, 2008 from http://www.gizmoszone.com

Graves, E. (1993). *Vital and Heatlth Statistics.* Data from the National Health Survey No. 122. U.S. Department of Health and Human Services, Hyattsville, MD.

Hill, J. W., & Jensen, J. F. (1998). Telepresence technology in medicine: Principles and applications. *Proceedings of the IEEE, 86*(3), 569-580.

Howe, R. D., & Matsuoka, Y. (1999). Robotics for surgery. *Annual Review of Biomedical Engineering, 1*(1), 211-240.

Hu, T., Allen, P.K., Hogle, N.J. & Fowler, D.L. (2008). Insertable surgical imaging device with pan, tilt, zoom, and lighting. *2008 IEEE International Conference on Robotics and Automation*, 2948-2953.

Institute for Rehabilitation Research and Development (2009). Motion Analysis Tools. Retrieved March, 2008 from http://www.irrd.ca/cag/matshock/mat.asp

Intuitive Surgical Inc. (2005). da Vinci Surgical System. http://www.intuitivesurgical.com

Intuitive Surgical. (2007, May). EndoWrist® Instrument & Accessory Catalog.

Kavoussi, L. R., Moore, R. G., Partin, A. W., Bender, J. S., Zenilman, M. E., & Satava, R. M. (1994). Telerobotic assisted laparoscopic surgery: Initial laboratory and clinical experience. *Urology, 44*(1), 15-19.

Knowledge Revolution (1996). Working Model 2D, version 4.0.

Kobayashi, Y., Chiyoda, S., Watabe, K., Okada, M. & Nakamura, Y. (2002, September). Small occupancy robotic mechanisms for endoscopic surgery. *Proceedings of 5th International Conference on Medical Image Computing and Computer-Assisted Intervention*, 75-82.

Kosaka, M, Yamane, M., Ogai, R., Kato, T., Ohnishi, N. & Simon, E. (2004). Human body temperature regulation in extremely stressful environment: epidemiology and pathophysiology of heat stroke. *Journal of Thermal Biology, 29*(7-8), 495-501.

Lehman, A.C., Wood, N.A., Dumpert, J., Oleynikov, D. & Farritor, S.M. (2008). Robotic natural orifice translumenal endoscopic surgery. *2008 IEEE International Conference on Robotics and Automation*, 2969-2974.

167

Madhani, A., Niemeyer, G., & Salisbury Jr, J. (1998, October). The black falcon: A teleoperated surgical instrument for minimally invasive surgery. *Proceedings of the 1998 IEEE/RSJ International Conference on Intelligent Robots and Systems,* 936-944.

Mashimo, T. & Toyama, S. (2008). Micro rotary-linear ultrasonic motor for endovascular diagnosis and surgery. *2008 IEEE International Conference on Robotics and Automation,* 3600-3605.

Matsuhira, N., Jinno, M., Miyagawa, T., Sunaoshi, T., Hato, T., Morikawa, Y., et al. (2003). Development of a functional model for a master–slave combined manipulator for laparoscopic surgery. *Advanced Robotics, 17*(6), 523-539.

MatWeb. (2009). Material property data. Retrieved February, 2008 from http://www.matweb.com/

Maxon Motor. (2009). Products and Specifications. Retrieved March 29, 2008 from http://www.maxonmotor.com

Mazurkiewicz, J (2007). Motion Control Basics. Baldor Electric. Retrieved April 2008 from http://www.motioncontrolonline.org/files/public/Motion_Control_Basics.pdf

MicroMo Electronics (2009). Motor calculations. Retrieved April 12, 2009 from http://www.micromo.com/n390432/n.html

Morita, T. (2003). Miniature piezoelectric motors. *Sensors and Actuators, A: Physical, 103,* 291-300.

Nakamura, Y., Matsui, A., Saito, T., & Yoshimoto, K. (1995). Shape-memory-alloy active forceps for laparoscopic surgery. *1995 IEEE International Conference on Robotics and Automation,* 2320-2327.

Nakamura, R., Kobayashi, E., Masamune, K., Sakuma, I., Dohi, T., Yahagi, N., et al. (2000, October). Multi-DOF forceps manipulator system for laparoscopic surgery. *Proc. Third International Conference on Medical Image Computing and Computer Assisted Interventions,* Pittsburgh, PA, USA, 11-14.

Nicoud, J.D., Matthey, O. & Caprari, G. (1998). Control and analysis of low inertia miniature synchronous motors. *IEEE International Symposium on Micromechatronics and Human Science,* 97-103.

O'Haver, T. (2008). *Interactive Fourier Filter.* Retrieved February, 2009 from http://terpconnect.umd.edu/~toh/spectrum/InteractiveFourierFilter.htm

OR-Live (2009). Videos of surgical procedures. Retrieved online September, 2007 from http://www.nlm.nih.gov/medlineplus/surgeryvideos.html

Peirs, J., Reynaerts, D., & Van Brussel, H. (2000). Design of miniature parallel manipulators for integration in a self-propelling endoscope. *Sensors & Actuators: A.Physical, 85*(1-3), 409-417.

Peirs, J., Reynaerts, D. & Van Brussel, H. (2001a). A miniature manipulator for integration in a self-propelling endoscope. *Sensors and Actuators A, 92,* 343-349.

Peirs, J., Reynaerts, D., & Van Brussel, H. (2001b). The 'true' power of SMA micro-actuation. *Proceedings MME 2001 (Micromechanics Europe Workshop),* 217-220.

Physikinstrument. (2009). P-915K094 Miniature Rotary PiezoMotor Product Spec Sheet. Retrieved January, 2009 from http://www.pi-china.cn/pdf/pdf/PI_PIline.pdf

Polla, D., Erdman, A., Peichel, D., Rizq, R., Gao, Y. & Markus, D. (2000, October). Precision micromotor for surgery. *1st Annual International IEEE-EMBS Special Topic Conference on Microtechnologies in Medicine & Biology.* 180-183.

Rassweiler, J., Binder, J. & Frede, T. (2001). Robotic and telesurgery: Will they change our future? *Current Opinion in Urology, 11,* 309-320.

Rattner D., Kalloo A.N. (2006). ASGE/SAGES Working Group. ASGE/SAGES working group on Natural Orifice Transluminal Endoscopy. *Gastrointest. Endosc., 63,* 199–203.

Reliance Precision Mechatronics. (2009). *Micro reli-a-flex couplings.* Retrieved April, 2009 from www.rpmechatronics.co.uk

Rentschler, M. E. & Oleynikov, D. (2007). Recent in vivo surgical robot and mechanism developments, *Surgical Endoscopy, 21,* 1477-1481.

Sastry, S. S., Cohn, M., & Tendick, F. (1997). Milli-robotics for remote, minimally invasive surgery. *Robotics and Autonomous Systems, 21*(3), 305-316.

Satava, R. M. (1993). Surgery 2001: A technologic framework for the future. *Surgical Endoscopy, 7*(2), 111-113.

SensAble Technologies Inc. (2009). Phantom haptic devices. Retrieved April, 2009 from http://www.sensable.com/

Sindrey, R. (2006). *Design and control of a miniature rotary joint.* M.A.Sc. dissertation, McMaster University, Hamilton, ON, Canada.

Shigley, J.E., Mischke, C.R., Budynas, R.G. (2003), Mechanical Engineering Design (7th ed.), McGraw Hill.

Small Parts, Inc. (2009). Online Catalogue. Retrieved April 2008 from www.smallparts.com

Stevens, J.M. & Buckner, G.D. (2005, December). Actuation and control strategies for miniature robotic surgical systems. *Journal of Dynamic Systems, Measurement, and Control, 127,* 537-549.

Stock Drive Products/Sterling Instrument. (2009). Online Catalogue. Retrieved March, 2009 from https://sdp-si.com/eStore/

Stoianovici, D. (2005). Multi-imager compatible actuation principles in surgical robots. *Int J Medical Robotics and Computer Assisted Surgery,* 1(2), 86–100.

Stryker (2009). Standard Length Laparoscopic instruments. Retrieved April 2009 from http://www.stryker.com/

Suzumori, K., Iikura, S., & Tanaka, H. (1991). Flexible microactuator for miniature robots. *Proceedings of the IEEE Micro Electro Mechanical Systems, an Investigation of Micro Structures, Sensors, Actuators, Machines and Robots.* 204-209.

Taylor, R.H., Funda, J., Eldridge, B., Larose, D., Gomory, S., Gruben, K., Talamini, M., Kavoussi, L. & Anderson, J. (1996). A Telerobotic Assistant for Laparoscopic Surgery. In Taylor, R.H., Lavallee, S., Burdea, G. and Mosges, R. (Eds.), *Computer-Integrated Surgery,* (581–592). Cambridge, MA: MIT Press.

Taylor, R.H. & Stoianovici, D. (2003, October). Medical robotics in computer-integrated surgery. *IEEE Transactions on Robotics and Automation,* 19(5), 765-781.

Tholey, G. & Desai, J. P. (2007). A modular, automated laparoscopic grasper with three-dimensional force measurement capability. *2007 IEEE International Conference on Robotics and Automation,* 250-255.

University of Southern California (2007). Videos of cardiothoracic surgeries. Retrieved online September, 2007 from http://www.cts.usc.edu/videos.html

Waldron, K.J. & Kinzel, G.L. (1999). *Kinematics, dynamics, and design of machinery.* The Ohio State University: John Wiley & Sons, Inc. 640.

Yamashita, H., Kim, D., Hata, N. & Dohi, T. (2003, October). Multi-slider linkage mechanism for endoscopic forceps manipulator. *Proceedings of the IEEE/RSJ International Conference on Intelligent Robots and Systems*, Las Vegas, Nevada. 2577-2582.

Yamashita, H., Hata, N., Hashizume, M., & Dohi, T. (2004). Handheld laparoscopic forceps manipulator using multi-slider linkage mechanisms. *Proceedings of the 7th International Conference on Medical Image Computing and Computer-Assisted Intervention (MICCAI 2004), Lecture Notes in Computer Science (LNCS), 3217*, 121-128.

Yesin, K.B. (2000). *Design of Meso-Scale Robotic Systems with Miniature Actuators*. UMN-AML-TR-00-02. Technical Report. Minneapolis, Minn: University of Minnesota.

APPENDIX A

SUTURING RESULTS

A.1 Video Motion Analysis
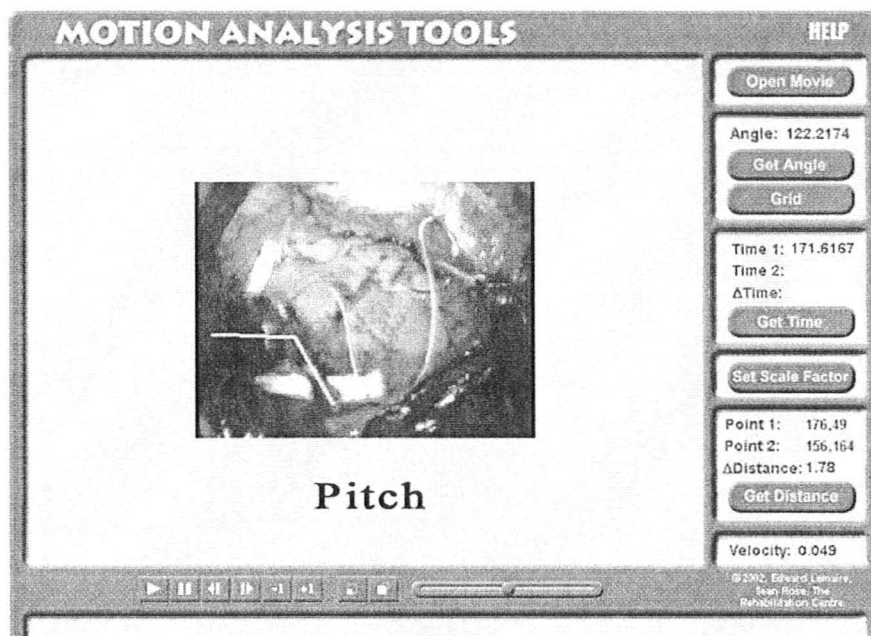
Figure A.1 First measurement of the pitch angle in a suturing procedure.
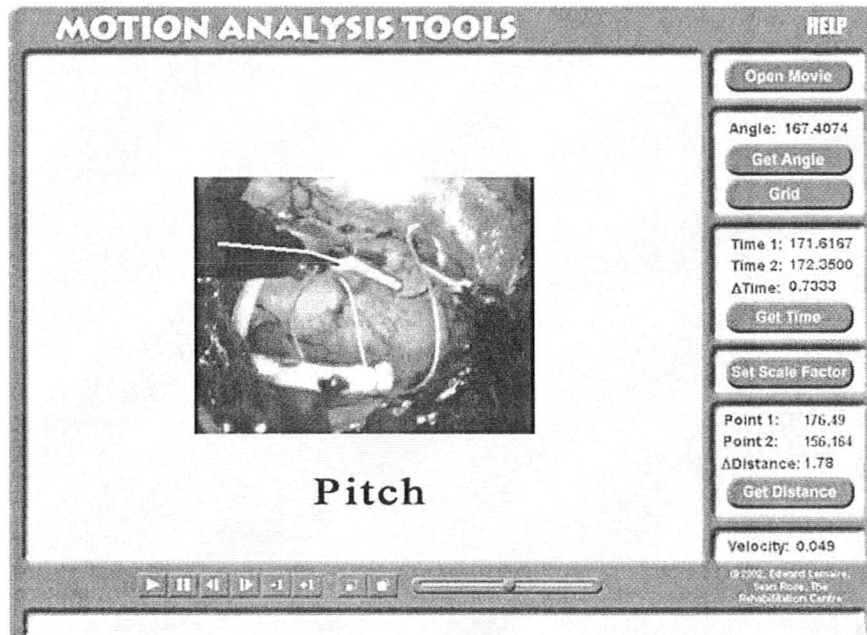
Figure A.2 Second measurement of the pitch angle in a suturing procedure.
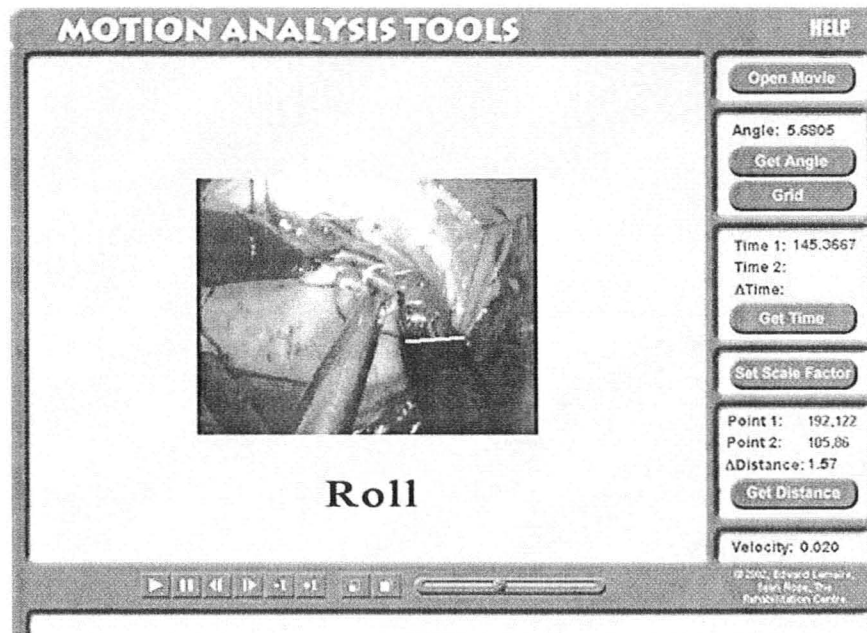
Figure A.3 First measurement of time before the instrument has rolled roughly 90° in a suturing procedure.
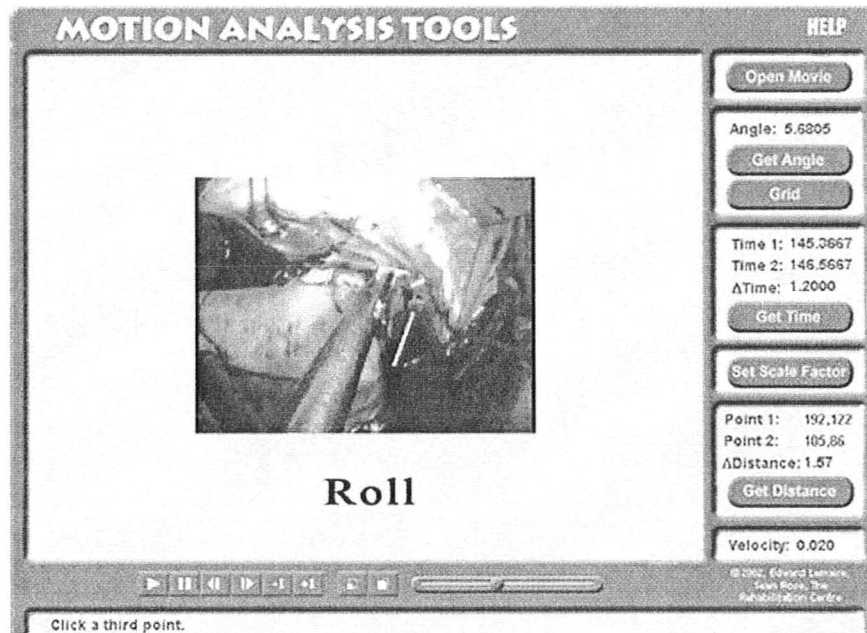
Figure A.4 Second measurement of time after the instrument has rolled roughly 90° in a suturing procedure.
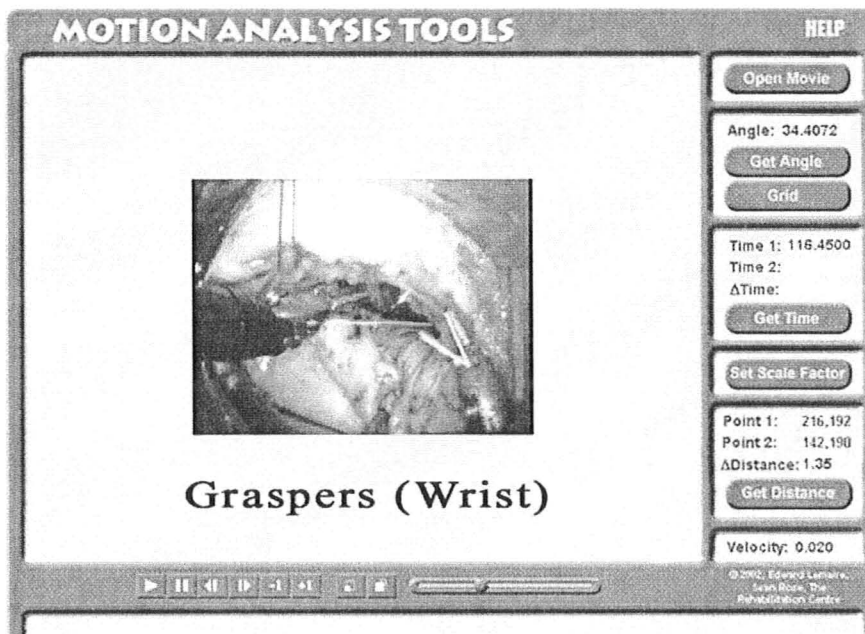
Figure A.5 First measurement of the gripper angle in a suturing procedure.
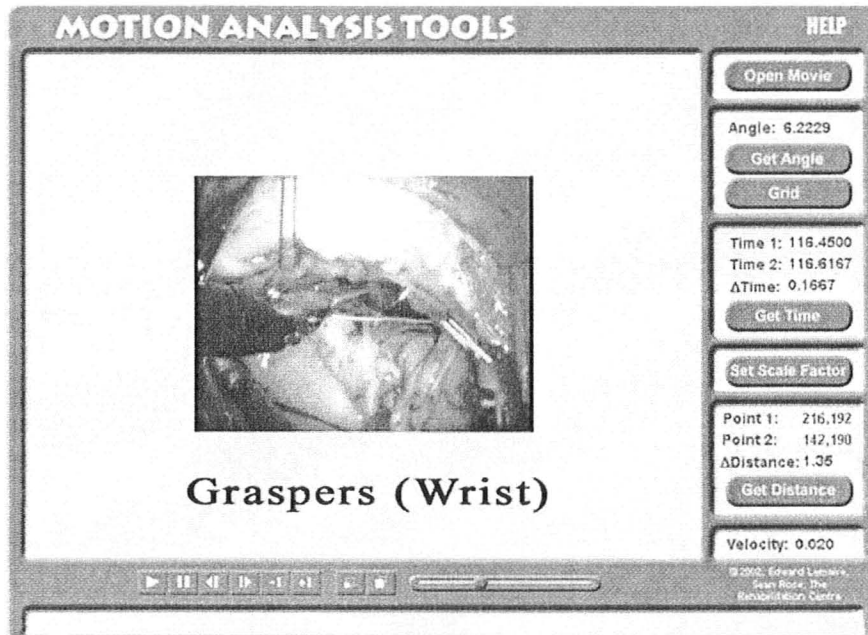
Figure A.6 Second measurement of the gripper angle in a suturing procedure.

A.2 Raw Data

Table A.1 Raw experimental data for the suturing tests.

Test	Trial	Time 1	Time 2	Angle 1	Angle 2	Angular Velocity (RPM)
Pitch	1	100.4667	100.7333	140.2	162.5	14
	2	101.7	102	180.0	155.6	14
	3	119.2167	119.45	145.8	180.0	24
	4	171.6167	172.35	122.2	167.4	10
	5	174.9833	175.1833	144.0	159.9	13
	6	183.1167	183.4833	133.2	162.3	13
	7	22.7833	22.9833	142.2	132.7	8
	8	30.15	30.3833	135.9	128.0	6
	9	44.1167	44.3833	150.0	143.9	4
	10	74.2667	74.4333	180.0	166.1	14
	11	76.5333	76.8667	136.8	146.6	5
Roll	1	114.6833	115.45	90	0	20
	2	116.7167	117.2167	90	0	30
	3	128.1667	128.7333	45	0	13
	4	145.3667	146.5667	90	0	13
	5	169.15	169.8167	45	0	11
	6	203.95	204.2167	40.7	0	25
Gripper	1	116.15	116.45	2.8	31.6	16
	2	116.45	116.6167	34.4	6.2	28
	3	120.5167	120.7833	39.3	4.1	22
	4	157.45	157.6167	39.2	0.0	39
	5	157.45	157.6833	18.6	3.2	11
	6	167.2167	167.5167	19.8	41.2	12

APPENDIX B

STRESS ANALYSIS

B.1 Elbow Joint Components
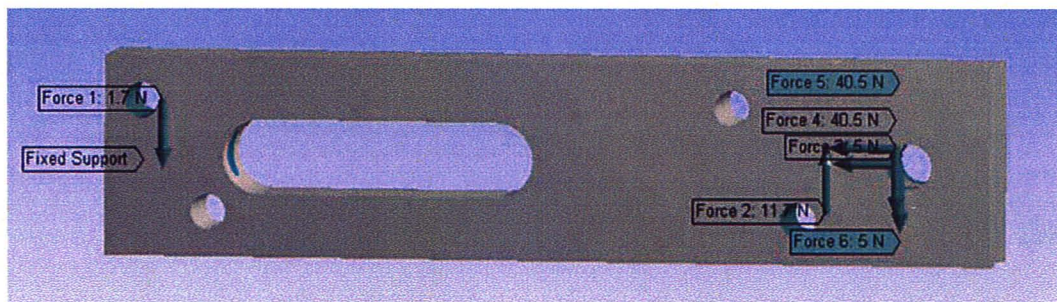
Figure B.1 Loading used for stress analysis of elbow slider.
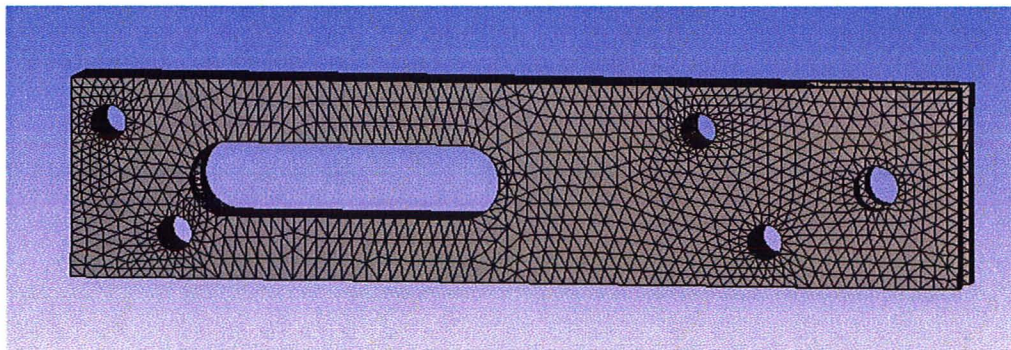
Figure B.2 Mesh used for stress analysis of elbow slider.
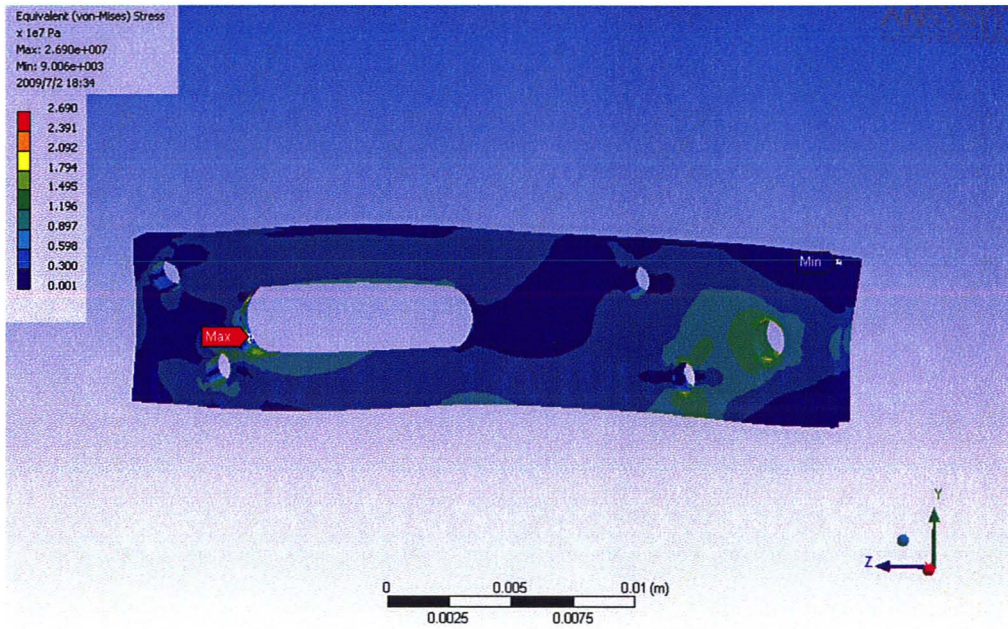
Figure B.3 Von Mises stress of elbow slider (max = 26.9 MPa).
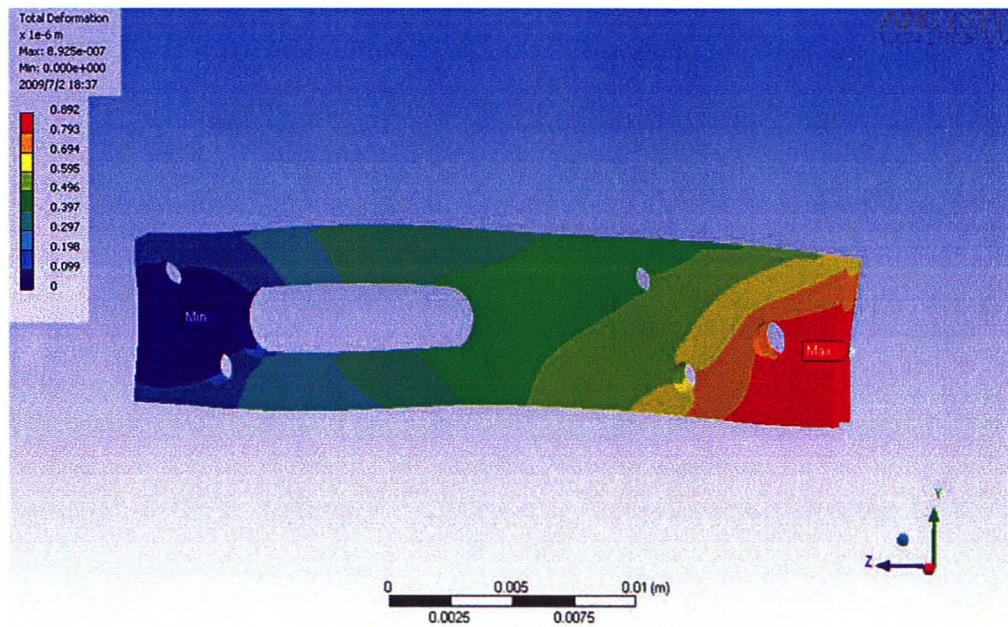
Figure B.4 Deformation of elbow slider (max = 0.89 μm).
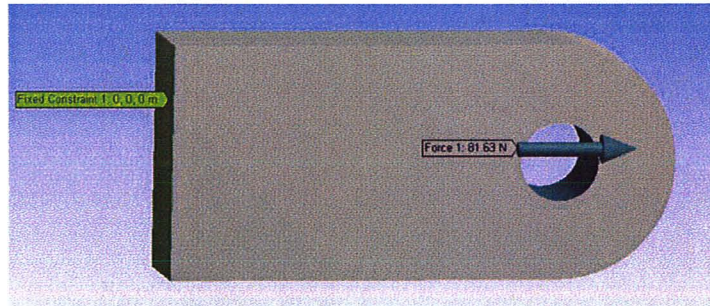
Figure B.5 Loading used for stress analysis of elbow coupler.
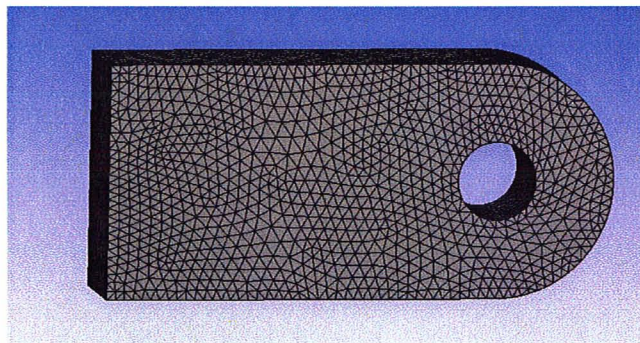
Figure B.6 Mesh used for stress analysis of elbow coupler.
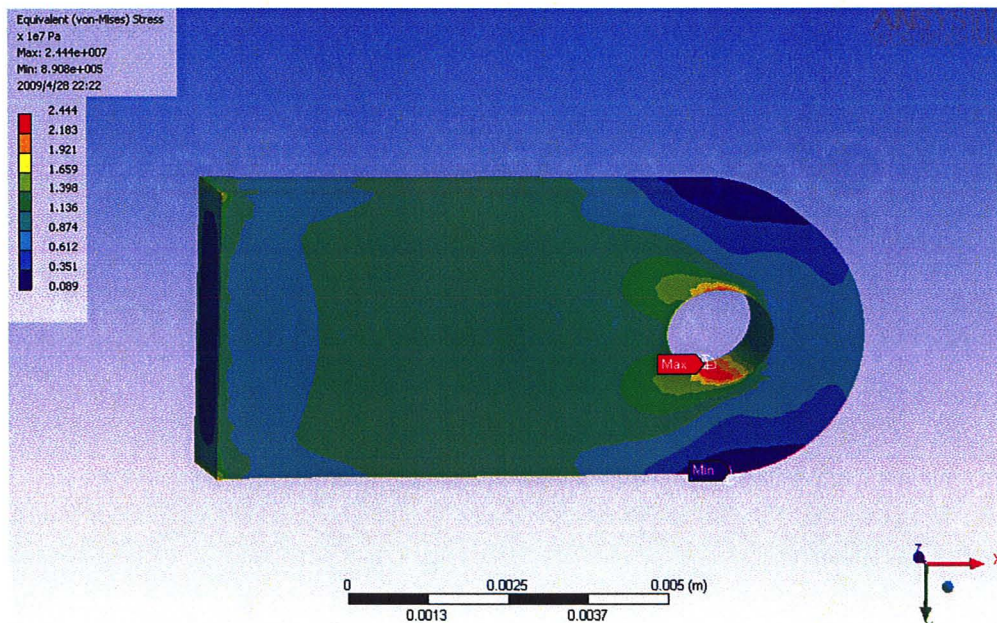
Figure B.7 Von Mises stress of elbow coupler (max = 24.4 MPa).
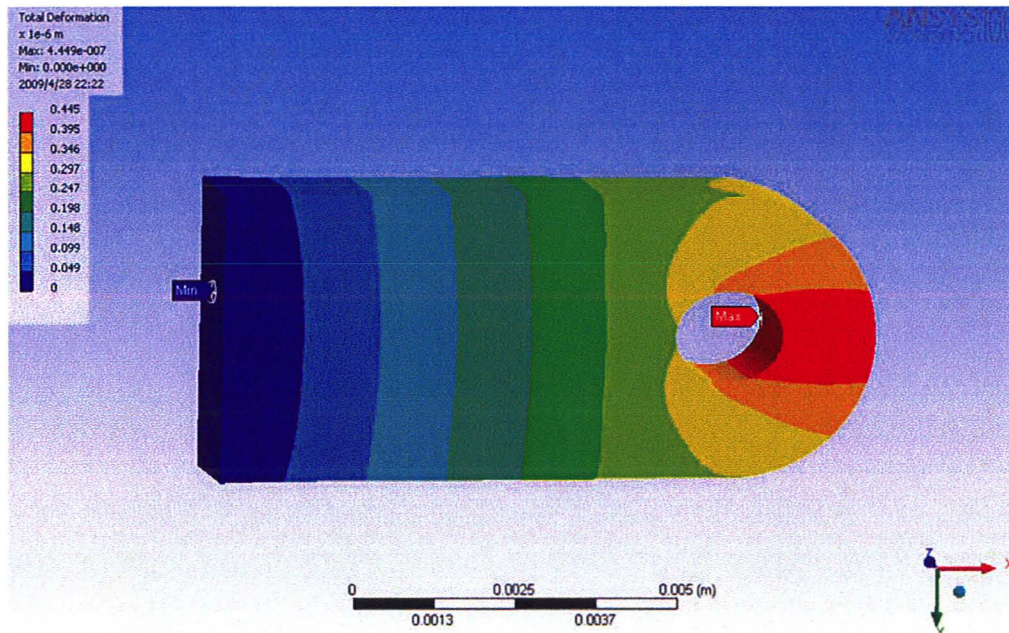
Figure B.8 Displacement of elbow coupler (max = 0.4 μm).
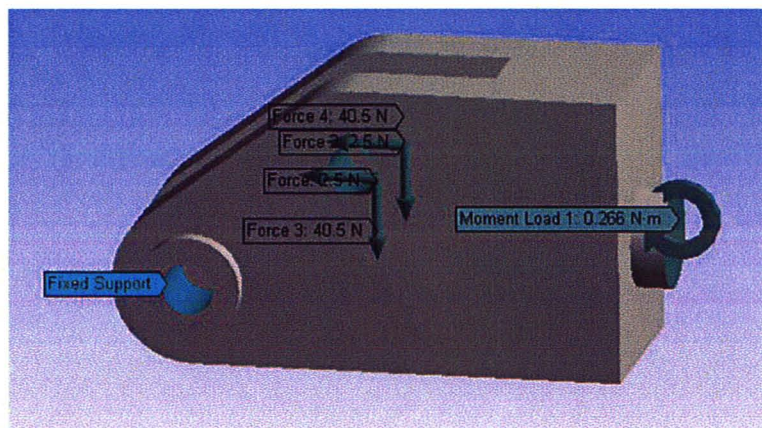
Figure B.9 Loading used for stress analysis of elbow crank.
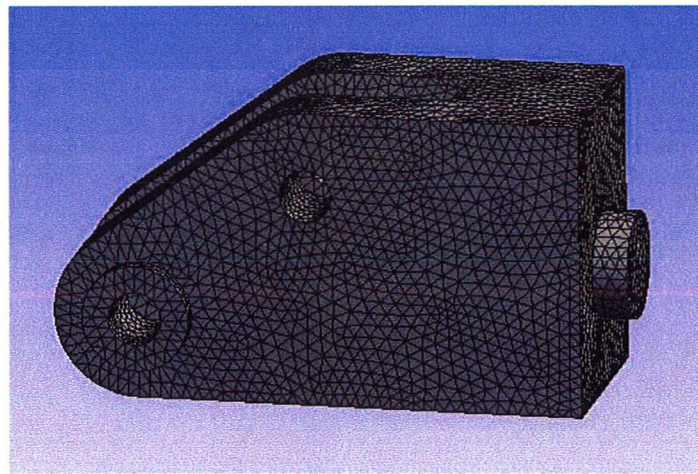
Figure B.10 Mesh used for stress analysis of elbow crank.
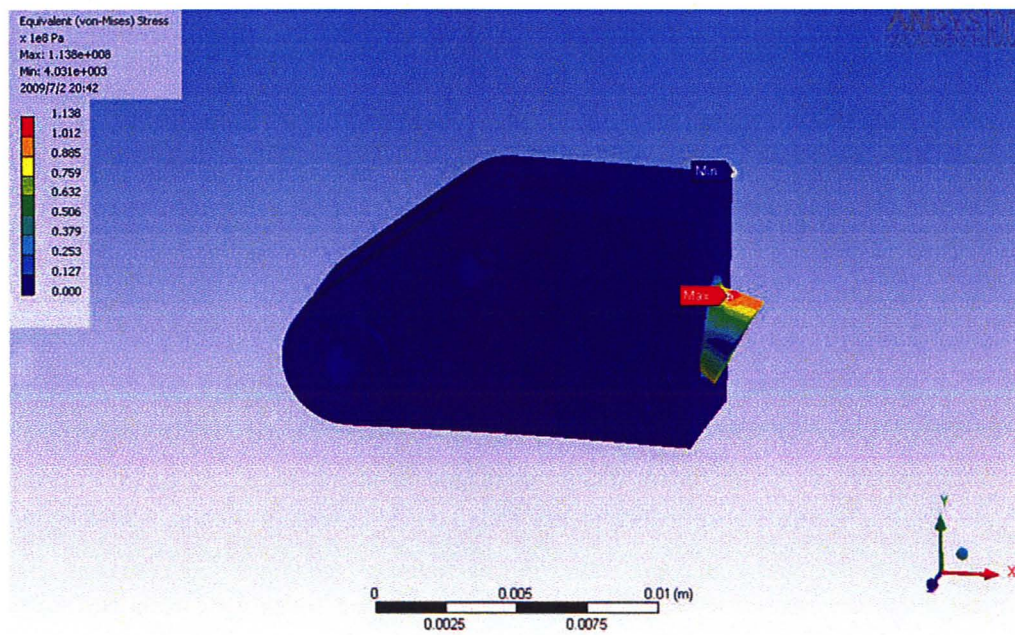
Figure B.11 Von Mises stress of elbow crank (max = 113.8 MPa).
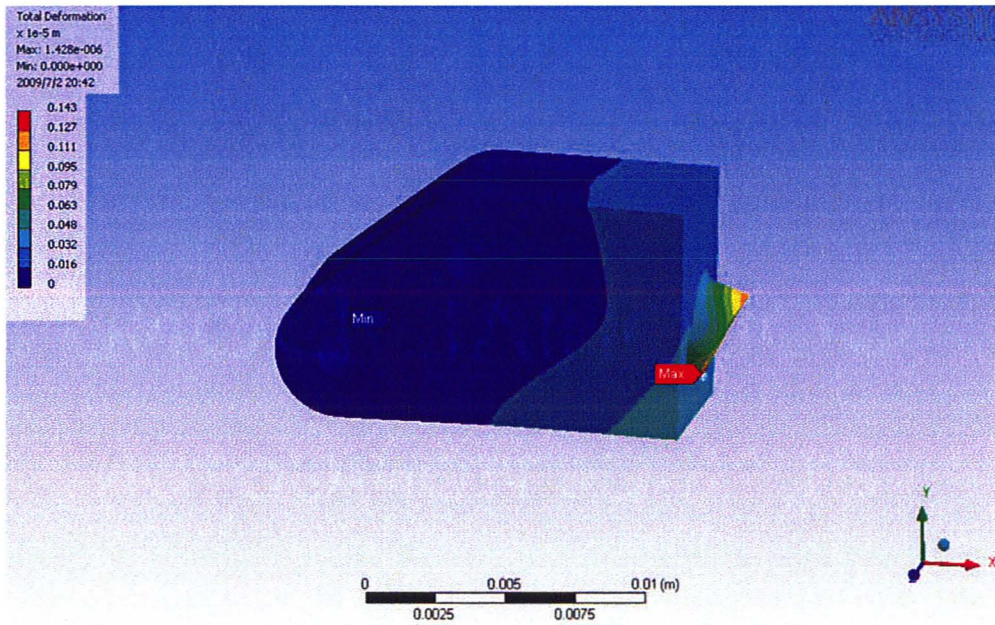
Figure B.12 Deformation of elbow crank (max = 1.4 μm).
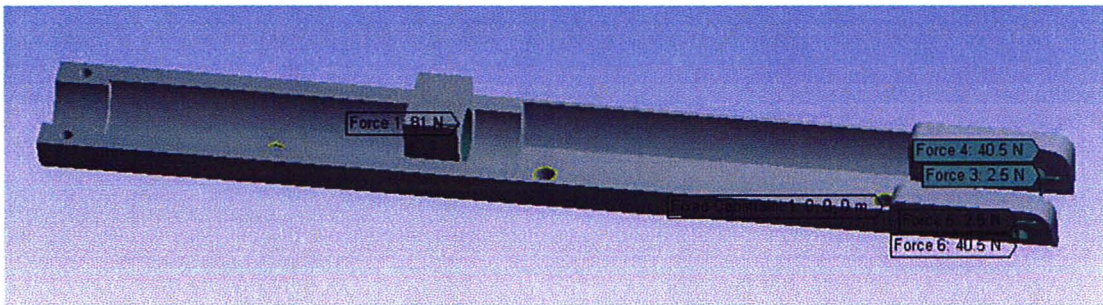
Figure B.13 Loading used for stress analysis of elbow support structure.
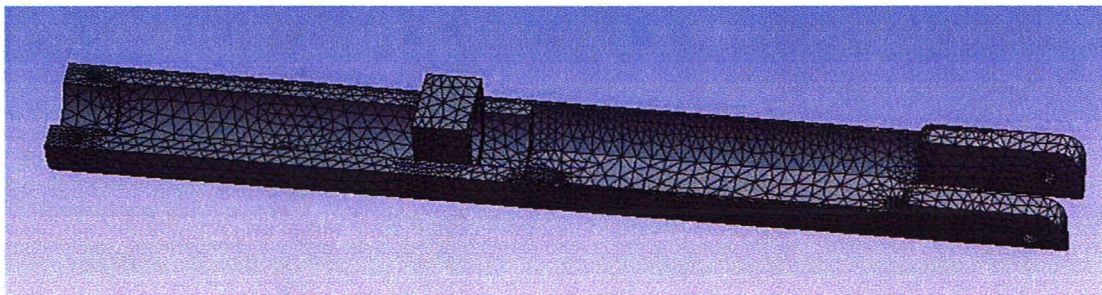
Figure B.14 Mesh used for stress analysis of elbow support structure.
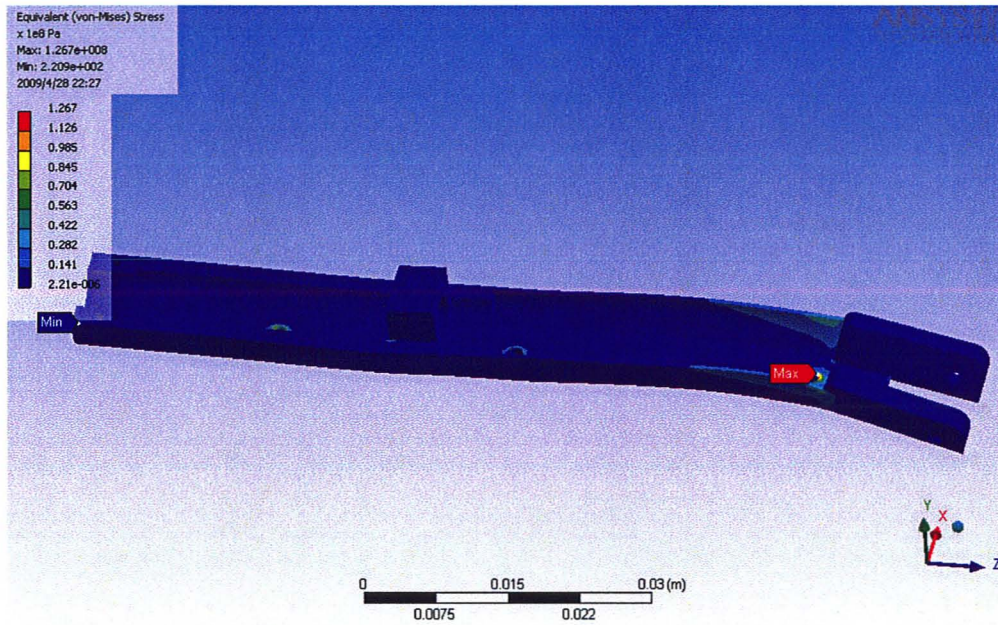
Figure B.15 Von Mises stress of elbow support structure (max = 126.7 MPa).
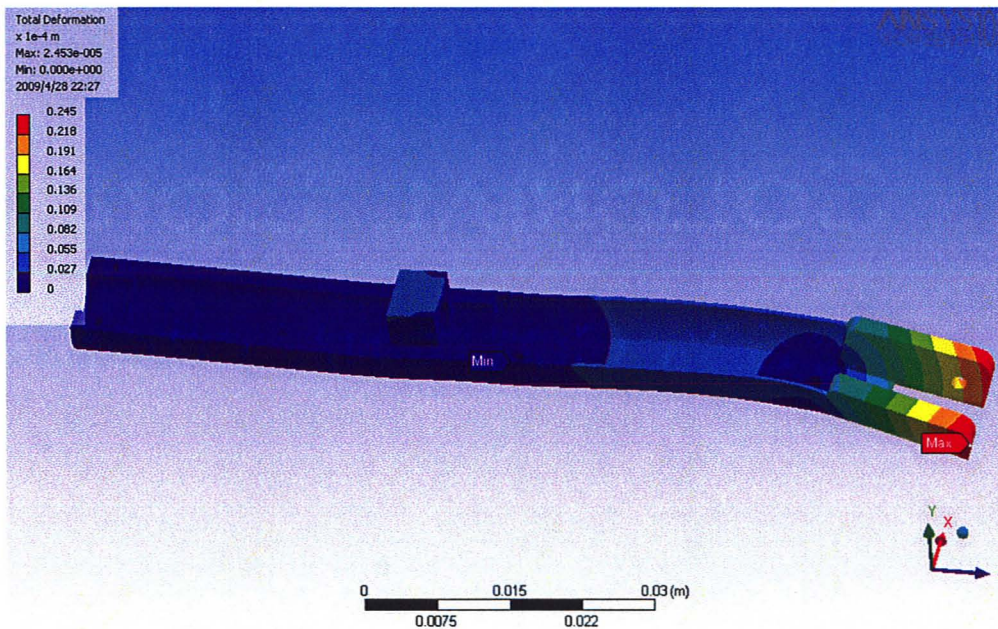
Figure B.16 Deformation of elbow support structure (max = 24.5 μm).

B.2 Roll Joint Components
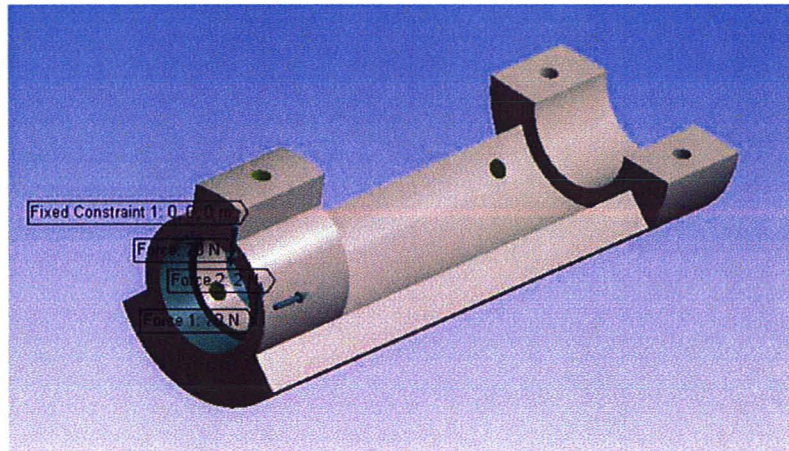
Figure B.17 Loading used for stress analysis of roll support structure.
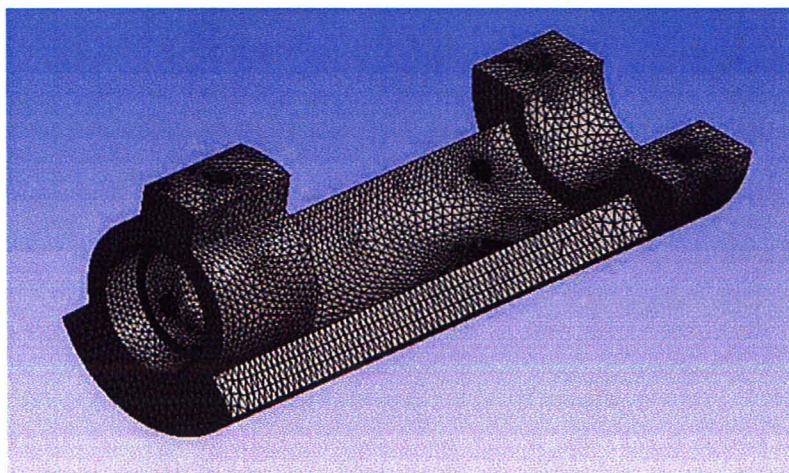
Figure B.18 Mesh used for stress analysis of roll support structure.
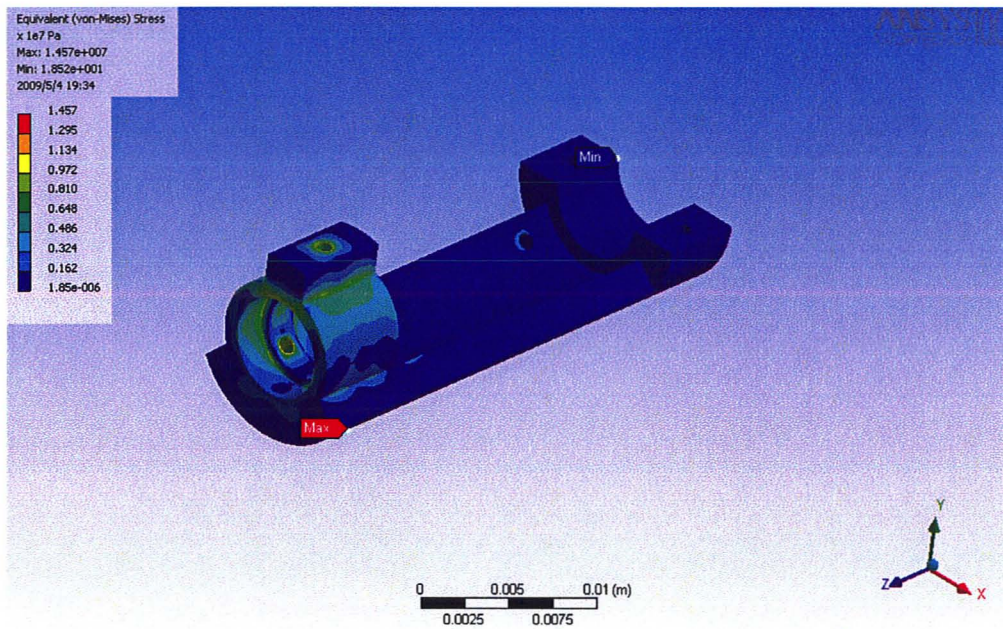
Figure B.19 Von Mises stress of roll support structure (max = 14.6 MPa).
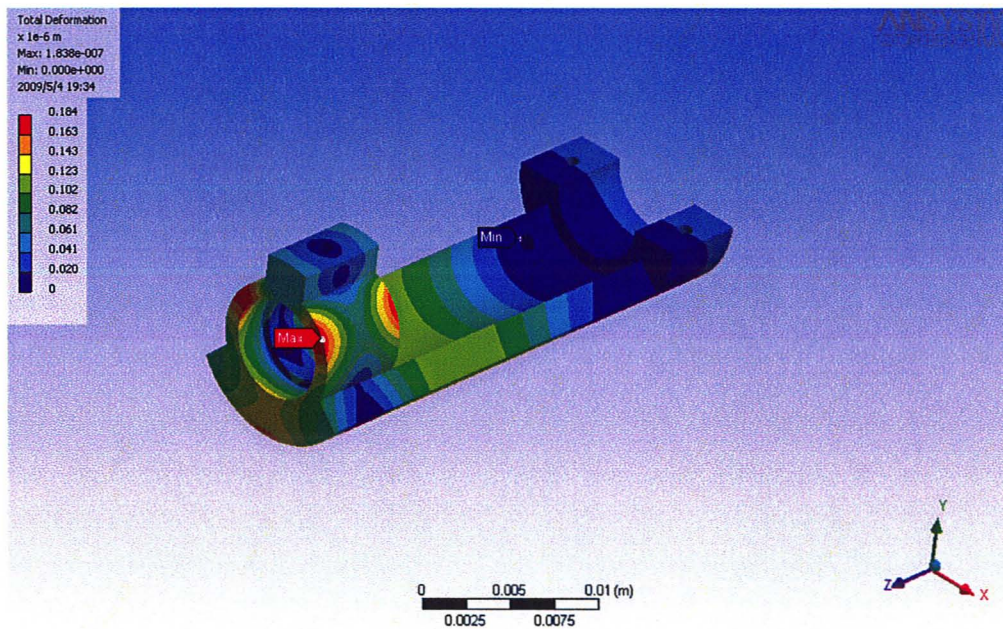
Figure B.20 Deformation of roll support structure (max = 0.2 μm).

B.3 Wrist Joint Components
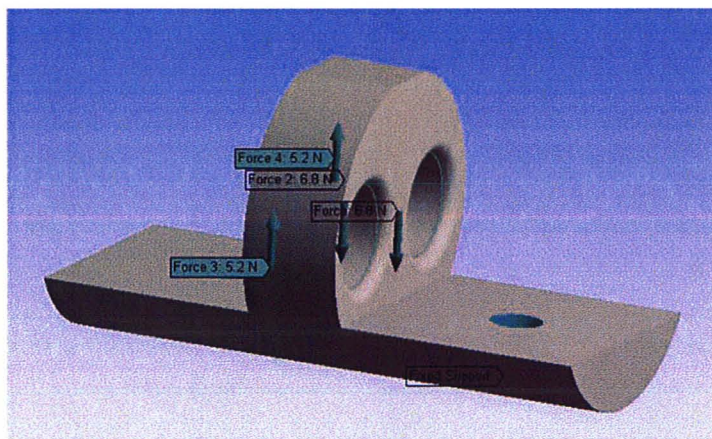
Figure B.21 Loading used for stress analysis of wrist slider support structure.
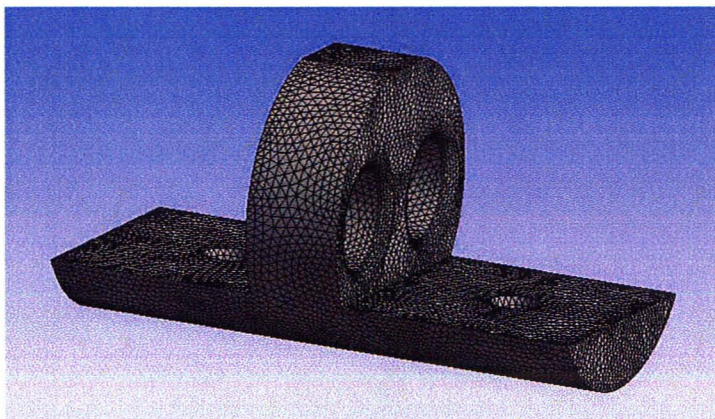
Figure B.22 Mesh used for stress analysis of wrist slider support structure.
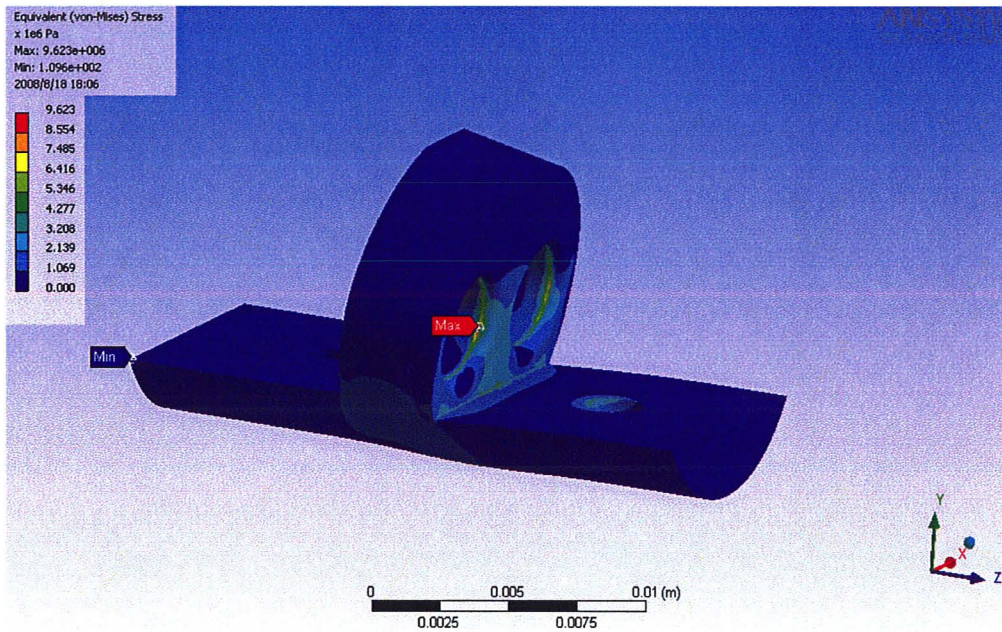
Figure B.23 Von Mises stress of wrist slider support structure (max = 9.6 MPa).
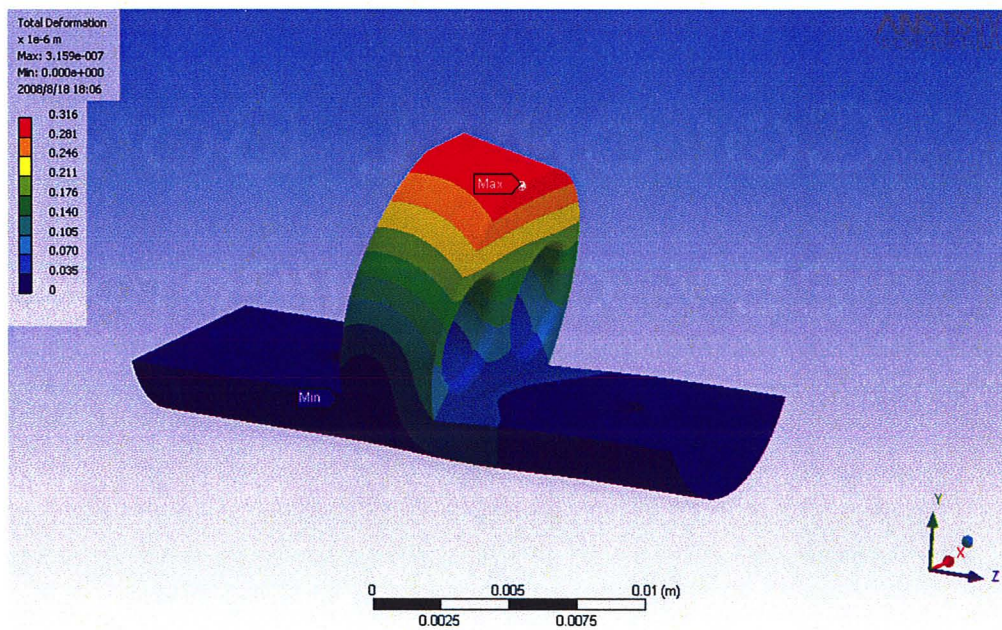
Figure B.24 Deformation of wrist slider support structure (max = 0.3 μm).
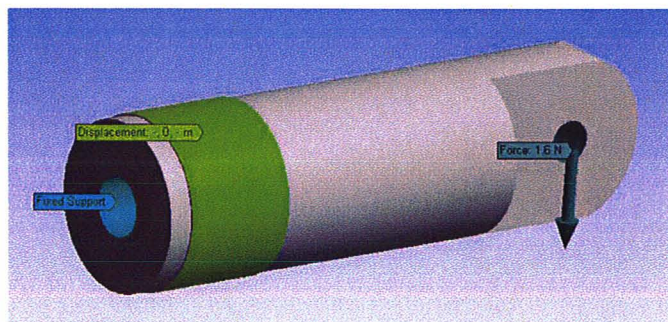
Figure B.25 Loading used for stress analysis of wrist slider.
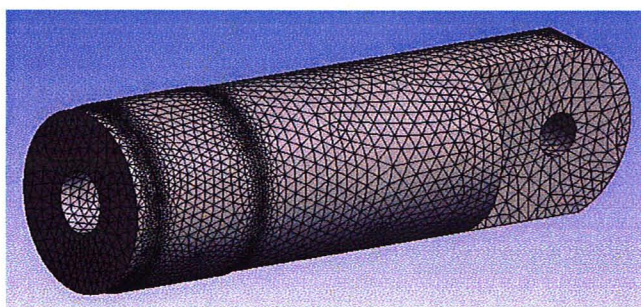
Figure B.26 Mesh used for stress analysis of wrist slider.
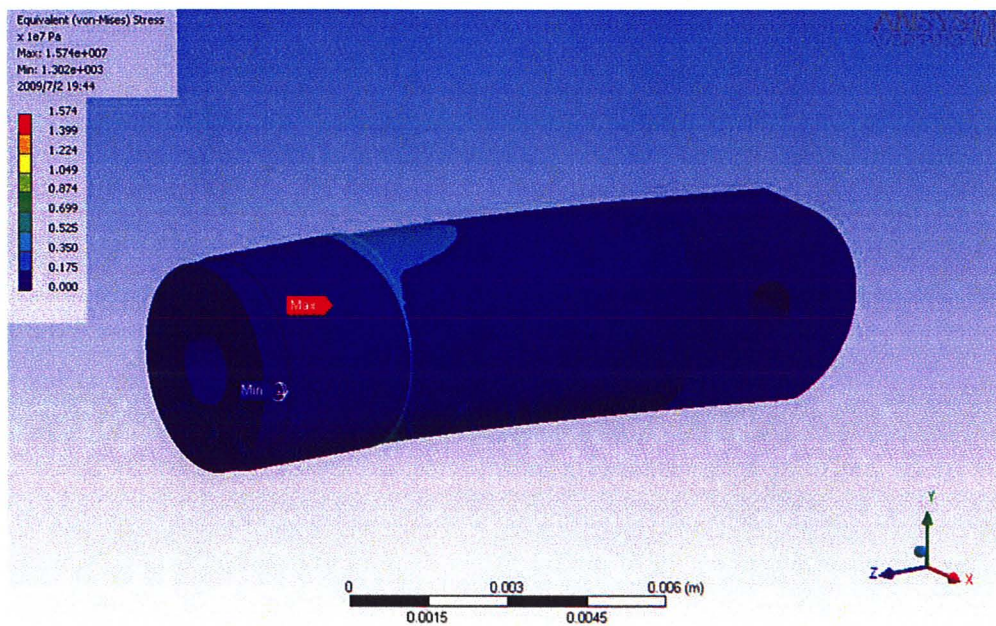
Figure B.27 Von Mises stress of wrist slider (max = 15.7 MPa).
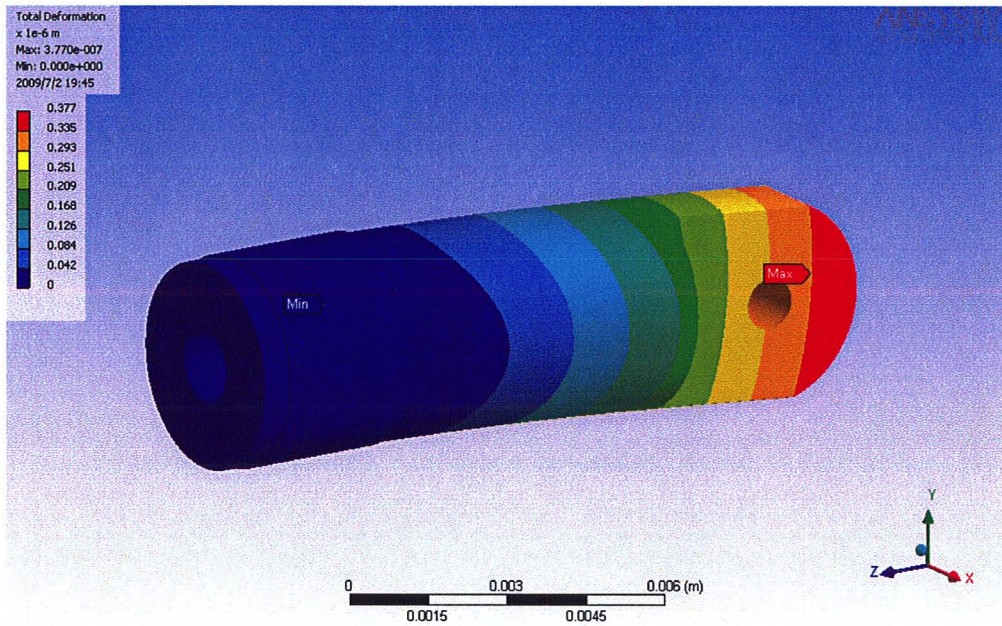
Figure B.28 Deformation of wrist slider support structure (max = 0.4 µm).
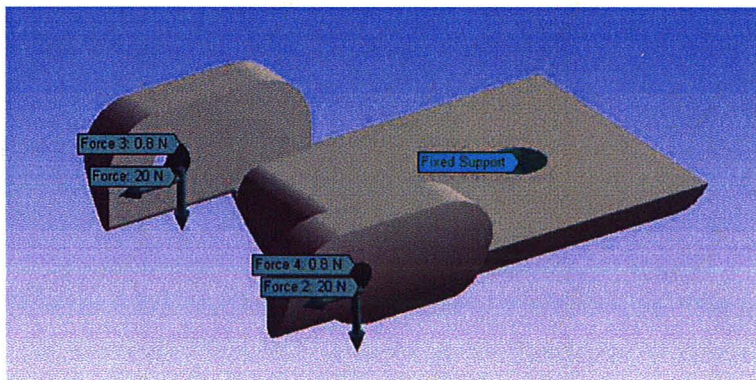
Figure B.29 Loading used for stress analysis of wrist pivot support structure.
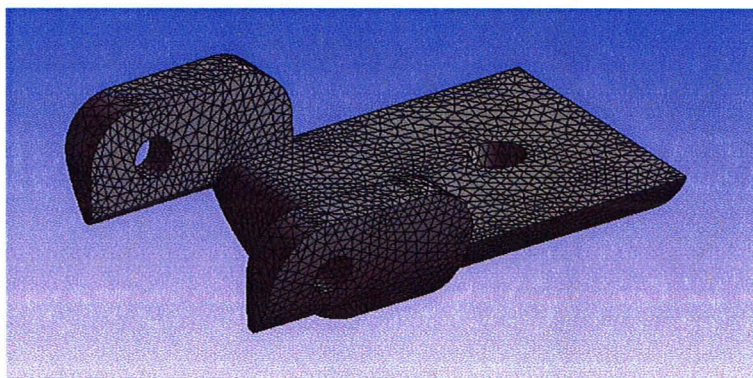
Figure B.30 Mesh used for stress analysis of wrist pivot support structure.
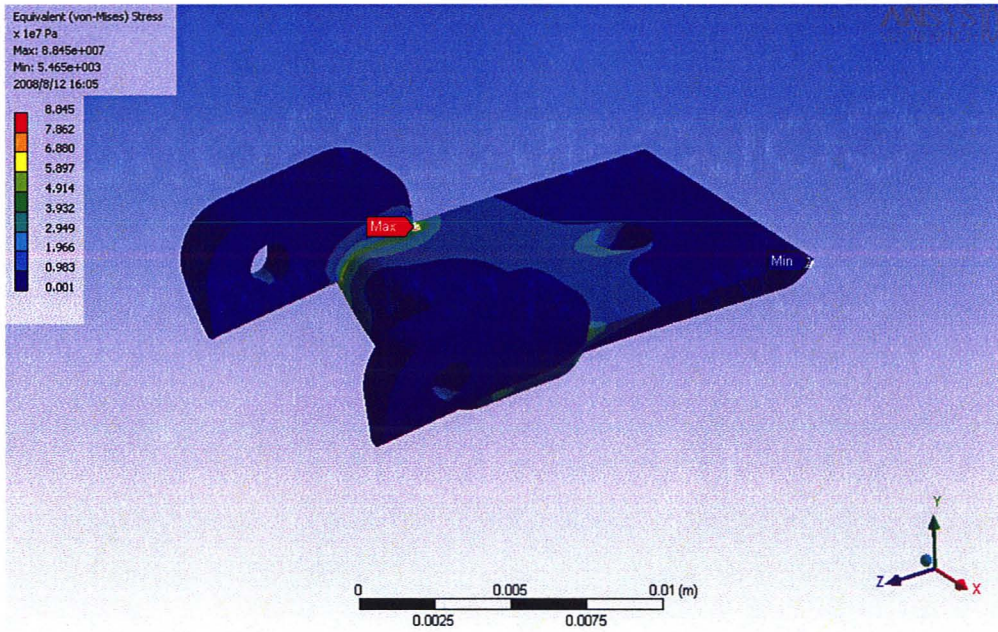
Figure B.31 Von Mises stress of wrist pivot support structure (max = 88.5 MPa).
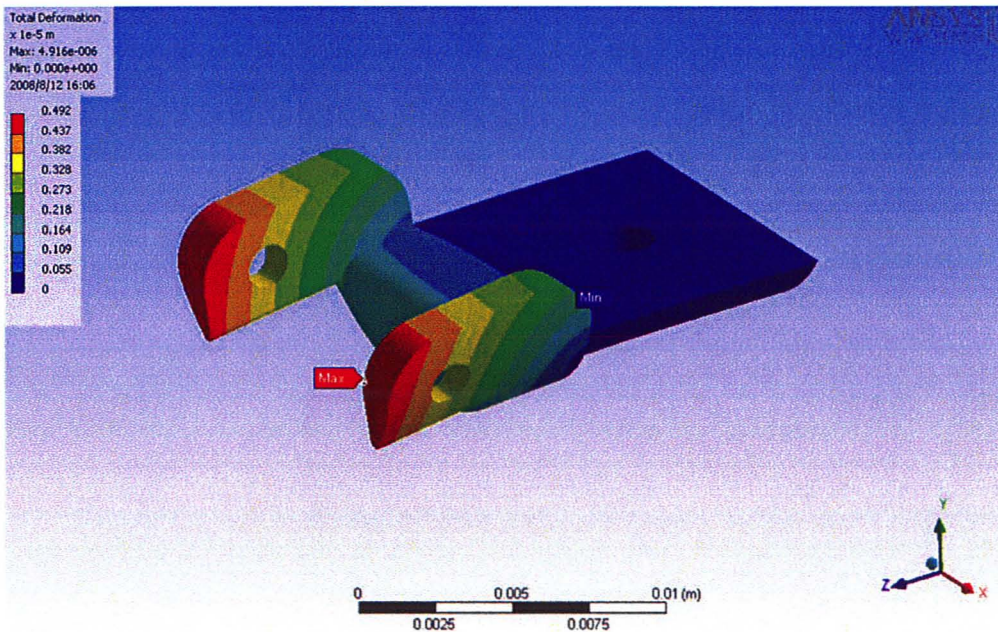
Figure B.32 Deformation of wrist pivot support structure (max = 4.9 μm).
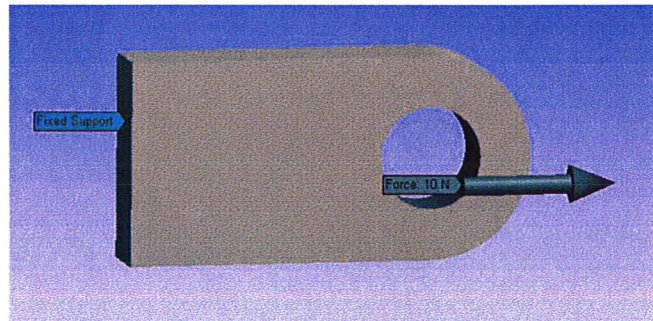
Figure B.33 Loading used for stress analysis of wrist coupler.
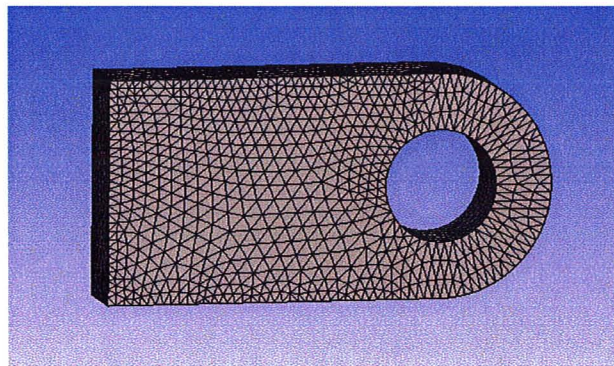
Figure B.34 Mesh used for stress analysis of wrist coupler.
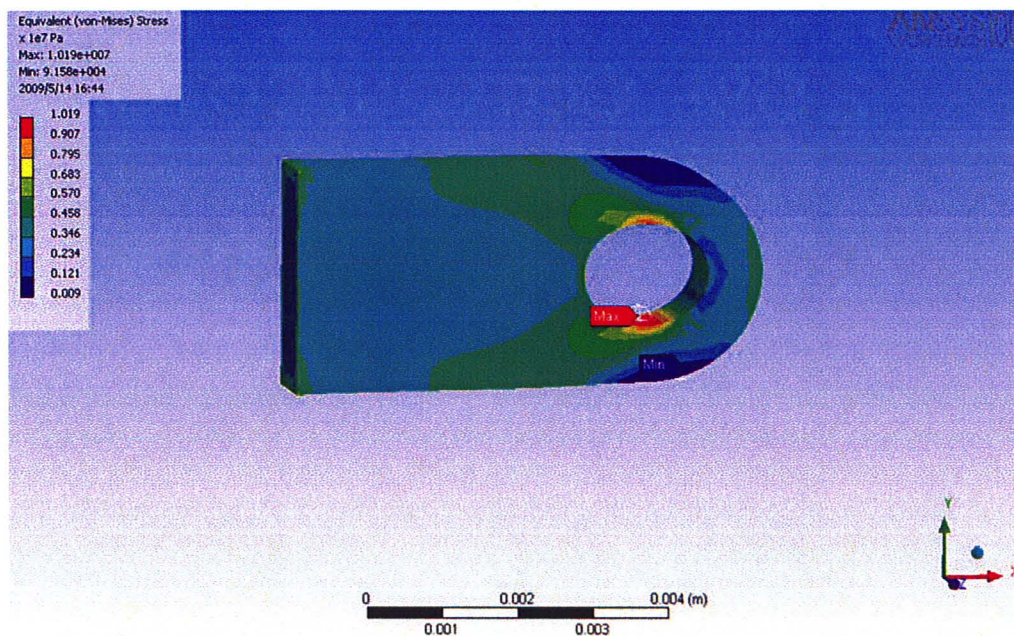
Figure B.35 Von Mises stress of wrist coupler (max = 10.2 MPa).
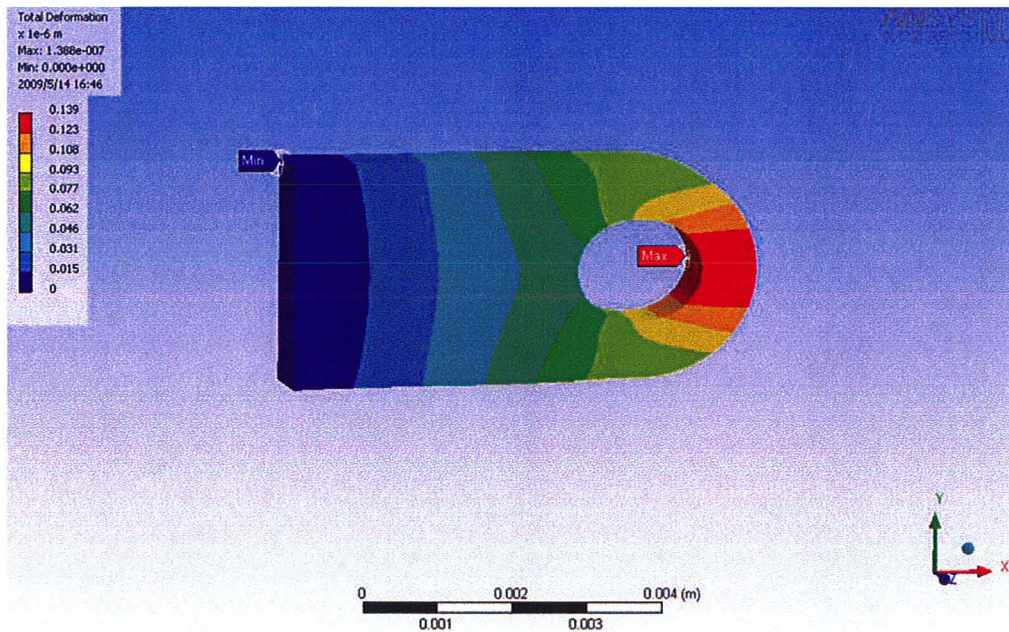
Figure B.36 Deformation of wrist coupler (max = 0.14 μm).

Figure B.37 Loading used for stress analysis of top gripper jaw.
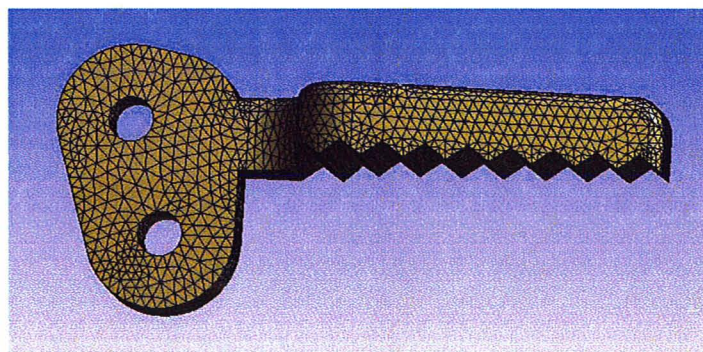
Figure B.38 Mesh used for stress analysis of top gripper jaw.
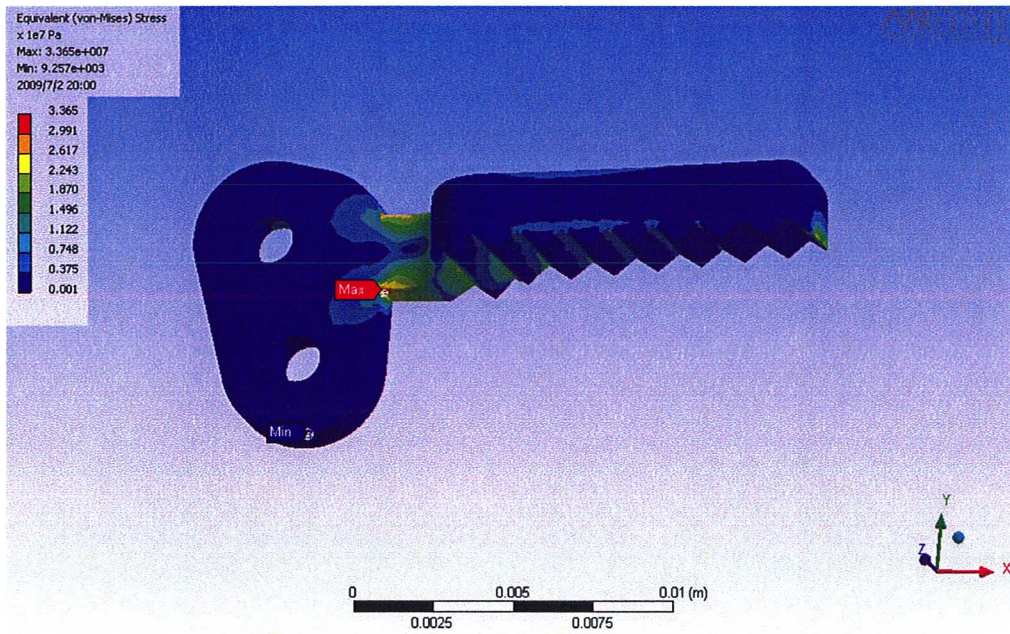
Figure B.39 Von Mises stress of top gripper jaw (max = 33.7 MPa).
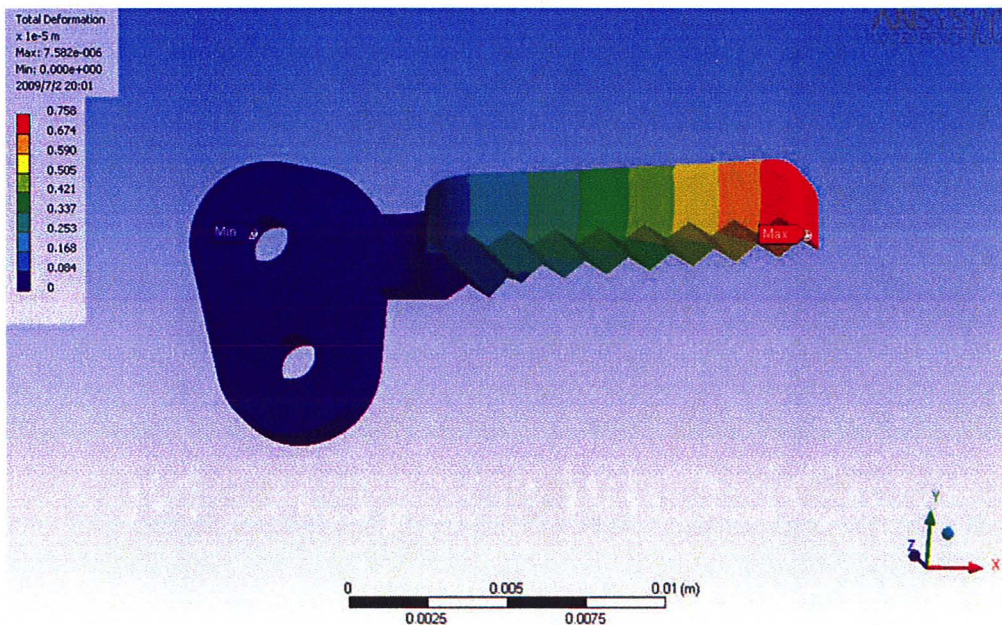
Figure B.40 Deformation of top gripper jaw (max = 7.6 μm).
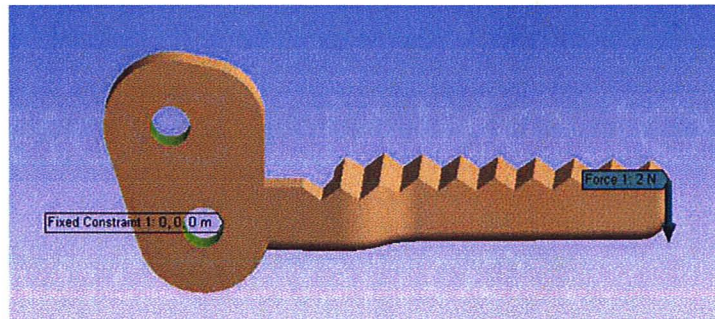
Figure B.41 Loading used for stress analysis of bottom gripper jaw.
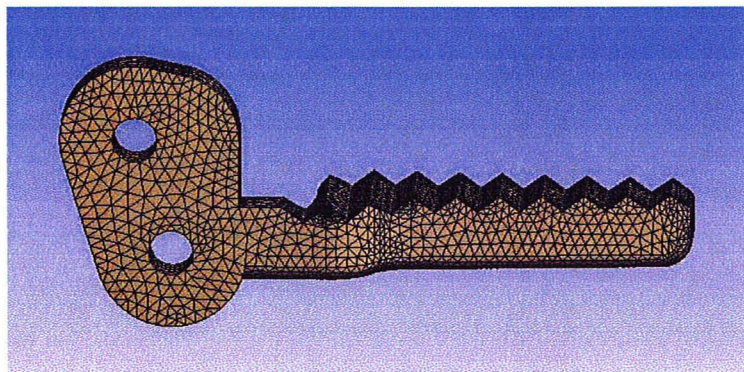
Figure B.42 Mesh used for stress analysis of bottom gripper jaw.
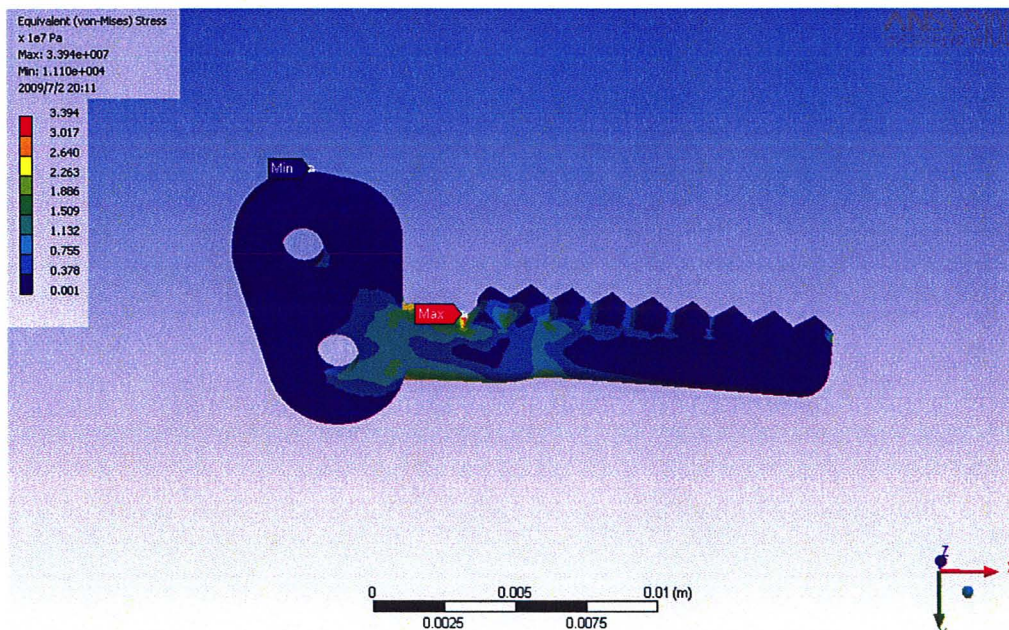
Figure B.43 Von Mises stress of bottom gripper jaw (max = 33.9 MPa).
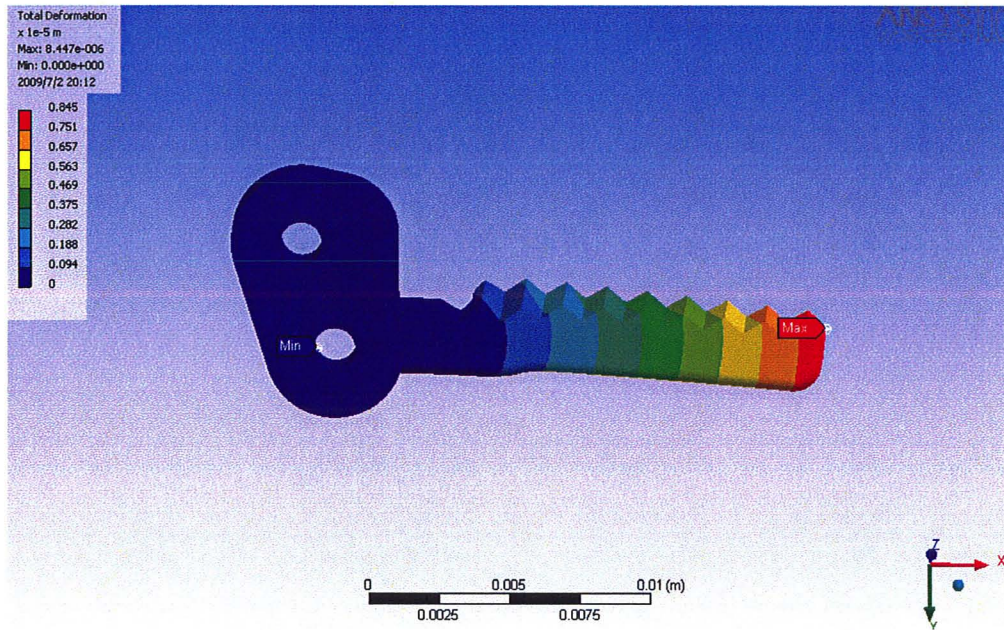
Figure B.44 Deformation of bottom gripper jaw (max = 8.4 µm).

APPENDIX C

MOTOR SPECIFICATIONS

C.1 Video Motion Analysis Results

Figure C.1 shows the speed results for the gizmoszone DC motor (GH6123S) with a 1:136 gear reduction without any mechanism attachments for various constant voltage inputs. As expected, the maximum speed at 3.0 V is at 200 rpm, as per the specs given by the company.
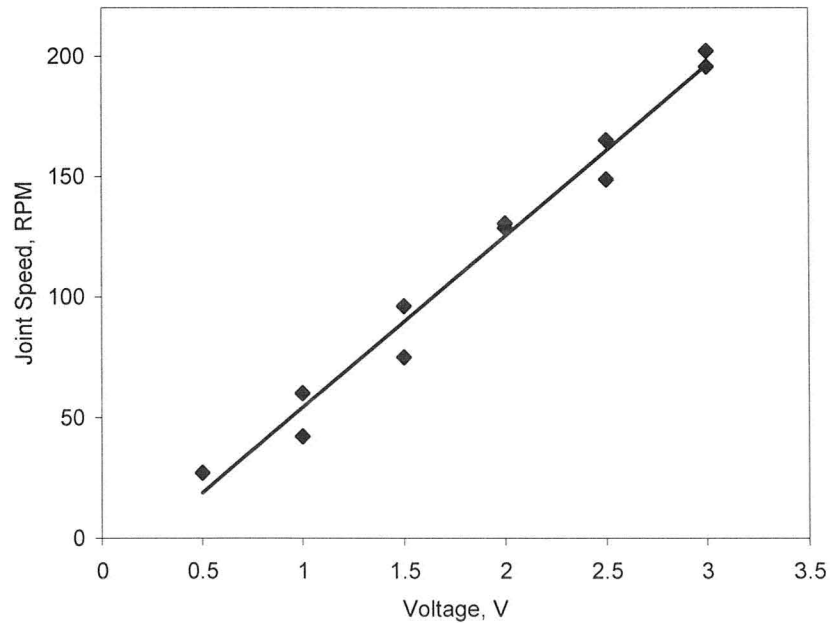
Figure C.1 Speeds of the gizmoszone DC motor (GH6123S) with a 1:136 gear reduction.

Figure C.2 shows the speed results for the gizmoszone DC motor (GH6124S) with a 1:700 gear reduction without any mechanism attachments for various constant voltage inputs. The maximum speed at 3.0 V was found to be 37.4 rpm, just under the expected value of 40 rpm from the manufacturer's specifications.
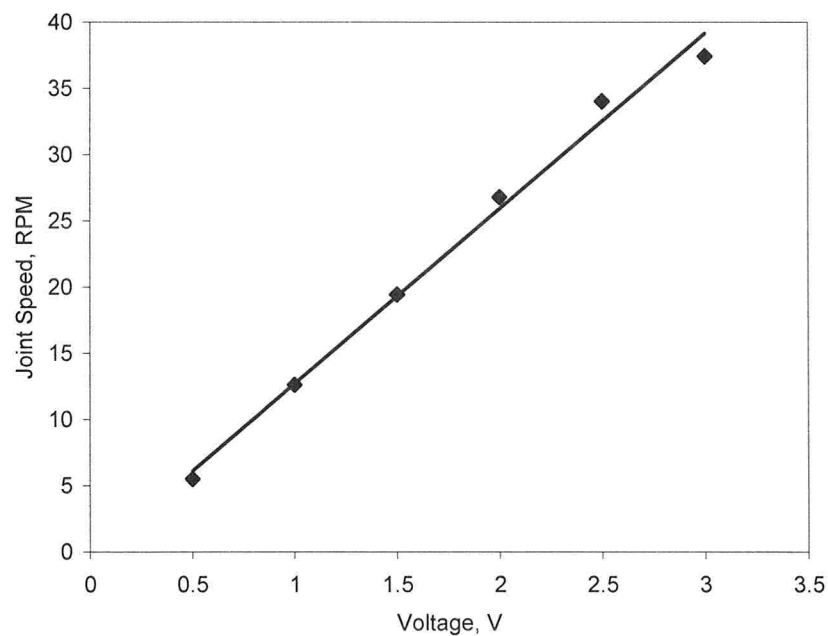
Figure C.2 Speeds of the gizmoszone DC motor (GH6124S) with a 1:700 gear reduction.

APPENDIX D

RAW EXPERIMENTAL DATA

D.1 Video Motion Analysis Tests

Table D.1 Raw experimental data for the horizontal elbow joint straightening tests.

Voltage	Trial	Direction	Time 1	Time 2	Angle 1	Angle 2	Angular Velocity (RPM)
1.25	1	Straighten	30.42	51.37	96.40	170.38	0.6
	2	Straighten	28.87	51.53	93.44	170.04	0.6
	3	Straighten	27.33	48.52	94.04	170.25	0.6
	4	Straighten	29.38	53.92	94.64	170.38	0.5
1.5	1	Straighten	19.20	34.30	93.39	170.12	0.8
	2	Straighten	24.22	40.77	95.71	170.08	0.7
	3	Straighten	23.57	40.90	94.73	169.95	0.7
	4	Straighten	25.45	43.00	97.18	169.99	0.7
2	1	Straighten	12.62	22.80	93.58	170.55	1.3
	2	Straighten	16.35	28.62	94.58	170.20	1.0
	3	Straighten	16.37	28.13	94.80	169.99	1.1
	4	Straighten	16.37	27.80	94.36	170.31	1.1
2.5	1	Straighten	10.38	18.07	93.91	170.53	1.7
	2	Straighten	12.03	20.23	94.00	170.39	1.6
	3	Straighten	12.18	20.55	92.97	170.10	1.5
	4	Straighten	11.72	20.05	94.42	169.95	1.5
3	1	Straighten	7.88	14.10	95.86	170.14	2.0
	2	Straighten	9.68	16.40	92.56	170.37	1.9
	3	Straighten	9.60	16.00	94.76	170.21	2.0
	4	Straighten	9.13	15.60	93.64	170.16	2.0

Table D.2 Raw experimental data for the horizontal elbow joint bending tests.

Voltage	Trial	Direction	Time 1	Time 2	Angle 1	Angle 2	Angular Velocity (RPM)
1.25	1	Bend	2.33	26.60	169.98	96.81	0.5
	2	Bend	2.37	25.70	170.24	93.68	0.5
	3	Bend	2.33	23.77	170.50	97.00	0.6
	4	Bend	2.37	27.68	170.28	94.30	0.5
1.5	1	Bend	1.43	17.37	169.86	93.37	0.8
	2	Bend	2.13	20.97	170.18	96.98	0.6
	3	Bend	2.37	20.53	170.12	96.22	0.7
	4	Bend	2.60	21.68	169.91	98.84	0.6
2	1	Bend	1.17	11.40	170.54	95.03	1.2
	2	Bend	1.77	14.48	170.43	95.67	1.0
	3	Bend	1.73	15.33	170.30	93.70	0.9
	4	Bend	1.77	14.50	170.21	95.90	1.0
2.5	1	Bend	1.30	9.18	170.64	93.73	1.6
	2	Bend	1.27	10.37	170.27	96.70	1.3
	3	Bend	1.43	10.82	169.96	94.51	1.3
	4	Bend	1.33	10.28	170.37	94.66	1.4
3	1	Bend	0.60	6.98	170.36	95.35	2.0
	2	Bend	1.47	8.62	166.19	94.26	1.7
	3	Bend	1.27	8.63	170.23	92.49	1.8
	4	Bend	1.00	8.17	169.93	93.60	1.8

Table D.3 Raw experimental data for the vertical elbow joint straightening tests.

Voltage	Trial	Direction	Time 1	Time 2	Angle 1	Angle 2	Angular Velocity (RPM)
1.25	1	Straighten	0.92	20.78	80.99	162.66	0.7
	2	Straighten	1.40	19.57	85.26	160.98	0.7
	3	Straighten	1.07	21.15	83.95	162.72	0.7
1.5	1	Straighten	25.17	36.45	91.00	160.65	1.0
	2	Straighten	29.17	41.27	88.94	161.20	1.0
	3	Straighten	30.02	42.08	88.91	167.12	1.1
2	1	Straighten	16.70	26.12	87.09	167.67	1.4
	2	Straighten	22.07	32.08	79.20	162.27	1.4
	3	Straighten	13.78	23.28	81.70	162.92	1.4
	4	Straighten	18.02	28.48	78.58	171.23	1.5
2.5	1	Straighten	10.35	18.02	79.72	167.47	1.9
	2	Straighten	10.58	18.38	78.12	170.92	2.0
	3	Straighten	11.23	19.00	78.18	167.70	1.9
	4	Straighten	11.07	18.78	77.18	167.78	2.0

Table D.3 (cont'd) Raw experimental data for the vertical elbow joint straightening tests.

Voltage	Trial	Direction	Time 1	Time 2	Angle 1	Angle 2	Angular Velocity (RPM)
3	1	Straighten	9.15	15.50	78.85	167.62	2.3
	2	Straighten	9.68	15.93	77.98	167.47	2.4
	3	Straighten	9.60	15.87	78.87	171.30	2.5
	4	Straighten	9.35	15.97	74.69	171.44	2.4
3.5	1	Straighten	7.82	13.00	84.66	171.19	2.8
	2	Straighten	7.07	11.97	83.51	165.30	2.8
	3	Straighten	7.87	12.90	85.02	167.69	2.7
	4	Straighten	6.33	11.22	86.32	167.62	2.8
4	1	Straighten	6.53	10.75	86.11	171.18	3.4
	2	Straighten	5.82	9.90	84.69	167.74	3.4
	3	Straighten	6.25	10.77	83.06	171.21	3.3

Table D.4 Raw experimental data for the vertical elbow joint bending tests.

Voltage	Trial	Direction	Time 1	Time 2	Angle 1	Angle 2	Angular Velocity (RPM)
2	1	Bend	0.87	15.47	171.09	87.37	1.0
	2	Bend	0.97	19.73	171.19	82.43	0.8
	3	Bend	1.57	12.92	171.21	80.92	1.3
	4	Bend	1.90	17.32	170.96	78.59	1.0
2.5	1	Bend	0.80	9.78	171.10	80.54	1.7
	2	Bend	1.10	9.98	171.19	77.31	1.8
	3	Bend	1.10	10.53	171.12	77.17	1.7
	4	Bend	0.93	10.43	171.22	77.09	1.7
3	1	Bend	0.87	8.55	170.96	77.92	2.0
	2	Bend	1.03	9.12	171.18	78.27	1.9
	3	Bend	0.90	9.07	171.16	79.32	1.9
	4	Bend	1.13	8.72	171.14	74.89	2.1
3.5	1	Bend	0.97	7.25	171.19	84.16	2.3
	2	Bend	0.70	6.50	171.15	82.61	2.5
	3	Bend	0.93	7.27	171.32	86.37	2.2
	4	Bend	0.60	5.83	167.67	87.85	2.5
4	1	Bend	0.97	5.90	167.64	85.17	2.8
	2	Bend	0.90	5.42	171.20	84.94	3.2
	3	Bend	1.07	5.78	171.32	81.73	3.2

Table D.5 Raw experimental data for video motion analysis of the roll joint.

Voltage	Trial	Direction	Time 1	Time 2	Reading 1	Reading 2	Angular Velocity (RPM)
3	1	CCW	0.57	1.23	15.00	5.00	37.3
	1	CW	1.87	2.50	5.00	15.00	39.2
	2	CCW	0.20	0.85	15.00	5.00	38.2
	2	CW	1.62	2.32	5.00	16.00	39.0
	3	CCW	0.60	1.28	15.00	4.00	40.0
	3	CW	1.95	2.57	5.00	15.00	40.3
	4	CCW	0.63	1.25	15.00	5.00	40.3
	4	CW	1.95	2.57	5.00	15.00	40.3
2.5	1	CCW	0.60	1.37	15.00	5.00	32.4
	1	CW	2.10	3.03	5.00	17.00	31.9
	2	CCW	0.63	1.37	15.00	5.00	33.9
	2	CW	2.10	2.85	5.00	15.00	33.1
	3	CCW	0.63	1.37	15.00	5.00	33.9
	3	CW	2.03	2.73	5.00	15.00	35.5
	4	CCW	0.50	1.27	15.00	5.00	32.4
	4	CW	2.00	2.77	5.00	15.00	32.4
2	1	CCW	0.77	1.73	15.00	5.00	25.7
	1	CW	2.30	3.27	5.00	15.00	25.7
	2	CCW	0.50	1.47	15.00	5.00	25.7
	2	CW	2.27	3.23	5.00	15.00	25.7
	3	CCW	0.80	1.78	15.00	5.00	25.3
	3	CW	2.48	3.55	5.00	16.00	25.6
	4	CCW	0.53	1.60	16.00	5.00	25.6
	4	CW	2.07	3.08	5.00	16.00	26.9
1.5	1	CCW	0.60	1.93	15.00	5.00	18.6
	1	CW	2.60	3.90	5.00	15.00	19.1
	2	CCW	0.30	1.63	15.00	5.00	18.6
	2	CW	2.53	3.87	5.00	15.00	18.6
	3	CCW	0.63	1.93	15.00	5.00	19.1
	3	CW	2.47	3.78	5.00	15.00	18.9
	4	CCW	0.43	1.75	15.00	5.00	18.9
	4	CW	2.25	3.57	5.00	15.00	18.9
1	1	CCW	0.53	2.62	15.00	5.00	11.9
	1	CW	3.42	5.43	5.00	15.00	12.3
	2	CCW	0.53	2.62	15.00	5.00	11.9
	2	CW	3.45	5.50	5.00	15.00	12.1
	3	CCW	0.83	2.88	15.00	5.00	12.1
	3	CW	3.62	5.65	5.00	15.00	12.2
	4	CCW	0.73	2.87	15.00	5.00	11.6
	4	CW	3.90	5.97	5.00	15.00	12.0

Table D.5 (cont'd) Raw experimental data for video motion analysis of the roll joint.

Voltage	Take	Direction	Time 1	Time 2	Reading 1	Reading 2	Angular Velocity (RPM)
0.5	1	CCW	0.83	5.17	13.00	5.00	4.6
	1	CW	7.63	12.47	5.00	15.00	5.1
	2	CCW	0.63	5.73	15.00	5.00	4.9
	2	CW	7.07	11.95	5.00	15.00	5.1
	3	CCW	0.83	5.90	15.00	5.00	4.9
	3	CW	7.37	12.15	5.00	15.00	5.2
	4	CCW	1.13	6.12	15.00	5.00	5.0
	4	CW	7.75	12.45	5.00	15.00	5.3

Table D.6 Raw experimental data for the top gripper of the wrist joint.

Voltage	Trial	Gripper	Direction	Time 1	Time 2	Angle 1	Angle 2	Angular Velocity (RPM)
3	1	Top	Open	0.77	5.13	3.39	98.47	3.6
	1	Top	Close	17.42	21.28	97.27	4.77	4.0
	2	Top	Open	0.77	4.62	0.00	93.45	4.0
	2	Top	Close	13.90	17.70	97.97	2.59	4.2
	3	Top	Open	0.67	4.67	2.57	92.61	3.8
	3	Top	Close	14.45	18.35	98.71	1.94	4.1
	4	Top	Open	0.63	5.07	0.00	103.95	3.9
	4	Top	Close	15.78	19.88	108.01	4.24	4.2
2.5	1	Top	Open	0.30	4.98	0.81	94.29	3.3
	1	Top	Close	16.27	20.65	92.86	1.83	3.5
	2	Top	Open	0.87	6.30	0.00	104.18	3.2
	2	Top	Close	19.53	24.57	106.45	3.98	3.4
	3	Top	Open	0.70	5.83	3.77	103.30	3.2
	3	Top	Close	17.83	22.55	97.55	1.88	3.4
	4	Top	Open	0.47	5.42	2.53	97.30	3.2
	4	Top	Close	16.72	21.38	96.38	2.28	3.4
2	1	Top	Open	0.80	6.40	1.49	91.98	2.7
	1	Top	Close	19.82	25.10	89.16	2.69	2.7
	2	Top	Open	0.80	7.75	3.29	109.03	2.5
	2	Top	Close	25.10	32.03	111.41	3.32	2.6
	3	Top	Open	0.60	7.55	2.42	108.27	2.5
	3	Top	Close	23.55	29.68	108.27	0.84	2.9
	4	Top	Open	0.43	7.05	0.00	102.05	2.6
	4	Top	Close	22.98	29.72	108.06	3.39	2.6

Table D.6 (cont'd) Raw experimental data for the top gripper of the wrist joint.

Voltage	Trial	Gripper	Direction	Time 1	Time 2	Angle 1	Angle 2	Angular Velocity (RPM)
1.5	1	Top	Open	0.73	9.48	0.00	98.98	1.9
	1	Top	Close	29.98	38.18	101.03	3.61	2.0
	2	Top	Open	0.67	10.20	1.69	110.64	1.9
	2	Top	Close	33.65	42.90	108.27	2.25	1.9
	3	Top	Open	1.10	10.47	2.92	103.56	1.8
	3	Top	Close	32.93	41.93	105.84	1.91	1.9
	4	Top	Open	1.43	11.70	1.52	107.38	1.7
	4	Top	Close	34.25	43.73	108.51	3.01	1.9
1	1	Top	Open	1.33	14.27	0.00	94.27	1.2
	1	Top	Close	43.85	56.75	92.82	1.64	1.2
	2	Top	Open	0.87	17.37	1.47	99.69	1.0
	2	Top	Close	51.00	65.48	99.41	2.53	1.1
	3	Top	Open	1.13	16.12	2.28	102.25	1.1
	3	Top	Close	50.70	65.47	100.59	2.53	1.1
	4	Top	Open	0.90	15.25	3.19	97.34	1.1
	4	Top	Close	48.38	62.08	101.36	3.42	1.2
0.75	1	Top	Open	1.63	19.52	3.37	90.84	0.8
	1	Top	Close	56.88	73.83	84.62	1.97	0.8
	2	Top	Open	0.97	21.00	2.12	97.07	0.8
	2	Top	Close	65.78	86.00	95.34	3.34	0.8
	3	Top	Open	1.13	26.87	2.49	98.01	0.6
	3	Top	Close	74.57	98.43	99.59	1.71	0.7
	4	Top	Open	1.33	23.98	1.54	93.28	0.7
	4	Top	Close	68.93	92.77	91.30	2.21	0.6

Table D.7 Raw experimental data for the bottom gripper of the wrist joint.

Voltage	Trial	Gripper	Direction	Time 1	Time 2	Angle 1	Angle 2	Angular Velocity (RPM)
3	1	Bottom	Close	5.83	10.23	97.77	7.86	3.4
	1	Bottom	Open	11.47	15.82	5.26	98.45	3.6
	2	Bottom	Close	4.85	8.93	91.38	3.37	3.6
	2	Bottom	Open	9.47	13.58	3.79	93.31	3.6
	3	Bottom	Close	5.00	9.08	91.55	2.25	3.6
	3	Bottom	Open	9.72	13.95	4.45	96.63	3.6
	4	Bottom	Close	5.43	10.07	103.30	4.02	3.6
	4	Bottom	Open	10.70	15.42	3.50	104.99	3.6

Table D.7 (cont'd) Raw experimental data for the bottom gripper of the wrist joint.

Voltage	Trial	Gripper	Direction	Time 1	Time 2	Angle 1	Angle 2	Angular Velocity (RPM)
2.5	1	Bottom	Close	5.22	10.28	96.69	2.35	3.1
	1	Bottom	Open	10.85	15.73	0.90	92.50	3.1
	2	Bottom	Close	6.63	12.53	106.93	2.43	3.0
	2	Bottom	Open	13.27	18.97	2.59	107.54	3.1
	3	Bottom	Close	6.23	11.68	104.16	2.44	3.1
	3	Bottom	Open	12.38	17.40	2.69	98.01	3.2
	4	Bottom	Close	5.75	10.78	95.43	3.05	3.1
	4	Bottom	Open	11.35	16.35	3.70	98.49	3.2
2	1	Bottom	Close	6.92	12.73	88.83	3.79	2.4
	1	Bottom	Open	13.72	19.35	4.53	89.43	2.5
	2	Bottom	Close	8.58	16.15	110.59	1.43	2.4
	2	Bottom	Open	16.98	24.00	2.51	108.27	2.5
	3	Bottom	Close	8.38	15.32	104.57	3.34	2.4
	3	Bottom	Open	16.18	22.95	2.64	105.89	2.5
	4	Bottom	Close	7.48	14.38	105.20	3.83	2.4
	4	Bottom	Open	15.15	22.28	2.59	107.85	2.5
1.5	1	Bottom	Close	10.02	19.28	101.60	2.29	1.8
	1	Bottom	Open	20.22	29.38	3.02	100.21	1.8
	2	Bottom	Close	11.30	21.22	108.47	3.20	1.8
	2	Bottom	Open	22.55	32.42	2.51	108.25	1.8
	3	Bottom	Close	11.23	21.20	103.14	2.64	1.7
	3	Bottom	Open	22.33	32.20	2.37	107.38	1.8
	4	Bottom	Close	12.27	22.32	107.63	4.22	1.7
	4	Bottom	Open	23.58	33.52	2.43	108.66	1.8
1	1	Bottom	Close	14.97	28.43	91.10	3.42	1.1
	1	Bottom	Open	29.57	43.18	3.93	91.05	1.1
	2	Bottom	Close	18.40	33.17	102.02	3.47	1.1
	2	Bottom	Open	34.80	49.67	2.69	97.33	1.1
	3	Bottom	Close	17.12	32.53	104.14	1.47	1.1
	3	Bottom	Open	34.23	49.40	0.87	105.02	1.1
	4	Bottom	Close	16.25	30.77	98.01	3.47	1.1
	4	Bottom	Open	32.50	47.55	1.86	99.19	1.1
0.75	1	Bottom	Close	20.62	37.50	84.51	3.76	0.8
	1	Bottom	Open	38.70	55.88	3.55	84.91	0.8
	2	Bottom	Close	22.33	42.00	92.34	3.70	0.8
	2	Bottom	Open	43.27	63.62	3.15	92.11	0.7
	3	Bottom	Close	28.53	49.78	101.14	2.88	0.8
	3	Bottom	Open	51.32	72.10	3.70	95.73	0.7
	4	Bottom	Close	25.18	44.07	89.21	3.47	0.8
	4	Bottom	Open	46.30	66.33	2.59	92.07	0.7

D.2 Potentiometer Tests
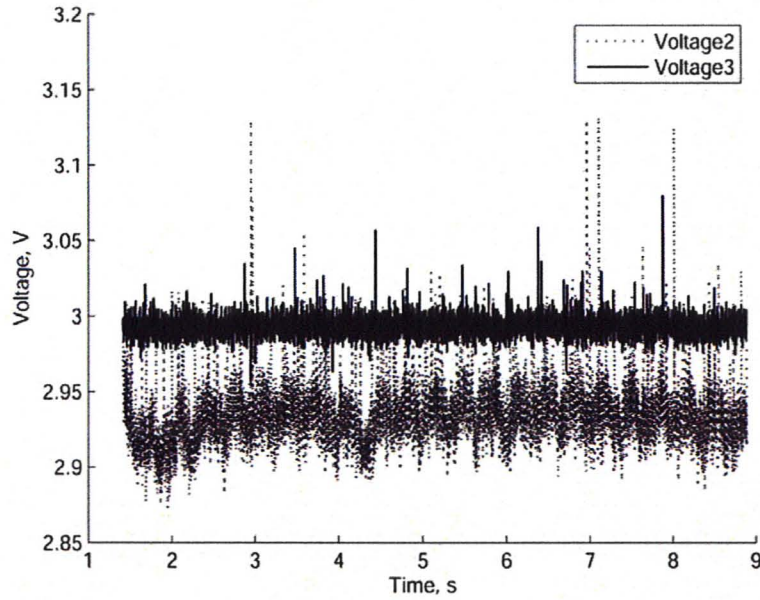
Figure D.1 Raw experimental data of voltages across motor and 1Ω resistor.
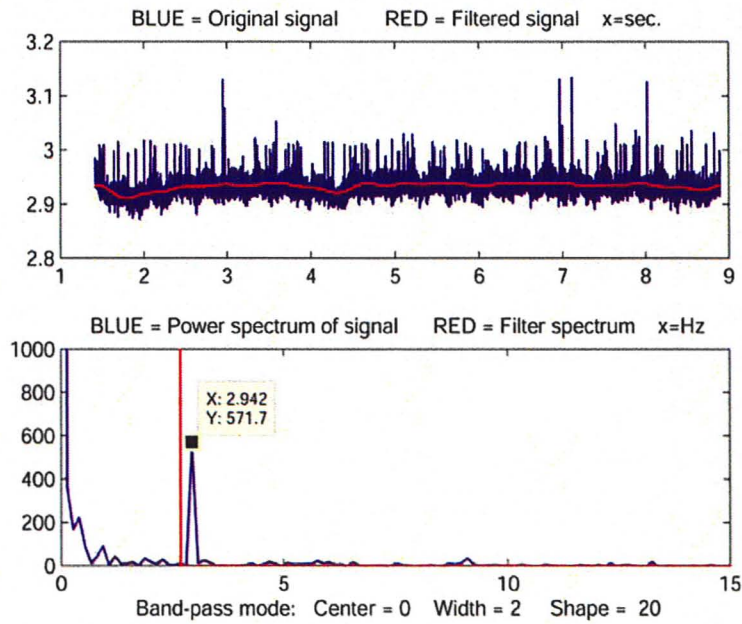
Figure D.2 Original and filtered signal of Voltage 2 (top) and power spectrum showing the low-pass filter with a 2 Hz cut-off (below).
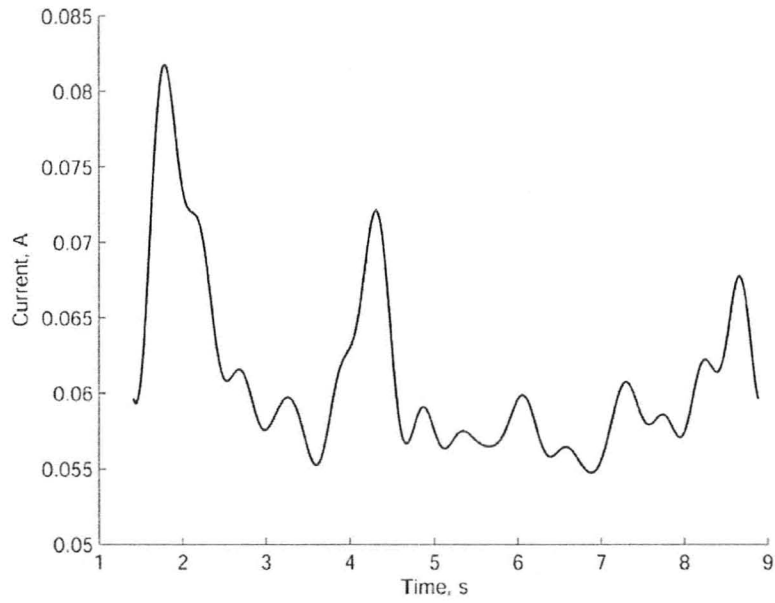
Figure D.3 Current to the motor plotted over time.
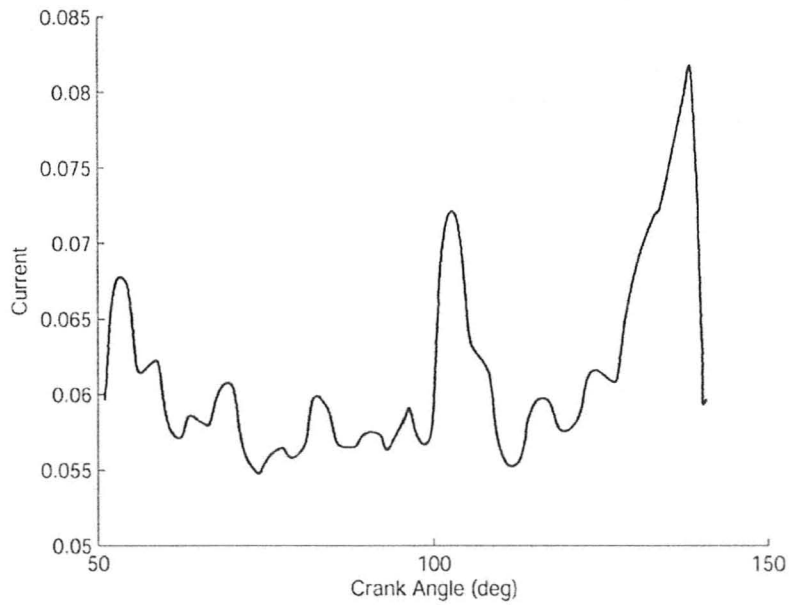
Figure D.4 Current to the motor vs. crank angle position.

206
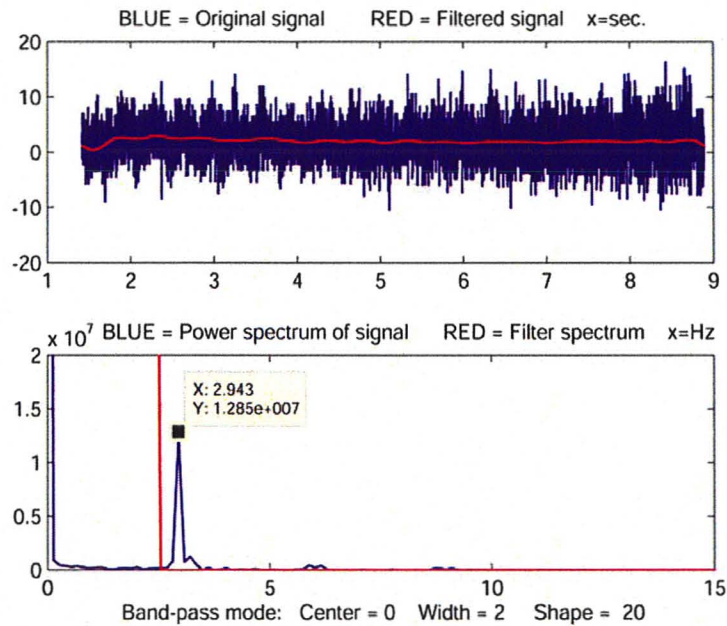
Figure D.5 Above: Experimental result for crank angular velocity by taking the central difference of the crank angle (blue line) and after filtering with a 2 Hz cutoff (red line). Below: Power spectrum showing the low-pass filter with a 2 Hz cut-off.

D.3 Force Test

An example of the raw voltage results is shown in Figure D.6. The values for V_0 and V_1 were calculated by taking the average of the voltage readings after reaching steady state. These results, along with the associated force readings, are given in Table D.8.
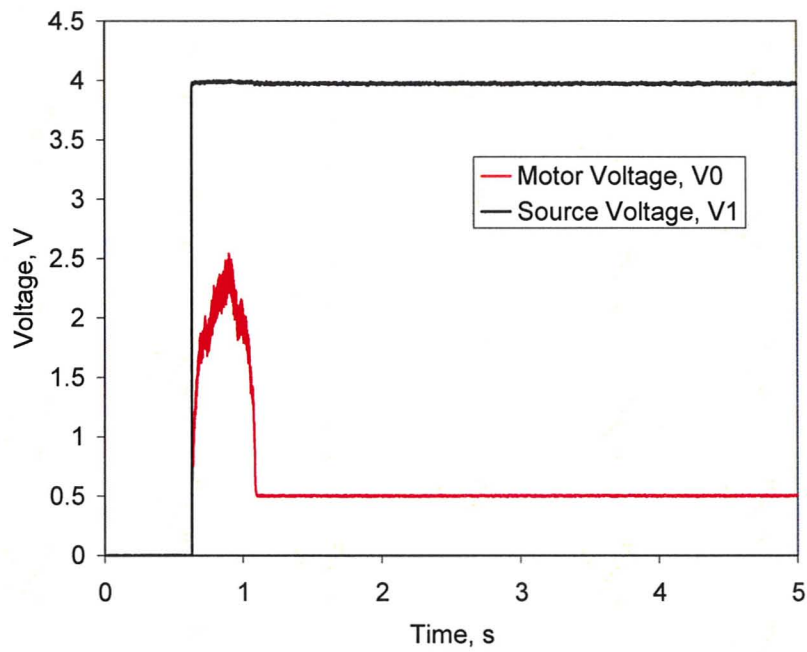
Figure D.6 Raw voltage results for the force tests.

Table D.8 Raw experimental data for the force tests.

Voltage	Trial	V_0	V_1	Force
4.0	1	0.506	3.977	5.3
4.0	2	0.506	3.977	3.5
4.0	3	0.503	3.973	3.9
4.0	4	0.504	3.969	4.3
4.0	5	0.503	3.972	7.6
4.5	1	0.566	4.471	8.1
4.5	2	0.567	4.463	10.3
4.5	3	0.566	4.468	10.2
4.5	4	0.566	4.475	10.8
4.5	5	0.569	4.473	10.9
5.0	1	0.632	4.971	10.7
5.0	2	0.631	4.966	11.5
5.0	3	0.631	4.966	13
5.0	4	0.630	4.968	14.1
5.0	5	0.630	4.967	13.6
5.5	1	0.692	5.454	15.1
5.5	2	0.693	5.456	13
5.5	3	0.694	5.456	13.2
5.5	4	0.693	5.457	17.2
5.5	5	0.693	5.456	17.4

Table D.8 (cont'd) Raw experimental data for the force tests.

Voltage	Trial	V_0	V_1	Force
6.0	1	0.757	5.956	19.8
6.0	2	0.748	5.890	19.7
6.0	3	0.756	5.951	19.8
6.0	4	0.750	5.894	19.3
6.0	5	0.756	5.944	19.8
6.5	1	0.819	6.446	21.1
6.5	2	0.822	6.458	21.1
6.5	3	0.821	6.462	21
6.5	4	0.823	6.464	20.7
6.5	5	0.824	6.468	19.3
7.0	1	0.882	6.931	21.8
7.0	2	0.884	6.948	19
7.0	3	0.886	6.959	22.2
7.0	4	0.887	6.958	21.1
7.0	5	0.883	6.958	20.7
7.5	1	0.812	7.455	23.1
7.5	2	0.948	7.456	21
7.5	3	0.952	7.455	22
7.5	4	0.950	7.452	22.1
7.5	5	0.944	7.407	22
8.0	1	1.008	7.900	21.2
8.0	2	1.008	7.909	20.8
8.0	3	1.011	7.920	22.5
8.0	4	1.016	7.956	22.6
8.0	5	1.012	7.956	25.4

APPENDIX E

MANUFACTURER'S MOTOR SPECIFICATIONS

▨▨ FAULHABER

Brushless DC-Servomotors
Electronic Commutation

0,37 mNm

For combination with (overview on page 14-15)
Gearheads:
06/1
Drive Electronics:
BLD 2401

Series 0620 ... B

			0620 K		006 B	012 B	
1	Nominal voltage	U_N			6	12	Volt
2	Terminal resistance, phase-phase	R			9,1	59,0	Ω
3	Output power [1]	$P_{2\,max.}$			1,56	1,58	W
4	Efficiency	$\eta_{max.}$			57	55	%
5	No-load speed	n_o			47 000	36 400	rpm
6	No-load current (with shaft ø 1,0 mm)	I_o			0,047	0,016	A
7	Stall torque	M_H			0,73	0,58	mNm
8	Friction torque, static	C_o			0,016	0,016	mNm
9	Friction torque, dynamic	C_v			$8,0 \cdot 10^{-7}$	$8,0 \cdot 10^{-7}$	mNm/rpm
10	Speed constant	k_n			8 421	3 282	rpm/V
11	Back-EMF constant	k_E			0,119	0,305	mV/rpm
12	Torque constant	k_M			1,13	2,91	mNm/A
13	Current constant	k_I			0,882	0,344	A/mNm
14	Slope of n-M curve	$\Delta n/\Delta M$			67 575	66 533	rpm/mNm
15	Terminal inductance, phase-phase	L			26	187	µH
16	Mechanical time constant	τ_m			6	6	ms
17	Rotor inertia	J			0,0095	0,0095	gcm²
18	Angular acceleration	$\alpha_{max.}$			772	607	$\cdot 10^3$rad/s²
19	Thermal resistance	$R_{th\,1}$ / $R_{th\,2}$	14 / 88,0				K/W
20	Thermal time constant	τ_{w1} / τ_{w2}	1 / 149				s
21	Operating temperature range:						
	– motor		– 20 ... +100				°C
	– coil, max. permissible		+125				°C
22	Shaft bearings		ball bearings, preloaded				
23	Shaft load max.:						
	– radial at 10 000/50 000 rpm (3,7 mm from mounting flange)		2,0 / 1,5				N
	– axial at 10 000/50 000 rpm (push-on only)		0,6 / 0,2				N
	– axial at standstill (push-on only)		10				N
24	Shaft play:						
	– radial	≤	0,012				mm
	– axial	=	0				mm
25	Housing material		aluminium, black anodized				
26	Weight		2,5				g
27	Direction of rotation		electronically reversible				

Recommended values - mathematically independent of each other

					006 B	012 B	
28	Speed up to [2]	$n_{e\,max.}$			100 000	100 000	rpm
29	Torque up to [1][2]	$M_{e\,max.}$			0,373	0,377	mNm
30	Current up to [1][2]	$I_{e\,max.}$			0,371	0,146	A

[1] at 40 000 rpm
[2] thermal resistance $R_{th\,2}$ by 55% reduced
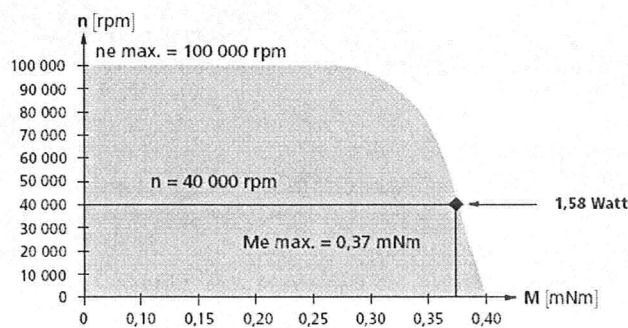
Recommended area for continuous operation

For details on technical information and lifetime performance refer to pages 72-75.

Specifications subject to change without notice.

▨▨▨ **FAULHABER**

Planetary Gearheads

25 mNm

For combination with (overview on page 14-15)
DC-Micromotors:
0615
Brushless DC-Servomotors:
0620

Series 06/1

	06/1	06/1 K
Housing material	steel	steel
Geartrain material	steel	steel
Recommended max. input speed for:		
– for continuous operation	8 000 rpm	8 000 rpm
Backlash, typical, at no-load	≤ 3°	≤ 3°
Bearings on output shaft	sintered sleeve bearings	ball bearings
Shaft load, max.		
– radial	≤ 0,5 N (3,5 mm from mounting face)	≤ 5 N (3,9 mm from mounting face)
– axial	≤ 0,5 N	≤ 3 N
Shaft press fit force, max.	≤ 3,5 N	≤ 5 N
Shaft play (on bearing output):		
– radial	≤ 0,03 mm	≤ 0,02 mm
– axial	≤ 0,1 mm	≤ 0,05 mm
Operating temperature range	– 30° … + 100° C	– 30° … + 100° C

Specifications

reduction ratio	weight without motor	length without motor	length with motor		output torque continuous operation	output torque intermittent operation	direction of rotation (reversible)	efficiency
		L2	0615 C L1	0620 C L1	M max.	M max.		
	g	mm	mm	mm	mNm	mNm		%
4 :1	2,0	9,2	24,2	29,2	25	35	=	90
16 :1	2,8	11,9	26,9	31,9	25	35	=	80
64 :1	3,4	14,6	29,6	34,6	25	35	=	70
256 :1	4,0	17,3	32,3	37,3	25	35	=	60
1 024 :1	4,4	20,0	35,0	40,0	25	35	=	55
4 096 :1	5,0	22,7	37,7	42,7	25	35	=	48

06/1

06/1 K
L1, L2 = + 1
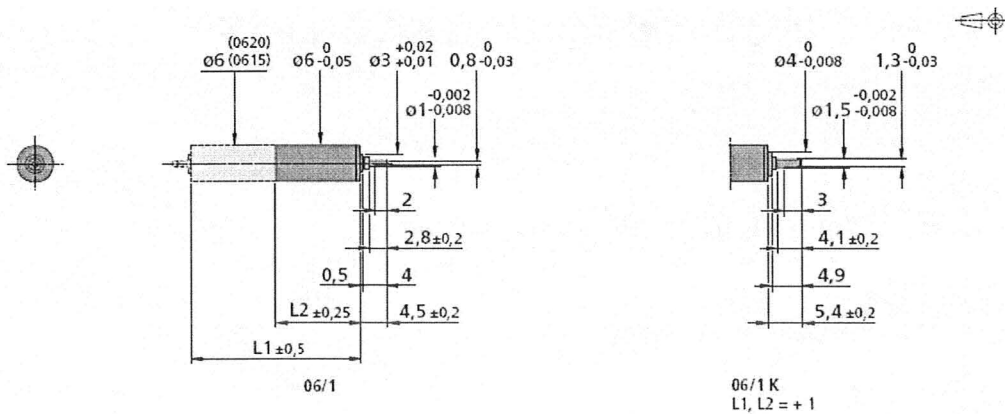
For details on technical information and lifetime performance
refer to pages 104-108.
Edition 2006-2007

Specifications subject to change without notice.

www.faulhaber-group.com

212

Gizmo'szone

gizmoszone.com

Motor Performance Chart

Motor Model: 6mm DC Coreless Motor of GH612 series
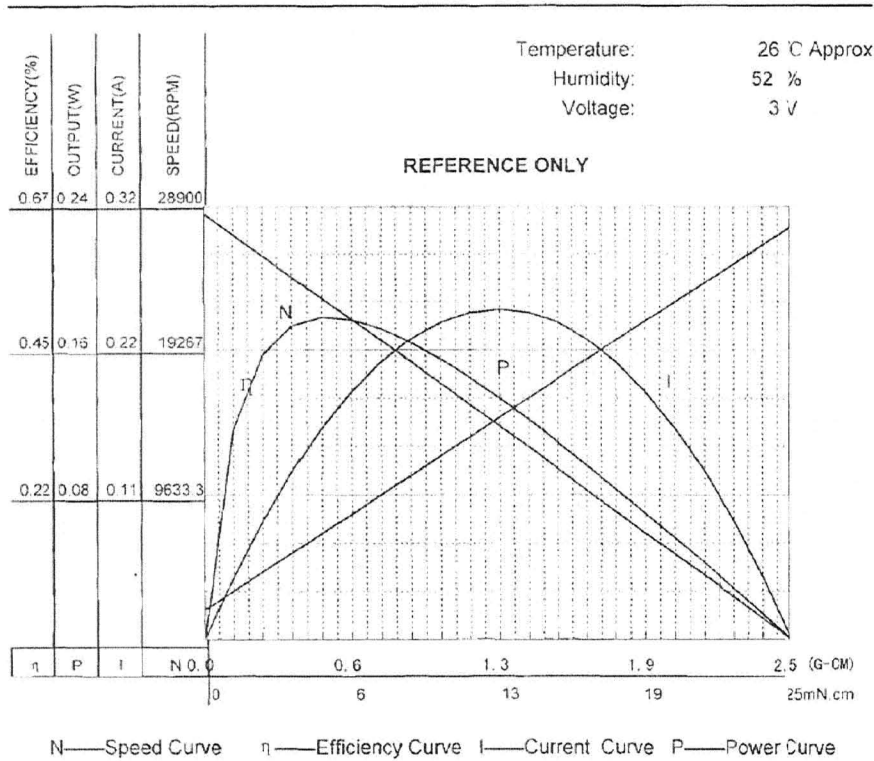
Performance(in all ambient temperature of 25/30 C)

Motor tested rapidly to prevent significant temperature rise.

At a constant voltage of
direction   CW

Temperature:	26 °C Approx		
Humidity:	52 %		
Voltage:	3 V		

REFERENCE ONLY

EFFICIENCY(%)	OUTPUT(W)	CURRENT(A)	SPEED(RPM)
0.67	0.24	0.32	28900
0.45	0.16	0.22	19267
0.22	0.08	0.11	9633.3
η	P	I	N 0.0

0.6   1.3   1.9   2.5 (G-CM)

0   6   13   19   25mN.cm

N——Speed Curve   η——Efficiency Curve   I——Current Curve   P——Power Curve

At No Load		
Speed	28110	RPM
Current	0.0216	AMPS
At Rated Load	0.4	G-CM
Speed	23620	RPM
Current	0.0678	AMPS
At Stall (extrapolated)		
Torque	2.50	G-CM
Current	0.31	AMPS
At maximum efficiency		
Efficiency	49.18	%
Torque	0.5	G-CM
Speed	22488	RPM
Current	0.08	AMPS
Output	0.116	Watts
At maximum power output		
Output	0.18	Watts
Torque	1.25	G-CM
Speed	14055	RPM
Current	0.16	AMPS

Gizmo'szone

gizmoszone.com

Ø6mm Miniature Planetary Gear Motors

GH612 SERIES

Mechanical Details And Specifications

Part no.	GH6121S	GH6122S	GH6123S	GH6124S	
Operating Voltage	3V	3V	3V	3V	Motor Spec
Speed (approx.)	31000 rpm	31000 rpm	31000 rpm	31000 rpm	
No. of gear stages	1	2	3	4	Gearhead Spec
Gear Ratio	1:5.14	1:26.45	1:136.02	1:699.55	
Voltage	3V	3V	3V	3V	No Load
Speed (approx.)	5000 rpm	1000 rpm	200 rpm	40 rpm	
Current(approx.)	40 mA	40 mA	40 mA	40 mA	
Maximum Torque (approx.)	5 gcm	25 gcm	120 gcm	200 gcm	Max. Output Torque
Length with motor L1	17.80 mm	19.60 mm	21.40 mm	23.20 mm	Physical
Motor Length L2	12 mm	12 mm	12 mm	12 mm	
Shaft Diameter	1.5 mm	1.5 mm	1.5 mm	1.5 mm	
Weight	1.6 g	1.7 g	1.8 g	1.9 g	
Gearhead Material	Plastic	Plastic	Plastic	Plastic	

Gearhead Layout

Ø6.00   L1
Ø1.50   L2
Red (+)
Blue (-)
Ø2.60
1.70
5.40
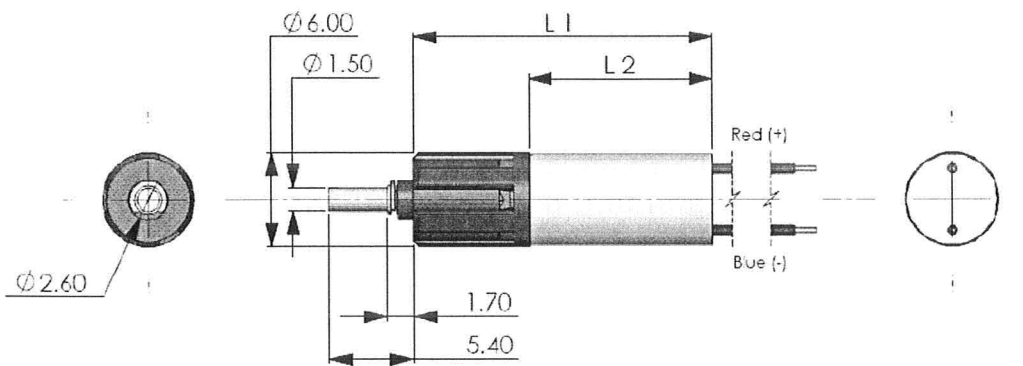
Nominal Tolerance +/- 0.1mm unless otherwise specified   Unit: mm

Specifications subject to change without notice.

214